Resul Özdemir

A Ph.D. Thesis

AGU 2021

FUNCTIONALIZED LOW LUMO [1]BENZOTHIENO[3,2-B][1]BENZOTHIOPHENE (BTBT)-BASED MOLECULAR SEMICONDUCTORS FOR ORGANIC FIELD EFFECT TRANSISTORS

A THESIS
SUBMITTED TO THE DEPARTMENT OF MATERIALS SCIENCE
AND MECHANICAL ENGINEERING
AND THE GRADUATE SCHOOL OF ENGINEERING AND SCIENCE
OF ABDULLAH GUL UNIVERSITY
IN PARTIAL FULFILLMENT OF THE REQUIREMENTS
FOR THE DEGREE OF
DOCTOR OF PHILOSOPHY

By
Resul Özdemir
February 2021

FUNCTIONALIZED LOW LUMO [1]BENZOTHIENO[3,2-B][1]BENZOTHIOPHENE (BTBT)-BASED MOLECULAR SEMICONDUCTORS FOR ORGANIC FIELD EFFECT TRANSISTORS

A THESIS
SUBMITTED TO THE DEPARTMENT OF MATERIALS SCIENCE AND MECHANICAL ENGINEERING
AND THE GRADUATE SCHOOL OF ENGINEERING AND SCIENCE OF ABDULLAH GUL UNIVERSITY
IN PARTIAL FULFILLMENT OF THE REQUIREMENTS
FOR THE DEGREE OF
DOCTOR OF PHILOSOPHY

By
Resul Özdemir
February 2021

SCIENTIFIC ETHICS COMPLIANCE

I hereby declare that all information in this document has been obtained in accordance with academic rules and ethical conduct. I also declare that, as required by these rules and conduct, I have fully cited and referenced all materials and results that are not original to this work.

Resul Özdemir

REGULATORY COMPLIANCE

Ph.D. thesis titled Functionalized Low LUMO [1]benzothieno[3,2-b][1]benzothiophene (BTBT)-Based Molecular Semiconductors for Organic Field Effect Transistors has been prepared in accordance with the Thesis Writing Guidelines of the Abdullah Gül University, Graduate School of Engineering & Science.

Prepared By	Advisor
Resul Özdemir	Prof. Dr. Hakan Usta

Deputy Head of the Materials Science and Mechanical Engineering Program
Asst. Prof. Fahri Alkan

ACCEPTANCE AND APPROVAL

Ph.D. thesis titled Functionalized Low LUMO [1]benzothieno[3,2-b][1]benzothiophene (BTBT)-Based Molecular Semiconductors for Organic Field Effect Transistors and prepared by Resul Özdemir has been accepted by the jury in the Materials Science and Mechanical Engineering Graduate Program at Abdullah Gül University, Graduate School of Engineering & Science.

……….. /……….. / ………..

(Thesis Defense Exam Date)

JURY:

Advisor : (Prof. Dr. Hakan Usta)

Member : (Prof. Dr. Ertuğrul Şahmetlioğlu)

Member : (Assoc. Prof. Evren Mutlugün)

Member : (Assoc. Prof. M. Serdar Önses)

Member : (Asst. Prof. Fahri Alkan)

APPROVAL:

The acceptance of this Ph.D. thesis has been approved by the decision of the Abdullah Gül University, Graduate School of Engineering & Science, Executive Board dated ….. /….. / ……….. and numbered ………….……. .

……….. /……….. / ………..

(Date)

Graduate School Dean
Prof. Dr. Hakan USTA

ABSTRACT

FUNCTIONALIZED LOW LUMO [1]BENZOTHIENO[3,2-B][1]BENZOTHIOPHENE (BTBT)-BASED MOLECULAR SEMICONDUCTORS FOR ORGANIC FIELD EFFECT TRANSISTORS

Resul Özdemir
Ph.D. in Materials Science and Mechanical Engineering
Advisor: Prof. Dr. Hakan Usta

February 2021

DAcTTs have provided an excellent π-framework for the development of high mobility *p*-type molecular semiconductors in the past decade. However, *n*-type DAcTTs are rare and their electron transporting characteristics remain largely unexplored. In the second chapter of this thesis, the first example of an *n*-type BTBT-based semiconductor, **D(Ph$_F$CO)-BTBT**, has been realized via a two-step transition metal-free process without using chromatographic purification. The corresponding TC/BG-OFET devices demonstrated $\mu_{e\ (max)}$ = ~0.6 cm^2/Vs and I_{on}/I_{off} ratio = 10^7-10^8. The large band-gap BTBT π-core is a promising candidate for high mobility *n*-type organic semiconductors and, combination of very large intrinsic charge transport capabilities and optical transparency, may open a new perspective for next-generation (opto)electronics.

In the third chapter of this thesis, a series of BTBT-based small molecules, **D(C$_7$CO)-BTBT**, **C$_7$CO-BTBT-CC(CN)$_2$C$_7$**, and **D(C$_7$CC(CN)$_2$)-BTBT**, have been developed in “S-F-BTBT-F-S (F/S: functional group/substituent)” molecular architecture. Combining with **D(Ph$_F$CO)-BTBT**, a molecular library with systematically varied chemical structures has been studied herein for the first time for low LUMO DAcTTs, and key relationships have been elucidated. The molecular engineering perspectives presented in this thesis may give unique insights into the design of novel electron transporting thienoacenes for unconventional optoelectronics.

Keywords: Organic Semiconductor, Small Molecule, N-type (electron transporting), low LUMO energy level, Organic Field Effect Transistors (OFETs).

ÖZET

YENİ [1]BENZOTHIENO[3,2-B][1]BENZOTHIOPHENE (BTBT)-TEMELLİ MOLEKÜLER YARIİLETKENLER VE ORGANİK ALAN ETKİLİ TRANSİSTÖR UYGULAMALARI

Resul Özdemir
Malzeme Bilimi ve Makine Mühendisliği Anabilim Dalı Doktora
Tez Yöneticisi: Prof. Dr. Hakan Usta

Şubat-2021

Son on yılda yüksek mobilite veren *p*-tipi moleküler yarı iletkenlerin geliştirilmesinde mükemmel bir π-çerçevesi olan DAcTTs'ler baş rolü oynamıştır. Bununla birlikte, *n*-tipi DAcTT'ler literatürde son derece nadirdir ve elektron taşıma özellikleri büyük ölçüde keşfedilmemiştir. Bu tezin ikinci bölümünde, literatürdeki ilk *N*-tipi BTBT tabanlı yarıiletken olan **D(Ph_FCO)-BTBT**, iki aşamada geçiş metali ve kromatografik saflaştırma kullanılmadan elde edilmiştir. Organik alan etkili transistör cihazları $\mu_{e\ (max)}$ = ~ 0.6 cm^2/V.s ve $I_{on}/I_{off} = 10^7$-10^8 oranı göstermiştir. Bu sonuçlar, geniş bant aralıklı BTBT π-çerçevesinin yüksek yük taşıma kabiliyetine sahip *n*-tipi organik yarı iletkenlerin geliştirilmesi için ümit verici bir aday olduğunu göstermiştir. Bu yarıiletkenin sunduğu yüksek yük taşıma kapasitesi ile optik şeffaflığın birleşimi, (opto) elektronik uygulamalara yeni bir bakış açısı getirebilir.

Bu tezin üçüncü bölümünde bir dizi BTBT-temelli küçük molekül, **D(C_7CO)-BTBT**, **C_7CO-BTBT-CC($CN)_2C_7$** ve **D($C_7CC(CN)_2$)-BTBT**, "S-F-BTBT-F-S (F/S: fonksiyonel grup/sübstitünet)" moleküler mimarisinde dizayn edildi ve sentezlendi. **D(Ph_FCO)-BTBT** ile birleştirildiğinde, düşük LUMO'lu DAcTT'ler için sistematik olarak çeşitli kimyasal yapılara sahip bir moleküler kitaplık burada ilk kez geliştirildi ve temel ilişkiler açıklığa çıkarıldı. Bu çalışmada sunulan moleküler mühendislik perspektifleri, optoelektronikler için yeni elektron taşıyan tiyenoasenlerin tasarımına benzersiz bir bakış açısı sağlayabilir.

Anahtar kelimeler: Organik yarıieletken, Küçük Molekül, N-Tipi (elektron taşıma), Düşük LUMO enerji seviyesi, Organik Alan Etkili Transistörler.

Acknowledgements

I would like to take a moment to thank everyone who helped me along with this long journey.

First, I wish to express my sincere gratitude to my advisor, Prof. Hakan Usta, for his patience and continuous support of my Ph.D study. He has such immense knowledge which helped me in all the time of research. His enthusiasm and passion for science have made an intense impact on my life. My Ph.D study would not have been possible without his guidance, inspiration and encouragement. I could not have had a better advisor or mentor.

I would like to thank my thesis committee: Prof. Evren Mutlugün and Prof. Serdar Önses, for their insights and hard questions which helped me to widen my research vision from different perspectives. Without their feedback, I would not have made it.

To my lab-mates, İbrahim, Ahmet Faruk, Ayşe and Hüsniye: thank you for your support during my research and everything we have been through in the last four years.

My sincere thanks to my parents, my brothers, my in-laws, who believes in me, and who supports me spiritually to reach my goal.

Finally, to my wife, Fundagül, and my daughters, Zeynep Serra & Elif Selin: your love and endless support helped me through the tough times. Without you guys, I would not have made it. It is time to celebrate; you earned this degree right along with me.

This Ph.D study was supported by the Scientific and Technological Research Council of Turkey (TUBITAK), grant number of 216M430.

Table of Contents

1. **OVERVIEW OF THE FIELD-EFFECT TRANSISTORS 1**

1.1 OFET Architecture and Operation 6
1.2 Fabrication Techniques.. 12
1.2.1 Solution-Processed Deposition 13
1.2.2 Physical Vapor Deposition... 15
1.3 Organic Materials for Field-Effect Transistors 15
1.3.1 P-Type Molecular/Polymeric Semiconductors 20
1.3.2 N-Type Molecular/Polymeric Semiconductors... 28

2. **HIGH ELECTRON MOBILITY IN [1]BENZOTHIENO[3,2-B][1]BENZOTHIOPHENE (BTBT)-BASED FIELD-EFFECT TRANSISTORS:TOWARD N-TYPE BTBTS.. 37**

2.1 Introduction 37
2.2 Experimental Section 40
2.2.1 Materials and Methods.. 40
2.2.2 Field-Effect Transistors and Characterization... 41
2.2.3 Synthesis and Characterization 42
2.2.4 Theoretical Methodology 43
2.3 Result and Discussion 43
2.3.1 Theoretical Calculations, Synthesis and Characterization 43
2.3.2 Single-Crystal Structure Analysis... 48
2.3.3 Optical and Electrochemical Properties 50
2.3.4 Thin-Film Microstructure/Morphology and Field-Effect Transistor Charazterization........... 54
2.4 Conclusions.. 64

3. **ENGINEERING FUNCTIONALIZED LOW LUMO [1]BENZOTHIENO[3,2-B][1]BENZOTHIOPHENES (BTBTS): UNUSUAL MOLECULAR AND CHARGE TRANSPORT PROPERTIES... 66**

3.1 Introduction 66
3.2 Experimental Section 71
3.2.1 Materials and Methods.. 71
3.2.2 Synthesis and Structural Characterization.. 72
3.2.3 Field-Effect Transistors Fabrication and Characterization..................................... 74
3.3 Results and Discussion.. 75
3.3.1 Synthesis, Characterization and Thermal Properties... 75
3.3.2 Single-Crystal Structure and Intermolecular Interactions 85
3.3.3 Photophysical and Electrochemical Properties 91
3.3.4 Thin-Film Microstructure/Morphology and Field-Effect Transistor Characterization 98
3.4 Conclusions.. 103

4. **CONCLUSIONS AND FUTURE PROSPECTS 105**

4.1 Conclusions.. 105
4.2 Societal Impact and Contribution to Global SustainabilitY 107
4.3 Future Prospects 108

List of Figures

Figure 1.1 Example of an 6 in × 6 in RFID circuit array fabricated on a polymeric substrate 2
Figure 1.2 Development of charge carrier mobility in OFETs over the past 25 years (measured under ambient conditions) 3
Figure 1.3 Example of a roll-to-roll coated OPV device on a PET foil (Polyethylene Terephthalate) substrate 4
Figure 1.4 Schematic view of various device architecture in OFETs, top contact/bottom gate (A), bottom contact/bottom gate (B), top contact/top gate (C), bottom contact/top gate (D) 7
Figure 1.5 On-state of OFETs and corresponding polarization in insulator layer and accumulation of charge carriers in organic semiconductor layer when positive gate voltage is applied (A), and negative gate voltage is applied (B) 8
Figure 1.6 Energy band diagrams of HOMO and LUMO levels at V_G=0 (A), during *p*-channel device operation (B and D), and *n*-channel device operation (C and E)... 10
Figure 1.7 A typical current-voltage characteristics of OFET, output curve (A) and transfer curve (B) 12
Figure 1.8 Schematic representation of π-conjugated (benzene) and non-conjugated (cyclohexane) units and corresponding overlapping/non-overlapping orbitals, HOMO/LUMO molecular orbitals and topologies of benzene and pentacene (fused π-conjugated core), structural connectivity in a highly planar π-core which results in conductivity, and intermolecular interaction in the solid state 16
Figure 1.9 Energetic stabilization of organics upon π-conjugation 17
Figure 1.10 Schematic representation of charge carriers motion between LUMOs and HOMOs of neighboring molecules/polymeric segments by hopping mechanism . 18
Figure 1.11 Energy band diagram of an organic semiconductor 19
Figure 1.12 Chemical structure of the first-generation *p*-type semiconducting polymers 21
Figure 1.13 Chemical structure of fused dithieno[3,2-b:2',3'-d]pyrrole (DTP) based *p*-type semiconducting polymers 22
Figure 1.14 Chemical structure of fused thiophene based *p*-type semiconducting polymers 23
Figure 1.15 Chemical structure of thienylenevinylene based *p*-type semiconducting polymers 23
Figure 1.16 Chemical structure of heteroarene based *p*-type semiconducting polymers 24
Figure 1.17 Chemical structure of isoindigo based *p*-type semiconducting polymers ... 25
Figure 1.18 Chemical structure of diketopyrrolopyrrole based *p*-type semiconducting polymers 26
Figure 1.19 Chemical structure of oligothiophene based *p*-type semiconducting small molecules 27
Figure 1.20 Chemical structure of heteroacene based *p*-type semiconducting small molecules 28
Figure 1.21 Chemical structure of the first-generation *n*-type semiconducting polymers 30
Figure 1.22 Chemical structure of NDI and PDI based *n*-type semiconducting polymers 31
Figure 1.23 Chemical structure of other *n*-type semiconducting polymers 33

Figure 1.24 Chemical structure of phthalocyanine based *n*-type semiconducting small molecules 34
Figure 1.25 Chemical structure of oligothiophene based *n*-type semiconducting small molecules 35
Figure 1.26 Chemical structure of fullerene based *n*-type semiconducting small molecules 36
Figure 1.27 Chemical structure of some high performing *n*-type semiconducting small molecules 36
Figure 2.1 A. Chemical structures of [1]Benzothieno[3,2-b][1]benzothiophene (BTBT) π-core and *p*-type molecular semiconductors DPh-BTBT, C_n-BTBT, and DPV-BTBT reported in the literature. B. synthesis of the current *n*-type semiconductor D(Ph_FCO)-BTBT 38
Figure 2.2 Chemical structures of *p*-type BTBT-based molecular semiconductors reported in the literature 38
Figure 2.3 Theoretical (DFT/B3LYP/6-31G**) HOMO/LUMO energy levels with topographical orbital representations for different functionalization positions on the BTBT π-core 44
Figure 2.4 Theoretical (DFT/B3LYP/6-31G**) HOMO/LUMO energy levels with topographical orbital representations for D(Ph_FCO)-BTBT and C_8-BTBT 45
Figure 2.5 ^{1}H NMR spectrum of D(Ph_FCO)-BTBT measured in $CDCl_3$ 46
Figure 2.6 Positive ion and linear mode MALDI TOF-MS spectrum of D(Ph_FCO)-BTBT 47
Figure 2.7 (A) Thermogravimetric analysis (TGA) curve at reduced pressure (~0.1 Torr) and (B) Differential scanning calorimetry (DSC) measurement curve under N_2 in the second heating–cooling cycle for D(Ph_FCO)-BTBT at a temperature ramp of 10 °C·min^{-1} 47
Figure 2.8 A. Capped-stick drawings of the crystal structure of D(Ph_FCO)-BTBT showing the corresponding dihedral and torsion angles and π-backbone coplanarity. B. Perspective views of the molecular arrangements along the *a,c*-axes and *b,c*-axes showing the alternately stacked layers and the two-dimensional herringbone-like packing, respectively. Inset shows the pairs of D(Ph_FCO)-BTBT molecules in the herringbone motif with CH···π(benzene/thiophene) (a = 3.45 Å; a$'$ = 3.25 Å/c = 3.46 Å), S···π (thiophene) (b = 3.38 Å), and F···π(pentafluorobenzene) (d = 3.30 Å; d$'$ = 3.16 Å) contacts 50
Figure 2.9 (A) Optical absorption spectra of D(Ph_FCO)-BTBT and the reference molecule C_8-BTBT in dichloromethane solutions, and cyclic voltammogram (inset) for D(Ph_FCO)-BTBT in dichloromethane (0.1 M $Bu_4N^+PF_6^-$, scan rate = 50 mV·s^{-1}). (B) Experimental HOMO/LUMO energy levels for D(Ph_FCO)-BTBT and C_8-BTBT, and topographical orbital representations (DFT/B3LYP/6-31G**) for D(Ph_FCO)-BTBT 52
Figure 2.10 Optical absorption spectra of D(Ph_FCO)-BTBT in dichloromethane solution and as vapor-deposited thin-film (30 nm) 52
Figure 2.11 Transmission optical spectrum of a 30 nm vapor-deposited thin-film of D(PhFCO)-BTBT on glass demonstrating the impressive transparency of this semiconductor between 400 and 800 nm 53
Figure 2.12 Cyclic voltammogram of C_8-BTBT in dichloromethane solution (0.1 M $Bu_4N^+PF_6^-$, scan rate = 50 mVs^{-1}) recorded using the exact same electrochemical set-up employed in this study 53
Figure 2.13 (A) Optical absorption spectra of D(C_7CO)-BTBT and the reference molecule C8-BTBT in dichloromethane solutions, and cyclic voltammogram

(inset) for D(C7CO)-BTBT in dichloromethane (0.1 M $Bu_4N^+PF_6^-$, scan rate = 50 $mV \cdot s^{-1}$). (B) Experimental HOMO/LUMO energy levels for D(C_7CO)-BTBT and C_8-BTBT, and topographical orbital representations (DFT/B3LYP/6-31G**) for D(C_7CO)-BTBT 54
Figure 2.14 (A) Transfer (V_{SD} = 100 V) and (B) Output characteristics for n^{++}-Si/SiO_2(200 nm)/HMDS/ D(Ph_FCO)-BTBT(30 nm)/LiF (1 nm)-Au(50 nm) OFET device. (C) Tapping mode atomic force microscopy (AFM) topographic image and two-dimensional grazing incidence X-ray diffraction (2D-GIXD) patterns for D(Ph_FCO)-BTBT thin-films (30 nm) vapor-deposited at 100 °C on n^{++}-Si/SiO_2(200 nm)/HMDS. Scale bar denotes 2 μm. (D) Views of the packing arrangement in the D(Ph_FCO)-BTBT semiconductor layer showing the *edge-on* molecular orientation (*out-of-plane*) and the herringbone packing motif (*in-plane*). Inset shows the BFDH (Bravais, Friedel, Donnay and Harker) theoretical crystal morphology and the corresponding crystalline planes 56
Figure 2.15 Tapping mode atomic force microscopy (AFM) topographic images of D(Ph_FCO)-BTBT thin-films vapor-deposited at room temperature 25 °C, 70 °C, and 100 °C on n^{++}-Si/SiO_2(200 nm)/HMDS and n^{++}-Si/SiO_2(200 nm) substrates 57
Figure 2.16 Tapping mode atomic force microscopy (AFM) topographic images of D(Ph_FCO)-BTBT thin-films vapor-deposited at 120 °C on n^{++}-Si/SiO_2(200 nm)/HMDS and n^{++}-Si/SiO_2(200 nm) substrates showing poor inter-grain connectivity 57
Figure 2.17 Two dimensional grazing incidence X-ray diffraction (2D-GIXD) patterns of D(Ph_FCO)-BTBT thin-films (30 nm) vapor-deposited at various temperatures (25 °C, 70 °C, 100 °C) on n^{++}-Si/SiO_2(200 nm) and n^{++}-Si/SiO_2(200 nm)/HMDS 58
Figure 2.18 Topographic image of terraced islands (AFM, tapping mode, 10×10 μm) and the corresponding sectional step-height profile for D(Ph_FCO)-BTBT thin-films (30 nm) vapor-deposited at 100 °C on n^{++}-Si/SiO_2(200 nm)/HMDS 58
Figure 2.19 Transfer plots of OFET devices with channel length and width of 1000 μm and 50 μm, respectively (V_{SD} = 100 V) 59
Figure 2.20 Output plots of OFET devices for channel length and width of 1000 μm and 50 μm, respectively 60
Figure 2.21 Transfer (A) and output (B) plots for OFET devices fabricated with Ag source-drain electrodes. Note that OFETs fabricated with Al source-drain electrodes did not operate 62
Figure 2.22 Crystal structures of C_8-BTBT (A) and D(Ph_FCO)-BTBT (B) along the *a*,*b*-axes and *b*,*c*-axes, respectively, underscoring the formation of two-dimensional *in-plane* herringbone-like packing. Alkyl chains of C_8-BTBT are omitted for clarity. DFT-estimates of the effective transfer integrals (in meV) for holes (t_h) and electrons (t_e) for the selected dimer pairs in face-to-edge (black dotted lines) and edge-to-edge manners (red dotted lines) are also shown 63
Figure 2.23 The first example of an *n*-type [1]Benzothieno[3,2-b][1]benzothiophene (BTBT)–based organic small molecular semiconductor. TC/BG-OFET devices based on physical vapor deposited thin films showed electron mobility up to ~0.6 cm^2/V. 65
Figure 3.1 The S-F-BTBT-F-S (F/S: functional group/substituent) design architecture for functionalized low LUMO BTBT molecules indicating the contributions of each substructure and the chemical structures of D(C_7CO)-BTBT, C_7CO-BTBT-CC$(CN)_2C_7$, and D(C_7CC$(CN)_2$)-BTBT developed in this study and D(Ph_FCO)-BTBT developed in our previous study 68

Figure 3.2 Theoretical (DFT/B3LYP/6-31G**) HOMO/LUMO energy levels of D(C_7CO)-BTBT along with topographical orbital representations for different functionalization positions 69

Figure 3.3 Theoretical (DFT/B3LYP/6-31G**) HOMO/LUMO energy levels of D(C_7CC(CN)$_2$)-BTBT along with topographical orbital representations for different functionalization positions 69

Figure 3.4 Synthesis of highly soluble functionalized low LUMO BTBT molecules D(C_7CO)-BTBT, C_7CO-BTBT-CC(CN)$_2$C$_7$, and D(C_7CC(CN)$_2$)-BTBT........ 76

Figure 3.5 ^{1}H NMR spectra of D(C_7CO)-BTBT measured in $CDCl_3$ 76

Figure 3.6 ^{13}C NMR spectra of D(C_7CO)-BTBT measured in $CDCl_3$ 77

Figure 3.7 Positive ion and linear mode MALDI TOF-MS spectrum of D(C_7CO)-BTBT........ 77

Figure 3.8 ^{1}H NMR spectra of C_7CO-BTBT-CC(CN)$_2$C$_7$ measured in $CDCl_3$........ 78

Figure 3.9 ^{13}C NMR spectra of C_7CO-BTBT-CC(CN)$_2$C$_7$ measured in $CDCl_3$ 78

Figure 3.10 Positive ion and linear mode MALDI TOF-MS spectrum of C_7CO-BTBT-CC(CN)$_2$C$_7$........ 79

Figure 3.11 ^{1}H NMR spectra of D(C_7CC(CN)$_2$)-BTBT measured in $CDCl_3$........ 79

Figure 3.12 ^{13}C NMR spectra of D(C_7CC(CN)$_2$)-BTBT measured in $CDCl_3$........ 80

Figure 3.13 Positive ion and linear mode MALDI TOF-MS spectrum of D(C_7CC(CN)$_2$)-BTBT 80

Figure 3.14 FT-IR spectra of D(C_7CO)-BTBT, C_7CO-BTBT-CC(CN)$_2$C$_7$, and D(C_7CC(CN)$_2$)-BTBT showing C=O (1680 cm^{-1}) and C≡N (2227 cm^{-1}) stretching vibrational peak........ 81

Figure 3.15 The ^{1}H NMR spectra of D(C_7CC(CN)$_2$)-BTBT (top), C_7CO-BTBT-CC(CN)$_2$C$_7$ (middle), and D(C_7CO)-BTBT (bottom) in $CDCl_3$ showing the chemical shifts of non-exchangeable aromatic protons “a-f” 83

Figure 3.16 A. Thermogravimetric analysis (TGA) and B. Differential scanning calorimetry (DSC) measurement curves of D(C_7CO)-BTBT, C_7CO-BTBT-C(CCN$_2$)C$_7$, and D(C_7CC(CN)$_2$)-BTBT at a temperature ramp of 10 °C/min under N_2 85

Figure 3.17 Ball and stick drawings of the molecular structures showing the corresponding torsion/dihedral angles (between the BTBT π-core and functional groups) and π-backbone coplanarity, perspective views of the molecular arrangements and packings along the crystallographic *a*,*c*-axes and *b*,*c*-axes showing the alternately stacked layers and the herringbone motifs/packing, and the intermolecular interactions for D(C_7CO)-BTBT (A) (*a* = S···S; *b*, *c*, *e* = C-H(phenyl)···π(phenyl); *d* = S···π(thienyl); *f* = C=O(δ^-)···C(δ^+)=O), D(C_7CC(CN)$_2$)-BTBT (B) (a = N≡C···π(phenyl); b, c = C=C(dicyanovinylene)···π(thienyl); d, e = C-H(phenyl)··· π(thienyl/phenyl)), and our previously reported *n*-type semiconductor D(Ph$_F$CO)-BTBT (C) (*a* = S···S; *b*, *e* = C-H(phenyl)···π(phenyl); *c* = S···π(thienyl); *d* = C-H(phenyl)···π(thienyl); *f* = C=O···π(phenyl); *g* = C=O(δ^-)···C(δ^+)=O; *h* = F··· π(pentafluorophenyl)). Heptyl chains are omitted for clarity in the herringbone motif/packing in panel B 88

Figure 3.18 Computationally optimized (DFT/B3LYP/6-31G**) molecular structures for D(C_7CO)-BTBT (A) and D(C_7CC(CN)$_2$)-BTBT (B) showing the torsion and dihedral angles ($\theta_{torsion}$ and $\theta_{dihedral}$) between BTBT π-system and carbonyl/dicyanovinylene functional groups........ 89

Figure 3.19 Computationally optimized (DFT/B3LYP/6-31G**) molecular structure of a hypothetical dicyanovinylene-functionalized BTBT compound, D(HCC(CN)$_2$)-

BTBT, showing the dihedral angle ($\theta_{dihedral}$) between BTBT π-system and dicyanovinylene functional groups 89
Figure 3.20 A. Optical absorption spectra (in dichloromethane and as spin-coated thin films), B. Cyclic voltammograms *vs.* Ag/AgCl (3.0 M NaCl) (in 0.1 M $Bu_4N^+PF_6^-$ dichloromethane, scan rate = 50 mV/s), and C. Experimentally determined frontier molecular orbital energies along with topographical orbital representations (DFT/B3LYP/6-31G**) for D(C_7CO)-BTBT, C_7CO-BTBT-C(CCN_2)C_7, and D(C_7CC(CN)$_2$)-BTBT 92
Figure 3.21 Optical absorption spectra of D(C_7CO)-BTBT (A), C_7CO-BTBT-CC(CN)$_2$$C_7$ (B), and D(C_7CC(CN)$_2$)-BTBT (C) in hexane, tetrahydrofuran (THF), dichloromethane (DCM), N,N’-dimethylformamide (DMF), and dimethyl sulfoxide (DMSO) 93
Figure 3.22 Optical absorption spectrum and cyclic voltammogram (0.1 M $Bu_4N^+PF_6^-$, scan rate = 50 mV/s) of C_8-BTBT in dichloromethane solutions 95
Figure 3.23 Theoretical (DFT/B3LYP/6-31G**) frontier orbital energies along with topographical representations for conformations of D(C_7CC(CN)$_2$)-BTBT with varied dihedral angles ($\theta_{dihedral}$) between the BTBT π-system and dicyanovinylene units 95
Figure 3.24 A. Photoluminescence spectra of D(C_7CO)-BTBT (λ_{exc} = 385 nm) and D(C_7CC(CN)$_2$)-BTBT (λ_{exc} = 405 nm) in dichloromethane (1.0×10^{-5} M). The inset shows the transient photoluminescence decay profiles (λ_{exc} = 375 nm and 200 ps pulse width) measured at 410 nm and 483 nm for D(C_7CO)-BTBT and D(C_7CC(CN)$_2$)-BTBT, respectively, in dichloromethane (10^{-5} M) under nitrogen atmosphere. B. The transient photoluminescence decay profiles measured at 483 nm for D(C_7CC(CN)$_2$)-BTBT (λ_{exc} = 375 nm and 200 ps pulse width) in methanol (solid) and ethylene glycol (dashed) solutions (10^{-5} M) under nitrogen atmosphere. Inset shows the solvent viscosity-dependent (methanol (0.54 cP) and ethylene glycol (16.1 cP)) photoluminescence spectra for D(C_7CC(CN)$_2$)-BTBT 97
Figure 3.25 The solvent polarity-dependent (toluene ($f(\varepsilon,n) = 0.014$) → dichloromethane ($f(\varepsilon,n) = 0.217$) → acetonitrile ($f(\varepsilon,n) = 0.305$)) photoluminescence spectra of D(C_7CC(CN)$_2$)-BTBT (λ_{exc} = 405 nm) in solution (1.0×10^{-5} M) 97
Figure 3.26 Tapping mode atomic force microscopy (AFM) topographic images and grazing incidence X-ray diffraction (GIXRD) scans for D(C_7CO)-BTBT (A and C-left) and D(C_7CC(CN)$_2$)-BTBT (B and C-right) thin films deposited on n^{++}-Si/SiO$_2$(200 nm)/HMDS at 25 °C and 70 °C, and the molecular arrangements in the out-of-plane directions. The scale bar denotes 1 μm. D. The Bravais-Friedel-Donnay-Harker (BFDH) theoretical crystal morphologies, the views of the packing arrangements in the 2D plate-like crystalline grains, and the corresponding lattice planes. E. Transfer (V_{SD} = -100 V for D(C_7CO)-BTBT and V_{SD} = 100 V for D(C_7CC(CN)$_2$)-BTBT) characteristics for the n^{++}-Si/SiO$_2$(200 nm)/HMDS/D(C_7CO)-BTBT(30 nm)/Au(50 nm) (top) and n^{++}-Si/SiO$_2$(200 nm)/HMDS/D(C_7CC(CN)$_2$)-BTBT(30 nm)/LiF(1 nm)/Au(50 nm) (bottom) OFET devices 99
Figure 3.27 Simulated XRD powder patterns based on the single-crystal structures for D(C_7CO)-BTBT (A) and D(C_7CC(CN)$_2$)-BTBT (B) indicating the selected matching diffraction peaks and lattice planes at 2θ = 5.79(400)/8.70˚(600) and at 2θ = 5.25˚(100), respectively 100

Figure 3.28 Grazing incidence X-ray diffraction (GIXD) of D(C_7CO)-BTBT (30 nm) thin film deposited on n^{++}-Si/SiO_2(200 nm)/HMDS substrate at a deposition temperature of 25 °C and the corresponding (020) lattice plane/molecular arrangement 100
Figure 3.29 A unique molecular library of functionalized low LUMO BTBT semiconductors was developed and studied in detail to reveal key design principles for electron transport in DAcTTs........ 104

List of Tables

Table 2.1 Crystal data and refinement parameters for D(Ph_FCO)-BTBT 49
Table 2.2 Representative field-effect transistor device characteristics using D(Ph_FCO)-BTBT as channel layer 62
Table 2.3 DFT-calculated transfer integrals for holes (t_h) and electrons (t_e) in D(Ph_FCO)-BTBT dimers 64
Table 2.4 DFT-calculated transfer integrals for holes (t_h) and electrons (t_e) in C_8-BTBT dimers.. 64
Table 3.1 Crystal data and refinement parameters for D(C_7CO)-BTBT and D(C_7CC(CN)$_2$)-BTBT 90

List of Abbreviations

OFETs	Organic Fiel Effect tTransistors
BTBT	[1]benzothieno[3,2-b][1]benzothiophene
DAcTT	Diacene-fused Thienothiophene
HOMO	Highest Occupied Molecular Orbital
LUMO	Lowest Unoccupied Molecular Orbital
P-Type	Hole Transporting Semiconductor
N-Type	Electron Transporting Semiconductor
AFM	Atomic Force Microscopy
GIXD	Grazing Incidence X-ray Diffraction
TGA	Thermogravimetric Analysis
DSC	Differential Scanning Calorimetry
PVD	Physical Vapor Deposition

Chapter 1

Overview of the Field-Effect Transistors

Plastic materials are known as excellent insulators so far since they are used almost everywhere requiring electrical isolation. In the 1970s the discovery of conducted polymers changed the history of plastics. This breakthrough showed that halojen doped carbon-based materials can reach the electrical conductivity level of metals. Afterwards, people from academia and industry showed their interest in these materials and finally a new research field of “organic electronics” is borned. The inventors, Alan J. Heeger, Alan G. MacDiarmid and Hideki Shirakawa were awarded the Nobel Prize in chemistry in 2000 [1].

The word “organic” in the name of the field comes from the use of carbon-based polymers and small molecules as active semiconducting materials in this new technology. Silicon is an inorganic semiconductor and fundamental building block of microelectronics which is the technology behind today’s electronic devices abundance and usefulness. Currently, the raw material of over 95% of chips produced is silicon. However, it is not possible to reach a low cost product with silicon due to its high infrastructure and fabrication cost. At this point organic semiconductors offer superior properties including low cost of fabrication, compatibility with plastic substrate, large area coverage, flexibility, facile synthesis and more importantly tunable physicochemical/optoelectronic properties based on the application. All these parameters make organics excellent materials where silicon use is not feasible.

Our modern lifestyle is enriched and shaped with electronic devices, in the near future development of new materials and applications will undoubtedly be the mainstream. One of the possible organic-based applications which we might face soon is Radio Frequency Identification (RFID) (Figure 1.1). This technology will eliminate reading individual items at the checkout, replace the barcode reader and make shopping very fast. RFID tags found on milk or juice in a refrigerator can inform you about the expiration date and make a shopping list for you. You can also read a daily newspaper with foldable electronic papers which you can carry in your pocket. You can even charge your phone with wearable polymer solar cells. All these innovations and many others will be a part of our lives soon thanks to organic electronic technology. Recent advances in the field of Organic Field Effect Transistors (OFETs), Organic Photovoltaics (OPVs) and Organic Light-Emitting Diodes (OLEDs) have made impressive progress to make all these technologies a reality.

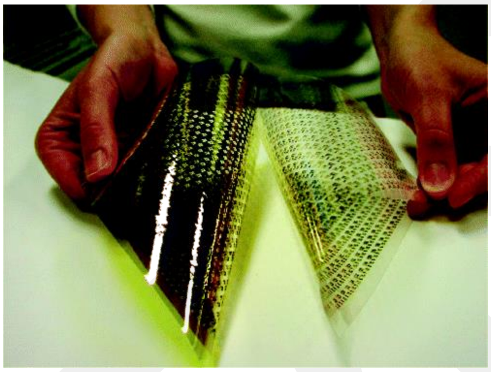

Figure 1.1 Example of an 6 in × 6 in RFID circuit array fabricated on a polymeric substrate [2]. Copyright 2004 by the American Chemical Society.

Among various applications of organic (opto)electronics, research in the field of OFETs has been ongoing for a long time. However, industrial interest has grown significantly in recent years due to the improvement of new semiconductors that show higher charge carrier mobility than those amorphous silicon-based (a-Si) materials [3].

Today, various device types and semiconducting materials are used in the field. Majority of the transistors are based on inorganic semiconductors including Si, Ge, and GaAs in crystalline or amorphous forms. In particular, doped Si and GaAs inorganic crystals exhibited extremely high hole mobility over 1000 cm^2/Vs at room temperatıre. Today's microprocessors belong to the class Metal Oxide Semiconductor Field Effect Transistors (MOSFETs) and compose of thin oxide as a dielectric layer, metal as a gate, and these inorganics as active components. On the other hand, thermally evoparted amorphous silicon ultrathin-films on corresponding substrates are used to switch the pixels with active matrix addressing. Typical hole mobility of these amorphous silicon layers is between 0.1-1 cm^2/Vs. The main disadvantage of all Si-based transistors is the high-temperature manufacturing process and the incompatibility with plastic substrates preventing large-area covered electronics.

The first Organic Field-Effect Transistor (OFET) was reported in the late 1980s, based on polythiophene as a semiconducting material [4]. But, this devices suffered from the low charge carrier mobility of ~10^{-5} cm^2/Vs. Since then, the electronic performance of FETs based on polymeric/molecular semiconductors has continuously improved (Figure 1.2). Currently, OFETs with charge carrier mobility approaching the performance of amorphous silicon based transistors have been developed.

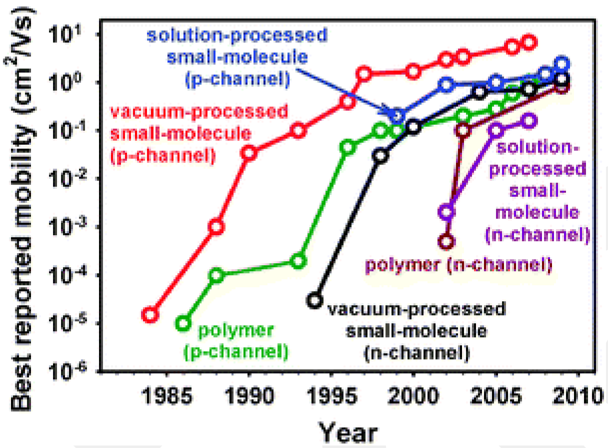

Figure 1.2 Development of charge carrier mobility in OFETs over the past 25 years (measured under ambient conditions) [5]. Copyright 2010 by the Royal Society of Chemistry.

Using carbon-based materials as an active component in FETs has two main advantages. First, thin films fabricated with solution-processed techniques such as spin-coating and ink-jet printing allow large area coverage. These transistors can be used in electronic applications where it is not possible to produce such large area devices with conventional inorganic semiconductors. Second advantage is the superior mechanical properties and flexibility of organics, and with the compatibility of plastic substrates it is possible to reach flexible/bendable electronic devices. Also, carbon-based semiconductors do not require a high temperature fabrication process, which significantly reduces the cost of manufacturing and consequently enables disposable products for short-run applications. However, it is not currently possible to calculate the cost of carbon-based electronic devices.

Integration of complex micro-systems with low-cost and short run applications could be achieved with roll to roll production (Figure 1.3). Up to now, pixel driver circuits in Liquid Crystal Display (LCD) screens were based on amorphous silicon transistors, OFETs might replace these conventional devices and allow RFID tags and smart cards to enter our lives. On plastic substrates it is possible to print hundreds of

OFET circuits in less than in a minute thanks to the advanced printing and conveyor systems. This process is called “roll to roll” and this method allows various materials to be deposited on the same surface.

Figure 1.3 Example of a roll-to-roll coated OPV device on a PET foil (Polyethylene Terephthalate) substrate [6]. Copyright 2011 by Elsevier.

On the other hand, organic materials have poor self-organization characteristics in the solid state because of the weak intermolecular interactions (Van der Waals forces). The final thin-film morphology/microstructure is highly responsive to the technique used to fabricate the semiconducting layer. Generally, solution-processed thin films exhibit poorly ordered films, while vacuum-deposited thin films show well-organized films. At this point, the ideal materials for high performance FETs with large-area coverage are expected to have a delicate balance between favorable solid state packing and good solubility in common organic solvents.

In organic electronic systems, all components are made primarily of carbon, hydrogen atoms and rarely heteroatoms (i.e. sulfur, oxygen, nitrogen), which facilitates the integration step and reduces the fabrication cost. For example; in an RFID tag, it is important to add an antenna, memory, rectifier diode and control circuit with the same process. At this point, the performance of field-effect transistors, the main constituent of the circuits, will be very effective and decisive in commercial success of integrated systems.

Organic Field Effect Transistors have similar working principles to other field-effect transistors. Upon applying a voltage to the gate electrode above a certain threshold value at the boundary between the semiconductor and dielectric layers, a 5-10 nm thick channel consisting of majority charge carriers (i.e, holes (*p*-type), electrons (*n*-type), or both (ambipolar) is formed. When a potential difference is applied between the source and drain electrodes, an active channel is formed and current starts to flow through it.

There are several parameters which are very important in the electrical characterization of OFETs such as i) charge carrier mobility, ii) current modulation ratio, and iii) threshold voltage. Average device performance in the literature has exhibited a hole mobility of 0.01-1.0 cm^2/Vs, a 10^5-10^6 I_{on}/I_{off} ratio and a threshold voltage of 10-40 V. Although, this values are acceptable for many low-cost applications, the developments in the synthesis and fabrication techniques of polymeric/molecular semiconductors will enable us to reach high performance transistors. Even the increase in the charge carrier mobility will pave the way of analog circuits which will greatly expand the application of OFETs.

Mobility (μ) is an important parameter in FETs, which shows how fast charge carriers drift along the active channel in response to electric fields. At low electric fields, there is a correlation between the velocity of drift (V_d) and strength of electric field (E). The unit of this proportion constant is cm^2/Vs.

$$\mu = \frac{V_d}{E} \tag{1.1}$$

The mobility is also related with the conductivity (σ) where *n* is the density of states and e is the electron charge:

$$\mu = \frac{\sigma}{n\,e} \tag{1.2}$$

Second important characteristic of a FET is the On/Off (current modulation) ratio which is the ratio of on-state current to the off-state current.

Increasing a device's performance, especially charge carrier mobility can be realized either by synthesizing novel organic semiconductors or by improving the device fabrication technique. From the organic materials point, π-conjugated systems are divided in two, small molecular and polymeric semiconductors. Solution-processable polymers typically exhibit disordered/amorphous thin-film morphology which results in poor charge carrier mobility. Another disadvantage of polymers is the purification of residual extrinsic doping typically results in high intrinsic conductivity which distorts the I_{on}/I_{off} ratio of the transistor. On the other hand, small molecular π-conjugated systems offer some unique properties when compared with the polymers including high solubility, higher purity level, high degree of crystallinity, and small batch to batch variation (better synthetic reproducibility).

The manufacturing technique of field-effect transistors is based on depositing materials as thin-films on plastic, silicon or glass substrate. It is possible to produce OFETs with various device architecture, but typically bottom contact/bottom gate (BG/BC) device geometry preferred due to stabilization. The coating of the highly sensitive organic semiconductor was performed in the last step of the fabrication process and the risks that may arise from the production are minimized.

1.1 OFET Architecture and Operation

The OFET consists of a gate electrode, a dielectric insulating layer, and an organic semiconducting material sandwiched between the source and drain contacts. Two of its electrodes are in direct contact with the semiconductor and the third, gate electrode, is isolated from the active semiconducting channel through a dielectric layer.

The device architecture of OFETs have several variants and Figure 1.4 shows several examples. Among them top-contact and bottom-contact device geometries are most commonly used in OFETs. In both architectures, organic semiconducting material is deposited on the dielectric/gate substrate (~30-50 nm thickness) and contacted with source and drain electrodes. The main difference between these two geometries is the order of semiconducting layer deposition. In top-contact/bottom gate (TC/BG) devices (Figure 1.4A) organic semiconductor is deposited at first by vacuum or solution based technique, then metallic source and drain electrodes are deposited by means of shadow mask. The advantage of this geometry is the lower contact resistance and its major drawback is the loss of resolution. In bottom-contact/bottom gate (BC/BG) structure (Figure 1.4B), the metal contacts are deposited in the initial stage, while organics are deposited in the final stage. Thus, the risks that may arise from the production could be minimized. The dielectric layer is typically made of thermally grown SiO_2 with thickness of 200-300 nm. In this scenario, source and drain electrodes can be patterned via micro lithographic techniques. All these device structures have their advantages and drawbacks. In top-contact/top-gate (TC/TG) (Figure 1.4C) and bottom-contact/top-gate (BC/TG) (Fig 1.4D) geometries sensitive organic semiconductors are not exposed to air, sandwiched between substrate and dielectric layer, this may increased the device stability.

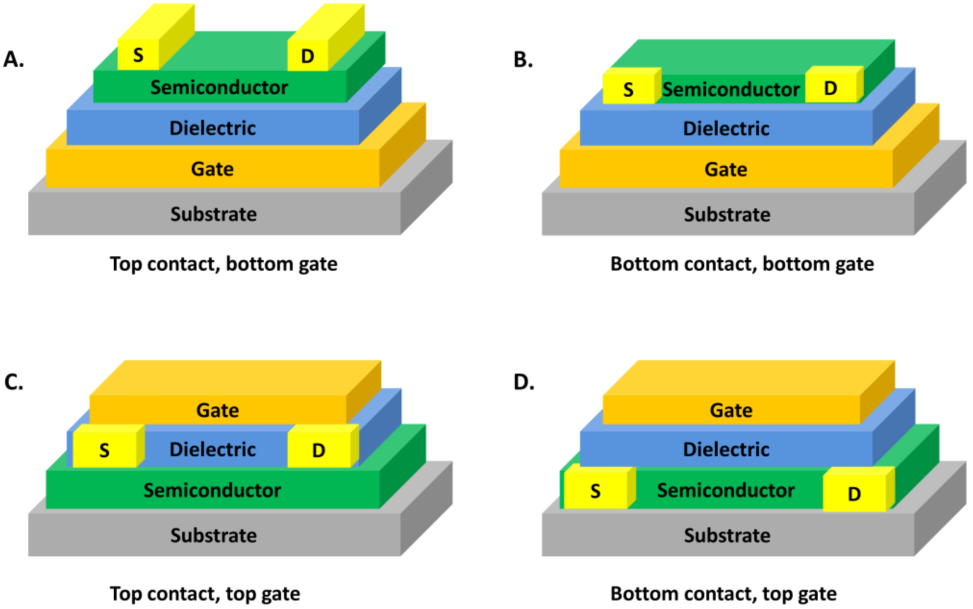

Top contact, bottom gate

Bottom contact, bottom gate

Top contact, top gate

Bottom contact, top gate

Figure 1.4 Schematic view of various device architecture in OFETs, top contact/bottom gate (A), bottom contact/bottom gate (B), top contact/top gate (C), bottom contact/top gate (D).

The organic field-effect transistor (OFET) is an “electronic valve” where the semiconductor channel conductance is modulated and controlled by two independent potentials. In these devices the semiconductor is always a small molecule or a polymer. This device is essential in several electronic components and particularly in circuits for display controlling the image as well as for fabricating unconventional integrated circuits for memories and sensors. Note that the organic semiconductor used in OTFTs should not be intentionally doped so that it does not to depress the current modulation. Consequently, the semiconductor carrier concentration is very low, usually $< 10^{14}$ cm^{-3}. When a voltage is applied between the source and drain electrodes (V_{SD}) and the gate potential versus the grounded source electrode is zero (source-gate voltage = 0 V) the source-drain current is very low and the device is “off”. When the gate potential is applied (V_{SG}), accumulation of charges at the interface between the gate dielectric and the semiconductor (carrier concentration $> 10^{20}$ cm^{-3}) occurs. Upon application of the positive or negative source-gate bias electrons or holes, respectively, are accumulated at the interface between the semiconductor and the dielectric and the S–D current (I_{SD})

increases (Figure 1.5). This is called the ‘on’ state of the transistor. The basic relationships describing the OFET drain currents are given in equations (1.3) and (1.4).

$$(I_{SD})_{\text{lin}} = \left(\frac{W}{L}\right) \mu_{FET}\, C_i \left(\frac{V_{SG} - V_T - V_{SD}}{2}\right) V_{SD} \tag{1.3}$$

$$(I_{SD})_{\text{sat}} = \left(\frac{W}{2L}\right) \mu_{FET}\, C_i\, (V_{SG} - V_T)^2 \tag{1.4}$$

where μ_{FET} is the field-effect carrier mobility of the semiconductor (the average drift velocity per unit electric field), W the channel width (~100-1000 μm),, L the channel length (~10-100 μm), C_i the capacitance per unit area of the dielectric, V_T the threshold voltage. On increasing the magnitudes of V_{SD} for a given V_{SG}, a “linear regime” (eq. 1) is initially observed at low source-drain voltages ($V_{SD} < V_{SG}$) where the current increases linearly, followed by a regime where the current saturate (“saturation regime”, eq. 2) when the drain voltage exceeds the gate voltage ($V_{SD} > V_{SG}$). Note that these equations assume that the field-effect mobility of the material is constant. μ_{FET}, V_T , as well as the current on-off ratio (I_{on}/I_{off}) are among the most important OTFT performance parameters.

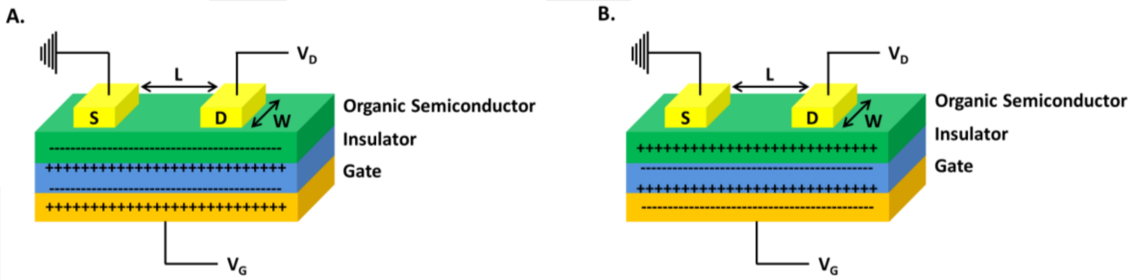

Figure 1.5 On-state of OFETs and corresponding polarization in insulator layer and accumulation of charge carriers in organic semiconductor layer when positive gate voltage is applied (A), and negative gate voltage is applied (B).

The name field-effect is originated from the gate-induced control of the transistor. Figure 1.6 shows the energy band diagrams of frontier orbitals during the operation of the field-effect transistor. When gate voltage is applied the shift in Highest Occupied Molecular Orbital (HOMO) and Lowest Unoccupied Molecular Orbital (LUMO) energy levels with regards to the fermi level of source and drain metallic electrodes enables the accumulation of charges at the interface between the gate dielectric and the semiconductor layer. Upon applying a source-drain bias, current starts to flow from source to drain in the active channel. When the gate voltage is zero (Figure 1.6A) there is no conduction because charge carriers are not mobile. How the energy levels of frontier orbitals are shifted upon a negative gate voltage is applied when the source-drain bias is zero or negative are represented in Figure 1.6B and D, respectively. A negative gate voltage results in a strong electrical field at the interface between the gate dielectric and the semiconductor layer. HOMO and LUMO energy levels of the semiconductor will shift up (higher in energy) because of this large electric field. On the other hand, the fermi energy level of the metal contacts will be preserved due to their externally controlled potentials. When the applied gate voltage is high enough the energy level of HOMO will be in resonance with the fermi energy level of the contacts. Now, holes can flow from metal contacts to the HOMO which results in the accumulation of hole charge carriers at the dielectric/semiconductor interface, Figure. 1.6B This mobile charge carriers (holes) cause an electrical current between source and drain electrodes when negative source-drain bias is applied, Figure 1.6D.

In other case, upon application of a positive gate bias, the change in the HOMO and LUMO energy levels of a semiconductor is pictured when the source-drain bias is zero or positive in Figure 1.6C and E, respectively. Unlike the negative, the positive gate voltage causes both frontier molecular orbitals to shift towards the lower energy level and LUMO becomes resonant with the fermi energy level of metal contacts. Now, electrons can flow from metal contacts to the LUMO which results in the accumulation of electron charge carriers at the dielectric/semiconductor interface, Figure 16C. This mobile charge carriers (electrons) cause an electrical current between source and drain electrodes when positive source-drain bias is applied, Figure 1.6E. In both cases, charge injection is performed from source to the semiconductor regardless of the sign of the gate voltage applied.

Figure 1.6 illustrates how the conduction mechanism of OFETs can be modulated with applied gate voltage in a simplistic manner (w/o charge traps and residual dopants). Note that, any organic semiconducting material can not conduct electrons or holes based on the sign of the gate bias applied. Typically, organic semiconductors exhibit unipolar device characteristics (more electron or hole conductive behavior) regardless of whether the gate voltage is positive or negative. This electron or hole transporting ability of an organic semiconductor is intrinsic which is related with the frontier orbital energy levels and wave-function distributions. Therefore organic semiconductors are classified as *p*-type (hole transporting) and *n*-type (electron transporting) conductors. In addition, there is another type of organic semiconductors which is called as ambipolar and based on simultaneous transportation of both holes and electrons. The semiconducting behavior of an OFET can only be switched within these types of materials because of the possible charge injection of both (electron and hole) from the contact thanks to the accessible HOMO and LUMO orbitals. The majority of the charge carriers at the dielectric/semiconductor interface can be adjusted according to the sign of the applied gate voltage.

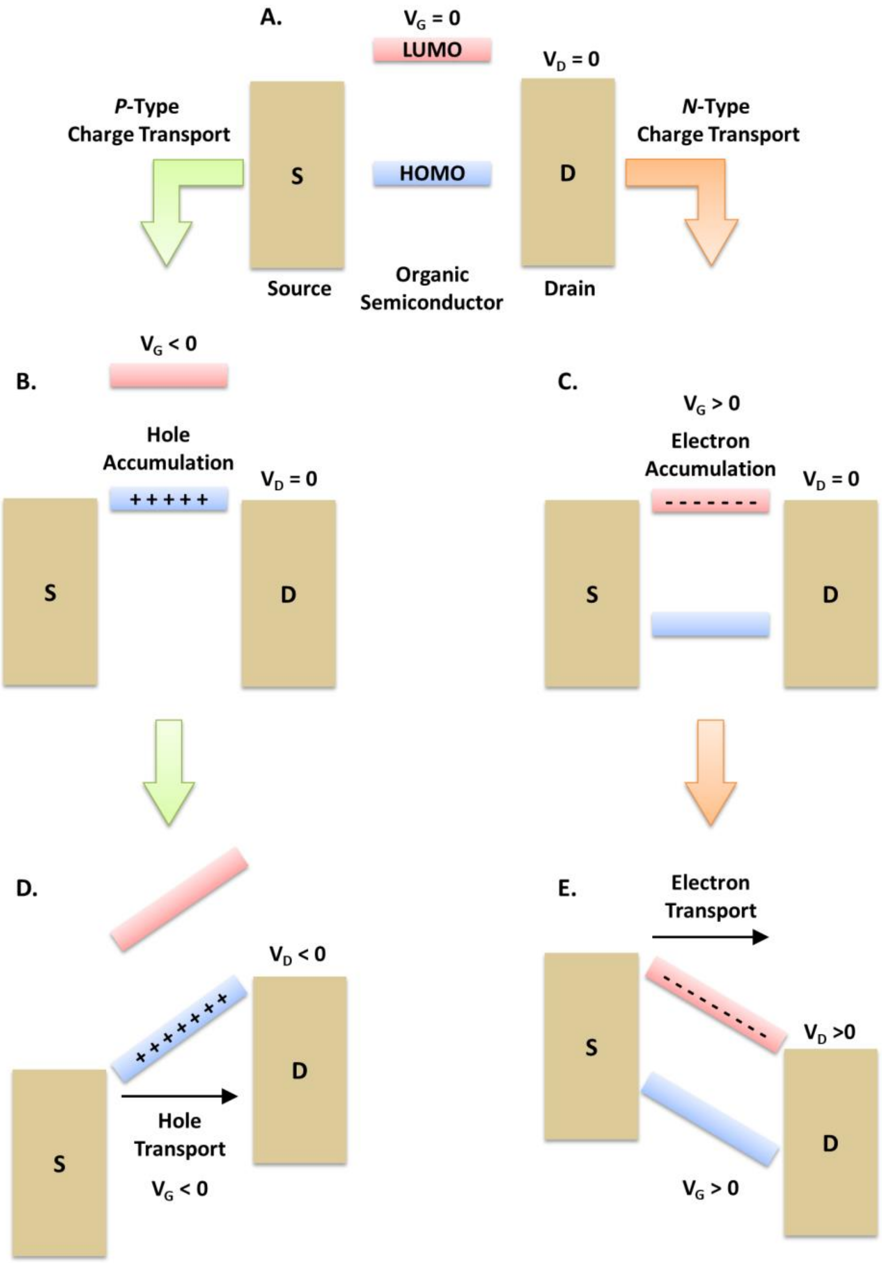

Figure 1.6 Energy band diagrams of HOMO and LUMO levels at $V_G=0$ (A), during *p*-channel device operation (B and D), and *n*-channel device operation (C and E).

Upon application of negative gate voltage, hole charge carriers will be equally distributed at the dielectric/semiconductor interface, if we assume that there is an easy charge flow between the source electrode and organic semiconducting layer (ohmic contact) and the threshold voltage is zero, Figure 1.6B, When there is no source-drain voltage, the density of the holes will be uniform through the active channel. But when there is a drain bias, the density of the charge carriers will gradually decrease going from source to drain.

The first introduction of charge carriers in organic semiconductors is not related with the zero gate bias. For a *p*-type semiconducting material, charge transfer between metal and organic originates from the energy difference between HOMO level (similar to the valence band of convenient semiconductors) of organic and fermi level of metal contacts, which causes a band bending and dipole in the organic. Therefore, application of non-zero gate voltage enables the flat band model. In addition, if there are lots of charge traps throughout the organic thin-film, these traps must be filled to obtain a conduction layer. In contrast, if the channel unintentionally doped with residual impurities, the device may show conductance even at zero gate bias.

To further understand these circumstances, it is better to define the threshold voltage (V_T) which is the minimum voltage to create mobile charge carriers (in other words the amount of bias required to shut down the device). For example, doping an *n*-type semiconducting material shifts V_T to further negative, and mismatch between the fermi level of metal contacts and LUMO energy level of organic semiconductor could shift the V_T to negative or positive direction based on the type of the corresponding misalignment.

OFETs are mainly characterized in two ways, firstly keeping the gate bias at zero and sweeping the drain bias, resulting in I_D-V_D curve or “output curve”, Figure 1.7A. Secondly, holding the drain bias at zero and sweeping the gate bias, give us I_D-V_G curve or “transfer curve”, Figure 1.7B.

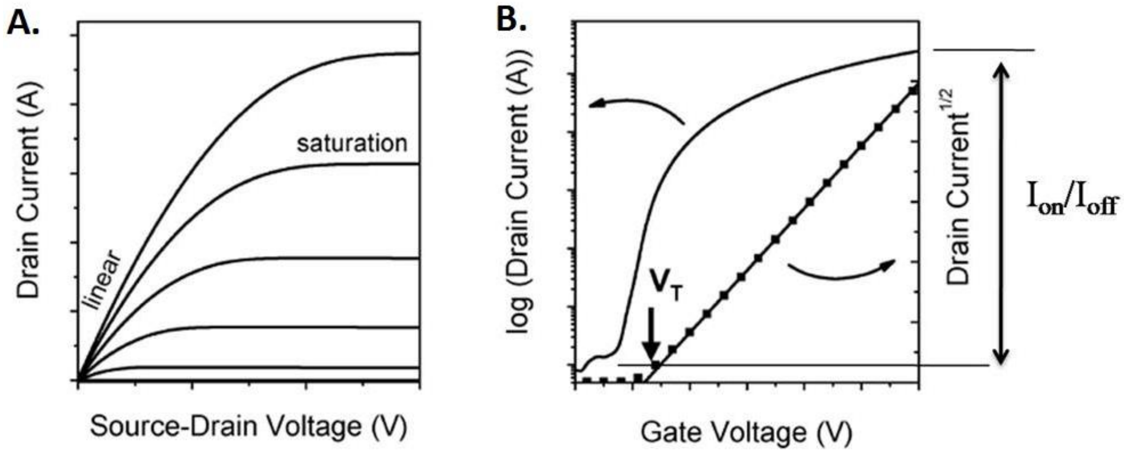

Figure 1.7 A typical current-voltage characteristics of OFET, output curve (A) and transfer curve (B).

1.2 Fabrication Techniques

Organic semiconducting materials behave so differently than their inorganic counterparts with regard to mechanical properties, solubility and melting point. Typically, it is difficult to process bulky organics, for instance their single crystals are highly brittle. For this reason, organic thin-film fabrication processes are highly responsive to the physicochemical properties of the material. So, it is not possible to fabricate organic optoelectronic devices with the same processing techniques that are used for conventional microelectronics. But, some fabrication techniques including thermal oxidation and photolithography were used as a model in the early days of OFETs. Typically, organic field-effect transistors consisted of heavily doped silicon substrate (p^{++}-Si or n^{--}-Si) as the gate with thermally grown oxide layer (≈200-300 nm) as the dielectric layer, and lithographically patterned metal electrodes (i.e. Au, Ag) as source and drain. In order to minimize the risks that may arise from the production, organic semiconductors are deposited at the last stage of the fabrication process.

Thin-film (1-200 nm) growth and patterning is the key to achieve high performing optoelectronic devices. The most common techniques used to create thin-films are spin-coating, thermal evaporation and chemical vapor deposition. The fabrication of optoelectronic components with nano scale resolution varies depending on the deposition technique.

1.2.1 Solution-Processed Deposition

Solution-processed deposition techniques are widely used in the formation of semiconducting layers, which is used as an active channel in optoelectronic devices, for taking advantage of using organic materials including low cost and large area coverage. Although the doping process was performed via simultaneous deposition of different materials in physical vapor deposition (PVD) under vacuum, it can be done more practically in solution-based deposition by mixing organic materials in a solvent medium.

Spin-coating is a solution-processed deposition technique to fabricate optoelectronic devices which composed of organic small molecular/polymeric solution coating onto a substrate, spinning for a period of time according to the desired thickness and eventually forming a thin-film because of the solvent evaporation, respectively. From the material perspective, the main requirement for this technique is a good solubility in common organic solvents (chloroform, dichloromethane, tetrahydrofuran, toluene, etc.). Unfortunately, the majority of organic semiconductors are not soluble. To overcome this problem, linear/swallow-tailed alkyl chains substituted small molecules and polymers grafted with solubilizing groups are largely used. To decrease the duration of the drying process, solvents with low boiling points and/or vapor pressure are often preferred. The advantage of this method is obtaining ultrathin films with very uniform morphology, low cost, simplicity and facile operation conditions. High revolution per minute (rpm) results in reduced drying time and consistency in the macro/nanoscale. The main problems with this technique is the high amount of material wastage due to spreading around during spinning.

Langmuir-Blodgett (LB) is an alternative technique to fabricate homogenous ultra-thin films of organic small molecules which enables well controlled structure and thickness of the corresponding film. This method is based on spreading of amphiphilic molecules at the water-air interface as a single layer. However, it is not the case for the majority of small molecules used in OFETs. Amphiphilic small molecules consisting of hydrophilic head and hydrophobic chain group have strong dipole moment and can make hydrogen bonding thanks to –OH, -COOH, $-NH_2$ functional groups. The hydrophilic parts prefer to be submerged in water, while the hydrophobic part prefers to orient towards the air. As soon as homogeneity and surface balance is achieved, the deposition process takes place. All these hydrophilic and hydrophobic properties of organic molecules are important in the fabrication of LB films. In addition, the stability of surface active molecules is important in terms of depositing two or more single layers by this method.

LB films are prepared by dissolving a small amount of amphiphilic compound in a volatile solvent in the lower phase and depositing at the surface of purified water. When the solvent evaporates, organic molecules can be compressed to form a floating two-dimensional solid. During this compression in monolayer films, a large number of phases can be seen which is similar to the mesophase of liquid crystals. When the substrate When the substrate is immersed in the liquid, it interacts with monolayer and the langmuir film adheres to the substrate by itself and is coated on it as monolayer.

Printing technology is adaptable to the production of large volumes of organic electronics, especially inkjet printing allows fast and convenient fabrication of optoelectronic devices including serial OPVs and OLEDs. The appeal of this technology is its non-contact patterning capability and its ability to be used without a mask. The direct printing capability of inkjet printing allows the enlargement of versatile films whose designs can easily change from print to print. The other advantages of this technology are reduced material waste, low-cost and large area coverage. Most importantly, inkjet printing reduces the cost, number of steps and complexity of lithography in industrial fabrication. All organic optoelectronic devices require contacts and conductive materials that integrate themselves into larger circuits. Safety measures including sensors (i.e. light sensor) and detectors (i.e. security and gas sensors) are part of modern life and most of these applications require short run/disposable devices which might be possible with inkjet printing.

Since ink jet printing is used for liquid phase materials, it provides significant material savings. These materials or inks consist of a solute which is dissolved in a solvent or dispersed in another method. In principle, inkjet printing is based on the ejection of a constant amount of a solution in a reservoir from a nozzle in a sudden semi-adiabatic process via piezoelectric effect. The volume can be compressed by applying an external voltage to the solution-filled reservoir which causes a drop of fluid to come out of the nozzle. This drop is exposed to gravity and air resistance until it falls on the substrate, spread by the momentum that is obtained by motion, and flows through the surface thanks to surface tension. Eventually, drop expands on the surface via solvent evaporation. This final step is highly responsive to the viscosity of the semiconducting material which is related with the concentration and molar mass. Highly soluble polymers, macromolecules and small molecules with favorable viscosity can be used in inkjet printing.

1.2.2 Physical Vapor Deposition

Spin-coating technique requires solutions with high viscosity that can be a problem for small molecular semiconductors. Physical Vapor Deposition (PVD) is the ideal thin-film fabrication method for these types of materials. In principle, this technique consists of heating an organic material and deposition on the substrate in a high vacuum chamber ($\approx 10^{-6}$-10^{-9} torr). The organic semiconducting material is placed into a metal boat (W, Mo, Ta, etc.) that is subjected to Joule heating and then begins to evaporate from the source in molecular form, eventually deposited on the substrate which is placed a few centimeters above the boat. Therefore, this method is not suitable for the polymers since they can be easily decomposed via cracking upon heating. The main advantages of this method are simply/well mastered thickness control and highly-ordered thin films with high purity. The growth ratio and temperature of substrate can be adjusted according to desired properties of the corresponding thin-film. Multi-layered coatings and very thick films can also be obtained with this system. Its primary drawbacks are expensive and complex instrumentation compared to spin-coating, and cleaning problems of the vacuum chamber. In organic electronic devices including OFETs, OLEDs, and OPVs, typically small molecules evaporate under reduced pressure ($<10^{-6}$ torr) with low growth ratio of 0.1-3 Å/s. Modelling of deposition masks and pixels are easy in this method. So, vacuum equipment, which is currently used in the semiconductor industry, can easily find a place in organic optoelectronic device fabrication.

1.3 Organic Materials for Field-Effect Transistors

π-Conjugated semiconductors (small molecular or polymeric) have drawn huge attention from researchers because of their unique optical/electrical properties which enable us to reach new functional optoelectronics [7–9]. Only, the discovery of novel semiconductors is not enough itself, the relation between chemical structure-optoelectronic properties-electronic performance must be revealed [10–13]. All these properties are related with the optimization of carbon-based semiconductors including electronic structure, charge transport and light-semiconductor interactions on the way to reach high charge transport ability and current modulation ratio. To this end, we will first focus on basic structural requirements of organic semiconductors and then introduce typical semiconductors in the literature based on the majority of the charge carrier type along the active channel.

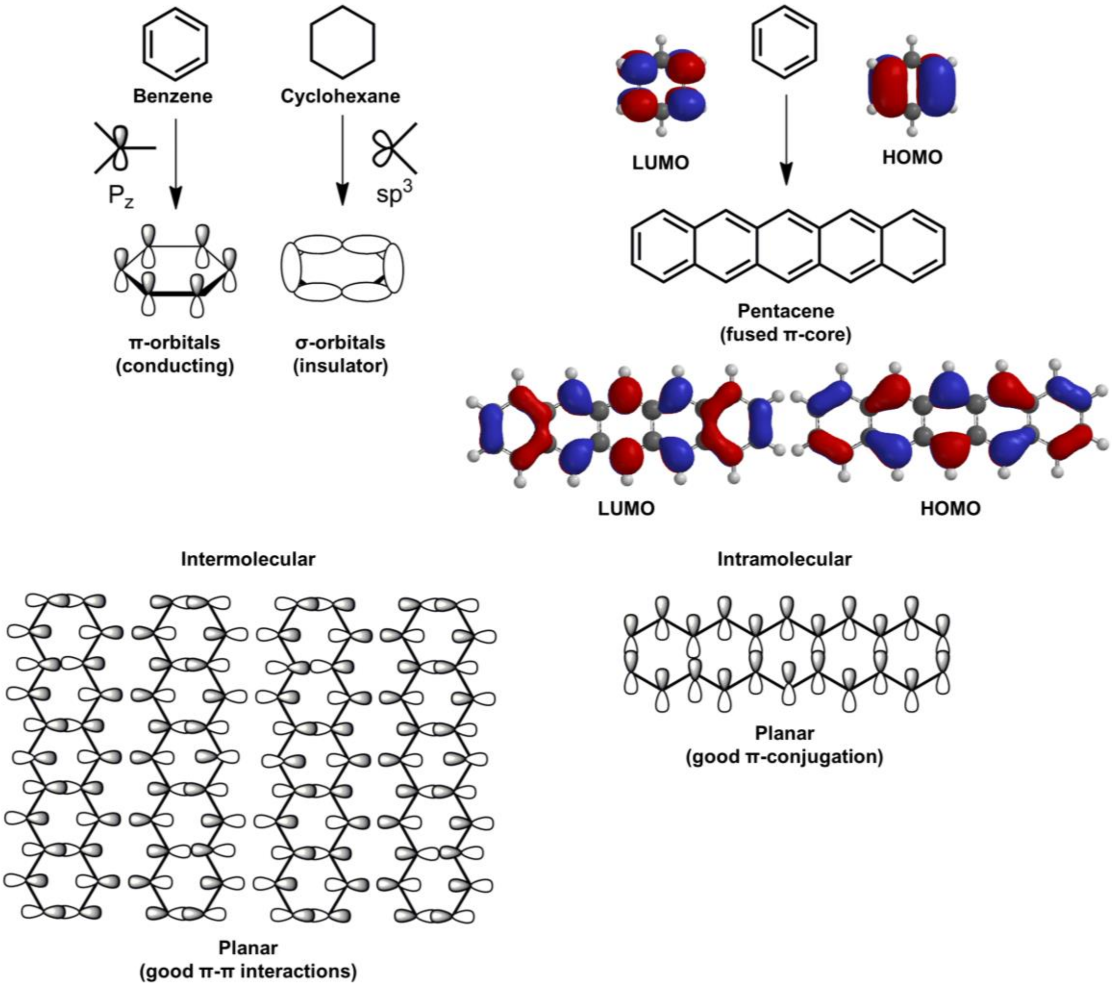

Figure 1.8 Schematic representation of π-conjugated (benzene) and non-conjugated (cyclohexane) units and corresponding overlapping/non-overlapping orbitals, HOMO/LUMO molecular orbitals and topologies of benzene and pentacene (fused π-conjugated core), structural connectivity in a highly planar π-core which results in conductivity, and intermolecular interaction in the solid state.

There are two main requirements for organic semiconductors to implement them into printed electronic applications (Figure 1.8) [14]. The first one is the π-conjugated system which is composed of alternating carbon-carbon single and double bonds and that allow the delocalization of π-electrons throughout the core. Conjugation lowers the energy and stabilizes the molecule (Figure 1.9). The spatial overlap of the p_z atomic orbitals of each carbon atom combines the molecular π-orbitals in the system, causing the extension of the conjugation throughout the system. This extension of π-orbitals results in unique charge transport and optical properties [15,16]. In the undoped state, there is a complete occupation of electrons in a definite number of molecular orbitals which is called as highest occupied molecular orbitals (HOMO). Also, there is no occupation in the molecular orbitals with higher energy which is denoted as LUMO (lowest unoccupied molecular orbitals). As shown in Figure 1.10, in the bulk state, mobile hole charge carriers move via hopping mechanism between HOMOs of neighboring molecules (and electrons move between LUMOs by hopping). Thus, the energy of HOMO corresponds to the energy of the valence band, the LUMO energy level translates into the energy of the conduction band and the distance between HOMO and LUMO corresponds to the band gap of the semiconductor (Figure 1.11). Typical HOMO-LUMO band gap is between 2-4 eV in a semiconducting material with a very low mobile charge carrier intrinsic density.

Charge transport ability of organic semiconductors is highly sensitive to the degree of order in the solid state which means charge carrier mobility will be greater in highly ordered/well organized thin films. Intermolecular charge transport is relatively difficult compared to intramolecular charge transport because of the disorder between the molecular structures. Charge carrier transport between localized states is explained by hopping mechanism which is based on a thermally activated tunneling.

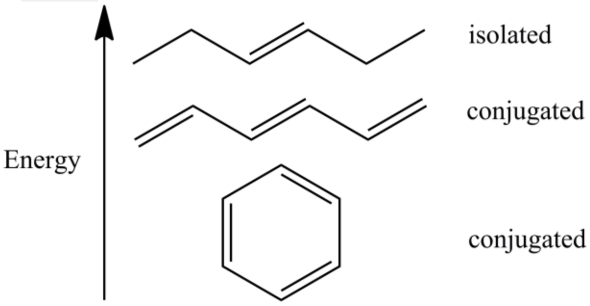

Figure 1.9 Energetic stabilization of organics upon π-conjugation

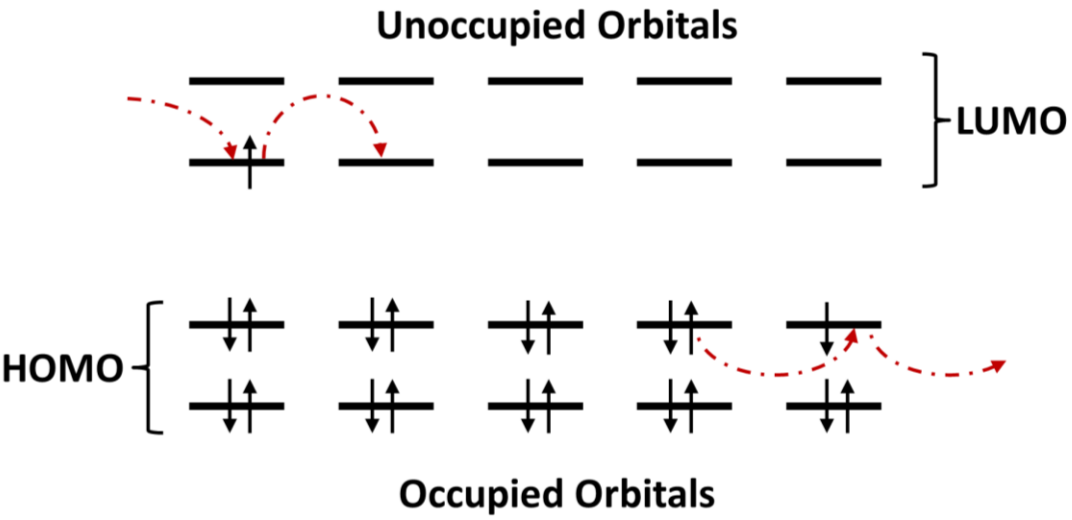

Figure 1.10 Schematic representation of charge carriers motion between LUMOs and HOMOs of neighboring molecules/polymeric segments by hopping mechanism.

The second requirement for organic semiconductors to implement them into printed electronic applications is functionalization of π-core with solubilizing substituents including linear/swallow-tail alkyl chains to reduce the cost of fabrication with solution-processed techniques. This also increases intermolecular interactions between π-cores in the solid state [17,18]. This feature was not reported in initial studies since most of thin-film in these devices were fabricated with vacuum sublimation method. Most commonly used π-cores with an unsaturated units are mono/polycyclic aromatic hydrocarbons (i.e. naphthalene, anthracene, and pentacene), aromatic heterocycles with sulfur, nitrogen and oxygen atoms (thiophene, furan, and pyridine etc.), bonzofused systems and olefinic/acetylenic groups. The degree of conjugation and/or interaction between above mentioned units plays a key role in the electronic character of the semiconductor in both solution and solid state. This directly affects the optical absorption/emission profile, redox properties and the energy level of frontier molecular orbitals (FMO). From the polymeric semiconductor case, molecular weight (M_w) and polydispersity index (PDI) are the two crucial parameters which influence the solubility, aggregation, thin film formation and morphology of the material. In polymers, the electronic structure, thermal characteristics and microstructure change significantly as they move from small to high molecular weight, and therefore, obtaining appropriate M*w*/PDI ratio is very important to achieve small batch-to-batch variations. This ratio is highly sensitive to the structure of the polymer, for example soluble thiophene-based polymers typically show number average molecular weights of 20-30 kDa and 1.2-1.8 of PDI [19].

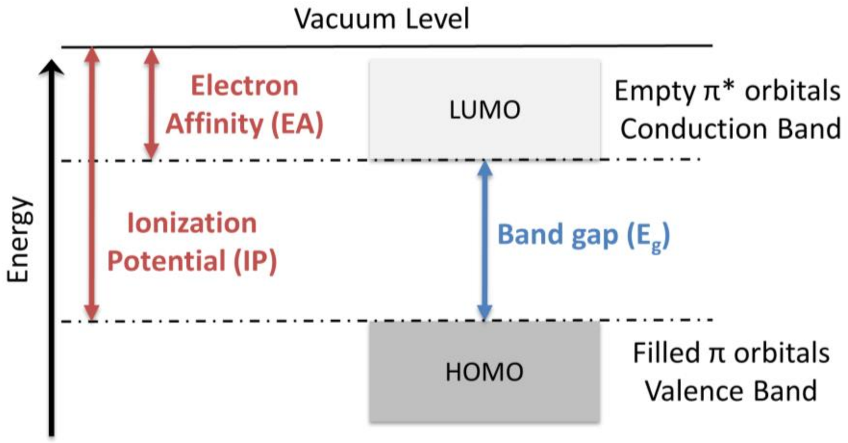

Figure 1.11 Energy band diagram of an organic semiconductor

From the semiconducting π-conjugated materials perspective, the use of polymers has many advantages over small molecules. Thin films of polymers generally show uniform microstructure and very low root mean square (RMS) value which allows well mastered control of the structural and morphological properties of the corresponding thin films. Rheological characteristics of the solution is a very important parameter in printing which can be greatly adjusted for polymeric semiconducting materials. In addition, crystalline domain sizea of polymers are typically smaller than the length of various optoelectronic devices and enable isotropic charge transport capability. For instance, organics have an exciton diffusion length in ~10 nm range which makes polymers excellent donor/acceptor materials in organic photovoltaic devices. Reproducible device performance can be realized by using a polymeric semiconductor with small crystals, this is mainly important for the integration of thin film transistors into circuits. Also, substantial exposure to solvent and annealing occurs during the fabrication of multilayer devices. The limited solubility and large viscosity of polymers increase the options to find suitable orthogonal solvents for the deposition of a layer with solution processed technique on top of the polymer layer. Lastly, polymers typically do not vaporize before decomposition and therefore have very low vapor pressure, making them resistant to interlayer diffusion during the thermal processes as a part of device fabrication. It is also possible to deposit a very thin film with a thickness of several nanometers by using polymeric semiconductors, which is compatible with the roll-to-roll fabrication method. This can be achieved thanks to the robust mechanical properties of polymers. On the other hand, in recent years various small molecular semiconductors have demonstrated improved solution processability with new design approaches.

1.3.1 *P*-Type Molecular/Polymeric Semiconductors

Most of the organic semiconductors in the literature are of *p*-type (hole transporting) and best performing devices have been achieved using such materials. Besides, above mentioned basic structural requirements, to obtain good *p*-type semiconductors for field effect transistor applications, the energy level of HOMO is crucial. Good hole transporting semiconductors typically have HOMO energy levels around -5.0 to -5.5 eV. For semiconductors with higher HOMO energy level (lower ionization potential(IP)) there is an ambient stability due to easy oxidation by air. Thus also dramatically hampers the current modulation ratio (I_{on}/I_{off}). When E_{HOMO} is deeper than -5.5 eV (higher IP), OFETs with good hole mobility and very large I_{on}/I_{off} ratio can be achieved, but these devices mostly suffer from very large threshold voltages (V_T). Here, key *p*-type semiconductors in the literature and recent reports about the development of molecular/polymeric semiconducting materials will be summarized.

Poly(3-alkylsubstituted-thiophene)s are one of the most popular polymeric semiconductors in organic optoelectronics. The main advantage here is the position of the substituent group which not only enhances the solubility in common organic solvents but also affects film formation capability. Among the other members in this family of polymers, poly(3-hexylthiophene) (P3HT, P-1) (Figure 1.12) has been widely studied to investigate the effects various parameters on OFET device performances including molecular weight [20–22], solvent used in thin-film deposition [23], morphology of thin films [24,25], film thickness[26] and alkyl chain length [27]. But, well mastered control over regioregularity and I_{on}/I_{off} ratio degradation upon exposure to air, still remained as big concerns. The latter mainly originates from the increased charge carrier density. For this reason, high current modulation ratio can only be achieved under inert atmosphere device characterization conditions [28]. To solve these problems, new polythiophene based semiconductors have been developed. Solution-processable regioregular polyquarterthiophenes (PQTs) have been reported by Ong. *et al.* which showed good OFET device performance under open air [29]. As an example, PQT-12 based thin films exhibited hole mobility of 0.14 cm^2/Vs and I_{on}/I_{off} ratio of $>10^7$. Chabinyc *et al.* reported how humidity affects unencapsulated devices based on the same polymeric semiconductor (PQT-12, P-2) (Figure 1.12) [30]. This study showed that not only *n*-type semiconductors are moisture sensitive because when humidity increased, OFET performance decreased and amount of charge traps was increased. McCulloch *et al.* investigated the effects of reducing sterically twisting thiophene units in the polymer backbone and used fused thieno[3,2-b]thiophene co-monomers instead (PBTTT-14, P-3) (Figure 1.12) [31]. This design approach resulted in lower HOMO level due to limited electron delocalization throughout the backbone compared to single thiophene co-monomers. OFET devices based on PBTTT-14 showed average hole mobilities of 0.2-0.6 cm^2/Vs and max of 0.7 cm^2/Vs under inert atmosphere. Also, other common polymeric semiconductors which is developed in earlier studies based on dialkylfluornen-alt-bithiophene (F8T2, P-4) [32,33] triarylamine (PTTA, P-5) [31] and carbazole (PCB-R, P-6) [32, 33] π-units are shown in Figure 1.12.

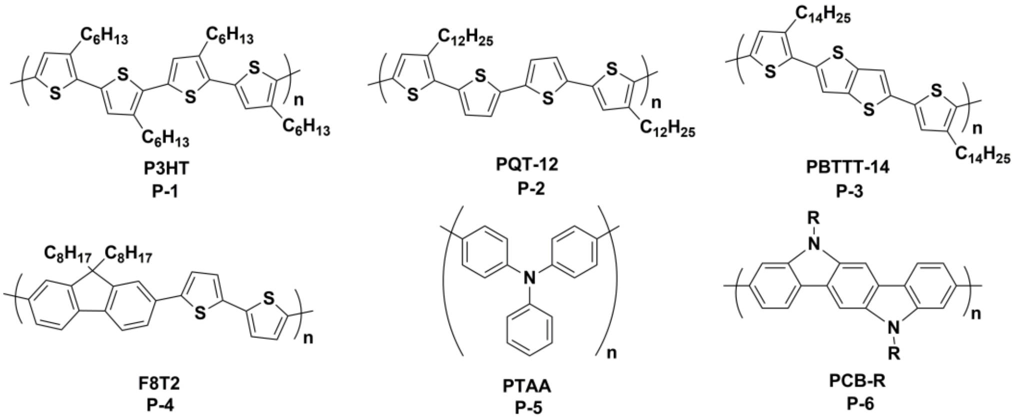

Figure 1.12 Chemical structure of the first-generation *p*-type semiconducting polymers

During the last decade, several new π-systems, particularly fused aromatic based structures, have been developed to reach higher OFET device performances. Rasmussen *et al.* reported the first alkyl substituted dithieno[3,2-b:2',3'-d]pyrrole (DTP) unit for optoelectronics [34]. The main advantage of this core was its high coplanarity, resulting good π-conjugation through the system. Low band gap DTP polymeric semiconductors showed good stability in oxidized states and effective red fluorescent in solution-phase, while limited solubility and low M_w reduced application variety [35]. To solve this problem, McCullough *et al.* synthesized a new group of alkyl substituted DTP-thiophene copolymers (Figure 1.13, P-7→P-12) [36]. The design approach here was based on planar DTP to extend π-conjugation, and thiophene to reach good solubility and high hole mobility. This study also revealed that amorphous semiconductors with a long range π-connection could have high charge carrier mobility and excellent reproducibility both electrically and structurally. To solve the air stability problem of these DTP-thiophene based polymers, implementation of electron deficient units into the polymer backbone have been studied by the same group [37]. The use of bithiazole (Tz) unit will increase the ionization potential of the π-system. Alkyl substituted DTP-bithiazole copolymers as shown in Figure 1.13, exhibited good OFET performance with charge carrier mobility of as high as 0.14 cm^2/Vs and I_{on}/I_{off} ratio of 10^6 with an outstanding air stability (no degradation after 2 months) (P-13 and P-14).

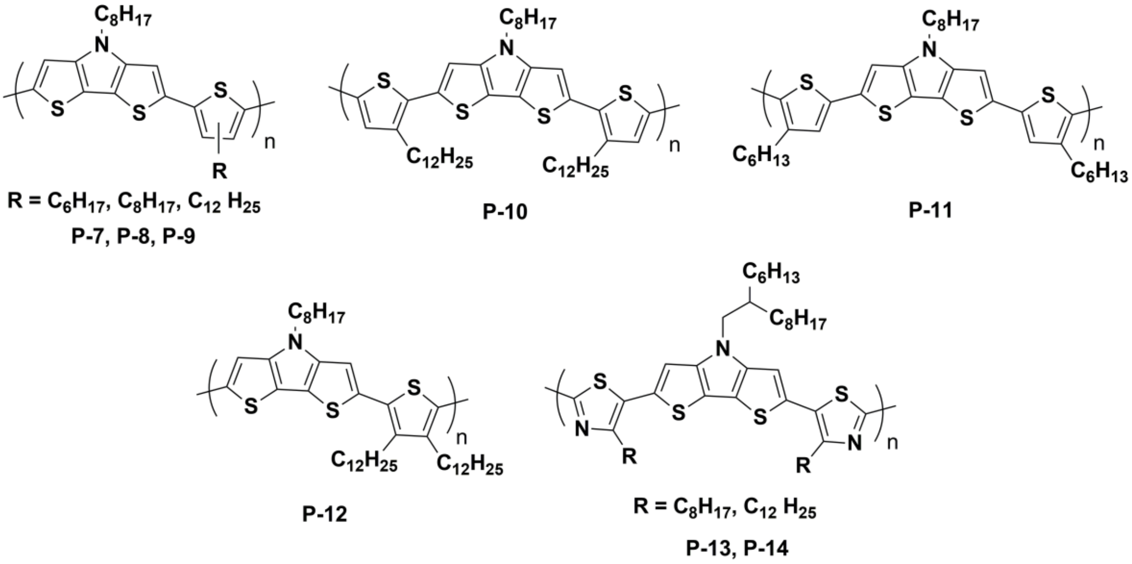

Figure 1.13 Chemical structure of fused dithieno[3,2-b:2',3'-d]pyrrole (DTP) based *p*-type semiconducting polymers

Another family of polymeric semiconductor in OFET application is fused thiophene copolymers. He *et al.* reported a study in which odd numbered fused thiophenes exhibited larger lamellar spacing compared to even numbered fused thiophene cores (Figure 1.14, P-15 and P-17 vs. P-16) [38]. Therefore, OFET devices fabricated based on odd numbered fused rings showed much lower charge carrier mobility than the others. To further understand the structure-property relation here, same group reported additional polymers which clearly revealed the effect of symmetry on its structure and device performance [39]. Polymers with four fused thiophene units exhibited a hole mobility of 0.087 cm^2/Vs (Figure 1.14, P-17), while polymers with three and five fused rings displayed charge carrier mobilities of 0.0017 and 0.0023 cm^2/Vs, respectively (Figure 1.14, P-15 and P-18).

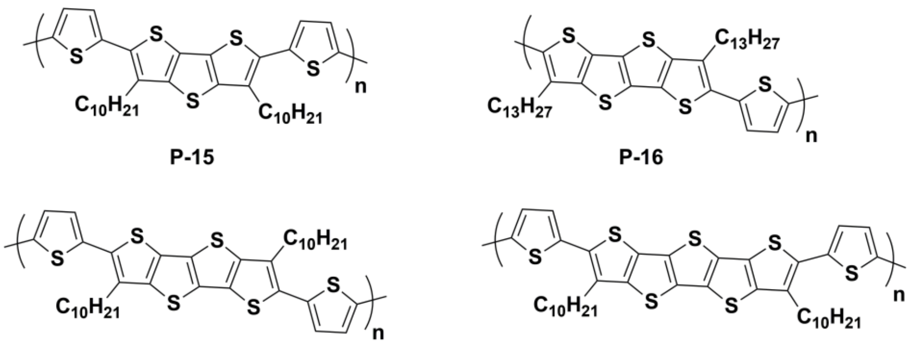

P-15 **P-16** **P-17** **P-18**

Figure 1.14 Chemical structure of fused thiophene based *p*-type semiconducting polymers

Addition of unsubstituted conjugated units into poly(alkyl-substituted thiophene)s backbone realized increased air stability due to better steadiness against oxidation. This is due to increased π- conjugation length resulting in a deeper HOMO energy level. Decreasing the length of alkyl side chains on thiophene units facilitates the interdigitation between these alkyl chains, providing highly organized crystalline domains and leading to higher charge carrier mobility. At this point, thienylenevinylene, based on vinyl group and thiophene, stand out as an important building block for optoelectronics [40]. Also, the addition of vinylene group into a polymeric backbone increases the degree of coplanarity of the corresponding backbone due to reduced steric hindrance on the aromatic units. For instance, Kim *et al.* synthesized a new thienylenevinylene based polymeric semiconductor with low HOMO energy level and high oxidative stability (Figure 1.15, P-19) [41]. This was mainly because of symmetrical insertion of an thienylenevinylene unit between 3-dodecylthiophenes, which allows rotational freedom between these units. Unoptimized OFET devices showed a hole mobility of 0.15 cm^2/Vs.

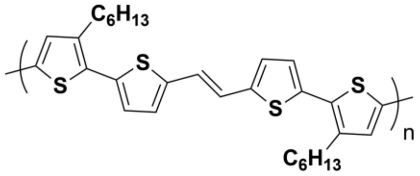

P-19

Figure 1.15 Chemical structure of thienylenevinylene based *p*-type semiconducting polymers

Takimiya and coworkers reported various heteroaromatic polymers and small molecules for OFETs (Figure 1.16). The design approach here was based on the fused thiophene units to block the rotation between the neighboring thiophenes. Previously synthesized PBTBT polymer which consist of [1]Benzothieno[3,2-b][1]benzothiophene (BTBT) and thiophene monomers did not function in OFETs while BTBT was successful as a small molecule [42]. Therefore, new design approach have been developed by same group in which center thienothiophene units were replaced with naphthalene. The new polymer consisted of naphthodithiophene (NDT) and regiosymmetricly substituted thiophene monomers. OFET devices based on P-21, P-22 and P-23 showed very good charge carrier mobilities of >0.3-0.5 cm^2/Vs [43,44]. Among the polymeric semiconductors reported to date, these field effect mobility values were among the highest.

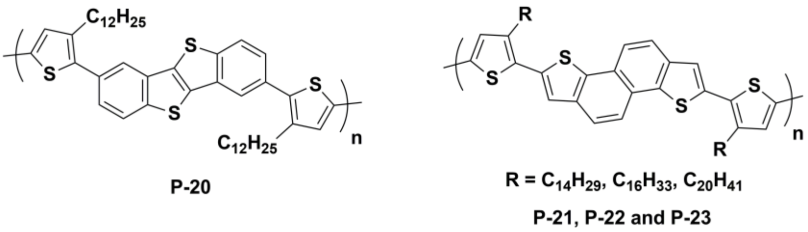

Figure 1.16 Chemical structure of heteroarene based *p*-type semiconducting polymers

Isoindigo based polymers have recently become one of the most popular π-systems in the literature due to their strong electron withdrawing (EWG) character of lactam rings. More importantly, isoindigo can be synthesized from numerous natural sources making it a great material for the sustainable synthesis of semiconductors. Reynolds *et al.* reported the first series of isoindigo based polymers consisting of isoindigo acceptor unit and various donor units including vinyl, unsubstituted/alkyl substituted thiophene, di-alkoxy substituted phenyl, and so on (Figure 1.17, P-24→P,29) [45]. Beyond the OFETs, OPV applications of these polymers were attractive because of their deep frontier orbital energy levels and tunable absorption profile which can be extended over 800 nm. To further develop the OPV performance of isoindigo based polymers, various electron donating groups have been reported. Among them terthiophene units showed a power conversion efficiency of 6.3% which is one of the highest efficiency for a polymeric semiconductor with a band gap of lower than 1.5 eV (Figure 1.17, P-30) [46].

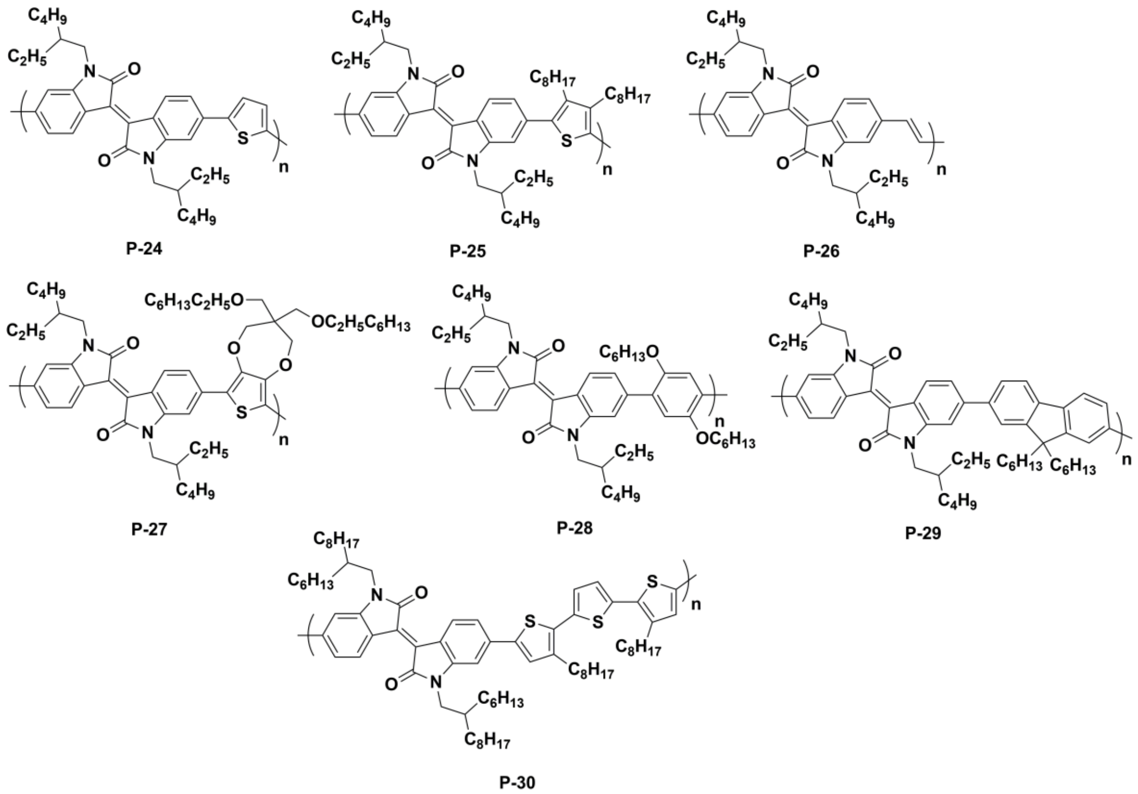

Figure 1.17 Chemical structure of isoindigo based *p*-type semiconducting polymers

Lastly, diketopyrrolopyrrole (DPP) is one of the polymeric semiconductors that shows high charge carrier mobility over 1 cm^2/Vs in OFET devices. After the first reported DPP-based semiconductor in 2008 [47], many other donor-acceptor polymers with DPP electron deficient units have been developed. Charge carrier mobilities in these devices was between 0.1 to 2.0 cm^2/Vs and mostly around 1.0 cm^2/Vs [48–50]. Ong *et al.* reported one of the record high hole mobilities in the literature for a *p*-type polymeric semiconductor (10.5 cm^2/Vs) (Figure 1.18, P-31) [51]. This polymer was consist of unsubstituted thienothiophene as a donor moiety and DPP as acceptor unit. This design results in high coplanarity, which enables proper intermolecular interactions in the solid state and thus increases molecular orbital delocalization along the backbone. Also high molecular weight of this polymer (M_n) is another reason to achieve such a high OFET device performance. In another report, Kim and coworkers synthesized a DPP based polymer which has side chains with extended branching position (Figure 1.18, P-32) [52]. These polymeric semiconductors exhibited a very good charge carrier mobility of 5.0 cm^2/Vs at room temperature and 12.0 cm^2/Vs after thermal annealing due to enhanced intermolecular interactions and long range ordered edge-on oriented thin film microstructure. Li *et al.* reported another DPP based polymers which has furan donor units instead of unsubstituted thienothiophene in the former study (Figure 1.18, P-33) [53]. The thin films of this polymer showed a hole mobility of 1.54 cm^2/Vs after the annealing at 200 °C.

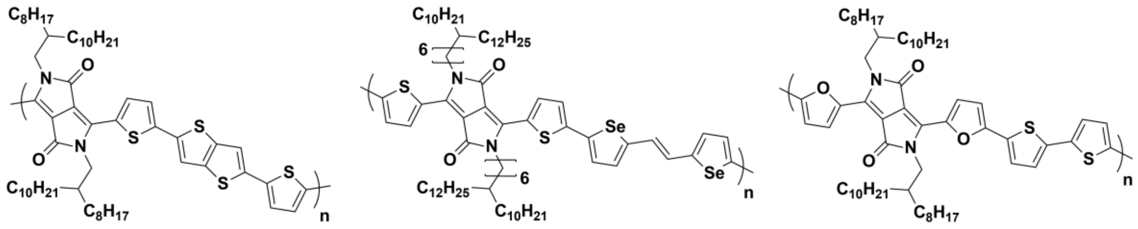

P-31 P-32 P-33

Figure 1.18 Chemical structure of diketopyrrolopyrrole based *p*-type semiconducting polymers

From the small molecular semiconductors perspective, oligothiophenes are the most commonly studied π-system for optoelectronic devices. Thiophenes with four [54], five [54], six [55] and eight [56] rings and their polycrystalline films have been widely investigated in the literature (Figure 1.19, M-1→M-4) [57]. All these molecules showed planar packing with herringbone motif in the solid state which facilitates good charge carrier mobility in OFETs. The four (4T) and six (6T) membered thiophene based oligomers exhibited hole mobilities of up to 0.006 cm^2/Vs and 0.08 cm^2/Vs, respectively [58]. For the eight thiophene (8T) rings highest mobility value reported in the literature is 0.33 cm^2/Vs for 120 °C annealed thin films [59]. Oligothiophene with six rings (6T) is the most commonly studied derivative of this family and showed charge carrier mobility of ~0.03 cm^2/Vs in OFETs with a bottom contact/bottom gate (BC/BG) device architecture [55]. Loi and coworkers reported molecular orientation of this molecule on top of the SiO_2 dielectric layer based on confocal microscopy and spectroscopy [60]. This study clearly showed that after completing the first self assembled monolayer on the substrate, all these molecules stand on the substrate. Thin films with more than two monolayer have mixed regions with both face-on and edge-on orientation.

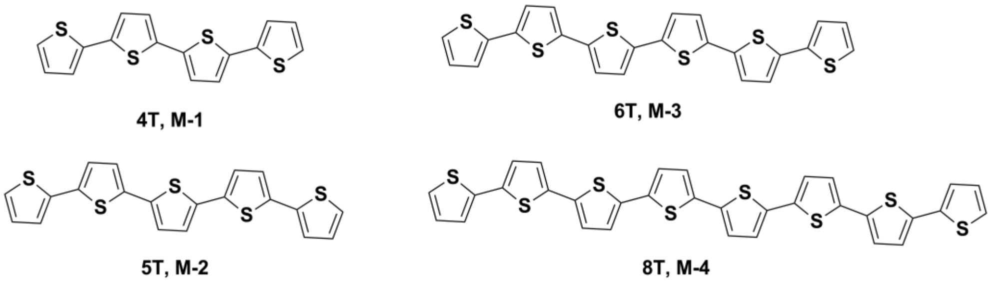

Figure 1.19 Chemical structure of oligothiophene based *p*-type semiconducting small molecules

Another family of *p*-type small molecular semiconductor is heteroacenes in which one or more acene is replaced with heteroaromatic π-units, while the ladder type molecular shape was preserved. There are two possible design strategies in heteroacenes, the first benzene rings are placed at the center and the heteroaromatic units are located at the molecular terminals, and vice versa in the second case. Typically, heteroacenes have deeper HOMO energy level (<-5.2 eV) compared to pentacene (-5.0 eV) due to their lower aromaticity which enables ambient stable hole transport through the active channel in OFETs [61]. Sirringhaus and coworkers synthesized a fused heteroacene derivative of dibenzothienobenzothiophene (Figure 1.20, M-5) with a OFET performance of $\mu_h = 0.15$ cm^2/Vs and I_{on}/I_{off} ratio of >10^6 [62]. The idea of implementation of thiophene end units into the pentacene π-core was promising to reach solution processable and air stable *p*-type molecular semiconductors with good solid state packing and orientation. To this end, the first series of anthradithiophene molecules was reported by Katz *et al.* with ten times lower charge carrier mobility (~0.1 cm^2/Vs) and higher I_{on}/I_{off} ratio than the parent pentacene molecule (Figure 1.20, M-6→M-9) [63]. Anthony and coworkers synthesized functionalized ADT derivative (M-10) to fabricate thin films based on a solution processed technique [64]. OFET devices based on thin films of this molecule showed a good performance of $\mu_h = 1.0$ cm^2/Vs and I_{on}/I_{off} ratio of ~10^7 due to strong π-π interactions in the solid state.

Takimiya *et al.* developed another design strategy which is based on placing heteroaromatic units at the center and benzene rings positioned at molecular terminals. This strategy enables us to reach higher hole mobilities in OFETs. Based on the number of end capped benzene rings, they developed a series of new heteroacene based semiconductors. BTBT (M-11→M-13), DNTT (M-14→M-16) and DATT (M-17) consisted of benzene, naphthalene and anthracene as end-capping rings, respectively, and a central fused thienothiophene unit common to all three molecule (Figure 1.20). The OFET devices based on these small molecules exhibited ambient stable characteristics due to their low degree of aromaticity which reduces the HOMO energy level. Short alkyl substituted BTBT derivatives (n = 5-14) showed a very good device performances of μ_h = 2.0 cm^2/Vs and I_{on}/I_{off} ratio of 10^7 with high solubility in common organic solvents [65]. On the other hand DNTT has limited solubility because of its further extended π-conjugation. Therefore, OFET devices of DNTT were fabricated with vapor deposited technique. The mobility performance of DNTT thin films was 2.9 cm^2/Vs [66]. Upon alkyl substitution in the molecular long axis direction, charge carrier mobility increased to 8 cm^2/Vs which is one of the highest value in OFETs for a small molecular semiconductors [67]. DATT is the longest π-conjugated small molecule in this family with eight fused aromatic units. This molecule has a HOMO energy level of 5.1 eV and highly extended π-conjugation. Although the microstructure of thin films of DATT was consisting of both edge-on and face-on orientation, vapor deposited thin films of this molecule showed a charge carrier mobility of 3.0 cm^2/Vs [68].

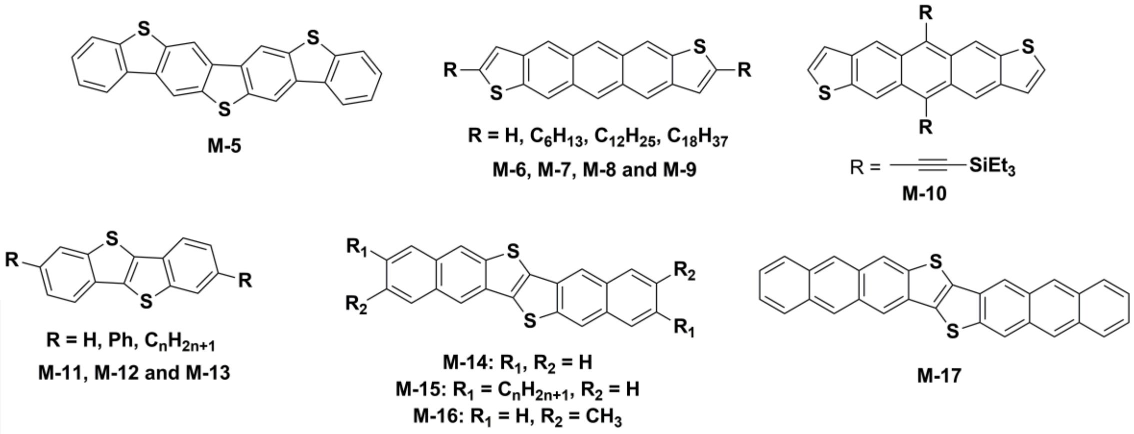

Figure 1.20 Chemical structure of heteroacene based *p*-type semiconducting small molecules

1.3.2 *N*-Type Molecular/Polymeric Semiconductors

N-type semiconductors lag behind *p*-type materials due to difficulties in material development. In principle, organic semiconductors are expected to transport electrons as efficiently as holes, based on several theoretical and experimental studies. Besides the electronic nature of semiconductors, there are three main factors that enable efficient electron transport in OFETs. The first one is gate-dielectric surface chemistry, since early dielectrics that are commonly used in OFETs were oxide materials (i.e. SiO_2) with efficient electron traps on their surfaces [69]. The second one is metal contacts where the energy barrier between fermi level of metal and LUMO energy level of semiconductor should be low to facilitate electron injection from metal electrode to the semiconductor. Low work function metals such as Al or Ca can be used for this purpose. But, the oxidation of these metals by air results in an insulating layer, which may destroy the advantage of having low fermi energy level. Lastly, the composition of ambient atmosphere where electron transport is hampered via O_2 and H_2O. Therefore, various semiconducting materials could not show the *n*-type device character. To overcome all these drawbacks, today most devices with electron transporting ability have surface passivation layer on top of dielectric layer and polymeric dielectric materials instead of SiO_2. It is known that semiconductors with LUMO energy levels around -4.0 to -4.3 eV are able to transport electrons efficiently under ambient conditions. The OFET device performance of semiconductors with higher LUMO level (low electron affinity) shows a rapid deterioration when exposed to air. This can not be avoided by using dielectric material without any electron traps. On the other hand, the energy barrier between the metal electrode and semiconductor becomes close in π-systems with lower LUMO level, which results in difficulties to turn the device off. Here, we will briefly describe the early *n*-type semiconductors and recent developments in the literature.

The first *n*-type polymeric semiconductor which was used as an active layer in OFETs was based on benzobisimidazobenzophenanthroline (BBL) π-system (Figure 1.21, P-34). And its derivative with a fused benzene ring (BBB, P-35) showed good electron mobility ~0.1 cm^2/Vs in spin coated thin films [70]. The Northwestern University group reported another electron transporting copolymer with dithenodiimide π-core. This solution processable polymer (N-(2-octyldodecyl)-2,2'-bithiophene-3,3'-dicarboximide) (DTI, P-36) exhibited electron mobility over 0.01 cm^2/Vs and I_{on}/I_{off} ratio of 10^7 [71]. Other *n*-type polymers based on rylene dicarboximide cores having perylene unit (PDI2DD-DTT) (Figure 1.21, P-37) showed limited molecular weight (~15 kDa), glass transition temperature of 215 °C and thermal onset of 410 °C [72]. OFET devices based on PDI2DD-DTT thin films with top-contact/bottom-gate geometry exhibited μ_e = ~0.01 cm^2/Vs and I_{on}/I_{off} ratio of $>10^4$ under inert atmosphere. Recently, Thelakkat *et al.* synthesized another electron deficient polymer with perylenediimide pendant group and oligoethyleneglycol substituents (Figure 1.21, P-38)

[73]. OFET device characterization with space charge limited current (SCLC) measurements showed an electron mobility of 0.01 cm^2/Vs. This study revealed that optical properties and device performance can be tuned by changing substituents on the side-chain of the polymers.

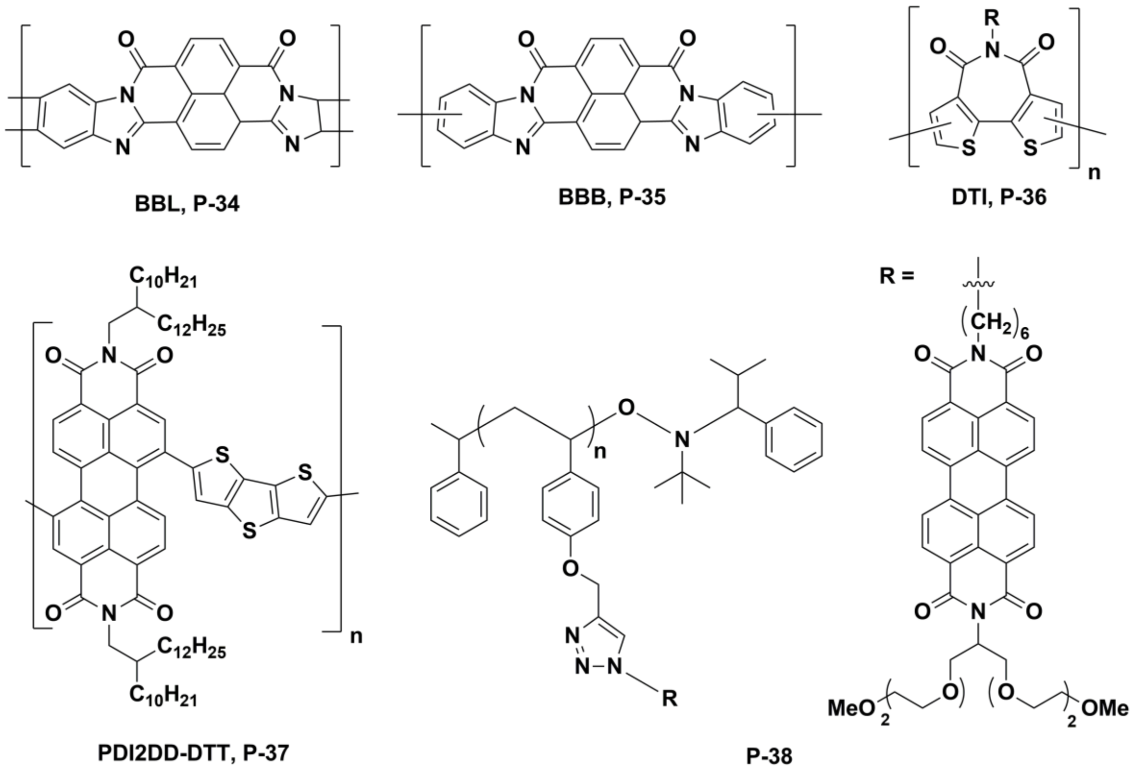

Figure 1.21 Chemical structure of the first-generation *n*-type semiconducting polymers

Polyera Corporation group reported a comparative study of copolymers based on NDIR-T2 (N,N’-dialkylnaphthalenedicarboximide-dithiophene) vs. PDIR-T2 (N,N’-dialkylperylenedicarboximide-dithiophene) to achieve high performance *n*-type OFET devices and air stable electron transport through the active channel (Figure 1.22, P-39 and P-40) [74]. The reasons behind this behavior are: i) large electron affinity of naphthalene core compared to more π-extended perylene unit, ii) facile synthesis of NDIR-Br_2 reagent which enable us to reach regioregular polymeric backbone, iii) well mastered alkyl chain substituent (2-OD) on nitrogen atom of rylene unit which results in high solubility and efficient charge transport ability, iv) lastly, stable and commercially available dithiophene was chosen as a co-monomer due to its known electronic structure which typically gives planar and rod-like polymers with π-extended conjugation. Electrical performance of bottom gate OFETs based on NDIR-T2 and PDIR-T2 were characterized both under vacuum and open-air. Under vacuum, these devices exhibited electron mobilities of ~0.08-0.06 cm^2/Vs and ~0.003-0.001 cm^2/Vs, respectively. On the other hand, PDIR-T2 based OFETs showed appreciable degradation (μ_e = ~0.0002 cm^2/Vs) upon exposure to air, while NDIR-T2 continued to function under ambient conditions (μ_e = ~0.01 cm^2/Vs) even after three months from the day of production.

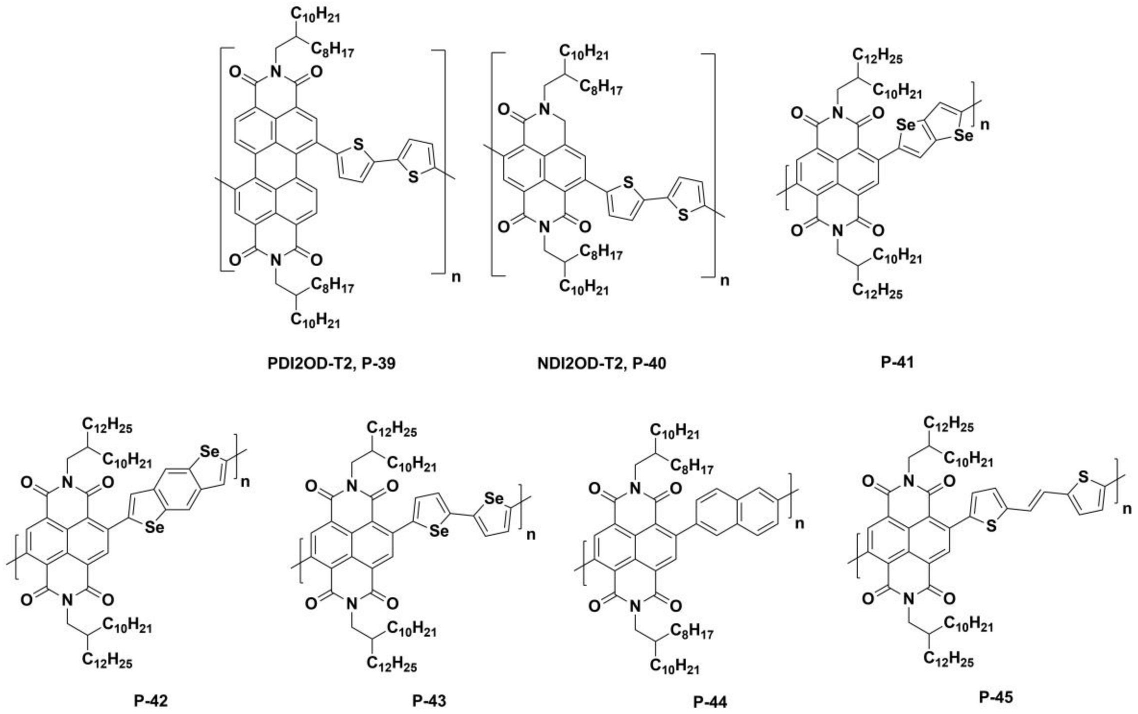
PDI2OD-T2, P-39 NDI2OD-T2, P-40 P-41

P-42 P-43 P-44 P-45

Figure 1.22 Chemical structure of NDI and PDI based *n*-type semiconducting polymers

Jenekhe *et al.* reported another electron deficient polymeric semiconductor based on naphthalene diimide (NDI) π-system (Figure 1.22, P-41, P-42 and P-43). In these designs, selenophene units are preferred over thiophene donor units [75]. OFET devices based on NDI based polymers showed a maximum electron mobility of 0.24 cm^2/Vs and current modulation ratio between 10^4-10^6. Changing donor moieties to phenyl resulted in large enhancement of charge carrier mobilities in OFETs. For this purpose, Yang *et al.* developed acene based NDI copolymer which exhibited an electron mobility of 0.056 cm^2/Vs in OFETs with bottom-gate/top-contact geometry (Figure 1.22, P-44) [76]. This study revealed that not only the strength of donor but also geometric properties of donor significantly affect the charge transport features. Recently, Noh and coworkers reported another NDI-based electron transporting polymer with high OFET device performance (Figure 1.22, P-45) [77]. The polymer design herein consisted of 2-decyltetradecyl substituted NDI acceptor unit and thienylene-vinylene-thienylene donor units. This new polymer has extended π-conjugation length and LUMO energy level of

-4.00 eV compared to NDIR-T2, P-39. OFET devices based on P-45 with top-gate/bottom-contact (TG/BC) architecture showed high performance of μ_e = 1.8 cm^2/Vs and I_{on}/I_{off} ratio of 10^6 with high stability against air and bias stress. This OFET device performance is among the best polymeric n-type semiconducting materials reported so far. The reasons behind this outstanding performance are improved interchain π-π stacking, enhanced crystallinity in solid state with lamellar structure, and both face-on and edge-on orientations.

Pei *et al.* synthesized a new poly(*p*-phenylemevinylene) (PPV) based electron transporting semiconductors which consist of strong electron withdrawing carbonyl functional groups on the double bonds. This not only extends the π-conjugation length but also forms hydrogen bonds to build coplanar scaffold thanks to the “locked” conformation (Figure 1.23, P-46) [78]. Alkyl substituents were used to enable solution processability and π-π intermolecular interactions. This design approach makes a new polymer such a high performing *n*-channel semiconductor due to lack of conformational disorder, strong intermolecular interactions and deeper LUMO energy level. Open-air electrical characterization of OFET devices based on P-46 with TG-BC geometry showed a maximum electron mobility of 1.1 cm^2/Vs. This OFET device is one of the highest charge carrier mobilities ever achieved for a *n*-type polymeric semiconductor.

Tetraazabenzodifluoranthenediimide (BFI) is another electron deficient building block and was first synthesized by Jenekhe and coworkers (Figure 1.23, P-47) [79]. These polymers based on BFI building block and thiophene donor monomer. OFET devices based on P-47 demonstrated electron mobility of 0.3 cm^2/Vs. Recently, Swager *et al.* reported a fluorinated n-type polymeric semiconductor, poly(2,3-bis(perfluorohexyl)thieno[3,4-b]pyrazine) (Figure 1.23, P-48) which showed high thermal/air stability and LUMO energy level of 4.12 eV [80]. Corresponding OFET devices exhibited poor electron mobilities of $\sim 10^{-5}$ cm^2/Vs due to unfavorable thin film morphology. Finally, DPP is an attractive electron deficient π-unit to form n-type polymeric semiconductors because of its high coplanarity, enhanced interchain π-π stacking. Patil and coworkers recently reported DPP-DPP based polymer with alkyl/triethylene glycol substituents (Figure 1.23, P-49) [81]. OFET devices based on P-49 showed a maximum electron mobility of 3.0 cm^2/Vs.

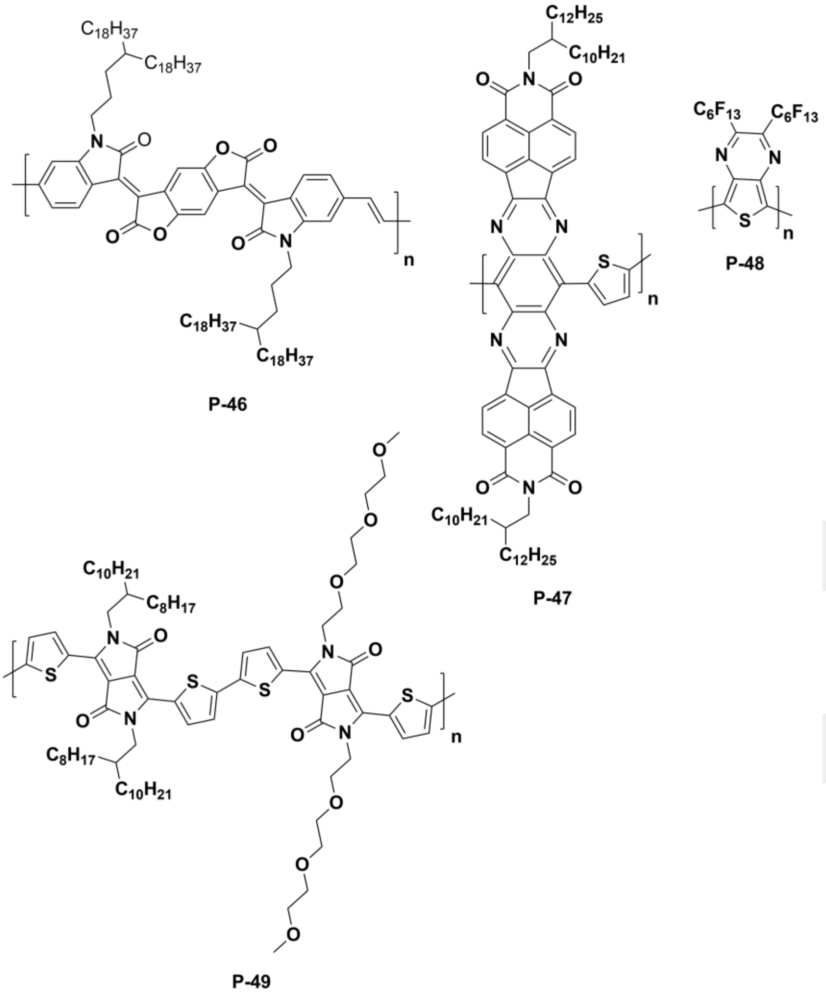

Figure 1.23 Chemical structure of other *n*-type semiconducting polymers

The first *n*-type small molecular semiconductor was reported by Guillaud and coworkers based on a lutetiumphthalocyanine (LuPc$_2$) [82]. OFET device characterizations were performed under vacuum and vapor deposited thin films of LuPc$_2$ showed electron mobilities of 10^{-5} cm^2/Vs. In another study, Bao *et al.* reported the first air stable *n*-type molecule, a perfluorinated phthalocyanine compound (F$_{16}$CuPc), and its vacuum deposited thin films deposited showed electron mobilities as high as ~0.03 cm^2/Vs under ambient conditions (Figure 1.24, M-18) [83]. This is the first example of air-stable n-type molecular semiconductor realized by functionalization of a p-type material (CuPc) with an electron withdrawing groups (F) in the literature. In a recent report, Ling and coworkers developed another phthalocyanine derivative (Cl$_{16}$CuPc) with electron mobility of ~0.01 cm^2/Vs (Figure 1.24, M-19) [84]. Song *et al.* reported a remarkable electron mobilities of 0.30 cm^2/Vs under ambient condition by using another phthalocyanine based semiconductor (SnCl$_2$Pc) (Figure 1.24, M-20) [85].

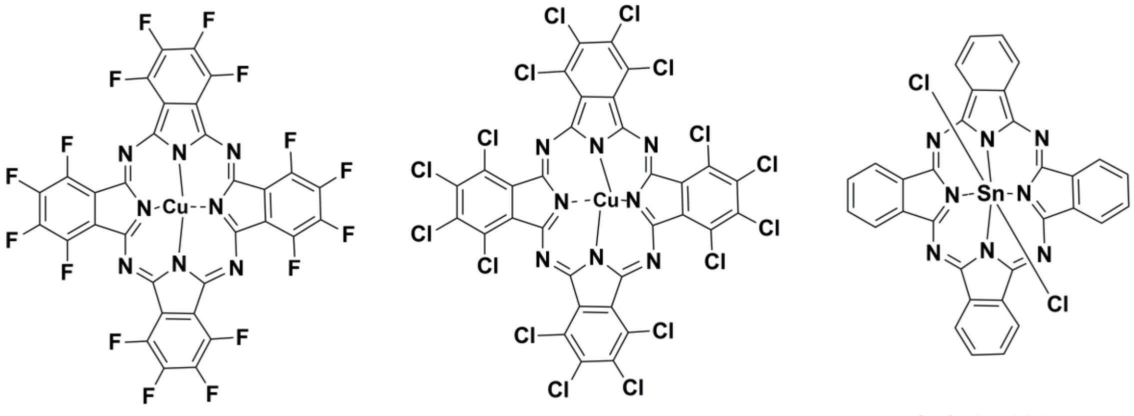

$F_{16}CuPc$, M-18 $Cl_{16}CuPc$, M-19 $SnCl_2Pc$, M-20

Figure 1.24 Chemical structure of phthalocyanine based *n*-type semiconducting small molecules

The first oligothiophene based electron transporting small molecules have been reported by Marks *et al.* in a series of study [86–88]. Depending on the length of conjugation, oligothiophenes with perfluorohexyl substitution at various positions (α,ω vs. β,β’) (Figure 1.25, M-21 and M-22) caused a decrease in both HOMO and LUMO energy levels. These studies revealed that substitution of oligothiophene plays a key role in determining the majority of the charge carriers in active layer. Thus, oligothiophenes with perfluoroalkyl chain exhibited *n*-type OFET device character while oligothiophenes with or without alkyl chain behaved as *p*-type semiconductors. Among these small molecules, DFH-4T showed one of the highest electron mobility (0.22 cm^2/Vs) and current modulation ratio for an electron transporting small molecular semiconductor. Functionalization of oligothiophenes with strong electron withdrawing group including carbonyl results in fine tuning of frontier orbital energy levels, optical properties and solid state packing. DFHCO-4T (Figure 1.25, M-23) showed appreciable electron mobility of 0.32 cm^2/Vs under vacuum with 25 °C annealed thin films. Another carbonyl functionalized oligothiophene derivative, DFPCO-4T (Figure 1.25, M-24) exhibited one of the shortest intercore distance of 3.50 Å with 2D herringbone patterned crystal motif [89]. OFET devices based on DFPCO-4T molecule showed electron mobility as high as 0.5 cm^2/Vs after thermal annealing at 80 °C. Frisbie *et al.* synthesized a new oligothiophene based electron transporting semiconductor which is based on quinomethane terthiophene (Figure 1.25, M-25) [90]. The corresponding OFET devices showed charge carrier mobility between ~0.002 – 0.5 cm^2/Vs.

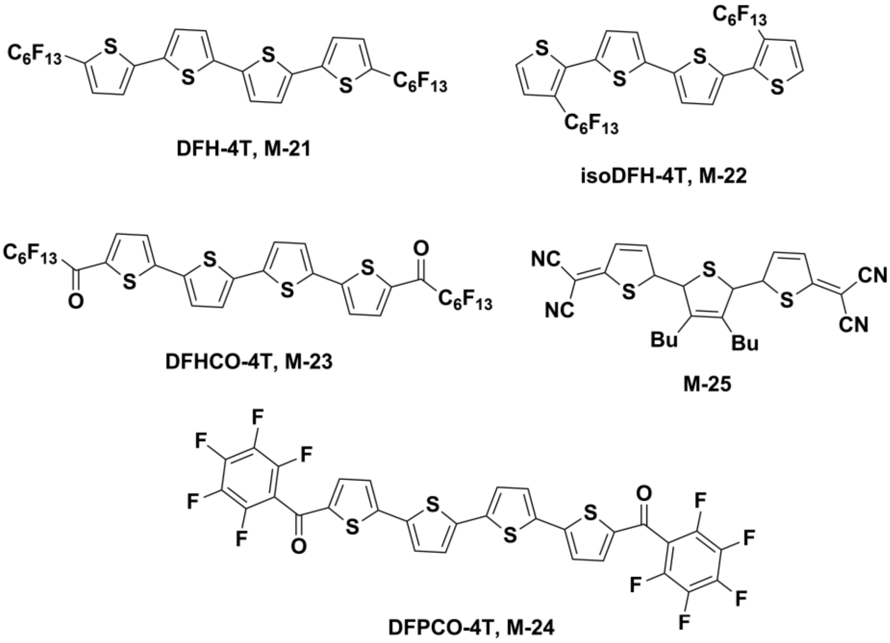

Figure 1.25 Chemical structure of oligothiophene based *n*-type semiconducting small molecules

Fullerene is another derivative of *n*-channel molecular semiconductors. The first C_{60} (Figure 1.26, M-25) based molecule showed very low electron mobilities of ~10^{-4} cm^2/Vs [91]. In another study, Fleming *et al.* reported charge carrier mobilities between $\mu_e = 0.2 - 0.56$ cm^2/Vs with C_{60} thin films deposited under ultrahigh vacuum and OFET devices electrically characterized without exposure to air [92]. In addition, the first *n*-type C_{70} based molecule have been reported in 1996 by Haddon [93]. This semiconductor exhibited electron mobilities of 0.002 cm^2/Vs and current modulation ratio of 10^5. The major drawback of and C_{70} based fullerenes is the quick degradation upon air exposure. Recently, Itaka *et al.* and Anthopoulos *et al.* reported field effect electron mobilities of ~2 -5 cm^2/Vs, ~6.0 cm^2/Vs, respectively with C_{60} based semiconductors [94,95]. Solution-processable fullerenes have been realized via functionalization. For this purpose, Chikamatsu and coworkers reported N-methylpyrrolidine-*meta*-C12 phenyl functionalized C_{60} molecule (Figure 1.26, M-26) which exhibited field effect mobility of $\mu_e =$ 0.07 cm^2/Vs [96]. [6,6]-phenyl-C61-butyric acid methyl ester (Figure 1.26, M-27) and [6,6]-phenyl-C71-butyric acid methyl ester have been widely used in organic photovoltaics as acceptor material [97].

M-25

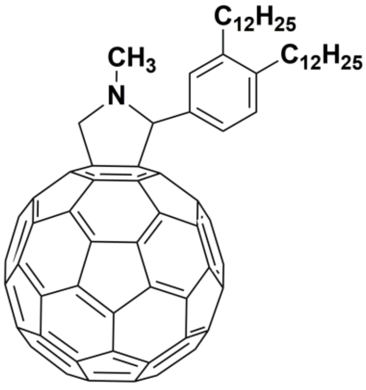

M-26

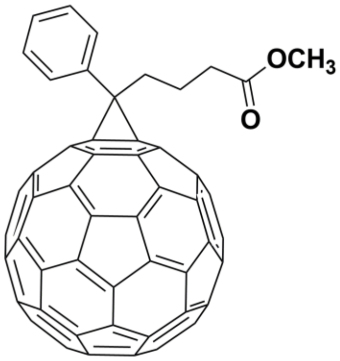

M-27

Figure 1.26 Chemical structure of fullerene based *n*-type semiconducting small molecules

Quinoidal small molecular π-systems with dicyanomethane substitution are excellent electron deficient molecules due to high coplanarity and low LUMO energy level. Recent studies about them showed electron mobilities of >0.5 cm^2/Vs in OFETs. The first DPP-based quinoidal molecular semiconductor have been reported by Zhu *et al.* and exhibited maximum field effect mobilities of 0.55 cm^2/Vs for vapor deposited thin films (Figure 1.27, M-28) [98].

Lastly, rylene diimide based molecular π-systems have been extensively studied as *n*-type semiconductors in OFETs. Recently, Zhu and coworkers synthesized various NDI derivative with different N-alkyl chain length [99,100]. Among them 3-Hexyl-Undecyl substituted small molecule, M-29, exhibited electron mobilities as high as 3.5 cm^2/Vs thanks to large grain size and favorable packing in solid state (Figure 1.27) [98].

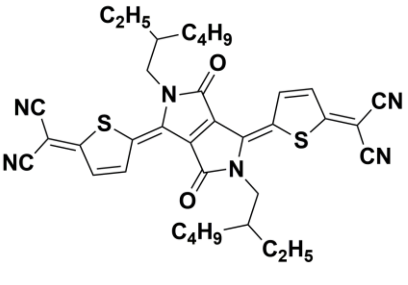

M-28

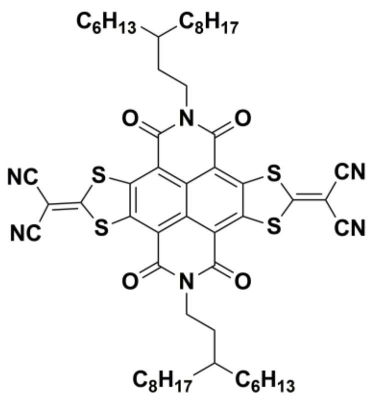

M-29

Figure 1.27 Chemical structure of some high performing *n*-type semiconducting small molecules

Chapter 2

High Electron Mobility in [1]Benzothieno[3,2-b][1]benzothiophene (BTBT)-Based Field-Effect Transistors: Toward N-Type BTBTs

2.1 Introduction

The development of π-conjugated small molecule semiconducting materials is an emerging and continuously growing research area in organic (opto)electronics [101–105]. Semiconducting small molecules are the key active layer component of high-performance organic field-effect transistors (OFETs) used for next-generation (opto)electronic technologies such as logic circuits on plastic substrates, flexible displays, and electronic skins [106–110]. The main motivations for continuously designing and synthesizing new π-conjugated frameworks in the past few decades do not only include improving charge-transport characteristics and realizing novel functions, but also to better understand and address fundamental structure-(opto)electronic property-electrical performance relationships [111–116]. Since the initial report of small molecule-based OFETs three decades ago [117], the search for semiconducting small molecules has primarily focused on fused (hetero)acene structures including [1]benzothieno[3,2-b][1]benzothiophene (BTBT) derivatives [68,118,119]. The synthesis of BTBT π-core was first conveyed in 1950s[120] and the earlier derivatives were studied as liquid crystals [121,122].

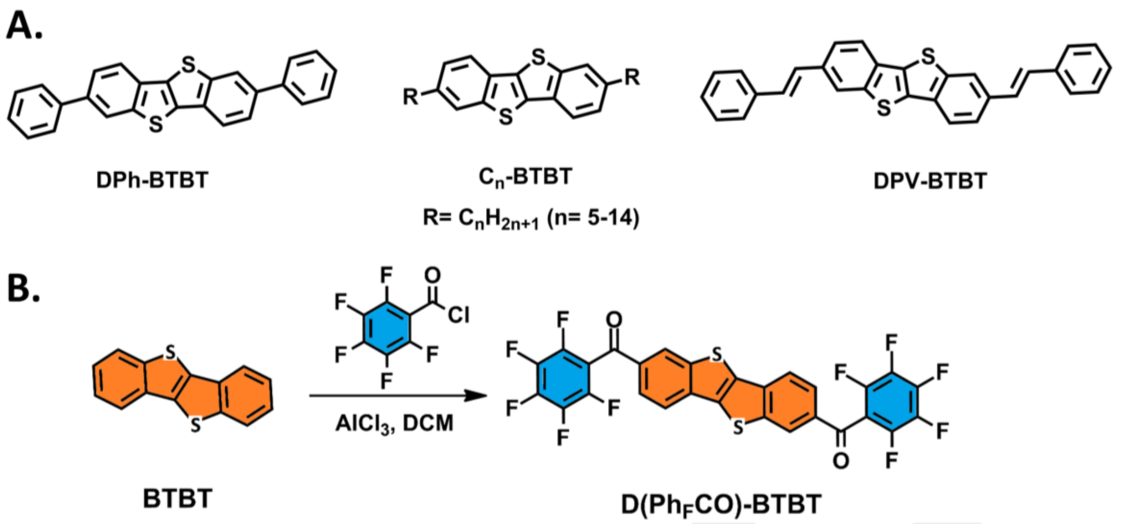

Figure 2.1 A. Chemical structures of [1]Benzothieno[3,2-b][1]benzothiophene (BTBT) π-core and *p*-type molecular semiconductors **DPh-BTBT**, **C_n-BTBT**, and **DPV-BTBT** reported in the literature [42,65,123]. B. Synthesis of the current *n*-type semiconductor **D(Ph_FCO)-BTBT**.

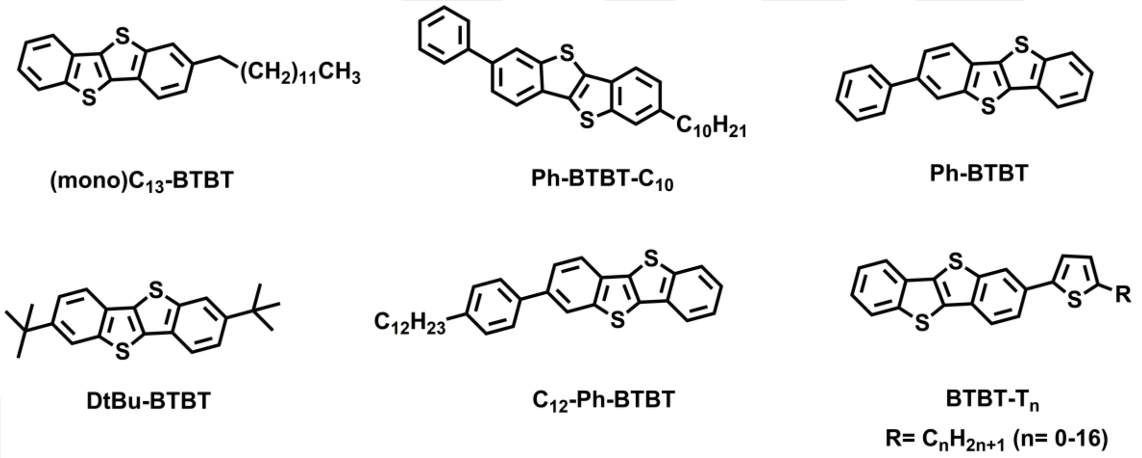

Figure 2.2 Chemical structures of *p*-type **BTBT**-based molecular semiconductors reported in the literature [124–129].

The semiconducting properties of this family were unexplored until the pioneering studies by Takimiya *et al.*, which demonstrated *p*-type charge transport for vapor-deposited films of 2,7-diphenylbenzo[*b*]benzo[4,5]thieno[2,3-*d*]thiophene (**DPh-BTBT**) and spin-coated films of 2,7-dialkyl[1]benzothieno[3,2-b][1]benzothiophene (**C_n-BTBT**, n = 5-14) (Figure 2.1A) [42,65]. Following these studies, numerous functionalized BTBT derivatives (Figure 2.2) have been developed for use in OFETs, including additional core functionalization and core extension by benzofusion

[42,65,123–130]. Furthermore, the crystallinity/packing properties of the well-known derivative **C_8-BTBT** (n = 8) have been tuned via unconventional solution-based film fabrication techniques (i.e., antisolvent-assisted inkjet printing and off-center spin-coating) yielding impressive charge-transport characteristics [131,132].

There are several reasons for incredibly rapid emergence of BTBT-based semiconducting molecules in the past decade: (i) facile π-core synthesis and functionalization allowing fine tuning of solid-state packing, solubility, and frontier orbital properties; (ii) presence of a fused rigid π-system with structural symmetry and high coplanarity, which facilitates charge carrier delocalization and intermolecular interactions; (iii) large frontier orbital coefficients on the sulfur atoms, which is beneficial for effective intermolecular orbital overlap and large transfer integrals [61]; (iv) presence of thieno[3,2-b]thiophene unit in the center of a thienoacene π-framework and phene-type π-electronic structure resulting in large optical band gap (>3.0 eV) and stabilized highest occupied molecular orbital (HOMO) energy level (<−5.5 eV) [61,133,134]. Despite these very attractive structural/electronic properties and great progresses shown until today, all reported BTBT derivatives are hole-transporting (*p*-type) semiconductors. To the best of our knowledge, an *n*-type (electron-transporting) BTBT semiconductor is currently unknown in the literature and the fundamentals remain to be established. This is most likely the result of very high LUMO energy level and large band gap of fused π-core in BTBT ($E_{g(opt)}$ = 3.65 eV, E_{LUMO} = -2.10 eV in C_8-BTBT)[42] as compared with those of similar sized non-fused π-systems such as quaterthiophene (E_g = 2.89 eV, E_{LUMO} = -2.90 eV) [86,87] and hexyl-substituted bis(phenyl)-bithiophene (E_g = 2.97 eV) [135]. The only known example of electron-transporting BTBT-based material involves a single-crystalline donor-acceptor mixture of *p*-type Cn-BTBT donor with *n*-type tetracyanoquinodimethane acceptor [136]. This arises an important question whether BTBT, as a wide band-gap π-core, would ever allow energetically stabilized (<−3.0 eV) lowest unoccupied molecular orbital (LUMO) and good electron-injection/transport characteristics. Towards this end, we focus on symmetric functionalization of the BTBT π-core in the molecular *long-axis* direction with pentafluorophenylcarbonyl (Ph_FCO) groups. The strong electron-withdrawing characteristics of the combined pentafluorophenyl (Ph_F) and carbonyl (C=O) units are envisioned to lower frontier orbital energies, extend π-conjugation, and facilitate electron injection/delocalization on the molecular π-backbone [89,137]. In addition, as a result of the presence of these groups along *long-axis* at the molecular termini, lateral noncovalent interactions between the BTBT π-cores should still be effective for efficient charge transport.

We present herein the design, synthesis, and full characterization of a new BTBT-based semiconducting small molecule, **D(Ph$_F$CO)-BTBT**, which was developed via a two-step transition metal-free process without using chromatographic purification. Physicochemical and optoelectronic characterizations of the new semiconductor were performed in detail and the crystal structure was accessed. The new molecule exhibits a large optical band gap (~2.9 eV) and highly stabilized (-3.64 eV)/π-delocalized LUMO mainly comprising the BTBT π-core and *in-plane* carbonyl units. The effect of *out-of-plane* twisted (64°) pentafluorophenyl groups on LUMO stabilization is found to be minimal. Polycrystalline **D(Ph$_F$CO)-BTBT** thin-films prepared by physical vapor deposition exhibit large grains (~2-5 μm sizes) and "layer-by-layer" stacked *edge-on* oriented molecules with an *in-plane* herringbone packing (intermolecular distances ~3.25-3.46 Å). The new molecule exhibits *n*-type semiconductor behavior in OFETs with a high electron mobility (μ_e) of 0.57 cm^2/V·s and current modulation (I_{on}/I_{off}) over 10^7-10^8. **D(Ph$_F$CO)-BTBT** is demonstrated to be the first *n*-type BTBT semiconductor, which could open new possibilities for future complementary optical and circuitry applications.

2.2 Experimental Section

2.2.1 Materials and Methods

Unless otherwise noted, all reagents were purchased from commercial sources and used without further purification. All non-aqueous reactions were carried out in dried glassware under an inert atmosphere of N_2. ^{1}H NMR spectroscopy characterizations were performed by using a Bruker 400 spectrometer (^{1}H at 400 MHz). Elemental analyses were recorded on a LecoTruspec Micro model instrument. The intensity data for D(Ph$_F$CO)-BTBT single-crystal were collected on a Bruker APEX II QUAZAR three-circle diffractometer using monochromatized Mo-K$_\alpha$ X-radiation (λ = 0.71073 Å). Single-crystal structure refinement was performed as explained in the Supporting

Information. Thermal characterizations of thermogravimmetric analysis (TGA) and differential scanning calorimetry (DSC) were performed under nitrogen at a heating rate of 10 °C/min using Perkin Elmer Diamond model instruments. Cyclic voltammetry measurements were carried out using BAS-Epsilon potentiostat/galvanostat from Bioanalytical Systems Inc. (Lafayette, IN) equipped with a C3-cell stand electrochemical station. Working and counter electrodes were Pt, and the reference electrode was Ag/AgCl(3M NaCl). All potentials were calibrated with standard ferrocene/ferrocenium redox couple (Fc/Fc^+: $E_{1/2}$ = +0.40 V measured in the current electrochemical set up). High-resolution mass spectra were measured on a Bruker Microflex LT MALDI-TOF-MS. UV-vis absorption spectra were recorded by using a Shimadzu UV-1800 spectrophotometer. The optimization of the molecular geometries and analysis of frontier molecular orbitals were carried out with Gaussian 09 by using DFT at B3LYP/6-31G** level [138].

2.2.2 Field-Effect Transistor Fabrication and Characterization

Heavily *n*-doped (100) silicon substrate (gate) with 200 nm thermally grown SiO_2 (gate dielectric) was used as the semiconductor thin-film platform. The substrates were sonicated in isopropyl alcohol for 10 min with subsequent drying under N_2 flow, which was followed by 100 W oxygen plasma treatment for 3 min (Cute, Femto Science, South Korea). The hydrophobic surface was obtained with hexamethyldisilazane (HMDS) vapor-treatment on 200 nm $SiO_2/n^{++}Si$. The 30 nm D(Ph_FCO)-BTBT thin-films were grown via thermal evaporation on O_2 plasma treated n^{++}-Si/SiO_2(200 nm) and n^{++}-Si/SiO_2(200 nm)/HMDS substrates under high vacuum (~10^{-6} torr) at various substrate temperatures (25 °C, 70 °C, 100 °C and 120 °C) using a growth rate of 0.1-0.2 Å/s. To complete the field-effect transistor device architecture, LiF (1 nm)/Au (50nm) or Au (50 nm) source-drain electrodes were thermally evaporated through shadow mask to define 50 μm semiconductor channel length and 1000 μm semiconductor channel width. The surface morphology and microstructure of the semiconductor thin films were characterized by atomic force microscopy (AFM, NX10, Park systems) and Grazing Incidence X-ray Diffraction (GIXD, PLS-II 9A U-SAXS beamline of Pohang Accelerator Laboratory in Korea) techniques, respectively. The electrical characteristics of the D(Ph_FCO)-BTBT-based field-effect transistor devices in top-contract/bottom-gate geometries were analyzed by using a vacuum probe station (M5VC, MSTech, South

Korea) and Keithley 4200-SCS semiconductor analyzer system (Tektronix Inc, USA). The saturation charge-carrier mobility (μ_{sat}) for each device fabrication condition was calculated as the average value of at least 10 OFET devices using the formula:

$$\mu_{sat} = (2I_{DS}L)/[WC_i\,(V_G - V_{th})^2] \qquad (2.1)$$

where I_{DS} is the source-drain current, L is the channel length, W is the channel width, C_i is the areal capacitance of the gate dielectric, V_G is the gate voltage, and V_{th} is the threshold voltage. The voltage ranges used in charge carrier mobility calculations are between 50-80 V.

2.2.3 Synthesis and Characterization

[1]Benzothieno[3,2-b][1]benzothiophene (BTBT) and the reference compounds D(C_7CO)-BTBT and C_8-BTBT were prepared in accordance with the reported procedure [42,122].

Caution: 2,3,4,5,6-Pentafluorobenzoyl chloride and aluminum chloride ($AlCl_3$) react violently with water and should be handled with great care.

Synthesis of benzo[b]benzo[4,5]thieno[2,3-d]thiophene-2,7-diylbis((perfluorophenyl) methanone) ***(D(Ph_FCO)-BTBT)****:* aluminum chloride ($AlCl_3$) (3.05 g, 22.88 mmol) was added into a solution of [1]benzothieno[3,2-b][1]benzothiophene (1.0 g, 4.16 mmol) in dichloromethane (100 mL) at −10 °C under nitrogen. The resulting reaction mixture was stirred at −10 °C for 30 min. Then, 2,3,4,5,6-pentafluorobenzoyl chloride (3.7 mL, 25.8 mmol) was added dropwise, and the mixture was stirred for 1 h at the same temperature. The reaction mixture was allowed to warm to room temperature and stirred for 2 days. The reaction mixture was quenched with water to give a pale yellow precipitate. The precipitate was collected by filtration, and washed with water and methanol in sequence. Due to its limited solubility in common organic solvents, the crude was purified by thermal gradient sublimation under high vacuum (P ~ 1×10^{-5} Torr). The product was obtained as a light yellow solid (0.54 g, 21% yield). Melting point: 336-337 °C; ^{1}H NMR (400 Mhz, $CDCl_3$), δ (ppm): 8.46 (s, 2H), 8.07 (d, J = 8.0 Hz, 2H), 7.99 (d, J = 8.0 Hz, 2H); MS (MALDI-TOF) *m/z* [M^+]: calcd for $C_{28}H_6F_{10}O_2S_2$: 627.96; found: 627.90. Elemental analysis (%) calcd for $C_{28}H_6F_{10}O_2S_2$: C, 53.51; H, 0.96; found: C, 53.36; H, 0.99.

2.2.4 Theoretical Methodology

The intramolecular reorganization energies associated with hole (λ_h) and electron transfer (λ_e) were calculated for **C_8-BTBT** and **D(Ph_FCO)-BTBT**, respectively, using a standard procedure reported in the literature [139]. The transfer integrals for electrons (t_e) in **D(Ph_FCO)-BTBT** dimers within the herringbone-layered structure were calculated by using the approach described by Valeev et al. [140] with the corresponding matrix elements evaluated with Gaussian 09 [138]. For comparison purposes, the transfer integrals for holes (t_h) in **C_8-BTBT** dimers within the herringbone-layered structure were also calculated. The B3LYP [141,142] and PW91PW91 [143,144] functionals are considered together with the 6-31G** basis set [145,146]. Note that the electronic coupling value is dependent on the functional employed in the calculation, and it generally increases with the percentage of Hartree–Fock exchange [147]. The transfer integrals calculated with the B3LYP exchange-correlation functional gives very similar trends to those obtained using PW91PW91 (Tables 2.3 and 2.4).

2.3 Results and Discussion

2.3.1 Theoretical Calculations, Synthesis, and Characterization

Prior to the synthesis of the new small molecule, electronic/structural effects of pentafluorophenylcarbonyl functionalization on the wide band-gap **BTBT** core were studied via DFT (B3LYP/6-31G**) computations. Among the four possible positions on the outer benzene rings of BTBT, functionalization at 2,7-positions is found to provide the lowest LUMO energy level with the greatest wave function delocalization (Figure 2.3). DFT calculations also show that "CO-BTBT-CO" π-segment adopts a good coplanarity with small torsional angles ($\theta_{C=C-C=O} < 5°$) between the carbonyl and the BTBT units (Figure 2.4). On the other hand, the pentaflurophenyl groups, as expected based on the crystal structures of previously developed Ph_FCO-functionalized arenes [89,148,149], adopt highly twisted conformations with respect to this coplanar π-segment with dihedral angles of 64.1°. These structural features at the molecular level lead to a unique electronic structure in **D(Ph$_F$CO)-BTBT** showing energetically stabilized frontier orbitals (ΔE_{HOMO} = -0.88 eV and ΔE_{LUMO} = -1.70) and significantly reduced HOMO-LUMO gap (ΔE = -0.82 eV) compared to the parent *p*-type semiconductor **C$_8$-BTBT** (Figure 2.4). The LUMO shows a significant contribution from carbonyl groups while the HOMO remains mostly localized on the central BTBT π-unit, which explains the much higher energetic stabilization of the LUMO *vs.* the HOMO. Interestingly, the pentafluorophenyl terminal units do not participate in both frontier orbitals as a result of the large torsion and, therefore, they are involved in the electronic stabilization of the molecular orbitals solely via a negative inductive (-I) effect on the π-system. On the other hand, the highly coplanar carbonyl units exhibit considerable negative resonance (-R) effect on the π-electron system. This result is consistent with the fact that they constitute a crucial part of the LUMO topology. The single-crystal structure and experimental frontier orbital energies are found to closely match the theoretical structural and electronic findings (*vide infra*).

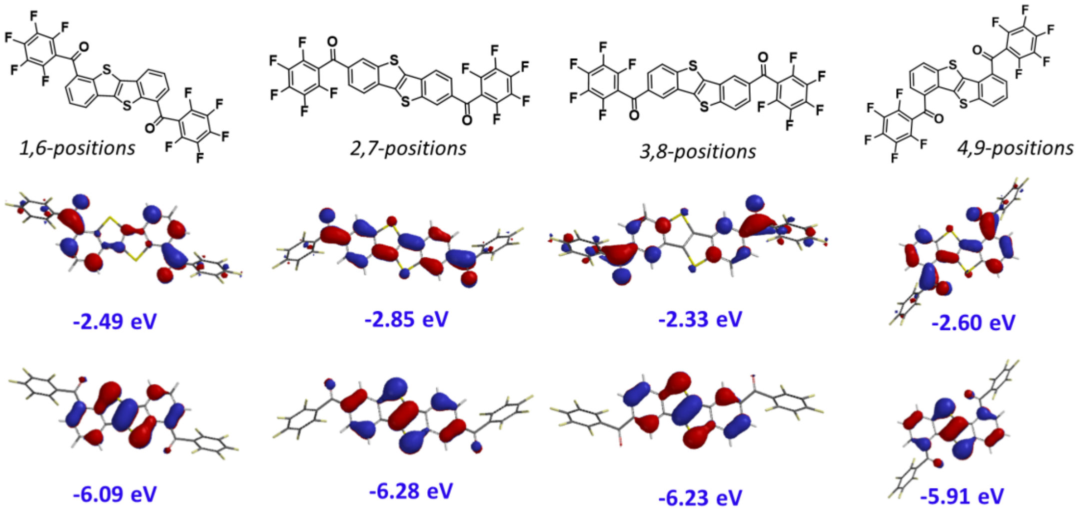

Figure 2.3 Theoretical (DFT/B3LYP/6-31G**) HOMO/LUMO energy levels with topographical orbital representations for different functionalization positions on the **BTBT** π-core.

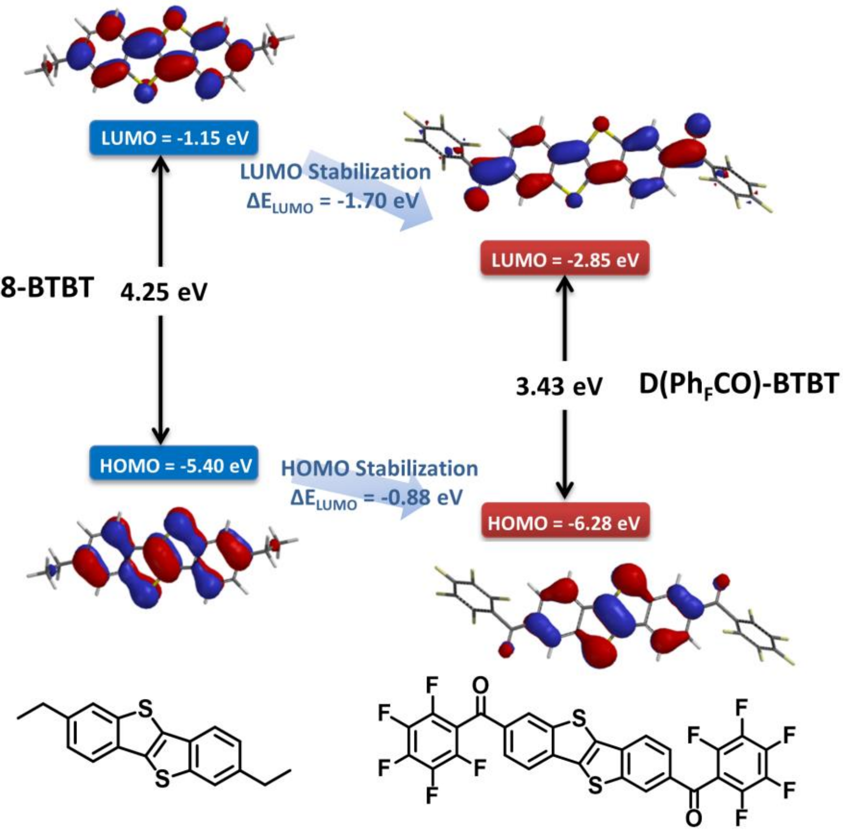

Figure 2.4 Theoretical (DFT/B3LYP/6-31G**) HOMO/LUMO energy levels with topographical orbital representations for **D(Ph$_F$CO)-BTBT** and **C$_8$-BTBT** (-C_2H_5 substituents are used to ease the calculations).

D(Ph$_F$CO)-BTBT was synthesized in 45% yield via double Friedel-Crafts acylation at the 2,7-positions of the BTBT (Figure 2.1B) and purified by thermal gradient sublimation under high vacuum (1×10^{-5} Torr). The chemical structure and purity of **D(Ph$_F$CO)-BTBT** were characterized and established by nuclear magnetic resonance (NMR) spectroscopy (Figure 2.5), elemental analysis, mass spectrometry (Figure 2.6), and single-crystal X-ray diffraction. From a materials production standpoint, it is quite promising that the new semiconductor could be synthesized in a two-step transition metal-free process without using chromatographic purification. Although **D(Ph$_F$CO)-BTBT** solubility in common organic solvents at room temperature is quite low, ^{1}H NMR spectrum recorded at an elevated temperature in $CDCl_3$ revealed that the chemical shifts of the aromatic protons in **D(Ph$_F$CO)-BTBT** moved downfield ($\Delta\delta \sim 0.7$-0.8 ppm) with respect to those in **C$_8$-BTBT** ($\delta_{Ar\text{-}H} = 7.2$-$7.8$ ppm → 8.0-8.5 ppm). This indicates substantially reduced electron-density (deshielding effect) on the BTBT π-system due to the presence of strongly electron-withdrawing pentafluorophenylcarbonyl (Ph$_F$CO) end-units.

Thermogravimetric analysis (TGA) at reduced pressure (~0.1 Torr) shows very clean, quantitative sublimation with good thermal robustness for the new **D(Ph$_F$CO)-BTBT** π-framework (Figure 2.7A). This is undoubtedly the result of arene-fluorination at the molecular termini that provides excellent volatility for reliable and quantitative film fabrication via physical vapor deposition (PVD). Differential scanning calorimetry (DSC) measurement shows endothermic (+146.7 J/g) and exothermic (-103.47 J/g) thermal transitions at 338 °C and 301 °C, respectively (Figure 2.7B). Conventional melting point measurement shows that these transitions correspond to melting (m.p. 336-337 °C) and crystallization processes, respectively. No evidence of mesophase formation was observed before melting, which is consistent with the previously reported pentafluorophenyl-substituted molecular semiconductors [89,150].

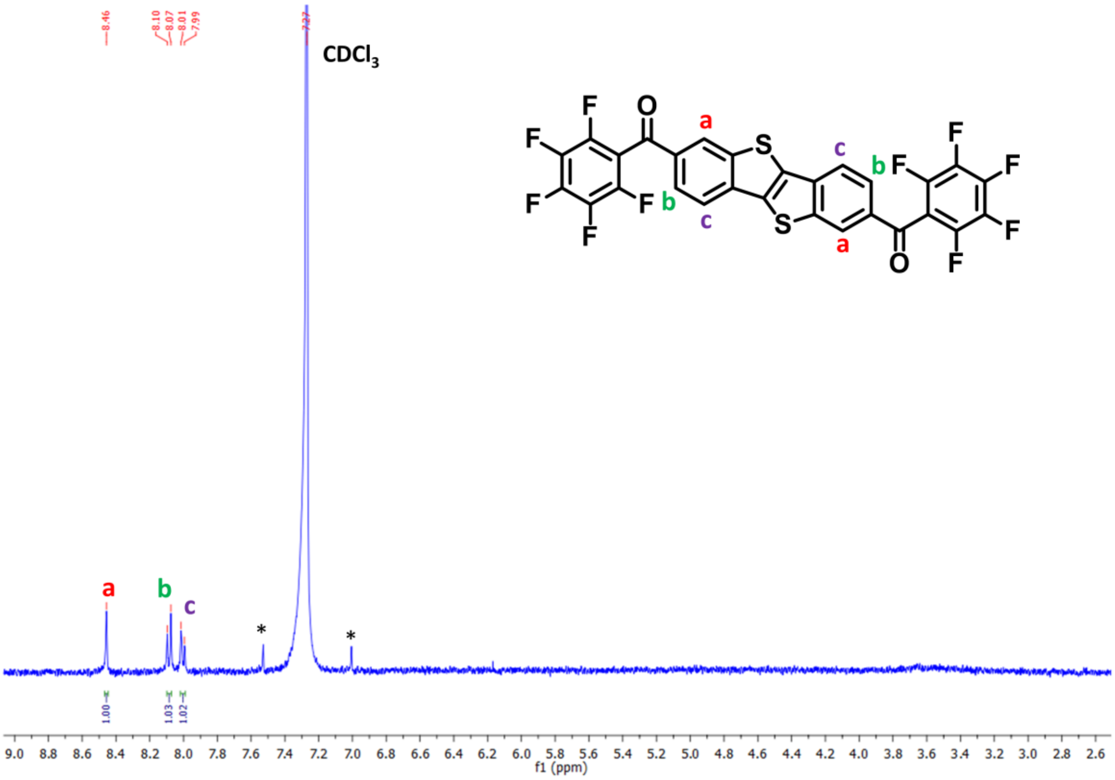

Figure 2.5 ^{1}H NMR spectrum of **D(Ph$_F$CO)-BTBT** measured in CDCl$_3$. ^{13}C satellite peaks for CDCl$_3$ are marked with asterisks.

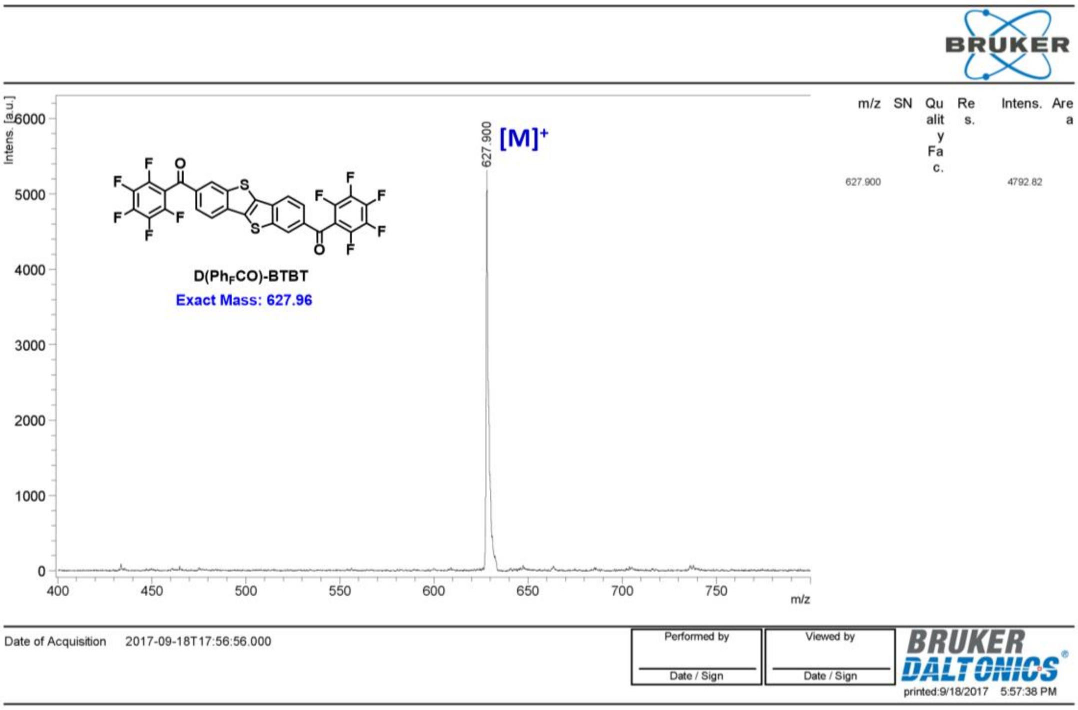

Figure 2.6 Positive ion and linear mode MALDI TOF-MS spectrum of **D(Ph$_F$CO)-BTBT**.

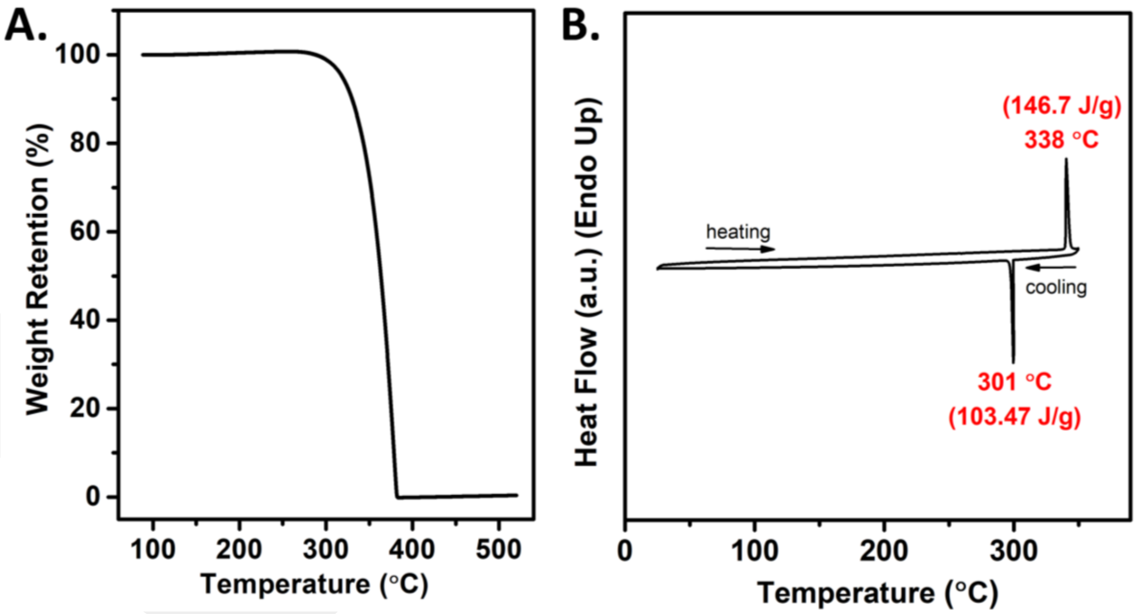

Figure 2.7 (A) Thermogravimetric analysis (TGA) curve at reduced pressure (~0.1 Torr) and (B) Differential scanning calorimetry (DSC) measurement curve under N_2 in the second heating–cooling cycle for **D(Ph$_F$CO)-BTBT** at a temperature ramp of 10 °C·min^{-1}.

2.3.2 Single-Crystal Structure Analysis

Light yellow crystals of **D(Ph$_F$CO)-BTBT** suitable for X-ray diffraction (Figure 2.8) were grown by thermal gradient sublimation. This molecule crystallizes in the monoclinic space group C2/c showing a "layer-by-layer" packing motif along the crystallographic *a*-axis consisting of alternately stacked "CO-BTBT-CO" and "pentafluorophenyl" layers (Figure 2.8B). These layers are extended into the *b*- and *c*-axes to form a typical herringbone-like molecular packing, which could facilitate two-dimensional (2D) charge transport. The major intermolecular interactions governing the herringbone motif are identified as CH···π(benzene/thiophene) (a = 3.45 Å; a' = 3.25 Å/c = 3.46 Å), S···π (thiophene) (b = 3.38 Å), and F···π(pentafluorobenzene) (d = 3.30 Å / d' = 3.16 Å) contacts (Figure 2.8B). In addition, short S···S (3.38 Å < $r_{vdw}(S)+r_{vdw}(S)$ = 3.60 Å) contacts also exist between the thiophene rings along the *c*-axis. As shown in Figure 2.8A, "CO-BTBT-CO" π-segment exhibits a substantially coplanar backbone with the carbonyl units lying perfectly in the plane; the torsion angle for C8-C7-C=O is only -1.9(4)°. The dihedral angle between pentafluorophenyl ring and the BTBT core is measured to be ~64.12°. The observed solid-state conformation is consistent with the DFT-calculated molecular structure (*vide supra*), and it yields extended π-conjugation along the molecular backbone including the BTBT and the carbonyl units.

X-ray data collection and structure refinement: Data were obtained with Bruker APEX II QUAZAR three-circle diffractometer. Indexing was performed using APEX2 [APEX2, version 2014.11-0, Bruker (2014), Bruker AXS Inc., Madison, WI]. Data integration and reduction were carried out with SAINT [SAINT, version 8.34A, Bruker (2013), Bruker AXS Inc., Madison, WI]. Absorption correction was performed by multi-scan method implemented in SADABS [SADABS, version2014/5, Bruker (2014), Bruker AXS Inc., Madison, WI.]. The structure was solved using SHELXT [151] and then refined by full-matrix least-squares refinements on F^2 using the SHELXL [152] in SHELXTL Software Package [Bruker, SHELXTL, version 6.14, Bruker AXS Inc., Madison, Wisconsin, USA, 2010]. Aromatic C-bound H atoms were positioned geometrically and refined using a riding mode. Crystallographic data and refinement details of the data collection for **D(PhFCO)-BTBT** are given in Table 2.1. Crystal structure validations and geometrical calculations were performed using Platon software

[153] Mercury software [154] was used for visualization of the cif files. Additional crystallographic data with CCDC reference number 1866567 (**D(Ph$_F$CO)-BTBT)** has been deposited within the Cambridge Crystallographic Data Center *via* www.ccdc.cam.ac.uk/deposit.

Table 2.1 Crystal data and refinement parameters for **D(Ph$_F$CO)-BTBT**.

	D(Ph$_F$CO)-BTBT
CCDC	1866567
Empirical Formula	$C_{28}H_6F_{10}O_2S_2$
Formula weight (g. mol^{-1})	628.45
Temperature (K)	293(2)
Wavelength (Å)	0.71073
Crystal system	Monoclinic
Space group	C_2/c
a **(Å)**	43.611(3)
b **(Å)**	7.3973(5)
c **(Å)**	7.1455(5)
α(°)	90
β(°)	96.283(4)
γ(°)	90
Crystal size (mm)	0.12 x 0.14 x 0.16
V **(Å^3)**	2291.3(3)
Z	4
ρ_{calcd} (g. cm^{-3})	1.822
μ (mm^{-1})	0.344
***F*(000)**	1248
θ range for data collection (°)	3.09 to 25.02
h*/*k*/*l	-46<=h<=51, -8<=k<=8, -8<=l<=8
Reflections collected	16026
Independent reflections	2027 [R(int) = 0.1291]
Data/restraints/parameters	2027 / 0 / 190
Goodness-of-fit on F^2 (S)	1.035
Final *R* indices [$I > 2\sigma(I)$]	R_1 = 0.0391, wR_2 = 0.0986
R **indices (all data)**	R_1 = 0.0488, wR_2 = 0.1040
Largest diff. peak and hole (e.Å^{-3})	0.336 and -0.276

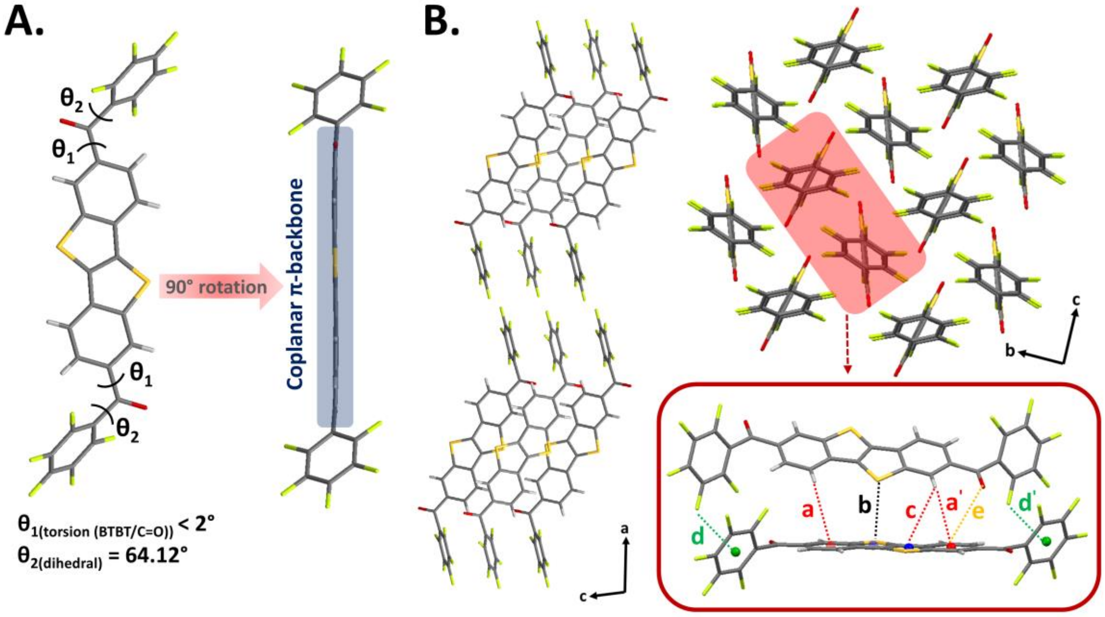

Figure 2.8 A. Capped-stick drawings of the crystal structure of **D(Ph$_F$CO)-BTBT** showing the corresponding dihedral and torsion angles and π-backbone coplanarity. B. Perspective views of the molecular arrangements along the *a,c*-axes and *b,c*-axes showing the alternately stacked layers and the two-dimensional herringbone-like packing, respectively. Inset shows the pairs of **D(Ph$_F$CO)-BTBT** molecules in the herringbone motif with CH···π(benzene/thiophene) (a = 3.45 Å; a' = 3.25 Å/c = 3.46 Å), S···π (thiophene) (b = 3.38 Å), and F···π(pentafluorobenzene) (d = 3.30 Å; d' = 3.16 Å) contacts.

2.3.3 Optical and Electrochemical Properties

The UV-vis absorption spectrum and cyclic voltammogram of **D(Ph$_F$CO)-BTBT**, along with the reference molecule **C$_8$-BTBT**, were recorded in dichloromethane solution to assess the effects of carbonyl and pentafluorophenyl substitutions on BTBT core optical absorption and the frontier orbital energies. As shown in Figure 2.9A, **D(Ph$_F$CO)-BTBT** exhibits typical vibronic features of a fused heteroacene π-system with substantially red-shifted (Δλ ~ 90-100 nm) low-energy absorption maximum (λ_{max} = 406 nm) and onset (λ_{onset} = 435 nm) values as compared with **C$_8$-BTBT**. The optical band gap for **D(Ph$_F$CO)-BTBT** is estimated as 2.85 eV, which is considerably smaller ($\Delta E_{g(opt)}$ = -0.80 eV) than that of **C$_8$-BTBT** ($E_{g(opt)}$ = 3.65 eV). When going from solution to a vapor-deposited thin-film, **D(Ph$_F$CO)-BTBT** exhibits a new low energy absorption maximum at 429 nm with an onset at 453 nm ($E_{g(opt\text{-}film)}$ = 2.75 eV), indicating intermolecular interactions in the solid-state (Figure 2.10). When compared with typical *n*-type semiconductors reported in the literature ($E_{g(opt)}$ = 1.3-2.5 eV) [11], the relatively large solid-state optical band gap of **D(Ph$_F$CO)-BTBT**, resulting in excellent transparency in the visible region (Figure 2.11), could be advantageous for carbon-based transparent electronics and multilayer green/blue-emitting transistors (OLETs) [155,156]. In contrast to the electrochemical behavior of *p*-type **C$_8$-BTBT** that only shows an oxidation peak at +0.89 V (*vs* Fc/Fc$^+$),[42] **D(Ph$_F$CO)-BTBT** exhibits a quasi-reversible reduction peak with the half-wave reduction potential at –0.76 V (*vs* Ag/AgCl). The LUMO and HOMO energies of the new molecule are estimated as -3.64 eV and -6.49 eV (Figure 2.9B), respectively, which are far lower than those of **C$_8$-BTBT (**E_{LUMO} = -2.10 eV and E_{HOMO} = -5.75 eV**)** measured in the same electrochemical set-up (Figure 2.12). Going from **C$_8$-BTBT** to **D(Ph$_F$CO)-BTBT**, the occurrence of an electrochemical reduction process, E_{LUMO}/E_{HOMO} stabilizations (noting with a much larger degree for the former orbital), and the reduction in the optical band gap are all in good agreement with the DFT calculations. This clearly points to the efficient electron-withdrawing capacities of the combined carbonyl and pentafluorophenyl units, which could induce electron-transport in semiconductor devices. Note that the LUMO energy level for **D(C$_7$CO)-BTBT**, which is a **BTBT** derivative with the combined electron-donating heptyl ($-C_7H_{15}$) and the electron-withdrawing carbonyl units, is already at -3.54 eV (Figure 2.13). Thus, it is clear that major LUMO stabilization for **D(Ph$_F$CO)-BTBT** (~1.44 eV) originates from the presence of the *in-plane* oriented carbonyl functionalities (negative resonance (-R) effect) while the *out-of-plane* twisted pentafluorophenyl units provide minimal stabilization (~0.1 eV) via a negative inductive (-I) effect. Similar LUMO stabilization trends were previously observed in pentafluorophenyl- *vs.* phenyl-substituted dicarbonyl oligothiophenes [89]. It is also noteworthy that (partial) fluorination of semiconducting cores can favorably affect electron transport by acting as kinetic barrier to adsorption of components (i.e., H_2O/O_2) acting as charge traps [137,157,158].

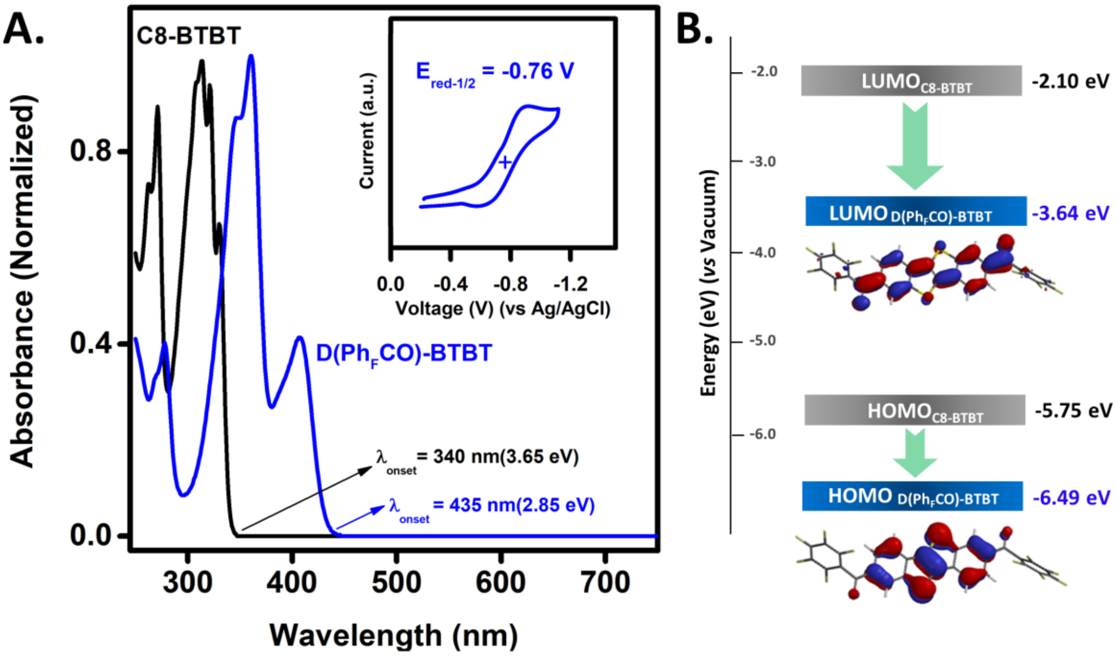

Figure 2.9 (A) Optical absorption spectra of **D(Ph$_F$CO)-BTBT** and the reference molecule **C$_8$-BTBT** in dichloromethane solutions, and cyclic voltammogram (inset) for **D(Ph$_F$CO)-BTBT** in dichloromethane (0.1 M Bu$_4$N$^+$PF$_6^-$, scan rate = 50 mV·s^{-1}). (B) Experimental HOMO/LUMO energy levels for **D(Ph$_F$CO)-BTBT** and **C$_8$-BTBT**, and topographical orbital representations (DFT/B3LYP/6-31G**) for **D(Ph$_F$CO)-BTBT**.

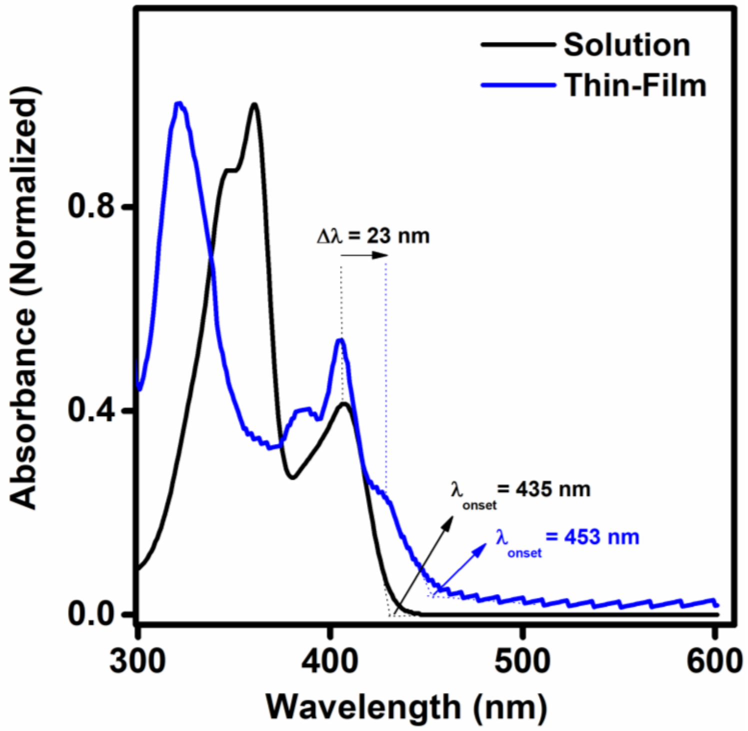

Figure 2.10 Optical absorption spectra of **D(Ph$_F$CO)-BTBT** in dichloromethane solution and as vapor-deposited thin-film (30 nm).

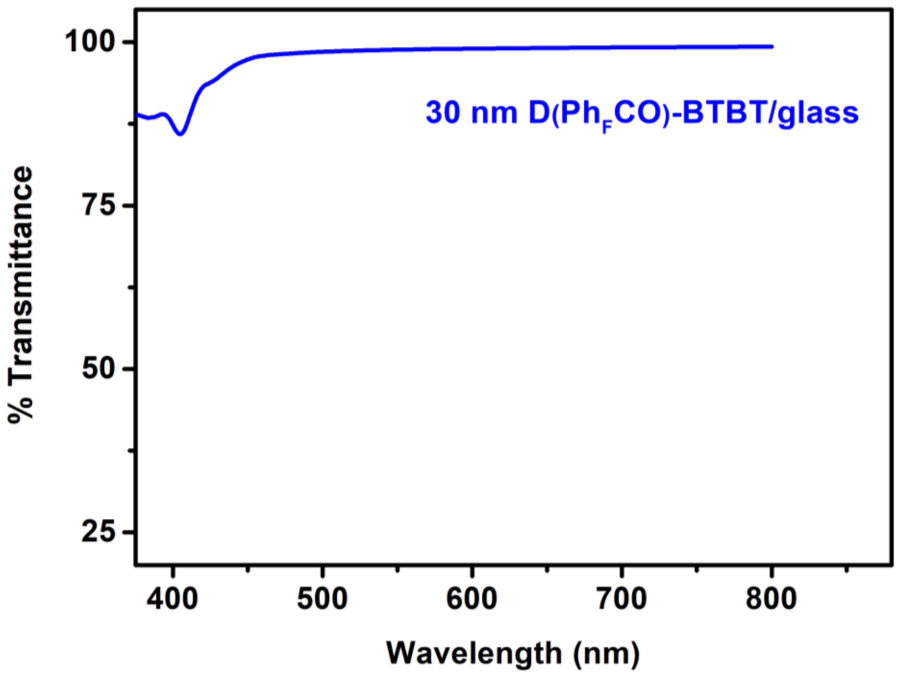

Figure 2.11 Transmission optical spectrum of a 30 nm vapor-deposited thin-film of **D(Ph$_F$CO)-BTBT** on glass demonstrating the impressive transparency of this semiconductor between 400 and 800 nm.

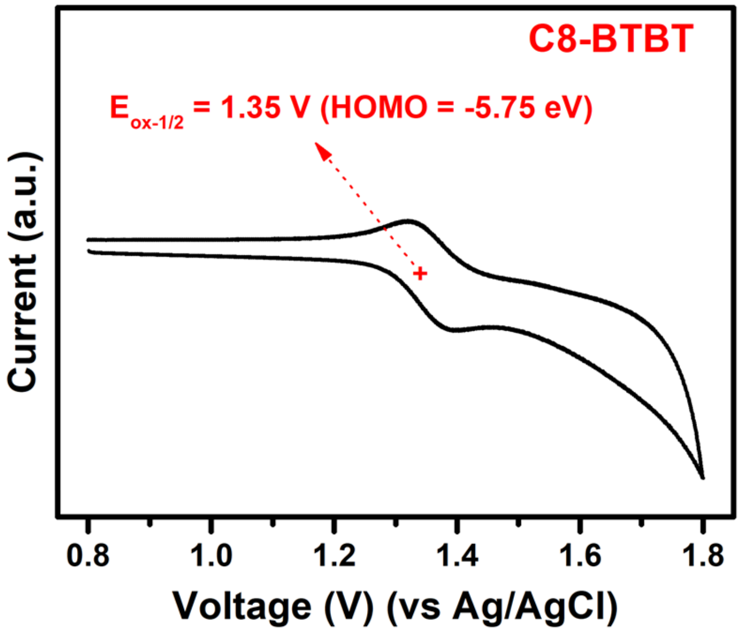

Figure 2.12 Cyclic voltammogram of **C_8-BTBT** in dichloromethane solution (0.1 M $Bu_4N^+PF_6^-$, scan rate = 50 mVs^{-1}) recorded using the exact same electrochemical set-up employed in this study.

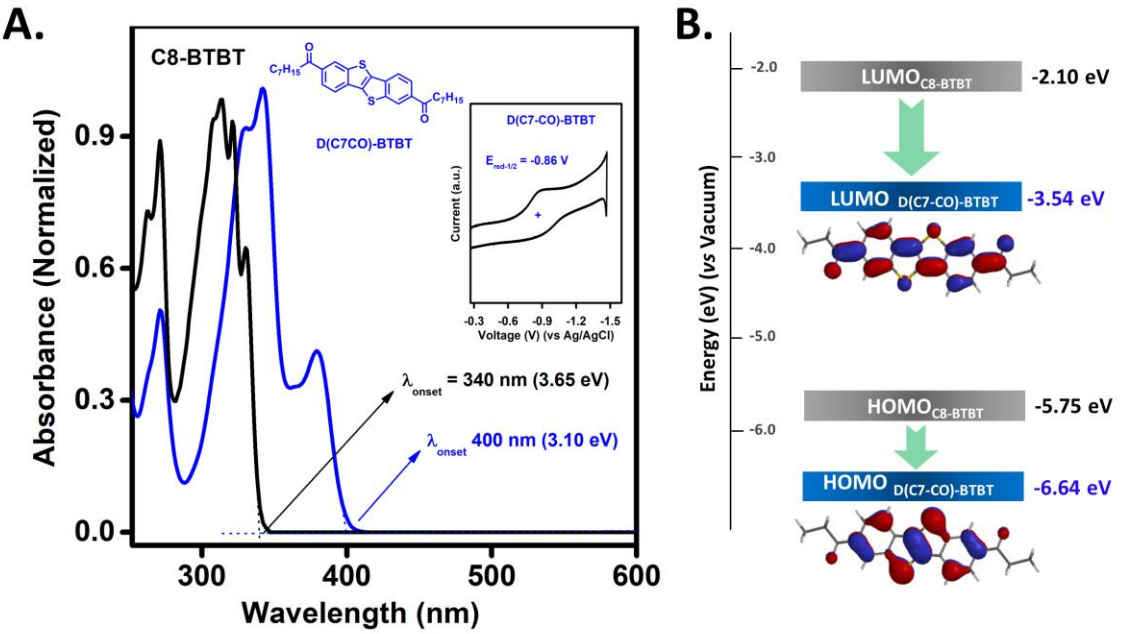

Figure 2.13 (A) Optical absorption spectra of **D(C_7CO)-BTBT** and the reference molecule **C8-BTBT** in dichloromethane solutions, and cyclic voltammogram (inset) for **D(C7CO)-BTBT** in dichloromethane (0.1 M $Bu_4N^+PF_6^-$, scan rate = 50 mV·s^{-1}). (B) Experimental HOMO/LUMO energy levels for **D(C_7CO)-BTBT** and **C_8-BTBT**, and topographical orbital representations (DFT/B3LYP/6-31G**) for **D(C_7CO)-BTBT.**

2.3.4 Thin-Film Microstructure/Morphology and Field-Effect Transistor Characterization

Charge transport characteristics of the new semiconductor were investigated in top-contact bottom-gate (TC/BG) OFETs, which were fabricated by vapor deposition of **D(Ph_FCO)-BTBT** thin-films (~30 nm) onto temperature-controlled n^{++}-Si/SiO_2(200 nm) and n^{++}-Si/SiO_2(200 nm)/HMDS substrates under high vacuum (~10^{-6} torr), followed by Au (50nm), LiF/Au (1 nm/50 nm), Ag (50 nm), or Al (50 nm) thermal evaporation to define source-drain electrodes and the semiconductor channel (1000 μm (W) x 50 μm (L)). During the semiconductor film deposition, the substrate temperature was maintained at 25 °C, 70 °C, 100 °C, and 120 °C. Before charge transport measurements, the morphology and microstructure of all the **D(Ph_FCO)-BTBT** films were explored by two-dimensional grazing incidence X-ray diffraction (2D-GIXD) and atomic force microscopy (AFM), which clearly reveals that **D(Ph_FCO)-BTBT** adopts an *edge-on* molecular orientation on the substrate surface forming two-dimensional plate-like grains of terraced islands along the substrate plane (Figures 2.14C, and 2.15-2.18). The strong diffractions observed by 2D-GIXD analysis correlate perfectly with the single-crystal phases; while (200), (400), and (600) planes are identified in the *out-of-plane* direction, (020), (111), and (002) planes are identified as the major diffractions in the *in-plane* direction. This result indicates the formation of *edge-on* molecular packing motif in the crystalline domains, in which the "**CO-BTBT-CO**" π-frameworks are tilted at ~35° from the substrate normal forming a herringbone packing with favorable intermolecular distances (3.25-3.46 Å) along the charge-transport direction (Figure 2.14D). The BFDH (Bravais-Friedel-Donnay-Harker) theoretical crystal morphology further confirms the formation of plate-like grains on the substrate surface, which extends its two-dimensional crystal plane along the (200) plane via herringbone packing (Figure 2.14D-inset). The step heights (~2.4-2.6 nm, Figure 2.18) along terraced islands match well with this model corresponding to the half of the unit cell parameter along the *a*-axis and the **D(Ph$_F$CO)-BTBT**'s molecular size (~2.2 nm).

Note, **D(Ph$_F$CO)-BTBT** films grown on HMDS-treated Si/SiO$_2$ substrates exhibit, compared with those deposited on the bare SiO$_2$ surface, larger crystallites (Figure 2.15) as a result of low surface energy better matching with the hydrophobic nature of the fluorinated semiconductor [159,160]. The 2D-GIXD measurements also reveal the effect of surface hydrophobicity on **D(Ph$_F$CO)-BTBT** thin-film growth. As shown in Figure 2.17, while the room temperature deposited semiconductor film on the bare SiO$_2$ surface shows ring patterns, indicating misaligned crystalline domains, the room temperature deposited films on HMDS-treated surface show phase-pure crystalline domains. Additionally, the semiconductor grain size is found to continuously increase with increasing the substrate temperature (25 °C → 100 °C) from 100-200 nm to ~0.5-1.0 μm on the base SiO$_2$ surfaces and from 300-500 nm to ~2-5 μm on the HMDS-treated substrates (Figure 2.15).

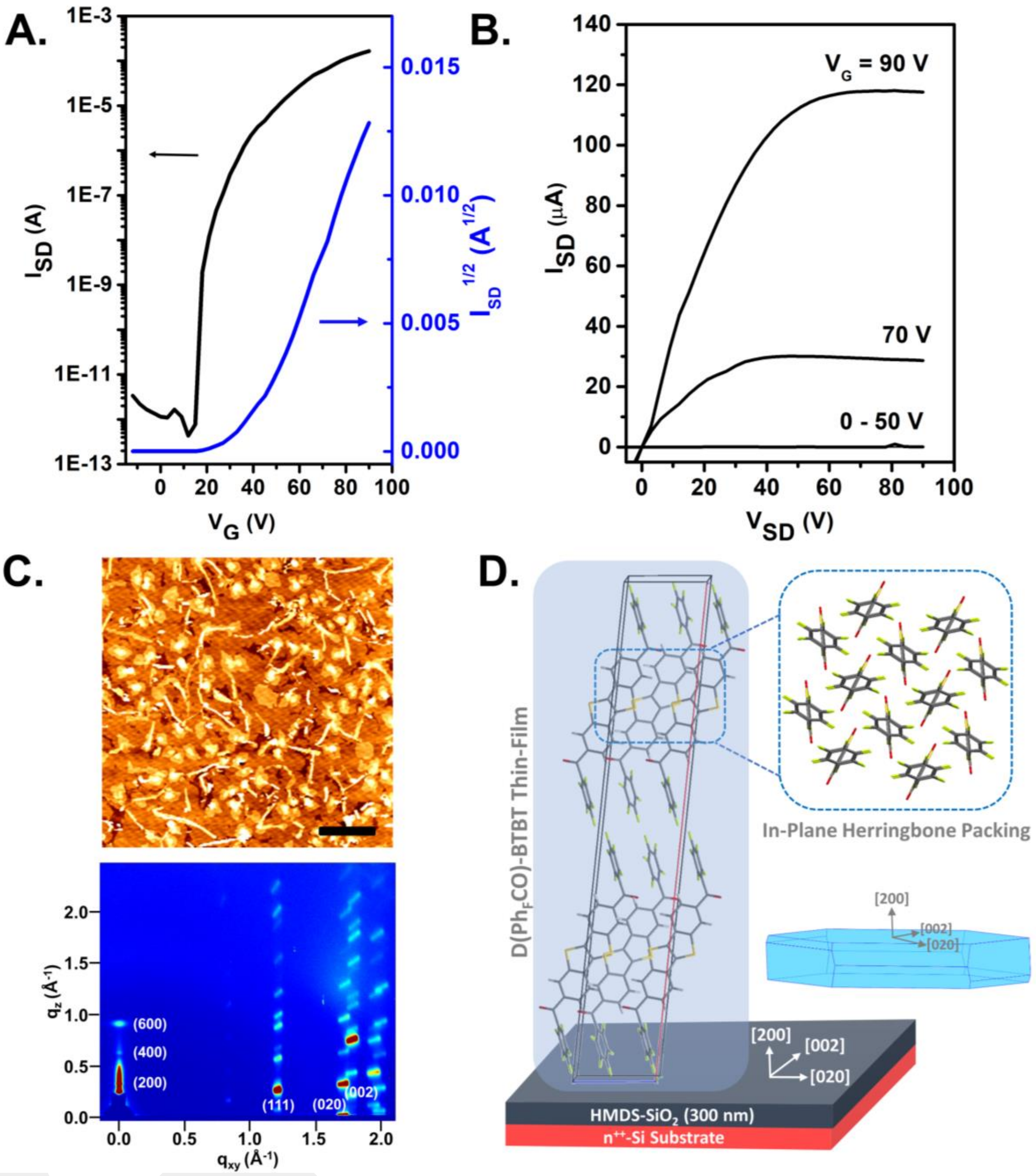

Figure 2.14 (A) Transfer (V_{SD} = 100 V) and (B) Output characteristics for n^{++}-Si/SiO_2(200 nm)/HMDS/ D(Ph_FCO)-BTBT(30 nm)/LiF (1 nm)-Au(50 nm) OFET device. (C) Tapping mode atomic force microscopy (AFM) topographic image and two-dimensional grazing incidence X-ray diffraction (2D-GIXD) patterns for **D(Ph_FCO)-BTBT** thin-films (30 nm) vapor-deposited at 100 °C on n^{++}-Si/SiO_2(200 nm)/HMDS. Scale bar denotes 2 μm. (D) Views of the packing arrangement in the **D(Ph_FCO)-BTBT** semiconductor layer showing the *edge-on* molecular orientation (*out-of-plane*) and the herringbone packing motif (*in-plane*). Inset shows the BFDH (Bravais, Friedel, Donnay and Harker) theoretical crystal morphology and the corresponding crystalline planes.

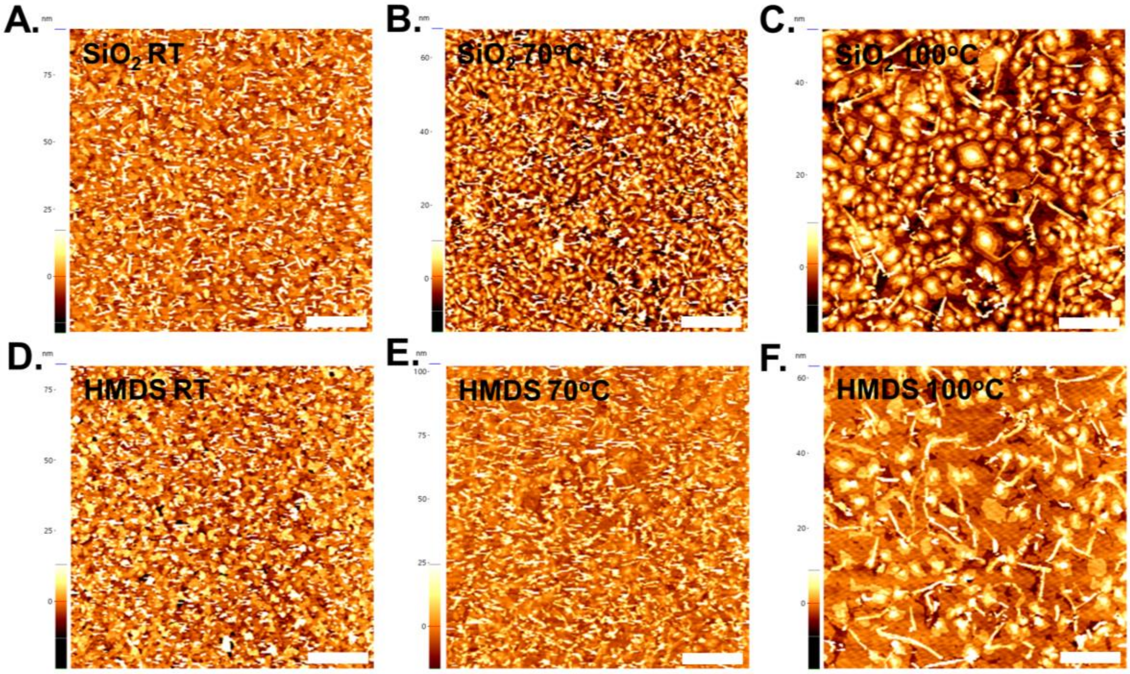

Figure 2.15 Tapping mode atomic force microscopy (AFM) topographic images of **D(Ph$_F$CO)-BTBT** thin-films vapor-deposited at room temperature 25 °C, 70 °C, and 100 °C on n^{++}-Si/SiO$_2$(200 nm)/HMDS and n^{++}-Si/SiO$_2$(200 nm) substrates. Scale bars denote 2 μm.

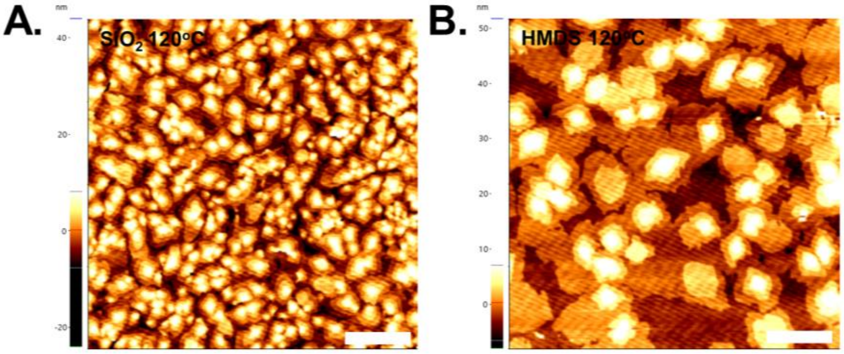

Figure 2.16 Tapping mode atomic force microscopy (AFM) topographic images of **D(Ph$_F$CO)-BTBT** thin-films vapor-deposited at 120 °C on n^{++}-Si/SiO$_2$(200 nm)/HMDS and n^{++}-Si/SiO$_2$(200 nm) substrates showing poor inter-grain connectivity. Scale bars denote 2 μm.

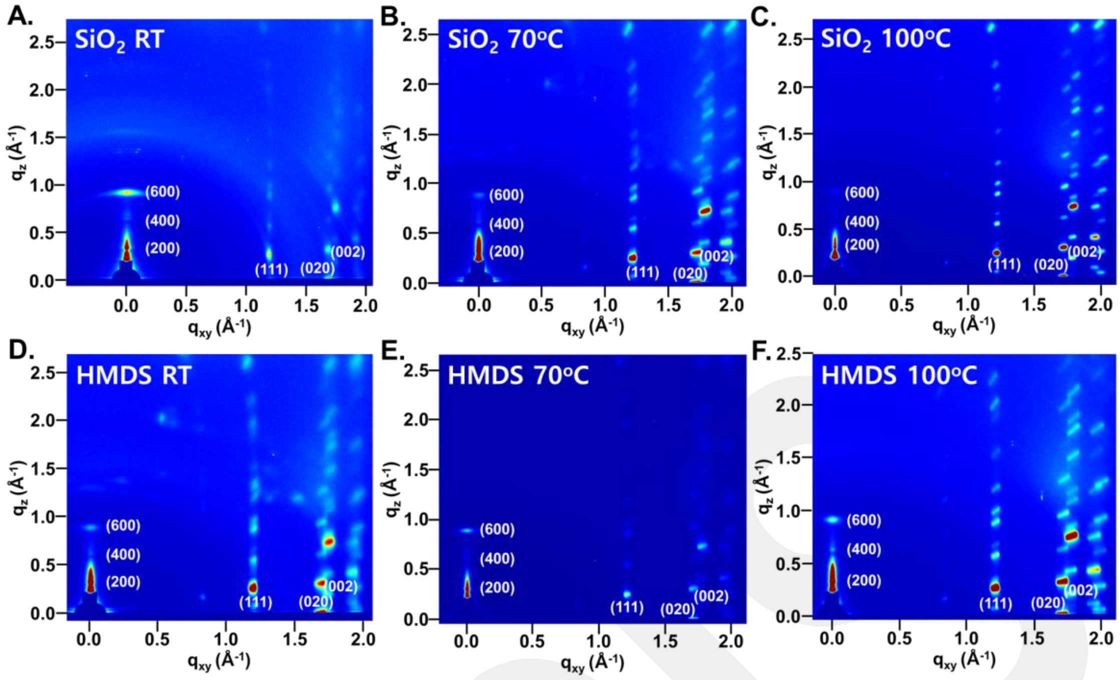

Figure 2.17 Two dimensional grazing incidence X-ray diffraction (2D-GIXD) patterns of **D(Ph$_F$CO)-BTBT** thin-films (30 nm) vapor-deposited at various temperatures (25 °C, 70 °C, 100 °C) on n^{++}-Si/SiO$_2$(200 nm) and n^{++}-Si/SiO$_2$(200 nm)/HMDS.

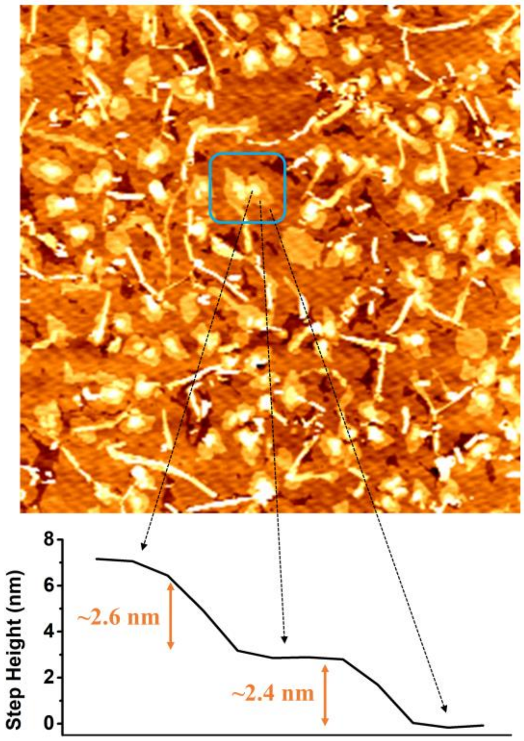

Figure 2.18 Topographic image of terraced islands (AFM, tapping mode, 10×10 μm) and the corresponding sectional step-height profile for **D(Ph$_F$CO)-BTBT** thin-films (30 nm) vapor-deposited at 100 °C on n^{++}-Si/SiO$_2$(200 nm)/HMDS.

The electrical characteristics of the **D(Ph$_F$CO)-BTBT**-based OFET devices were measured under positive and negative gate biases to explore the majority charge carrier type and evaluate the semiconductor performance. Considering that the LUMO level (-3.64 eV) for the new semiconductor is higher than those of typical air-stable *n*-type semiconductors (< ~ -4 eV) [102,119], our OFETs were tested under an inert (*vacuum*) atmosphere. Representative transfer/output plots are shown in Figures 2.14A, 2.14B, 2.19, and 2.20 while the OFET data are summarized in Table 2.2. All devices, regardless of the SiO$_2$ functionalization and substrate temperatures (T$_D$), exhibit *n*-channel behaviors with excellent current modulation characteristics. To the best of our knowledge, **D(Ph$_F$CO)-BTBT** is the first example of a BTBT-based electron-transporting organic semiconductor.

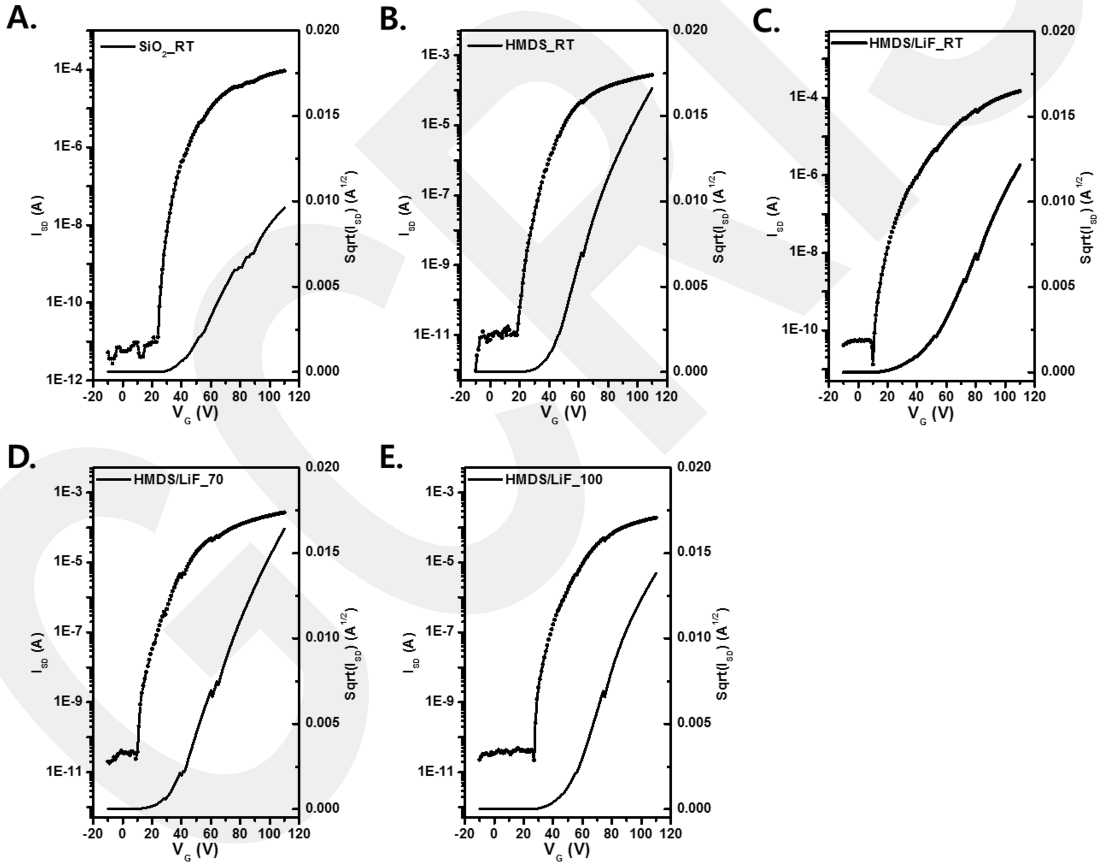

Figure 2.19 Transfer plots of OFET devices with channel length and width of 1000 μm and 50 μm, respectively (V_{SD} = 100 V).

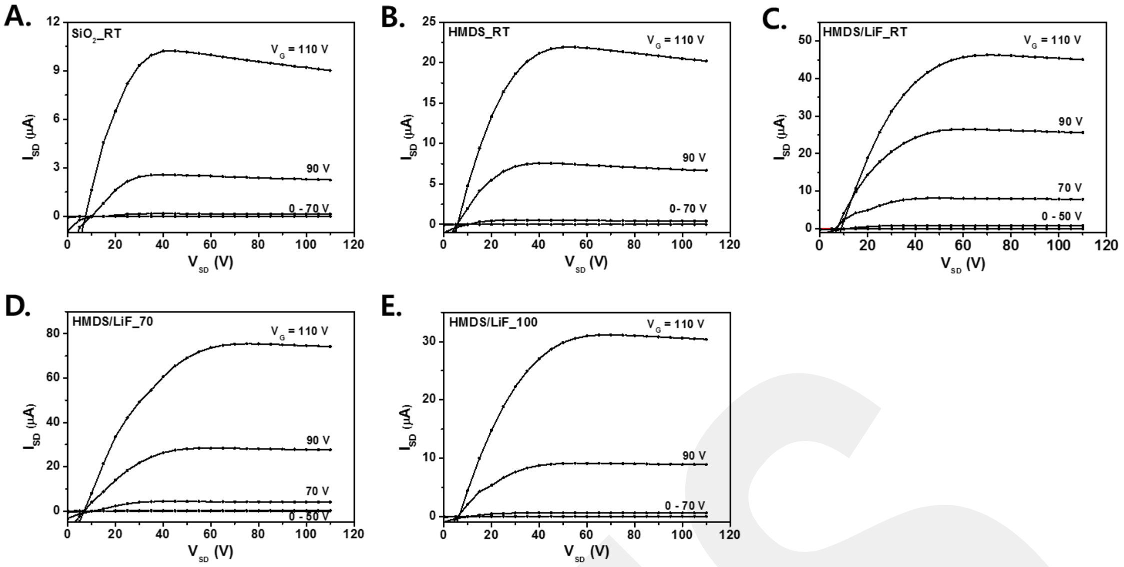

Figure 2.20 Output plots of OFET devices for channel length and width of 1000 μm and 50 μm, respectively.

The room temperature deposited OFET devices with Au (ϕ = 5.1 eV) S-D electrodes on bare and HMDS-treated SiO_2 exhibit μ_e's of 0.18 $cm^2/V{\cdot}s$ ($V_{th} = +40.9$ V) and 0.14 $cm^2/V{\cdot}s$ ($V_{th} = +39.0$ V), respectively with I_{on}/I_{off}'s of 10^7-10^8. In order to improve electron injection into the **D(Ph$_F$CO)-BTBT** semiconductor channel, lower work-function metals (i.e., Ag (ϕ = 4.6 eV) or Al (ϕ = 4.1 eV)) and modified gold (i.e., LiF/Au (ϕ = 3.6 eV)) source-drain electrodes were used as they better match with the LUMO level (-3.64 eV) of the new semiconductor [161,162]. While OFETs with Ag showed a reduced V_{th} of +29.0 V, the use of both Ag and Al electrodes deteriorated device performances (Table 2.2 and Figure 2.21) probably due to unfavorable metal/semiconductor contacts resulting in poor electron injection [163]. On the other hand, the devices with LiF/Au electrodes, which has the closest electrode/semiconductor-LUMO energy match, exhibited the best performance (μ_e of 0.12 $cm^2/V{\cdot}s$ and $I_{on}/I_{off} = 2{\times}10^6$) with a reduced V_{th} of +31.6 V [164]. For OFETs with LiF/Au electrodes, further improvement in the semiconducting characteristics was achieved by increasing T_D to 70 °C and 100 °C, which results in μ_e's of 0.45 $cm^2/V{\cdot}s$ ($V_{th} = +37.5$ V) and 0.57 $cm^2/V{\cdot}s$ ($V_{th} = +41.8$ V), respectively (I_{on}/I_{off}'s ~ 10^{7}-10^8). The enhanced device characteristics measured at higher deposition temperatures are consistent with the improved morphological/microstructural features (larger crystalline grains and improved *edge-on* orientation) observed at these deposition temperatures (*vide supra*). However, further increase of T_D to 120 °C degrades electron transport [μ_e

= 0.08 $cm^2/V \cdot s$, V_{th} = +47.4 V, I_{on}/I_{off} ~ 10^6]. The deteriorated performance is attributed to partial re-evaporation of **D(Ph$_F$CO)-BTBT** molecules at higher temperatures resulting in poor inter-grain connectivity (Figure 2.16). As expected, semiconductor depositions at higher substrate temperatures (T_D > 130 °C) did not yield any semiconductor film formation on the substrate. Although **D(Ph$_F$CO)-BTBT** demonstrates the first *n*-type BTBT-based semiconductor with a high electron mobility, one should note that the LUMO level is well-above the ambient stability threshold (~ -4 eV) and the work-functions of typical stable electrodes (~5 eV). This precludes not only thermodynamic ambient stability during transistor operation, but also introduces injection barriers at the metal/**D(Ph$_F$CO)-BTBT** contacts. Although LiF/Au seemed to address the latter issue partially, we note that further enhancement of electron injection into **D(Ph$_F$CO)-BTBT** thin-film by using different electrodes/interlayers could lead to additional improvements in the corresponding *n*-channel OFET performance [163]. For ambient-stable electron transport, we note that chemical functionalizations on the dicarbonyl BTBT π-system with much stronger electron-withdrawing substituents (e.g., -CN, $C=C(CN)_2$, and C=S) would be necessary to further lower the frontier orbital energetics.[165] However, **D(Ph$_F$CO)-BTBT**-based OFETs could operate with proper encapsulations, which is no matter needed when these TFTs drive, for instance, an OLED device [166,167]. In addition, thanks to **D(Ph$_F$CO)-BTBT**'s high electron mobility, HOMO/LUMO energy levels, wide optical band gap, and smooth two-dimensional film forming ability via vapor-deposition, it could find applications as an electron-transporting/hole-blocking interlayer in (encapsulated) multilayer (opto)electronic devices such as OLETs [156,168].

In order to elucidate the observed high electron mobility of **D(Ph$_F$CO)-BTBT** in comparison to the benchmark *p*-type analogue **C$_8$-BTBT**, two important molecular charge-transport parameters were studied via DFT calculations: (i) intramolecular reorganization energy (λ) and (ii) effective transfer integral (*t*). While the intramolecular reorganization energy ($\lambda_{h/e}$) characterizes the structural reorganization needed to accommodate a hole/electron, respectively, the effective transfer integral ($t_{h/e}$) reflects the degree of intermolecular electronic interactions for hole/electron transfer between nearest-neighbor molecular pairs, respectively

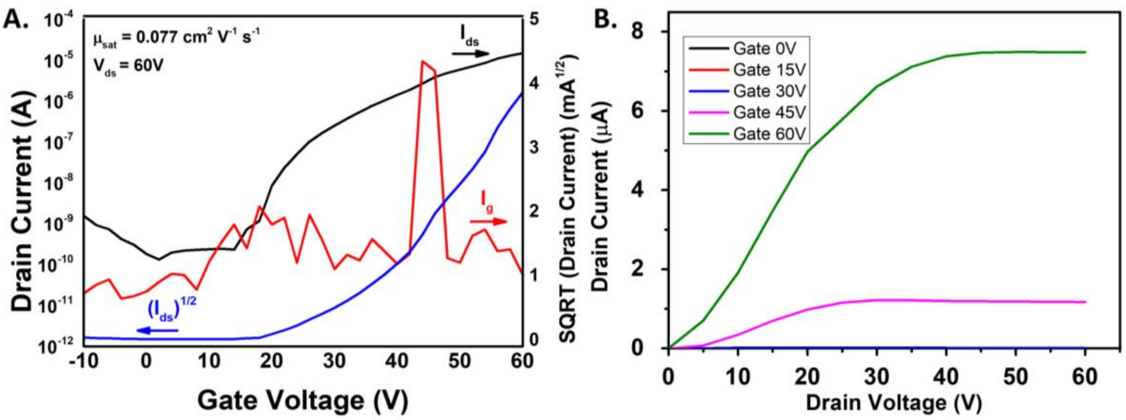

Figure 2.21 Transfer (A) and output (B) plots for OFET devices fabricated with Ag source-drain electrodes. Note that OFETs fabricated with Al source-drain electrodes did not operate.

Table 2.2 Representative field-effect transistor device characteristics using **D(Ph$_F$CO)-BTBT** as channel layer.

Dielectric	S/D electrode	$T_{Annealing}$	μ (cm^2/V·s)	I_{on}/I_{off}	V_{th} (V)
SiO$_2$	Au	R.T.	0.18	3 x 10^7	40.9
HMDS/SiO$_2$	Al	R.T.		Not Active	
	Ag	R.T.	0.077	4x 10^4	29.0
	Au	R.T.	0.14	9 x 10^7	39.0
	LiF/Au	R.T.	0.12	2 x 10^6	31.6
		70	0.45	1 x 10^7	37.5
		100	0.57	1 x 10^7	41.8

From a molecular level charge-transport perspective, a smaller $\lambda_{h/e}$ and larger $t_{h/e}$ values typically lead to high mobility for the corresponding charge carrier type. The reorganization energy associated with the electron transfer (λ_e) for **D(Ph$_F$CO)-BTBT** is calculated to be 315 meV, which is slightly larger than that associated with the hole transfer (λ_h) of the reference molecule **C$_8$-BTBT** (243 meV). However, the calculated λ_e value for **D(Ph$_F$CO)-BTBT** is in the same range of those calculated for benchmark molecular *n*-type semiconductors such as perylene tetracarboxylic diimides (250–322 meV) [169]. As shown in **Figure 2.22**, the transfer integrals for electron (t_e) and hole (t_h) transports in **D(Ph$_F$CO)-BTBT** and **C$_8$-BTBT** herringbone packings, respectively, are compared along various crystal directions. The corresponding data are collected in Tables 2.3 and 2.4. In agreement with the reported values [170], the largest transfer integrals for **C$_8$-BTBT** are obtained between π-stacked molecules along the crystallographic *a*-axis (39 meV) while smaller values (7 meV) are found between face-to-edge dimers. On the other hand, larger transfer integral values are calculated for **D(Ph$_F$CO)-BTBT** along both the π-stacking (47 meV) and face-to-edge (17 meV) directions. Despite the less pronounced sulphur contributions in **D(Ph$_F$CO)-BTBT**'s LUMO as compared to **C$_8$-BTBT**'s HOMO (Figure 2.4), LUMO wave function extension through *in-plane* carbonyl groups appear to play a key role facilitating intermolecular wave function overlaps in the new molecule. Since moderately larger reorganization energy is compensated by larger transfer integrals in the electronic structure of the new molecule, we note that similar charge transport properties could be rationally expected for **D(Ph$_F$CO)-BTBT** and **C$_8$-BTBT**. Furthermore, since a more pronounced 2D charge transport character is expected in **D(Ph$_F$CO)-BTBT**, thermal fluctuations and crystal orientations in the semiconducting channel would have a more limited impact when compared with the reference system of **C$_8$-BTBT**.

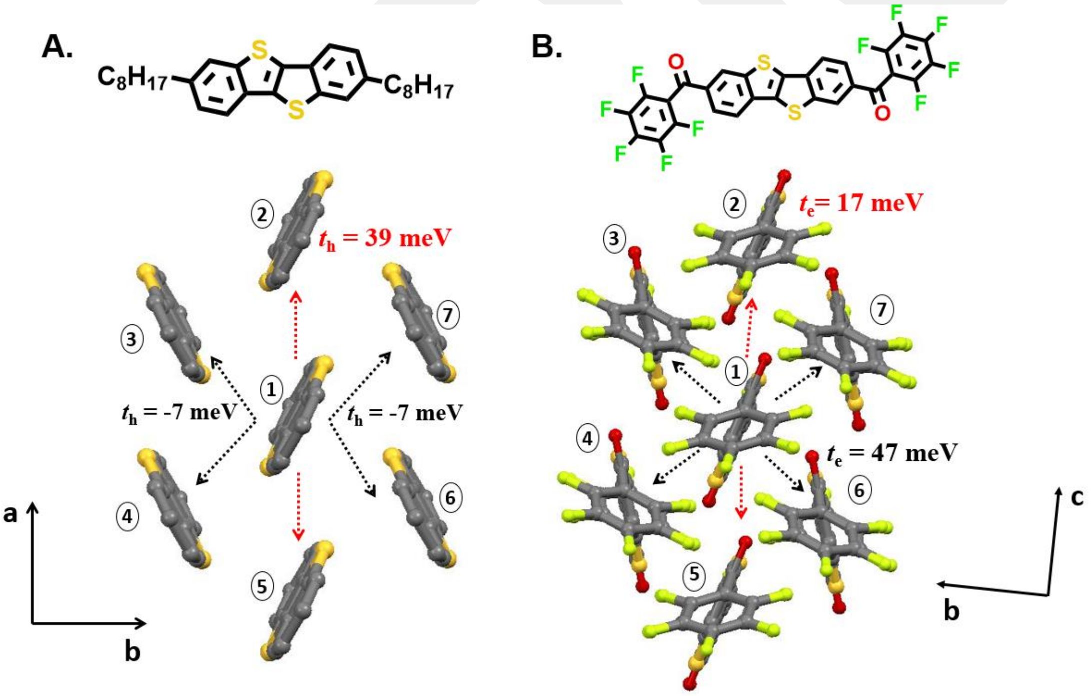

Figure 2.22 Crystal structures of **C$_8$-BTBT** (A**)** and **D(Ph$_F$CO)-BTBT** (B) along the *a*,*b*-axes and *b*,*c*-axes, respectively, underscoring the formation of two-dimensional *in-plane* herringbone-like packing. Alkyl chains of **C$_8$-BTBT** are omitted for clarity. DFT-estimates of the effective transfer integrals (in meV) for holes (t_h) and electrons (t_e) for the selected dimer pairs in face-to-edge (black dotted lines) and edge-to-edge manners (red dotted lines) are also shown.

Table 2.3 DFT-calculated transfer integrals for holes (t_h) and electrons (t_e) in **D(Ph$_F$CO)-BTBT** dimers.

	$t_{e\ (meV)}$	
D(Ph$_F$CO)-BTBT	**PW91PW91/6-31G****	**B3LYP/6-31G****
12	17	19
13	-47	-56
14	47	56
15	-17	-19
16	47	56
17	-47	56

Table 2.4 DFT-calculated transfer integrals for holes (t_h) and electrons (t_e) in **C$_8$-BTBT** dimers.

	$t_{h\ (meV)}$	
C$_8$-BTBT	**PW91PW91/6-31G****	**B3LYP/6-31G****
12	39	37
13	-7	3
14	-7	3
15	39	37
17	-7	3
18	-7	3

2.4 Conclusions

In summary, the first example of a BTBT-based *n*-type molecular semiconductor, **D(Ph$_F$CO)-BTBT**, has been designed, synthesized and characterized. The new semiconductor was synthesized in a two-step transition metal-free process without using chromatographic purification. The significant lowering of the LUMO level for **D(Ph$_F$CO)-BTBT**, versus other BTBTs, is attributed to extended π-conjugation along the molecular backbone including the BTBT and *in-plane* carbonyl units, and, to a less extent, the inductive effect of the *out-of-plane* pentafluorophenyl groups. Polycrystalline **D(Ph$_F$CO)-BTBT** thin-films exhibit large grains (~2-5 μm sizes) with "layer-by-layer" packing motifs on the substrate surface forming an *in-plane* herringbone packing with short intermolecular distances (3.25-3.46 Å), which doubtless favors two-dimensional (2D) source-to-drain (S→D) charge transport. TC/BG-OFET devices comprising a thermally evaporated **D(Ph$_F$CO)-BTBT** film on the hydrophobic HMDS-treated SiO_2 substrate and LiF/Au contacts exhibit high electron mobilities of ~0.6 cm^2/Vs and I_{on}/I_{off}'s over 10^7. The observed high electron mobility for **D(Ph$_F$CO)-BTBT** undoubtedly reflects a combination of highly π-delocalized/energetically stabilized LUMO, large film grain sizes with high crystallinity, and excellent texture with preferential *edge-on* molecular orientation and *in-plane* herringbone packing facilitating strong intermolecular π-orbital overlaps, as supported by DFT computations. Our results demonstrate that *n*-type semiconductors based on BTBT cores are possible which, based on the very large intrinsic charge transport capabilities of BTBT (> 10 cm^2/V·s) and its good optical transparency, may open new pathways to realize unconventional devices for next generation high performance organic (opto)electronics.

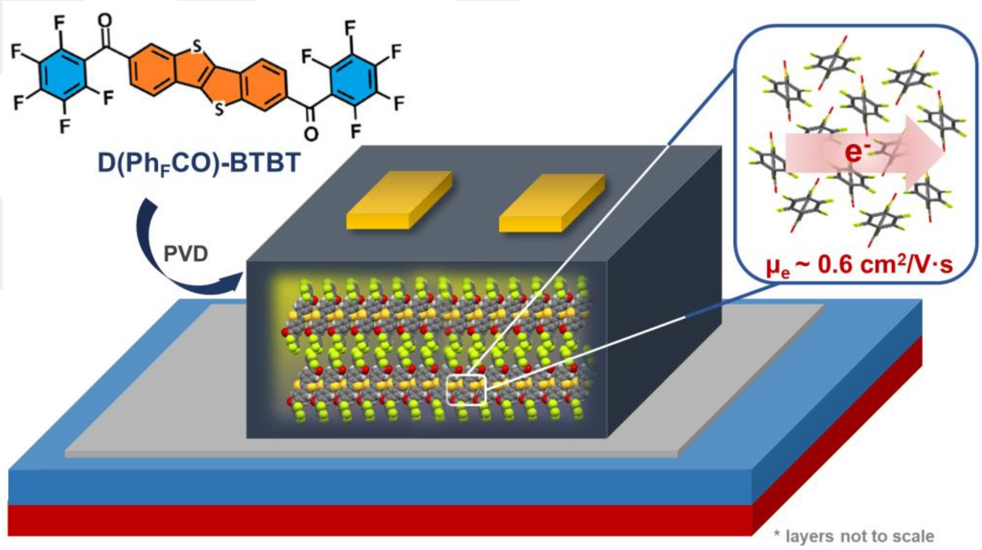

Figure 2.23 The first example of an *n*-type [1]Benzothieno[3,2-b][1]benzothiophene (BTBT)–based organic small molecular semiconductor. TC/BG-OFET devices based on physical vapor deposited thin films showed electron mobility up to ~0.6 cm^2/V.s.

Chapter 3

Engineering Functionalized Low LUMO [1]Benzothieno[3,2-b][1]benzothiophenes (BTBTs): Unusual Molecular and Charge Transport Properties

3.1 Introduction

Organic π-conjugated small molecules with fused rings offer great promise as semiconductors in the fields of fundamental charge transport studies and optoelectronic device applications [68,104,178,179,118,171–177]. The earlier approaches to the development of molecular semiconductors have focused on oligomeric π-structures such as oligo-thiophenes/phenylenes as a result of their structural versatility, convenient synthesis, and appreaciable charge-transport characteristics [86,108,163,180–182]. However, the realization of fused π-conjugated derivatives have greatly influenced molecular semiconductor developments as a result of their highly advantageous optoelectronic/physicochemical characteristics and much higher charge carrier mobilities compared to oligomers [68,183,184]. Attractive properties of fused π-systems include coplanar π-backbone with highly delocalized frontier molecular orbitals enabling effective charge injection/extraction and delocalization, low reorganization energies for charge hopping, and very effective intermolecular interactions (*large transfer integrals*) in solid-state [99,155,185,186]. While the majority of research efforts on fused π-systems has focused on low band-gap acenes and polycyclic aromatic compounds such as pentacene [5], TIPS-pentacene [187], and perylenediimide [188], diacene-fused thienothiophenes (DAcTTs) (e.g., [1]benzothieno[3,2-*b*][1]benzothiophene (BTBT)) have emerged in the past decade as new generation hole transporting (*p*-type) semiconductors with unprecedented charge carrier mobilities [133,189,190]. In this type of thienoacenes, the presence of a phene-like electronic structure with large sulfur atoms on the central thieno[3,2-b]thiophene enables a unique semiconductor π-structure with a large band gap, stabilized HOMO energy level, and impressive hole transport ability [61]. Particularly, their vapor-deposited and solution-processed thin films favor two dimensional (2D) in-plane herringbone packing motifs to yield very high hole mobilities in organic field-effect transistors (OFETs) [131,191]. Despite these premises, to the best of our knowledge, DAcTTs had never been studied in the design of low (< -3 eV) LUMO (lowest unoccupied molecular orbital) electron transporting (*n*-type) semiconducting molecules prior to our very recent report [192]. This had arisen two critical fundamental questions as to whether functionalization with electron withdrawing functional groups in DAcTTs, which are typically wide band-gap π-cores, could ever enable an efficient electron transport and what structure–molecular properties–semiconductivity relationships would be effective. The first question is particularly interesting because almost all *p*-type π-frameworks including acenes [193] have been tailored to yield *n*-type semiconductors via proper functionalizations [194–196]. To realize efficient electron transport from DAcTT derivatives that are as high as their hole mobilities would greatly contribute to the development of complementary organic circuits and wide-ranging optoelectronic applications wherever electron transport is desired [165,197–200]. It could also open up new opportunities in optoelectronics when combined with DAcTTs' other interesting properties such as relatively easy synthesis (multigram scale), wide optical band gaps (optical transparency), and deep HOMO energies [155]. To this end, we have recently demonstrated the first example of *n*-type DAcTT semiconductor in the literature, **D(Ph$_F$CO)-BTBT** [192] (Figure 1), which showed a highly stabilized (E_{LUMO} = -3.64 eV) LUMO as compared to *p*-type DAcTTs. The OFET devices with highly crystalline **D(Ph$_F$CO)-BTBT** films demonstrated high electron mobilities of ~0.6 $cm^2/V{\cdot}s$ and I_{on}/I_{off} ratios over 10^7–10^8. Prompted by these initial promising results, we are now interested in engineering new functionalized low LUMO BTBTs in "S-F-BTBT-F-S (F/S: functional group/substituent)" molecular architecture (Figure 3.1) and creating a molecular library to explore structure–molecular properties–semiconductivity relationships in this new class of molecular semiconductors. We are particularly keen to understand the electronic/structural factors governing electron transport in DAcTTs, and how these parameters could be tuned via functional groups and substituents. In our present study, BTBT is the preferred π-framework because it is the smallest member of DAcTT family with good charge transport properties, and functionalizations on the BTBT π-core is expected to have an immediate effect on the electronic structure. Also, BTBT π-core is open to Friedel-Crafts acylations and further functionalizations with ease, and its π-structural dimension is very likely to enable solubility via proper substitutions. To this end, as shown in Figure 3.1, BTBT is systematically functionalized with electron withdrawing carbonyl and dicyanovinylene functional groups *(in blue*) and substituted with heptyl chains (-C_7H_{15}) (*in red*).

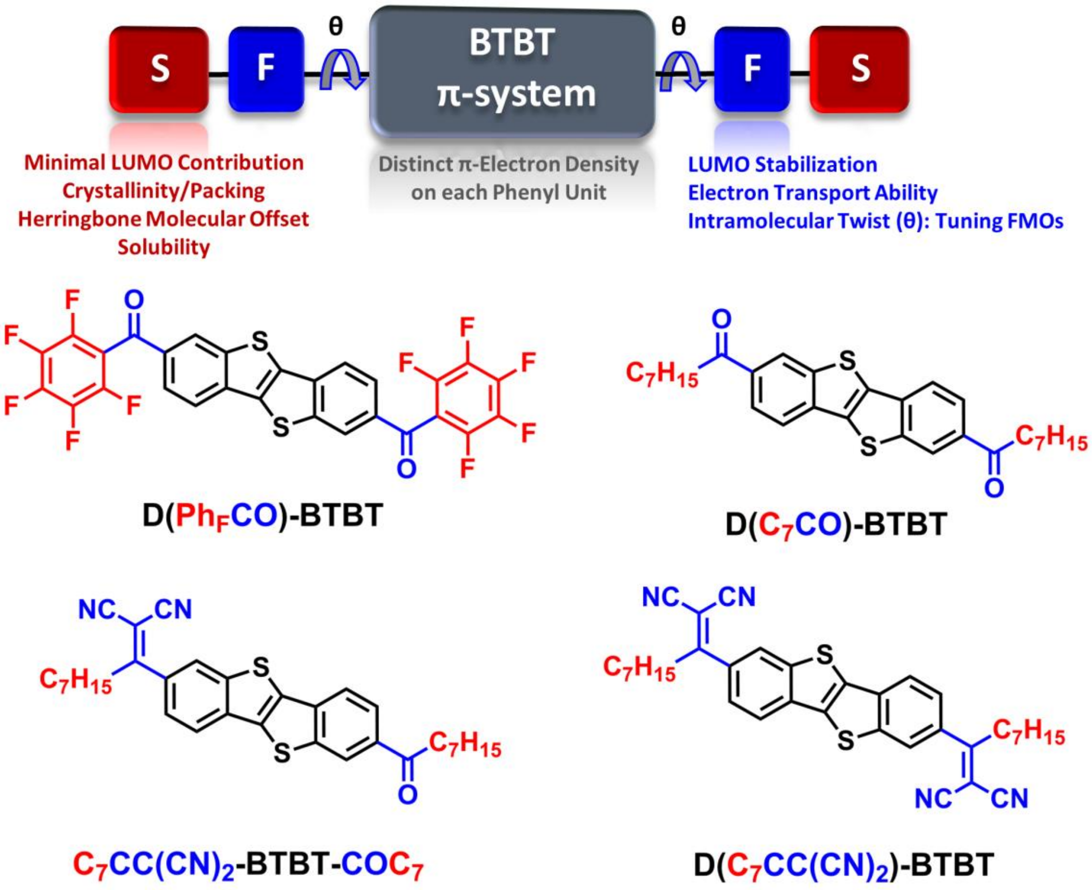

Figure 3.1 The S-F-BTBT-F-S (F/S: functional group/substituent) design architecture for functionalized low LUMO BTBT molecules indicating the contributions of each substructure and the chemical structures of **D(C_7CO)-BTBT**, **C_7CO-BTBT-CC(CN)$_2$C$_7$**, and **D(C_7CC(CN)$_2$)-BTBT** developed in this study and **D(Ph$_F$CO)-BTBT**[192] developed in our previous study.

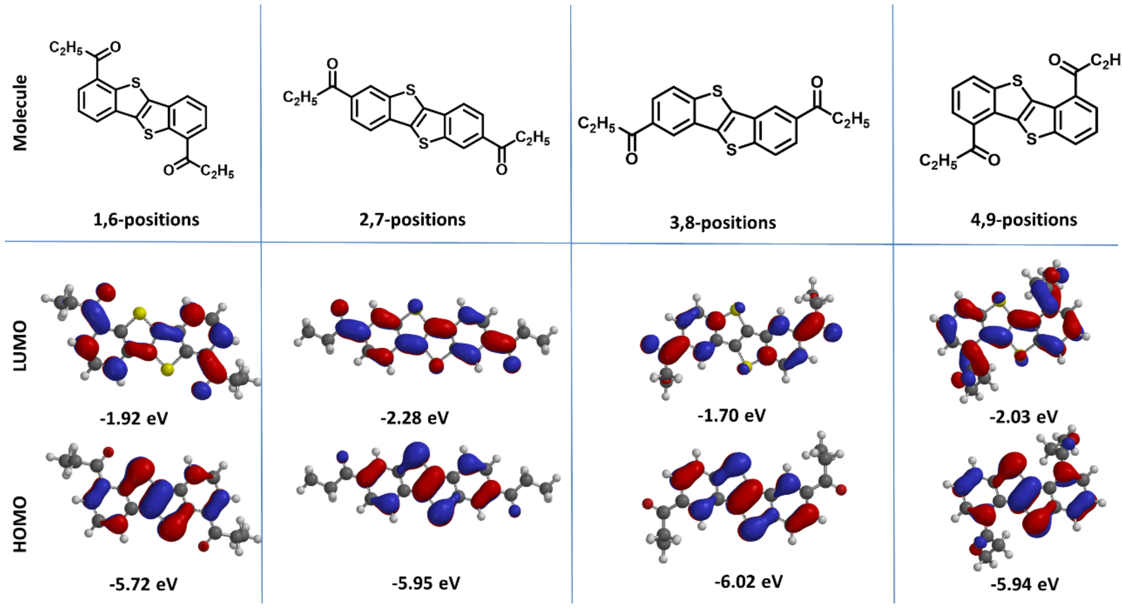

Figure 3.2 Theoretical (DFT/B3LYP/6-31G**) HOMO/LUMO energy levels of **D(C_7CO)-BTBT** along with topographical orbital representations for different functionalization positions.

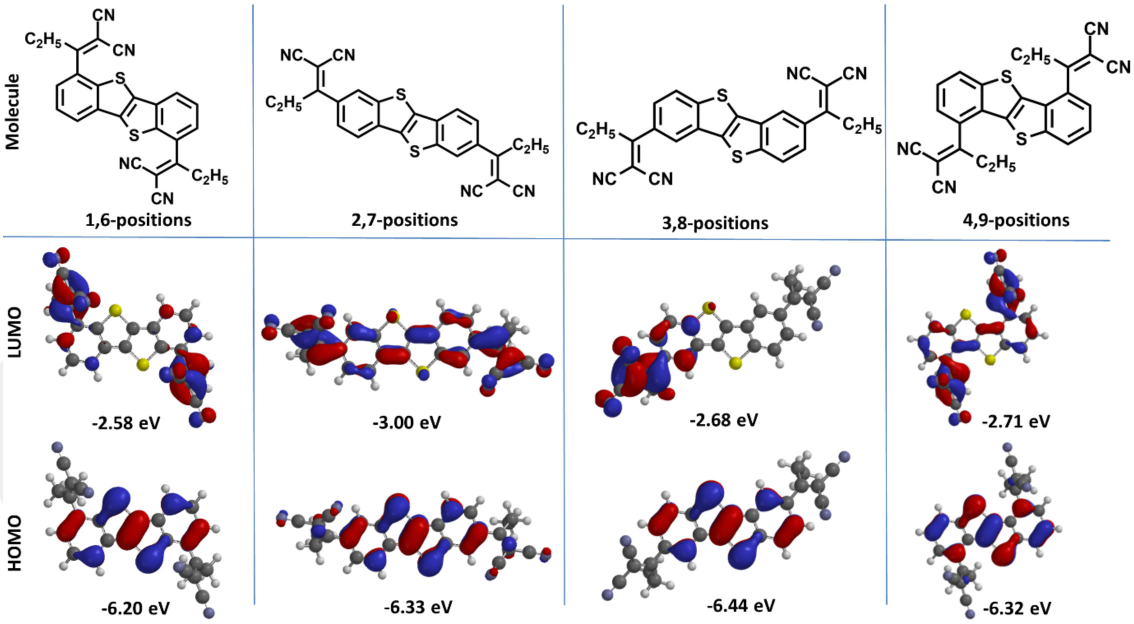

Figure 3.3 Theoretical (DFT/B3LYP/6-31G**) HOMO/LUMO energy levels of **D(C_7CC(CN)$_2$)-BTBT** along with topographical orbital representations for different functionalization positions.

This design is envisioned to yield a combination of low LUMO and good solubility for convenient synthesis/purification, and systematic functionalization could reveal the electronic effects of carbonyl *vs.* dicyanovinylene on the BTBT's π-electronic structure and electron transport characteristics. The quantum mechanical modeling

(DFT, B3LYP/6-31G**) used in the design of these molecules prior to the synthesis points out that for all compounds, among the four possible symmetric BTBT functionalization positions (1,6/2,7/3,8/4,9), 2,7-positions give the lowest LUMO energies with the most delocalized wave functions (Figures 3.2 and 3.3). The difference becomes especially pronounced in the case of dicyanovinylene functionalization that all positions other than 2,7 tend to localize LUMO wave functions on the dicyanovinylene units.

We present herein the design, synthesis, and full characterization of a series of functionalized low LUMO [1]benzothieno[3,2-b][1]benzothiophene (BTBT)-based small molecules, **D(C_7CO)-BTBT**, **C_7CO-BTBT-CC(CN)$_2$$C_7$**, and **D($C_7$CC(CN)$_2$)-BTBT** (Figure 3.1). Detailed structural, physicochemical, and optoelectronic characterizations were performed; the single-crystal structures for **D(C_7CO)-BTBT** and **D(C_7CC(CN)$_2$)-BTBT** were accessed. Note that while **C_7CO-BTBT-CC(CN)$_2$$C_7$** and **D($C_7$CC(CN)$_2$)-BTBT** are novel compounds, **D(C_7CO)-BTBT**[42] has previously been described as an intermediate compound, yet with no OFET characteristics or molecular/single-crystal properties, during the synthesis of *p*-channel BTBTs. As a result of functionalization with electron withdrawing carbonyl/dicyanovinylene units, the LUMOs are remarkably stabilized ($-\Delta E_{LUMO}$ = 1.2 eV-1.4 eV) while optical band gaps remain large (2.8-3.1 eV). Thermal and thin film characterizations reveal that symmetric functionalization is crucial to enable strong intermolecular interactions in solid-state. The carbonyl functionalities, regardless of the substituents (i.e., heptyl and pentafluorophenyl), adopt coplanar π-conformations with BTBT. However, dicyanovinylenes are found to be twisted (47.5°), which has unusual effects on π-electron deficiencies, thermal properties, frontier molecular orbital energetics, photophysical properties, and π-electronic structures. While functional groups and intramolecular twists govern LUMO stabilization/π-delocalization, substituents appear to be the key component to form a favorable three-dimensional π-electronic structure and a low intramolecular reorganization energy for electron transport. In our study, despite their twisted conformations, 2,7-dicyanovinylenes are shown for the first time to yield good electron transport in DAcTTs. **D(C_7CC(CN)$_2$)-BTBT** thin films exhibit large 2D plate-like crystalline grains (~1-2 μm sizes) of terraced islands and becomes a rare example of *n*-type DAcTT with an appreciable μ_e of 0.004 $cm^2/V \cdot s$ ($I_{on}/I_{off} = 10^6$-10^7) in TC/BG-OFETs. On the basis of these unique findings, structure–molecular properties–semiconductivity relationships are established for the first time in low LUMO DAcTTs.

3.2 Experimental Section

3.2.1 Materials and Methods

Conventional Schlenk techniques were used for the reactions performed under N_2 atmosphere. All of the chemicals were purchased from commercial sources and used without further purification unless otherwise noted. Column chromatography was carried out using 230-400 mesh particle size (60 Å pore size) silica gel as the stationary phase. $^1H/^{13}C$ NMR spectra were recorded on a Bruker 400 spectrometer (^1H, 400 MHz; ^{13}C, 100 MHz). Elemental analyses were done on a LecoTruspec Micro model instrument. High-resolution mass spectra were measured on a Bruker Microflex LT MALDI-TOF-MS Instrument. Thermogravimetric analysis (TGA) and differential scanning calorimetry (DSC) measurements were performed on Mettler Toledo-TGA/STDA 851 and Mettler Toledo-DSC 821 model instruments, respectively, at a heating rate of 10 °C/min under nitrogen atmosphere. UV-Vis absorption spectra were recorded via Shimadzu UV-1800 spectrophotometer. Photoluminescence (PL) characterizations were carried out with Agilent-Cary Eclipse fluorescence spectrophotometer. Time-correlated single photon counting measurements were performed using Pico Quant FluoTime 200 equipped with 375 nm pulsed (200 ps pulse width) laser diode. The PL quantum yields in solution were measured using the comparative method with a standard fluorescent Coumarin 153 dye solution (Φ_{PL} = 53% in ethanol) [201,202]. Electrochemical characterizations were carried out via cyclic voltammetry measurements on a C3 cell stand electrochemical station equipped with BAS-Epsilon software (Bioanalytical Systems, Inc. Lafayette, IN). The working and counter electrodes were Pt, and the reference electrode was Ag/AgCl(3 M NaCl). All the potentials were calibrated with respect to the standard ferrocene/ferrocenium redox couple (Fc/Fc^+: $E_{1/2}$ = +0.40 V measured in the same electrochemical set-up). The optimization of the molecular geometries and the analysis of the frontier molecular orbitals were carried out by Gaussian 09 using density functional theory (DFT) at

B3LYP/6-31G** level [138]. The intramolecular reorganization energies for hole (λ_h) and electron (λ_h) transfers for **D(Ph$_F$CO)-BTBT** and **D(C$_7$CO)-BTBT** were calculated in accordance with a standard procedure reported in the literature [139].

3.2.2 Synthesis and Structural Characterization

The synthesis of [1]Benzothieno[3,2-b][1]benzothiophene (BTBT) was carried out in accordance with the reported procedure [42,122].

Synthesis of 1,1'-(benzo[b]benzo[4,5]thieno[2,3-d]thiophene-2,7-diyl)bis(octan-1-one) ***(D(C$_7$CO)-BTBT)****:* $AlCl_3$ (3.03 g, 22.76 mmol) was added into a solution of [1]benzothieno[3,2-b][1]benzothiophene (1.0 g, 4.16 mmol) in anhydrous dichloromethane (100 mL) at −10 °C under nitrogen. The resulting solution was stirred at −10 °C for 30 min. Then, the reaction mixture cooled down to −78 °C. Octanoyl chloride (3.38 g, 20.8 mmol) was subsequently added dropwise, and the mixture was stirred for 1 h at the same temperature. The reaction mixture was allowed to warm to room temperature and stirred for 2 days. After completing the reaction, mixture was quenched with water to give a white precipitate. The precipitate was collected by filtration, and then washed with water and methanol, respectively. The product was obtained as a pale yellow solid (1.2 g, 58% yield). The compound was directly used in the next step without any further purification. For OFET device fabrication, 100 mg of this crude solid was purified via column chromatography on silica gel using chloroform as mobile phase to afford the pure semiconductor solid (80 mg). Melting point: 265-266 °C; ^{1}H NMR (400 MHz, $CDCl_3$), δ (ppm): 8.59 (s, 2H), 8.09 (d, 2H, J = 8.0 Hz), 7.98 (d, 2H, J = 8.0 Hz), 3.08 (t, 4H, J = 12.0 Hz), 1.78-1.85 (m, 4H), 1.33-1.44 (m, 16H), 0.89-0.93 (t, 6H, J = 16.0 Hz); ^{13}C NMR (100 MHz, $CDCl_3$), δ (ppm): 199.5, 142.8, 136.2, 135.8, 134.3, 124.9, 124.6, 121.9, 38.9, 31.7, 29.4, 29.2, 24.5, 22.6, 14.1; MS (MALDI-TOF) *m/z* calcd for $C_{30}H_{36}O_2S_2$: 492.22[M^+]; found: 492.44[M^+]; elemental analysis calcd (%) for $C_{30}H_{36}O_2S_2$: C, 73.13; H, 7.36; found: C, 73.46; H, 7.67.

Synthesis of 2-(1-(7-octanoylbenzo[b]benzo[4,5]thieno[2,3-d]thiophen-2-yl)octylidene) malononitrile ***(C$_7$CO-BTBT-C(CCN$_2$)C$_7$)****:* Piperidine (0.73 g, 8.51 mmol) was added into a solution of 1,1'-(benzo[b]benzo[4,5]thieno[2,3-d]thiophene-2,7-diyl)bis(octan-1-one) (D(C$_7$CO)-BTBT) (0.50 g, 1.01 mmol), and malononitrile (0.97 g, 14.61 mmol) in 50 mL of anhydrous DMSO under nitrogen. The resulting mixture was stirred at 110 °C for 2 hours. After completing reaction, it was allowed to cool down to room temperature. The reaction mixture quenched with water. After extraction with $CHCl_3$, organic layer dried with Na_2SO_4, filtered and concentrated to obtain the crude product. The crude was then purified through column chromatography on silica gel using chloroform as mobile phase to afford the final product as a yellow solid. (110 mg, 20% yield). Melting point: 102-103 °C; ^{1}H NMR (400 MHz, $CDCl_3$), δ (ppm): 8.59 (s, 1H), 8.10-8.12 (d, 2H, J = 8.0 Hz), 8.05-8.07 (d, 1H, J = 8.0 Hz), 7.99-8.01 (d, 1H, J = 8.0 Hz), 7.59-7.62 (d, 1H, J = 12.0 Hz), 3.06-3.11 (m, 4H), 1.78-1.85 (m, 2H), 1.24-1.49 (m, 18H), 0.84-0.92 (m, 6H); ^{13}C NMR (100 MHz, $CDCl_3$), δ (ppm): 199.5, 179.5, 143.2, 142.9, 135.6, 135.3, 134.5, 131.9, 124.6, 123.5, 122.6, 121.9, 112.9, 112.6, 84.8, 38.9, 37.8, 31.7, 31.5, 29.4, 29.2, 22.6, 22.5, 14.1, 14.0; MS (MALDI-TOF) *m/z* calcd for $C_{33}H_{36}N_2OS_2$: 540.23[M^+]; found: 540.34[M^+]; elemental analysis calcd (%) for $C_{33}H_{36}N_2OS_2$: C, 73.29; H, 6.71; N, 5.18; found: C, 73.47; H, 6.88; N, 5.01.

Synthesis of 2,2'-(benzo[b]benzo[4,5]thieno[2,3-d]thiophene-2,7-diylbis(octan-1-yl-1-ylidene))dimalononitrile ***(D(C$_7$CC(CN)$_2$)-BTBT)****:* A mixture of 1,1'-(benzo[b]benzo[4,5]thieno[2,3-d]thiophene-2,7-diyl)bis(octan-1-one) (D(C_7CO)-BTBT) (0.25 g, 0.51 mmol) and malononitrile (0.47 g, 7.14 mmol) was dissolved in anhydrous chlorobenzene (50 mL) under nitrogen, and stirred at 35 °C for 15 min. Afterwards, pyridine (0.77 g, 9.69 mmol) and $TiCl_4$ (0.97 g, 5.1 mmol) were added to the reaction mixture. The resulting mixture was heated and stirred at 110 °C for 90 min. After completing reaction, it was allowed to cool down to room temperature. The reaction mixture quenched with water. After extraction with $CHCl_3$, organic layer dried with Na_2SO_4, filtered and concentrated to obtain the crude product. The crude was then purified through column chromatography on silica gel using CH_2Cl_2 as a mobile phase to afford the final product as a pale yellow solid (138 mg, 46% yield). Melting point: 211-212 °C; ^{1}H NMR (400 MHz, $CDCl_3$), δ (ppm): 8.10 (s, 2H), 8.05-8.07 (d, 2H, J = 8.0 Hz), 7.60-7.62 (d, 2H, J = 8.0 Hz), 3.06-3.10 (t, 4H, J = 16.0 Hz), 1.34-1.41 (m, 4H), 1.24-1.32 (m, 16H), 0.84-0.87 (t, 6H, J = 12.0 Hz); ^{13}C NMR (100 MHz, $CDCl_3$), δ (ppm): 179.5, 143.3, 135.9, 135.1, 132.2, 124.4, 123.5, 122.6, 112.9, 112.5, 85.0, 37.9, 31.5, 29.1, 28.7, 28.6, 22.5, 14.0; MS (MALDI-TOF) *m/z* calcd for $C_{36}H_{36}N_4S_2$: 588.24[M^+]; found: 588.52[M^+]; elemental analysis calcd (%) for $C_{36}H_{36}N_4S_2$: C, 73.43; H, 6.16; N, 9.51; found: C, 73.74; H, 6.44; N, 9.42.

3.2.3 Field-Effect Transistor Fabrication and Characterization

A heavily *n*-doped (100) silicon (n^{++}-Si) with 200 nm thermally grown SiO_2 was used as the gate/dielectric substrate for OFET fabrication. The substrates were sonicated in acetone and isopropyl alcohol for 10 min with subsequent drying under N_2 flow. Then, the substrates were treated with 100 W oxygen plasma for 3 min (Cute, Femto Science, South Korea). To form the hydrophobic interfacial layer, n^{++}-Si/SiO_2(200 nm) substrates were treated with hexamethyldisilazane (HMDS). To deposit 30 nm thick organic semiconductor films, the **D(C_7CO)-BTBT** and **D(C_7CC(CN)$_2$)-BTBT** solids were thermally evaporated onto temperature-controlled (25 °C and 70 °C) n^{++}-Si/SiO_2(200 nm)/HMDS substrates under high vacuum (~10^{-6} Torr) using a growth rate of 0.1-0.2 Å/s. The surface morphology and microstructure of the evaporated semiconductor thin-films were characterized by atomic force microscopy (AFM, NX10, Park systems, South Korea) and grazing incidence X-ray diffraction (GIXRD, X'pert Pro, Malvern Panalytical Ltd). The source-drain electrodes (LiF (1 nm)/Au (50 nm) for *n*-channel testing and Au (50 nm) for *p*-channel testing) were defined via thermally evaporation through shadow mask to yield semiconducting channels of 1000 μm width and 50 μm length. The semiconductor channels were electrically isolated from each other using mechanical scratch. The electrical characterization of the OFETs was performed in a vacuum probe station (M5VC, MSTech, South Korea) using Keithley 4200-SCS semiconductor analyzer system (Tektronix Inc, USA). The saturation charge carrier mobility (μ_{sat}) was estimated based on a conventional metal-oxide-semiconductor field-effect transistor model using the formula

$$\mu_{sat} = (2I_{DS}L)/[WC_i(V_G - V_{th})^2] \tag{3.1}$$

where I_{DS} is the source−drain current, L is the channel length, W is the channel width, C_i is the areal capacitance of the gate dielectric, V_G is the gate voltage, and V_{th} is the threshold voltage.

3.3 Results and Discussion

3.3.1 Synthesis, Characterization, and Thermal Properties

The synthesis of the new molecules is shown in Figure 3.4. As the first step, **D(C_7CO)-BTBT** was synthesized via double Friedel-Crafts acylation with a yield of 58%. Note that this reaction has previously been carried out as an intermediate step in the synthesis of *p*-type BTBT compounds (e.g., **C_8-BTBT**), and it selectively functionalizes the BTBT π-core at the 2,7-positions [42,122]. Then, Knoevenagel condensations were carried out on **D(C_7CO)-BTBT** to convert carbonyls to dicyanovinylene groups. For single carbonyl conversion, malononitrile reacts with **D(C_7CO)-BTBT** in the presence of piperidine base to yield **C_7CO-BTBT-C(CCN_2)C_7** in 20% yield. In the synthesis of **D(C_7CC(CN)$_2$)-BTBT**, $TiCl_4$ Lewis acid was needed along with pyridine and malononitrile to achieve double carbonyl conversion (46% yield). All small molecules exhibit good solubilities in common organic solvents (e.g., >15-20 mg/ml in chloroform) allowing for convenient synthesis and chromatographic purification. As compared with previously developed **D(Ph_FCO)-BTBT** that had very low solubility, such good solubilities of the current molecules certainly reflect the solubilizing effect of the flexible alkyl ($-C_7H_{15}$) substituents. Similar to *p*-channel BTBT derivatives, medium-sized ($-C_nH_{2n+1}$, n = 5-8) linear alkyl chains are sufficient to provide good solubility in functionalized low LUMO BTBT derivatives. It is also noticed that the dicyanovinylene functionalization of the carbonyl unit improves solubility, which could be ascribed to the increased local dipoles and the twisted molecular conformation as evidenced from the DFT calculations and the single-crystal structures (*vide infra*).

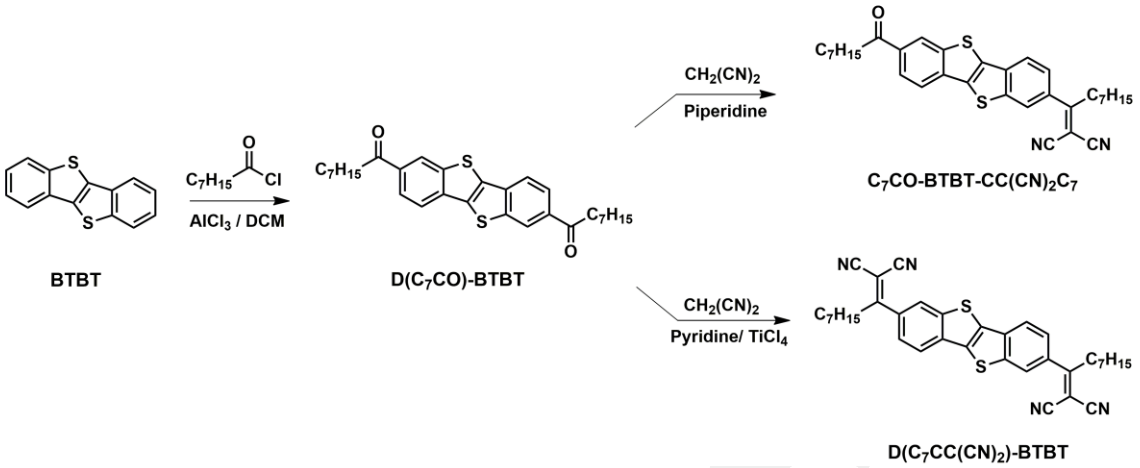

Figure 3.4 Synthesis of highly soluble functionalized low LUMO BTBT molecules **D(C_7CO)-BTBT**, **C_7CO-BTBT-CC(CN)$_2$$C_7$**, and **D($C_7$CC(CN)$_2$)-BTBT**.

The molecular structures and chemical purities were characterized by using ^{1}H and ^{13}C NMR spectroscopies (Figures 3.5, 3.6, 3.8, 3.9, 3.11, and 3.12), MALDI-TOF mass spectrometry (Figures 3.7, 3.10, and 3.13), elemental analysis, attenuated total reflection Fourier-transform IR (ATR-FTIR) (Figure 3.14), and single-crystal X-ray analysis.

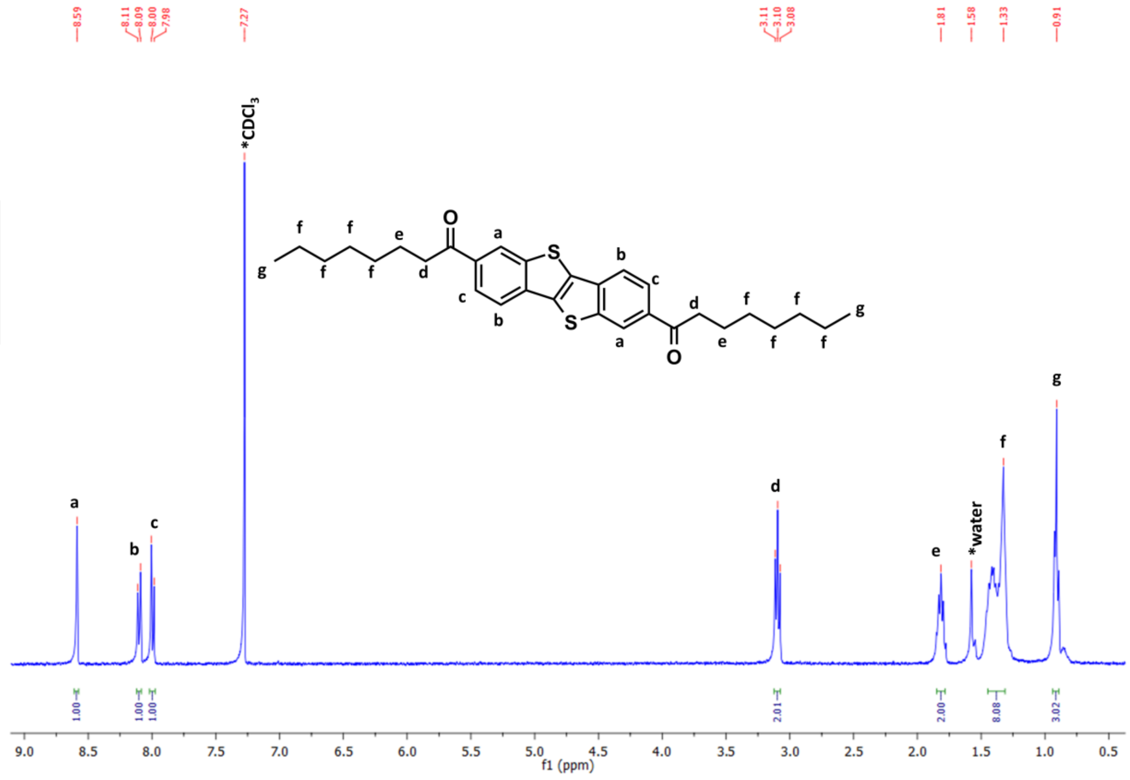

Figure 3.5 ^{1}H NMR spectra of **D(C_7CO)-BTBT** measured in $CDCl_3$.

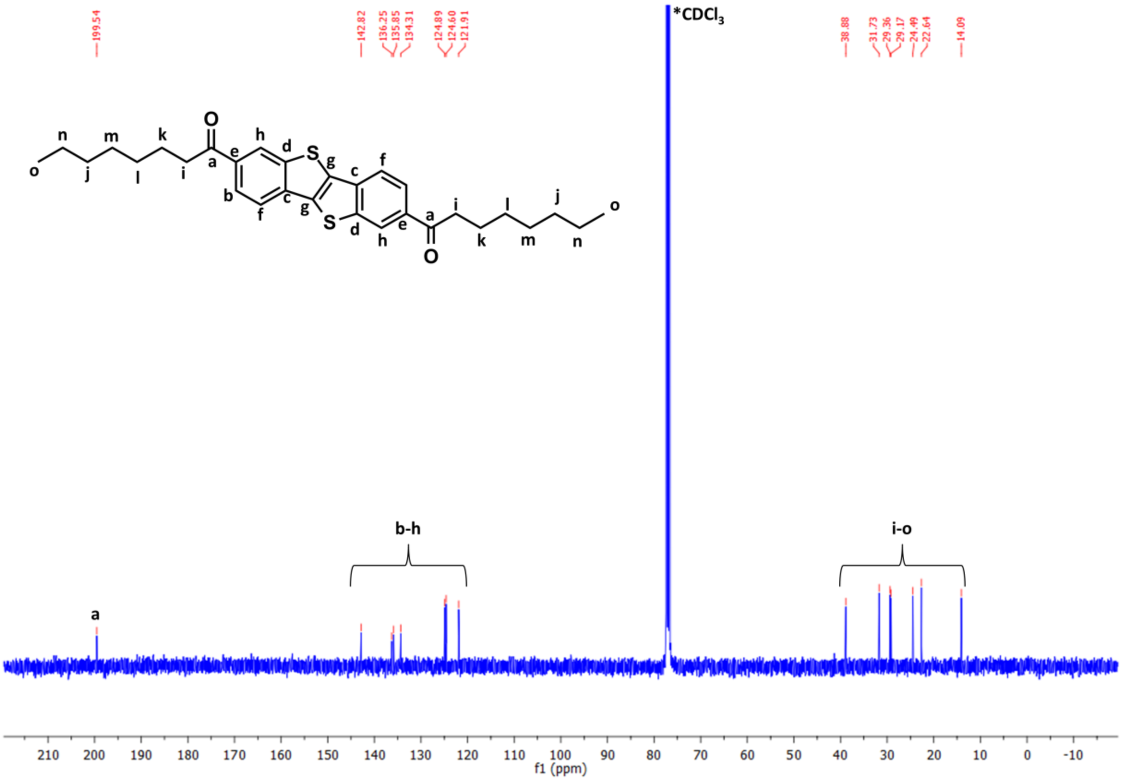

Figure 3.6 ^{13}C NMR spectra of **D(C$_7$CO)-BTBT** measured in CDCl$_3$.

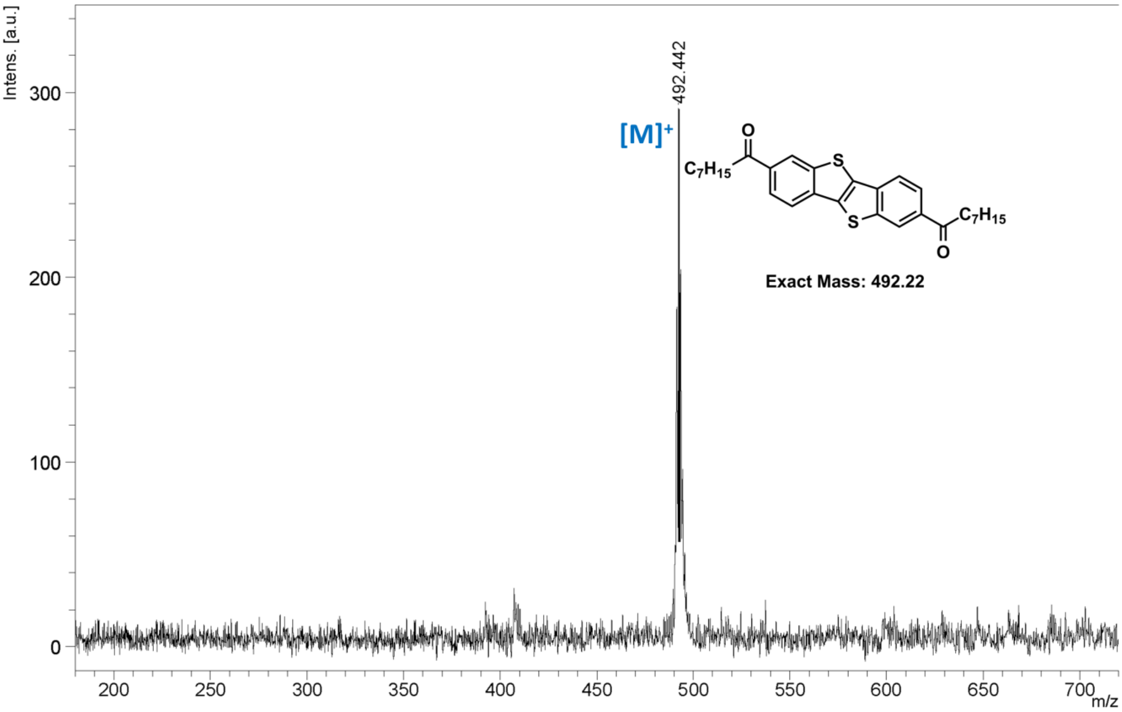

Figure 3.7 Positive ion and linear mode MALDI TOF-MS spectrum of **D(C$_7$CO)-BTBT**.

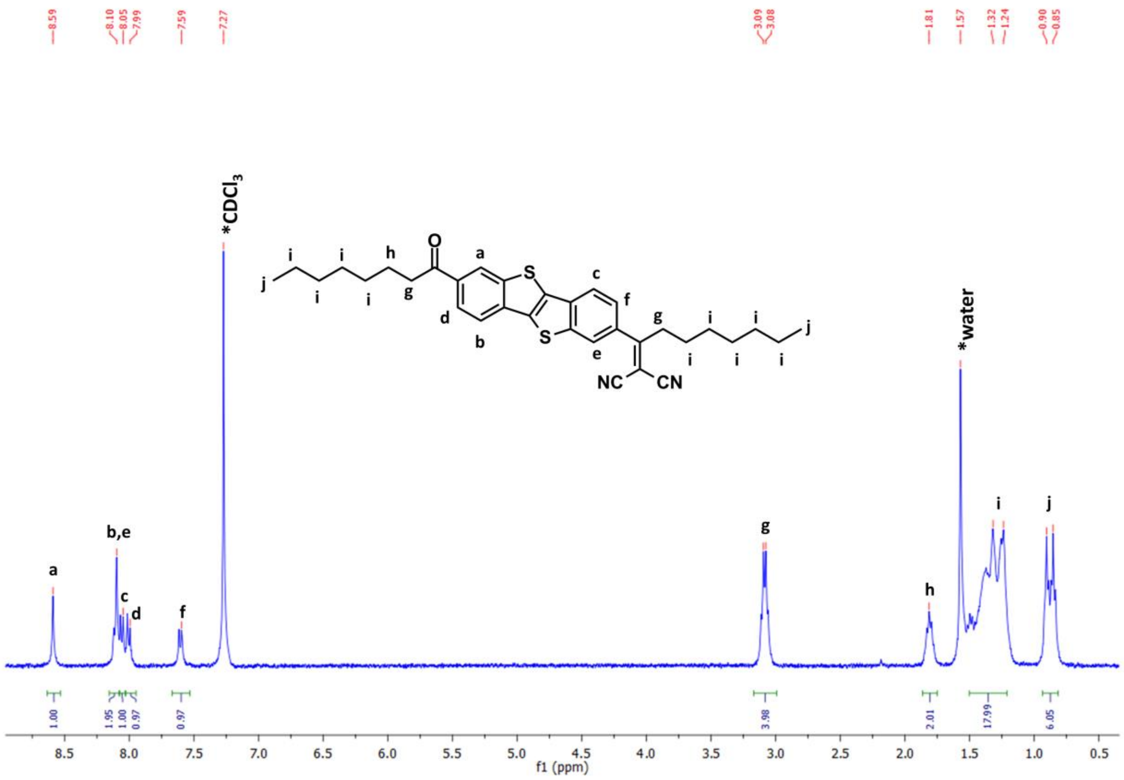

Figure 3.8 ^{1}H NMR spectra of **C_7CO-BTBT-CC(CN)$_2$C$_7$** measured in CDCl$_3$.

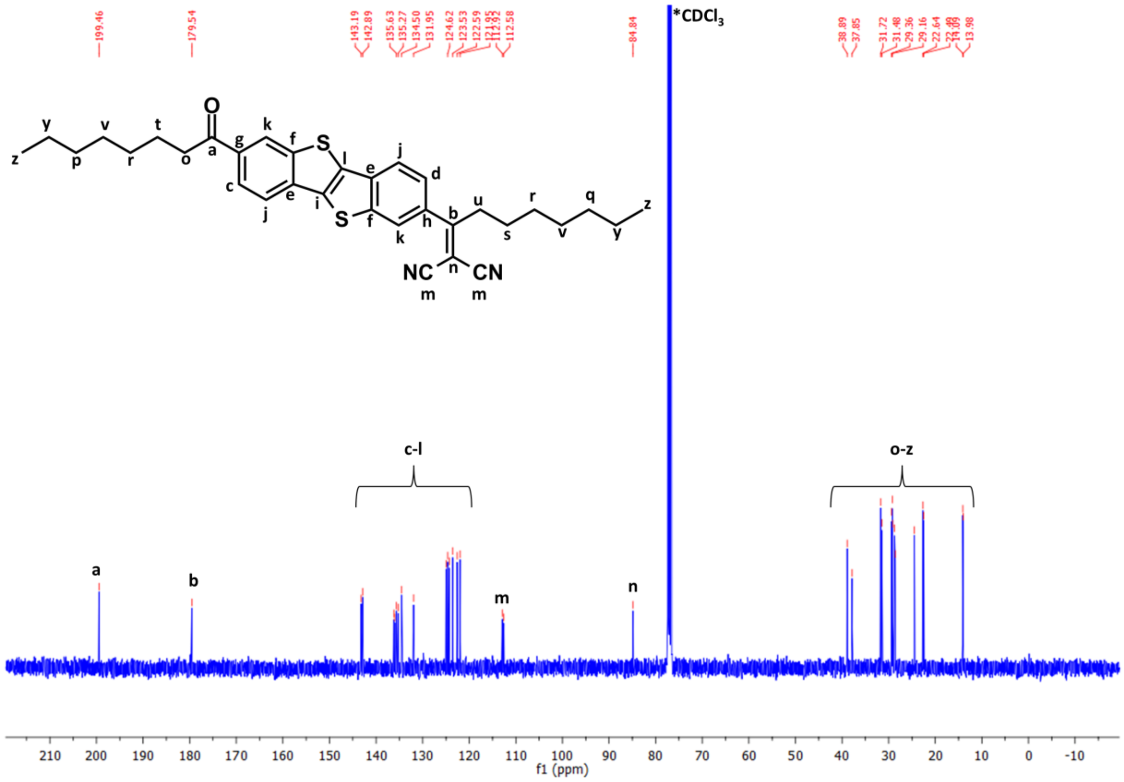

Figure 3.9 ^{13}C NMR spectra of **C_7CO-BTBT-CC(CN)$_2$C$_7$** measured in CDCl$_3$.

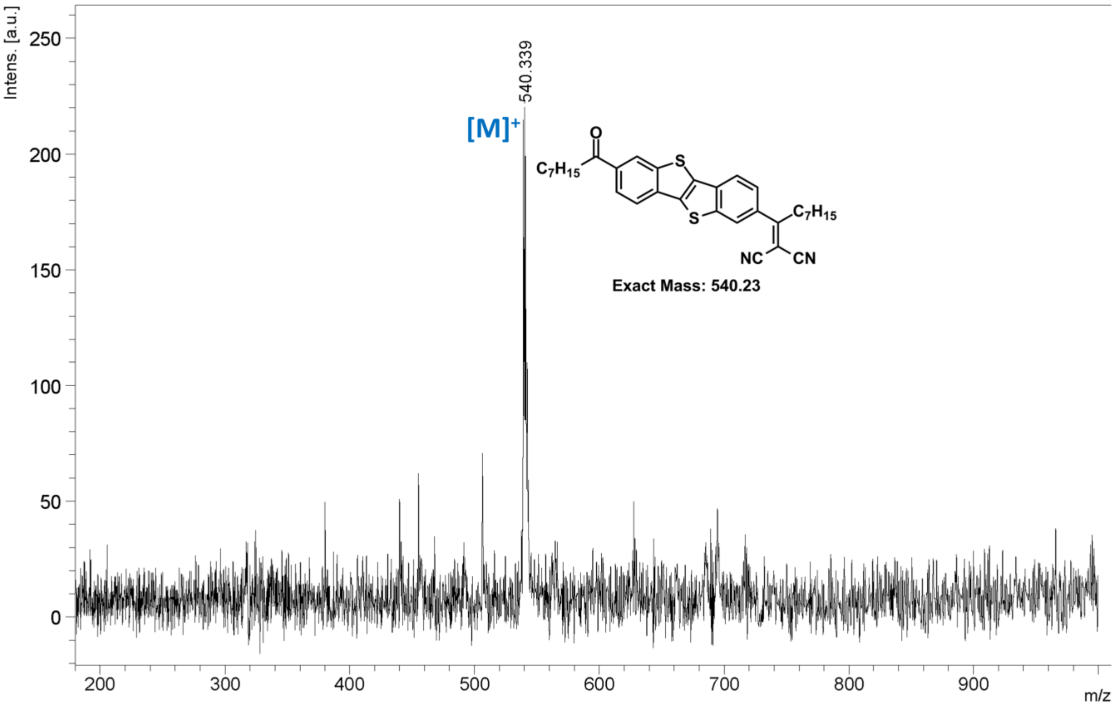

Figure 3.10 Positive ion and linear mode MALDI TOF-MS spectrum of **C_7CO-BTBT-CC(CN)$_2$C$_7$**.

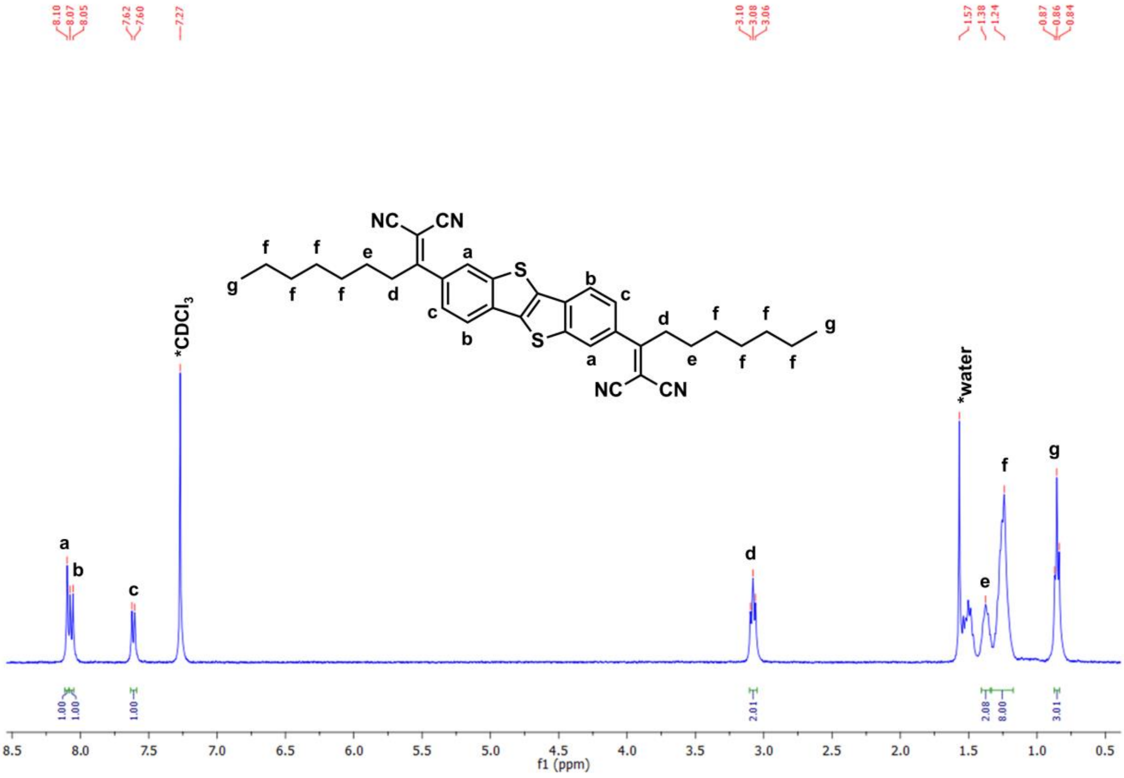

Figure 3.11 ^{1}H NMR spectra of **D(C$_7$CC(CN)$_2$)-BTBT** measured in $CDCl_3$.

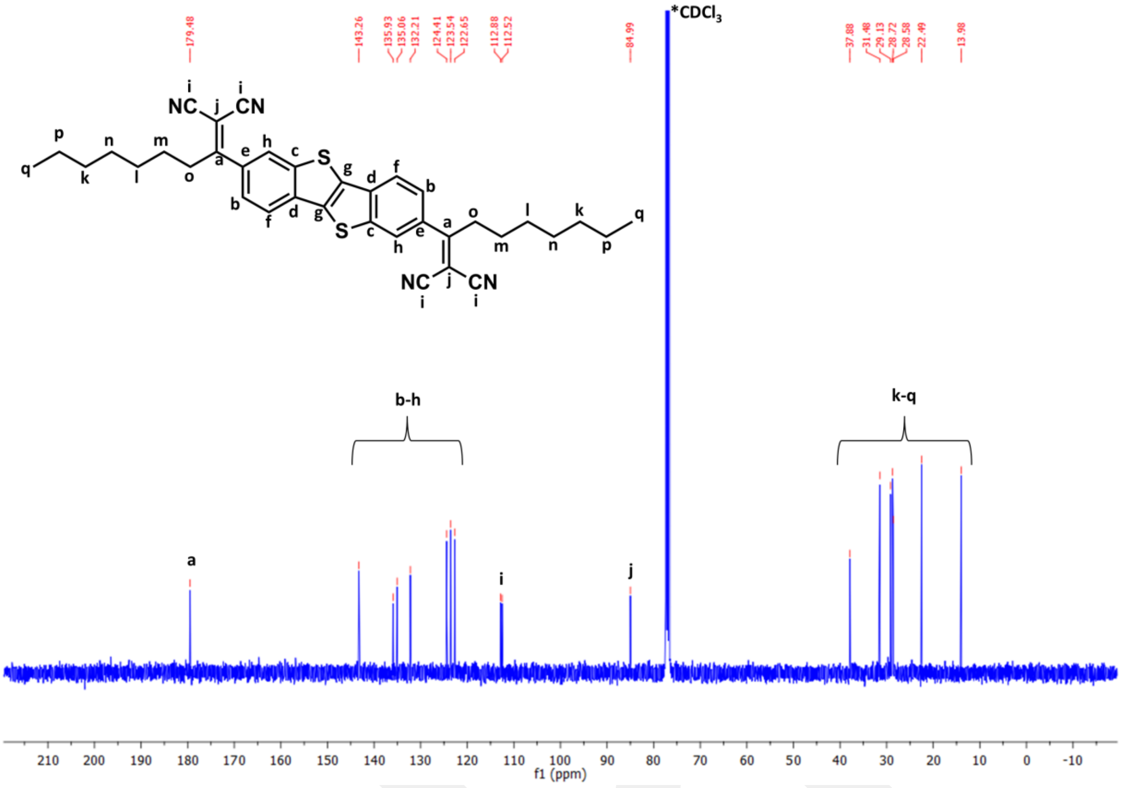

Figure 3.12 ^{13}C NMR spectra of **D(C$_7$CC(CN)$_2$)-BTBT** measured in CDCl$_3$.

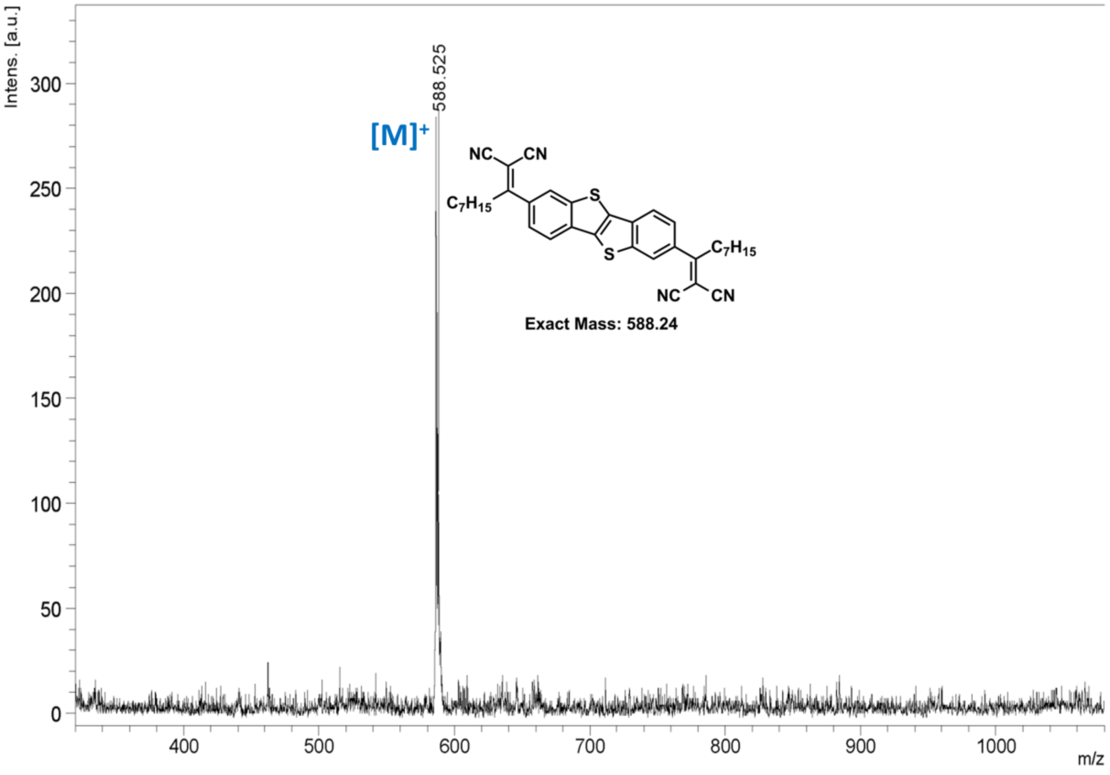

Figure 3.13 Positive ion and linear mode MALDI TOF-MS spectrum of **D(C$_7$CC(CN)$_2$)-BTBT**.

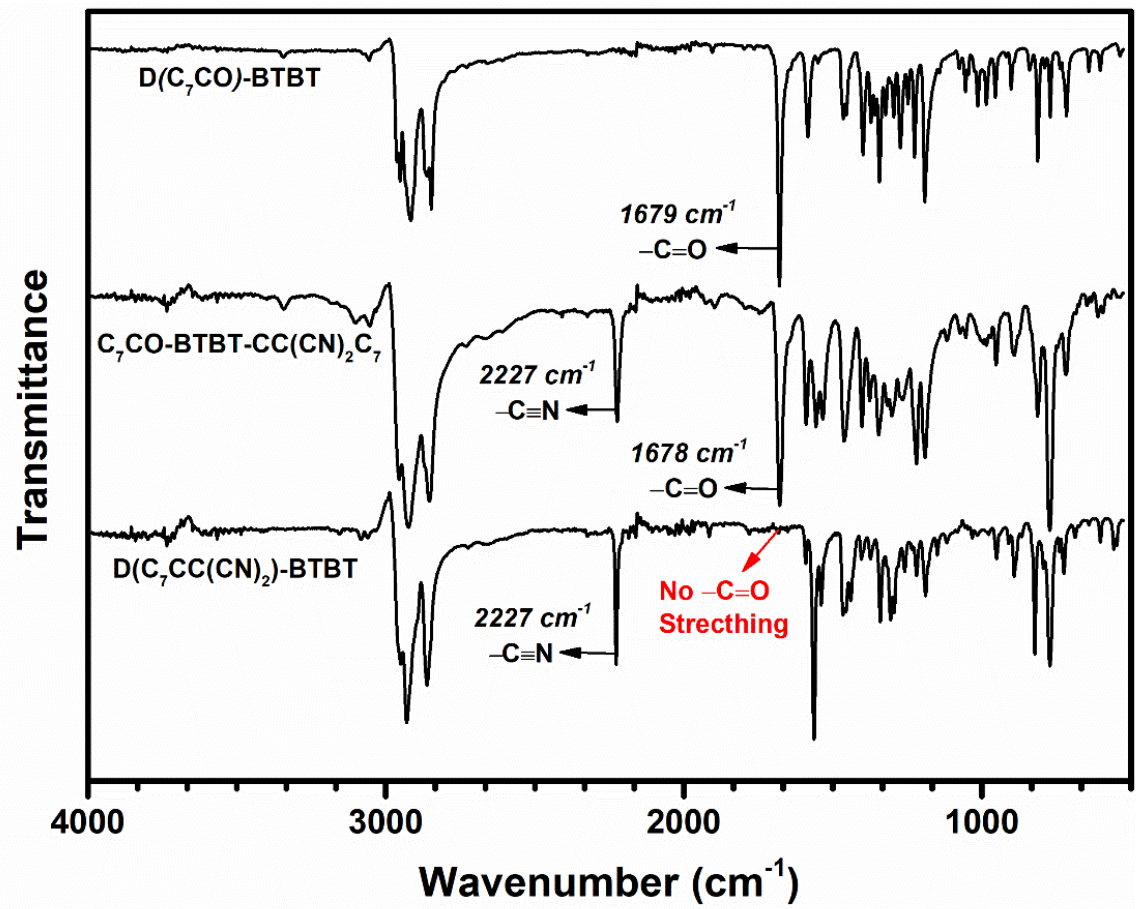

Figure 3.14 FT-IR spectra of **D(C_7CO)-BTBT**, **C_7CO-BTBT-CC(CN)$_2$$C_7$**, and **D($C_7$CC(CN)$_2$)-BTBT** showing C=O (1680 cm^{-1}) and C≡N (2227 cm^{-1}) stretching vibrational peak.

The chemical shifts of non-exchangeable aromatic protons on the outer phenyl rings revealed remarkable structural/electronic features of the current molecules. All aromatic proton chemical shifts for the new molecules are found to be downfield ($\Delta\delta_{Ar-H}$ ~ 0.4-0.8 ppm) with respect to those of the parent *p*-type **C_8-BTBT**. This is consistent with our original design rationales indicating reduced electron density (π-electron deficiency). However, the chemical shifts of the aromatic protons in the dicarbonyl derivative **D(C_7CO)-BTBT** are observed surprisingly further downfield as compared to those in the bis(dicyanovinylene) derivative **D(C_7CC(CN)$_2$)-BTBT** (δ_{Ar-H} = 7.6-8.1 ppm → 8.0-8.6 ppm) (Figure 3.15). Since dicyanovinylene is a much stronger electron withdrawing unit than carbonyl, one would expect an opposite trend in chemical shifts as typically observed with previously developed molecular semiconductors [203–205]. The rationales behind this interesting electron-deficiency behavior upon carbonyl → dicyanovinylene conversion are twofold. Firstly, dicyanovinylene units adopt out-of-plane twisted conformations with respect to the BTBT π-system as evidenced by the single-crystal structure, DFT calculations, and photoluminescence studies whereas carbonyls lie within the plane of the BTBT core providing much stronger negative resonance (-*R*)/inductive(-*I*) effects. Secondly, cyano groups (–CN) in twisted dicyanovinylene unit exert shielding effects on nearby aromatic protons "d and f". Similar shielding effect was evident also on aliphatic β-protons – but not on α-protons due to geometrical restraint – in **D(C_7CC(CN)$_2$)-BTBT** as compared to **D(C_7CO)-BTBT** ($\delta_{\text{aliphatic } \beta\text{-H}}$: ~1.8 ppm → ~1.3 ppm). On the other hand, when **D(C_7CO)-BTBT** is compared with our previously developed **D(Ph$_F$CO)-BTBT**, minimum differences are observed in ^{1}H NMR spectra, which reveals that the electronic effects of -C_7H_{15} *vs.* -Ph$_F$ substituents – although they have completely different electron deficiencies and π-densities – have a minimum impact on the BTBT π-system. This is also supported by theoretically and experimentally determined frontier molecular orbitals of these two molecules that showed very similar energetics/wave functions (*vide infra*). The protons on each outer phenyl ring in unsymmetrical **C_7CO-BTBT-C(CCN$_2$)C_7** are independently found to follow the specific chemical shift patterns of carbonyl and dicyanovinylene functionalized aromatic units (middle ^{1}H NMR spectrum in Figure 3.15). This reveals that there is minimal π-electronic interaction across the functionalized BTBT π-system avoiding the formation of a new set of chemical shifts. This is most likely the direct result of phene-like electronic structure of the BTBT π-system and it is further evidenced by electrochemical characterizations (*vide infra*). To the best of our knowledge, this is the first time that fully separated electronic behaviors are observed for outer phenylenes in a diacene-fused thienothiophene π-system.

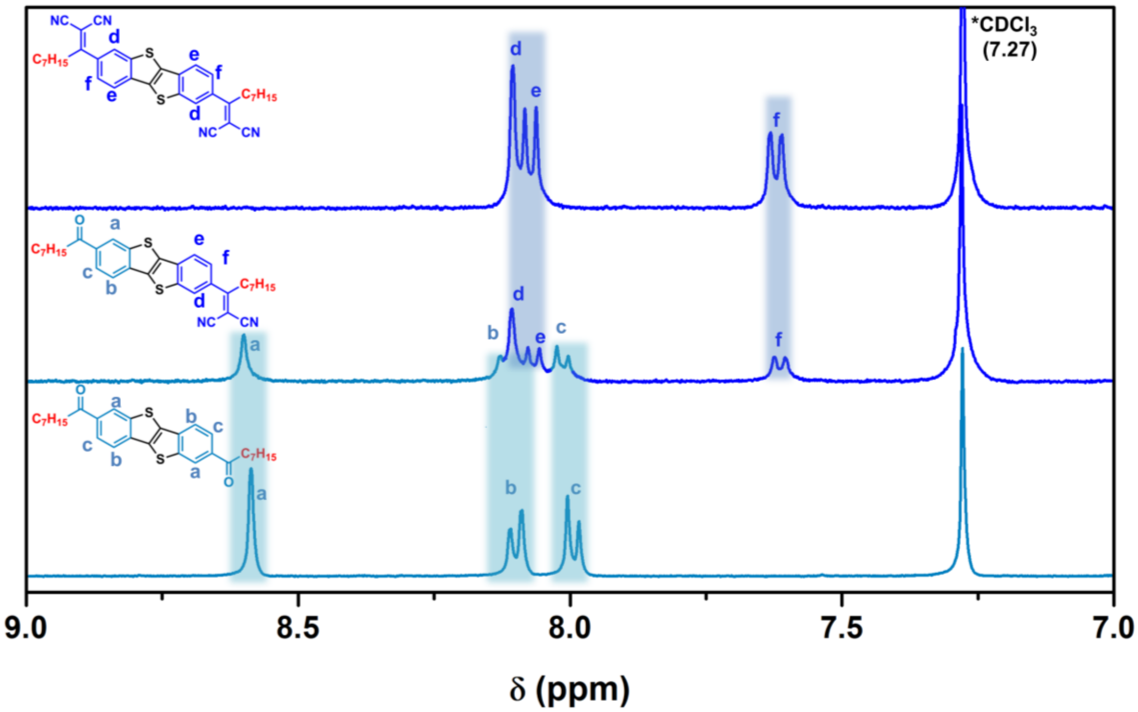

Figure 3.15 The ^{1}H NMR spectra of **$D(C_7CC(CN)_2)$-BTBT** (top), **C_7CO-BTBT-$CC(CN)_2C_7$** (middle), and **$D(C_7CO)$-BTBT** (bottom) in $CDCl_3$ showing the chemical shifts of non-exchangeable aromatic protons "a-f".

The thermal characterizations were carried out by thermogravimetric analysis (TGA) and differential scanning calorimetry (DSC) under a nitrogen atmosphere. As shown in Figure 3.16A, the current compounds exhibit high thermolysis onset temperatures (T_{onset}, corresponding to 5% weight loss) of > 300 °C, and dicyanovinylene functionalization was found to significantly increase the thermal stability (T_{onset} = 305 °C for **$D(C_7CO)$-BTBT** *vs.* T_{onset} = 375 °C for **$D(C_7CC(CN)_2)$-BTBT** and **C_7CO-BTBT-$CC(CN)_2C_7$**). **$D(C_7CO)$-BTBT**, **C_7CO-BTBT-$CC(CN)_2C_7$**, and **$D(C_7CC(CN)_2)$-BTBT** show the major endothermic thermal transitions at 266 °C (26.9 J/g), 103 °C (28.4 J/g), and 212 °C (75.7 J/g), respectively, with the corresponding exothermic peaks at 265 °C (25.7 J/g), 61 °C (30.9 J/g), and 108 °C (77.0 J/g), respectively. These transitions are attributed to the melting (T_{mp}'s: 265-266 °C, 102-103 °C, and 211-212 °C, respectively) and crystallization processes as observed by conventional melting point measurements. Interestingly, in contrast to the increased melting point (ΔT_{mp} > 100 °C) upon dicyanovinylene functionalization on formerly reported carbonyl-functionalized molecular semiconductors [204], the melting point of dicyanovinylene-functionalized **$D(C_7CC(CN)_2)$-BTBT** is found to be considerably lower (ΔT_{mp} = -54 °C) than that of carbonyl-functionalized **D(C$_7$CO)-BTBT**. Solid-state structural analysis (*vide infra*) reveals that although carbonyls in **D(C$_7$CO)-BTBT** are completely in the BTBT π-plane ($\theta_{torsion}$ = 4.17° for BTBT/C=O) leading to the formation of a "layer-by-layer" stacking motif with herringbone-like packing between "CO-BTBT-CO" units, dicyanovinylenes in **D(C$_7$CC(CN)$_2$)-BTBT** are significantly twisted ($\theta_{dihedral}$ = 47.55° for BTBT/C=C(CN)$_2$) with respect to BTBT hampering π-coplanarity. On the other hand, much lower melting point (ΔT_{mp} = -109/-163 °C) observed for unsymmetrically functionalized **C$_7$CO-BTBT-CC(CN)$_2$C$_7$**, which would be expected to stay between those of symmetrically functionalized derivatives, points to considerably weakened cohesive forces in the solid state. This indicates that in the design of low LUMO BTBT molecules symmetrical functionalization is key to realize effective solid-state intermolecular interactions (i.e., *cohesive energetics*) for both efficient charge transport and technologically relevant thermal behavior (i.e., T_{mp} > 150-200 °C for device processing). Note that, for the same reason, single-crystal of **C$_7$CO-BTBT-CC(CN)$_2$C$_7$** solid with sufficient diffraction quality could not be obtained while the other two molecules yield single-crystals (*vide infra*). The melting temperatures of symmetrically functionalized **D(C$_7$CO)-BTBT** and **D(C$_7$CC(CN)$_2$)-BTBT**) are much higher than that of **C$_8$-BTBT** (T_{mp} = 129-130 °C) [42] having the same alkyl chain length, which could be attributed to the presence of polar functional groups and slightly more extended π-framework leading to enhanced intermolecular cohesion. For **D(C$_7$CO)-BTBT** and **D(C$_7$CC(CN)$_2$)-BTBT**), additional thermal peaks at 169 (16.2 J/g)/219 °C (51.3 J/g) and 169 °C (4.6 J/g), respectively, were observed prior to the highest transition temperature to the isotropic liquid phase. These thermal transitions could be attributed to the formation of liquid-crystal (LC) phase(s) as previously observed for BTBT derivatives with similar alkyl chains [206], and it reflects the presence of flexible heptyl chains at the molecular ends. Note that our previously developed *n*-channel BTBT semiconductor **D(Ph$_F$CO)-BTBT** did not exhibit any thermal transition prior to melting as a result of having rigid perfluorophenyl (-Ph$_F$) rings.

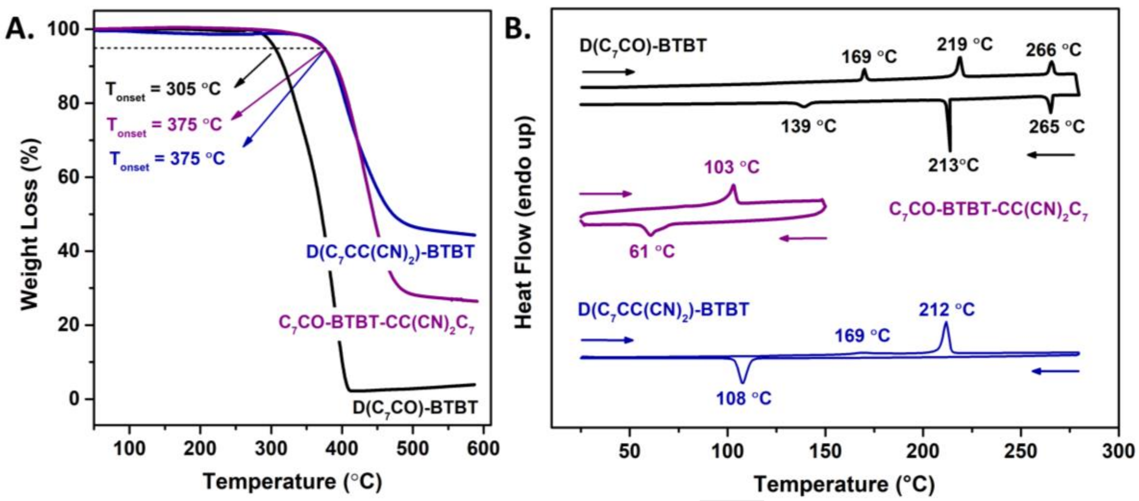

Figure 3.16 A. Thermogravimetric analysis (TGA) and B. Differential scanning calorimetry (DSC) measurement curves of **D(C$_7$CO)-BTBT**, **C$_7$CO-BTBT-C(CCN$_2$)C$_7$**, and **D(C$_7$CC(CN)$_2$)-BTBT** at a temperature ramp of 10 °C/min under N$_2$.

3.3.2 Single-Crystal Structure and Intermolecular Interactions

Single-crystals of **D(C$_7$CO)-BTBT** and **D(C$_7$CC(CN)$_2$)-BTBT** were grown as clear yellow needles by slow diffusion of methanol into chloroform solution and as red plates by slow evaporation of chloroform solution, respectively. The crystal structures determined by single-crystal X-ray diffraction are shown in Figure 3.17, and the crystallographic data is provided in Table 3.1. The crystal structures and packing properties of the current compounds are discussed in comparison to our recently developed high mobility *n*-type semiconductor **D(Ph$_F$CO)-BTBT** [192] in order to gain a complete insight into this new class of functionalized low LUMO BTBTs. Although the conjugated backbone of the BTBT unit in **D(C$_7$CO)-BTBT** and **D(C$_7$CC(CN)$_2$)-BTBT** is highly coplanar with no ring-to-ring twist angles ($\theta_{Ar\text{-}Ar}$ ~ 0°; Ar is phenyl or thienyl) as in **D(Ph$_F$CO)-BTBT** and other (un)substituted BTBT molecular π-skeletons [42,192,207], the three-dimensional configurations of the functional groups and the substituents are found to be quite different. While small torsion angle of 4.17° is measured between carbonyls and BTBT π-unit (C6-C1(*phenylene*)-C=O) in **D(C$_7$CO)-BTBT** leading to a substantially coplanar molecular backbone with extended π-conjugation, dicyanovinylenes in **D(C$_7$CC(CN)$_2$)-BTBT** are found to be twisted ($\theta_{torsion}$ = 44.92° for C6-C1(*phenylene*)-C11-C10(*dicyanovinylene*) and $\theta_{dihedral}$ = 47.55° for BTBT/C=C(CN)$_2$) out of the BTBT π-plane. These twist angles for dicyanovinylene units are slightly higher than the ~40° maximum value beyond which electronic communication weakens to support intramolecular π-conjugation [204,208]. Both of these solid-state conformations are consistent with the DFT-calculated molecular structures that exhibit ~0°/~44° torsion/dihedral angles between BTBT and carbonyl/dicyanovinylene functionalities (Figure 3.18). The solid-state molecular conformation of **D(C_7CO)-BTBT** matches well with that of our recently reported dicarbonyl BTBT molecule **D(Ph_FCO)-BTBT** ($\theta_{torsion}$ = 1.87° for C8-C7(*phenylene*)-C=O) [192] suggesting that 2,7-carbonyls, regardless of the substituents (heptyl *vs.* pentafluorophenyl), tend to stay within the BTBT π-plane yielding π-extended electron-deficient BTBTs. Although alkyl substitution, thus the presence of α-methylene, appears not to be detrimental to functional group coplanarity when used with carbonyl, it is found to cause twists with dicyanovinylene functionalities. The intramolecular twists in **D(C_7CC(CN)$_2$)-BTBT** most likely originate from an interplay of C6-H6(*phenylene*)/C8≡N1(*dicyanovinylene*) and C2-H2(*phenylene*)/C12-H12A/B(*α-methylene*) steric interactions. Theoretical modelling on a hypothetical unsubstituted dicyanovinylene-functionalized BTBT molecule **D(HCC(CN)$_2$)-BTBT** (Figure 3.19), although it would be a relatively difficult synthetic target with low solubility, reveals that dicyanovinylene groups could be effectively within the BTBT π-plane upon removal of the alkyl substituents. This provides a valuable insight into future design of π-extended low LUMO DAcTTs.

D(C_7CO)-BTBT crystallizes in the monoclinic space group C2/c showing alternating layers of conductive π-segments (CO-BTBT-CO) and insulating alkyl substituents (-C_7H_{15}) along the crystallographic *a*-axis (Figure 3.17A). The heptyl chains at the molecular termini display fully extended all-trans conformation, and they are perfectly aligned along the molecular long-axis allowing for the formation of pure hydrocarbon layers along the *a*-axis. **D(C_7CO)-BTBT** molecules display slipped stacked packing arrangement along the *c*-axis using short intermolecular S···S contacts (a = 3.43 Å < r_{vdw} (S) + r_{vdw} (S) = 3.60 Å) [209]. Along the *b,c*-axes, herringbone-like molecular packing was identified with major intermolecular interactions of C-H(phenyl)···π(phenyl) (b, c, e = 3.57, 2.78, 3.27 Å), S···π(thienyl) (d = 3.22 Å), and C=O(δ^-)···C(δ^+)=O (f = 3.52 Å). When crystal properties for **D(C_7CO)-BTBT** and **D(Ph_FCO)-BTBT** [192] (Figure 3.17C) are compared, although packing motifs and intermolecular interactions are found to be very similar, specific herringbone-like arrangements are found to show a clear distinction with regard to molecular offsets along the long-axis directions. While **D(Ph_FCO)-BTBT** shows a molecular offset of half aromatic unit resulting in strong three dimensional BTBT···carbonyl intermolecular interactions, **D(C$_7$CO)-BTBT** molecules are found to adopt a perfectly matched (i.e., no molecular offset) herringbone packing without BTBT···carbonyl interactions. **D(C$_7$CC(CN)$_2$)-BTBT** crystallizes in the monoclinic space group $P2_1/c$. Although the heptyl chains at the molecular termini are not in their fully extended all-trans conformation, and they are found to align towards the top and bottom of the BTBT π-system, **D(C$_7$CC(CN)$_2$)-BTBT** crystals show alternating layers of conductive π-segments ($(CN)_2C{=}C$-BTBT-$C{=}C(CN)_2$) and insulating alkyl substituents ($-C_7H_{15}$) along the crystallographic *a*-axis (Figure 3.17B). However, herringbone packing along the *b*,*c*-axes becomes more complicated due to its twisted molecular structure. Each **D(C$_7$CC(CN)$_2$)-BTBT** molecule is found to interact with four other molecules in three dimensions (only two are shown in Figure 3.17B to avoid visual crowding) to form intermolecular N≡C···π(phenyl) (a = 3.55 Å), C=C(dicyanovinylene)···π(thienyl) (b, c = 3.67, 3.89 Å), and C-H(phenyl)···π(thienyl/phenyl) (d, e = 3.27, 3.22 Å) contacts. Different than the carbonyl-functionalized BTBT derivatives, **D(C$_7$CC(CN)$_2$)-BTBT** molecules did not exhibit any S···S contacts, instead short intermolecular N···H contacts (2.52 Å < r_{vdw} (N) + r_{vdw} (H) = 2.75 Å) are identified [209]. Similar to our previously reported *n*-type **D(Ph$_F$CO)-BTBT**, strong BTBT···dicyanovinylene intermolecular interactions are identified in **D(C$_7$CC(CN)$_2$)-BTBT** solid-state. The electron withdrawing carbonyl and dicyanovinylene functionalities in **D(Ph$_F$CO)-BTBT** and **D(C$_7$CC(CN)$_2$)-BTBT** electronically interacts with the BTBT π-system contributing to the formation of three dimensional electron transporting π-electronic structures that enables *n*-channel transport efficiently in the solid-state (*vide infra*). In contrast, carbonyls in **D(C$_7$CO)-BTBT** do not show the same type of π-interaction, and BTBT units interact only with themselves as typically seen in previously reported *p*-type DAcTTs [42,61] resulting in hole transport (*vide infra*) despite its low LUMO. For both molecules, the observed herringbone-like packing and short intermolecular interactions involving π-conjugated units is expected to enable two-dimensional charge transport when crystalline domains are properly oriented in the corresponding semiconductor thin films.

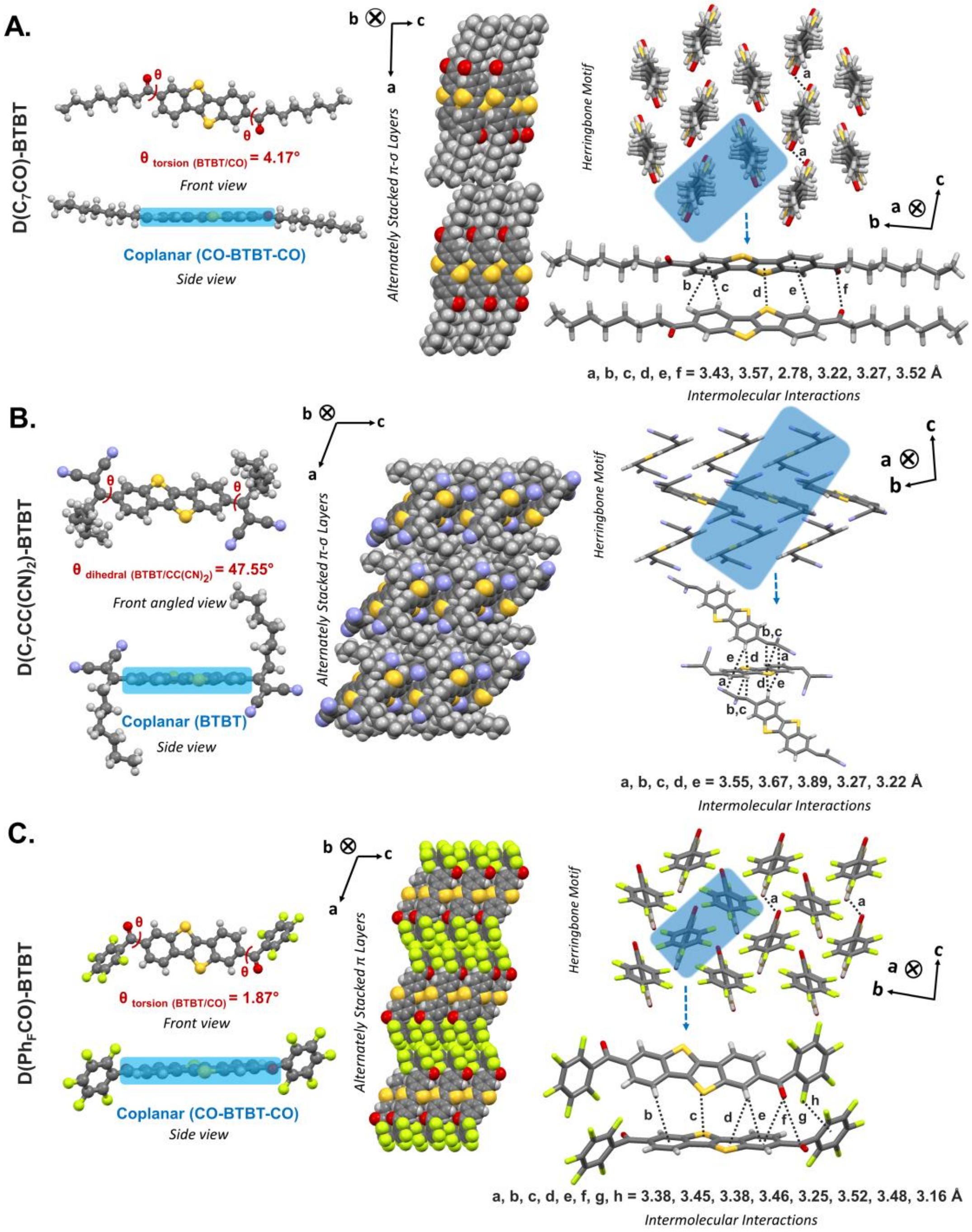

Figure 3.17 Ball and stick drawings of the molecular structures showing the corresponding torsion/dihedral angles (between the BTBT π-core and functional groups) and π-backbone coplanarity, perspective views of the molecular arrangements and packings along the crystallographic *a*,*c*-axes and *b*,*c*-axes showing the alternately stacked layers and the herringbone motifs/packing, and the intermolecular interactions for **D(C$_7$CO)-BTBT** (A) (*a* = S···S; *b*, *c*, *e* = C-H(phenyl)···π(phenyl); *d* = S···π(thienyl); *f* = C=O(δ$^-$)···C(δ$^+$)=O), **D(C$_7$CC(CN)$_2$)-BTBT** (B) (a = N≡C···π(phenyl); b, c = C=C(dicyanovinylene)···π(thienyl); d, e = C-H(phenyl)···π(thienyl/phenyl)), and our previously reported *n*-type semiconductor **D(Ph$_F$CO)-BTBT** [192] (C) (*a* = S···S; *b, e* = C-H(phenyl)···π(phenyl); *c* = S···π(thienyl); *d* = C-H(phenyl)···π(thienyl); *f* = C=O···π(phenyl); *g* = C=O(δ$^-$)···C(δ$^+$)=O; *h* = F···π(pentafluorophenyl)). Heptyl chains are omitted for clarity in the herringbone motif/packing in panel B.

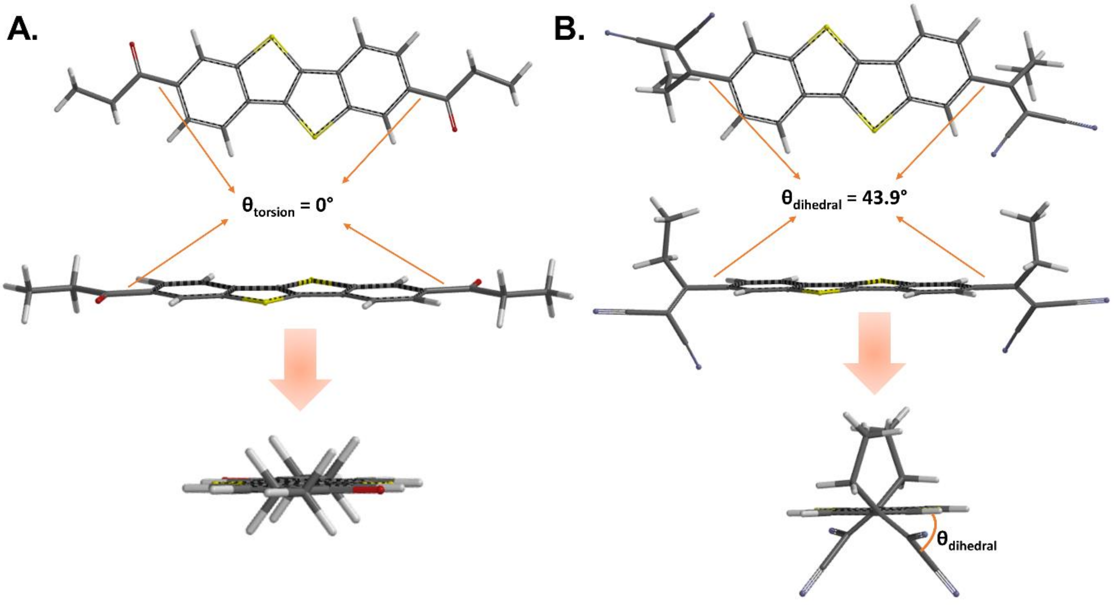

Figure 3.18 Computationally optimized (DFT/B3LYP/6-31G**) molecular structures for **D(C$_7$CO)-BTBT** (A) and **D(C$_7$CC(CN)$_2$)-BTBT** (B) showing the torsion and dihedral angles ($\theta_{torsion}$ and $\theta_{dihedral}$) between BTBT π-system and carbonyl/dicyanovinylene functional groups.

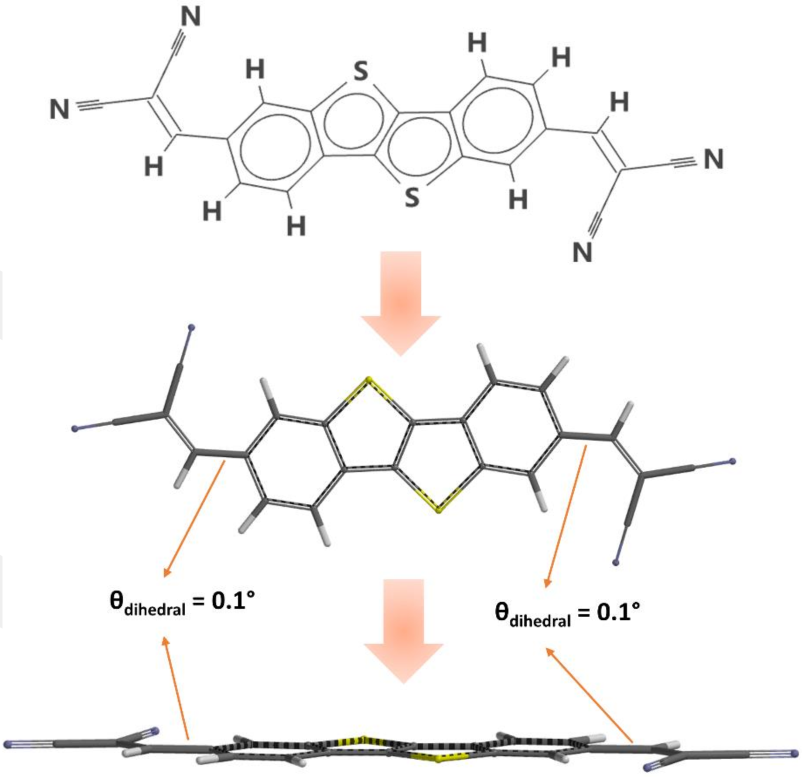

Figure 3.19 Computationally optimized (DFT/B3LYP/6-31G**) molecular structure of a hypothetical dicyanovinylene-functionalized BTBT compound, **D(HCC(CN)$_2$)-BTBT**, showing the dihedral angle ($\theta_{dihedral}$) between BTBT π-system and dicyanovinylene functional groups.

Table 3.1 Crystal data and refinement parameters for **D(C_7CO)-BTBT** and **D(C_7CC(CN)$_2$)-BTBT**.

	D(C_7CO)-BTBT	**D(C_7CC(CN)$_2$)-BTBT**
CCDC	1946322	1946323
Empirical Formula	$C_{30}H_{36}O_2S_2$	$C_{36}H_{36}N_4S_2$
Formula weight (g. mol^{-1})	492.71	588.81
Temperature (K)	296.15	296.15
Wavelength (Å)	MoK$_\alpha$ (λ = 0.71073)	MoK$_\alpha$ (λ = 0.71073)
Crystal system	Monoclinic	Monoclinic
Space group	C2/c	P2$_1$/c
a **(Å)**	60.991(12)	17.703(10)
b **(Å)**	7.6857(18)	7.556(3)
c **(Å)**	5.7799(13)	12.385(5)
α(°)	90	90
β(°)	92.122(16)	106.60(3)
γ(°)	90	90
Crystal size (mm)	0.12 × 0.04 × 0.03	0.25 × 0.22 × 0.08
V **(Å^3)**	2707.5(10)	1587.6(13)
Z	4	2
ρ_{calcd} (g. cm^{-3})	1.209	1.232
μ (mm^{-1})	0.221	0.199
***F*(000)**	1056	624.0
2Θ range for data collection (°)	4.01 to 49.98	5.902 to 50.026
h*/*k*/*l	$-72 \leq h \leq 71, -9 \leq k \leq 8, -6 \leq l \leq 6$	$-12 \leq h \leq 21, -5 \leq k \leq 8, -14 \leq l \leq 13$
Reflections collected	9352	6702
Independent reflections	2264 [R_{int} = 0.1058, R_{sigma} = 0.1037]	2755 [R_{int} = 0.0913, R_{sigma} = 0.1648]
Data/restraints/parameters	2264/12/156	0.75/-0.55
Goodness-of-fit on F^2 (S)	1.743	0.964
Final *R* indices [$I > 2\sigma(I)$]	R_1 = 0.1840, wR_2 = 0.4296	R_1 = 0.0805, wR_2 = 0.1969
R **indices (all data)**	R_1 = 0.2107, wR_2 = 0.4418	R_1 = 0.1855, wR_2 = 0.2513
Largest diff. peak and hole (e.Å^{-3})	1.14/-0.89	0.75/-0.55

X-ray data collection and structure refinement: Data were obtained with Bruker APEX II QUAZAR three-circle diffractometer. Indexing was performed using APEX2 [APEX2, version 2014.11-0, Bruker (2014), Bruker AXS Inc., Madison, WI]. Data integration and reduction were carried out with SAINT [SAINT, version 8.34A, Bruker (2013), Bruker AXS Inc., Madison, WI]. Absorption correction was performed by multi-scan method implemented in SADABS [SADABS, version2014/5, Bruker (2014), Bruker AXS Inc., Madison, WI]. The structure was solved using SHELXT [151] and then refined by full-matrix least-squares refinements on F^2 using the SHELXL [152] in Olex2 Software Package [210]. For D(C_7CO)-BTBT single crystals obtained was very thin size (0.12 mm × 0.04 mm × 0.03 mm), even with high exposure times (second/frame) is used, they were obviously very weakly diffracting crystals, and it could not be obtained the intensity of higher angle diffraction signals (d = 0.77 Å, 2Θ =

55°) in the diffraction pattern, which lowered the completeness of higher angle data (completeness of D(C_7CO)-BTBT is only 0.945). In our study, in order to improve the crystal quality of D(C_7CO)-BTBT, we made a large number of crystallization experiments and the most ideal single crystal was reported in this study. Aromatic C-bound H atoms were positioned geometrically and refined using a riding mode. Crystallographic data and refinement details of the data collection for D(C_7CO)-BTBT and D(C_7CC(CN)$_2$)-BTBT are given in Table S1. Crystal structure validations and geometrical calculations were performed using Platon software [153]. Mercury software [154] was used for visualization of the cif files. Additional crystallographic data with CCDC reference numbers (1946322 for D(C_7CO)-BTBT and 1946323 for D(C_7CC(CN)$_2$)-BTBT) have been deposited within the Cambridge Crystallographic Data Center via www.ccdc.cam.ac.uk/deposit.

3.3.3 Photophysical and Electrochemical Properties

In order to reveal the effects of carbonyl *vs.* dicyanovinylene functionalizations and alkyl *vs.* pentafluorophenyl substitutions on the optoelectronic characteristics of the BTBT π-system, the current molecules are studied by UV-Vis absorption and photoluminescence spectroscopies, and cyclic voltammetry in dichloromethane solutions (1.0×10^{-5} M) and as thin-films. As shown in Figure 3.20A, typical vibronic features (~1400-1600/3000-3100 cm^{-1} for aromatic C=C/C-H bond stretches) of a fused heteroacene π-system is observed for all compounds with bathochromically shifted low-energy absorption maxima (λ_{max} = 380 nm for **D(C_7CO)-BTBT**, λ_{max} = 389 nm for **C_7CO-BTBT-C(CCN$_2$)C_7**, and λ_{max} = 400 nm for **D(C_7CC(CN)$_2$)-BTBT**) and onsets (λ_{onset} = 400 nm for **D(C_7CO)-BTBT**, λ_{onset} = 427 nm for **C_7CO-BTBT-C(CCN$_2$)C_7**, and λ_{onset} = 438 nm for **D(C_7CC(CN)$_2$)-BTBT**) with respect to the non-functionalized alkyl-substituted derivative **C_8-BTBT** (λ_{max} = 330 nm/λ_{onset} = 340 nm, Figure S15). The optical band gaps are estimated to be 3.10 eV for **D(C_7CO)-BTBT**, 2.90 eV for **C_7CO-BTBT-C(CCN$_2$)C_7**, and 2.83 eV for **D(C_7CC(CN)$_2$)-BTBT**, which are significantly smaller than that of **C_8-BTBT** (E_g^{opt} = 3.65 eV) reflecting the electronic (negative resonance (-*R*)/inductive(-*I*)) and π-extension effects of carbonyl/dicyanovinylene functionalities. The conversion of the carbonyl functionality into dicyanovinylene gradually decreases the optical band gap of the BTBT π-system (λ_{onset} = 400 nm → 427 nm → 438 nm).

As shown in Figure 3.20, the electrochemical characterization of the current BTBT molecules show clear (quasi)reversible first reduction peaks (*vs.* Ag/AgCl) at -0.89 V for **D(C_7CO)-BTBT**, -0.95 V for **C_7CO-BTBT-C(CCN$_2$)C_7**, and -1.10 V for **D(C_7CC(CN)$_2$)-BTBT**.

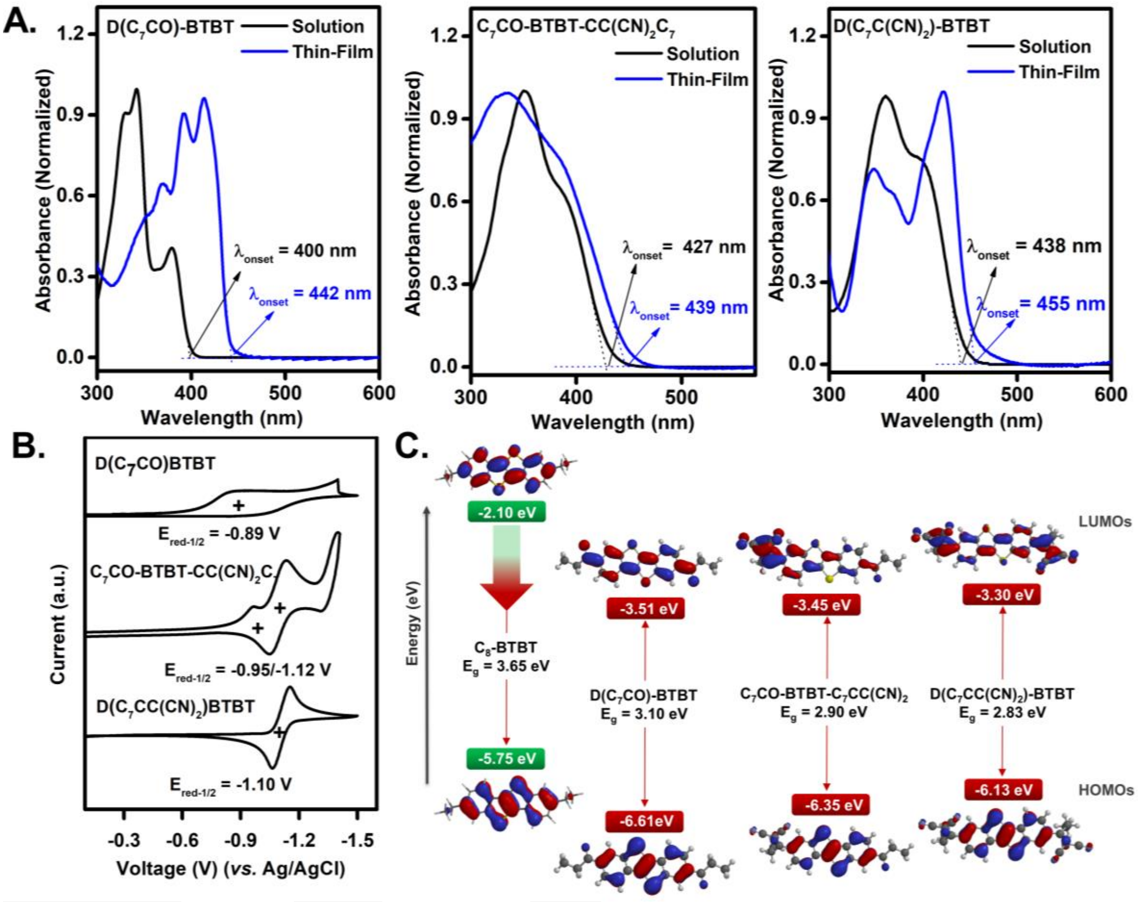

Figure 3.20 A. Optical absorption spectra (in dichloromethane and as spin-coated thin films), B. Cyclic voltammograms *vs.* Ag/AgCl (3.0 M NaCl) (in 0.1 M $Bu_4N^+PF_6^-$ dichloromethane, scan rate = 50 mV/s), and C. Experimentally determined frontier molecular orbital energies along with topographical orbital representations (DFT/B3LYP/6-31G**) for **D(C_7CO)-BTBT**, **C_7CO-BTBT-C(CCN$_2$)C_7**, and **D(C_7CC(CN)$_2$)-BTBT**.

As shown in Figure 3.21, upon changing the solvent media from low to medium polarity (hexane (*f* (ε,n) = 0.001) → dichloromethane (*f* (ε,n) = 0.217) low-energy absorption maxima and onsets for all three molecules show bathochromic shifts suggesting that the Franck-Condon excited state ($S_{1(FC)(\pi-\pi^*)}$) has a higher dipole than the ground state (S_0). This could be attributed to the presence of electron withdrawing end functionalities adjacent to a relatively π-electron rich BTBT. Note that the most notable red-shift (~30 nm) was observed with **D(C_7CC(CN)$_2$)-BTBT** having two strongly electron withdrawing dicyanovinylene end units. Surprisingly, when solvent polarity is further increased (N,N'-dimethylformamide (DMF) (*f* (ε,n) = 0.276) and dimethyl sulfoxide (DMSO) (*f* (ε,n) = 0.263)), the molecules having dicyanovinylene unit(s) (i.e., **C$_7$CO-BTBT-C(CCN$_2$)C$_7$** and **D(C$_7$CC(CN)$_2$)-BTBT**) show completely opposite spectral shifts to smaller wavelengths ($\Delta\lambda_{max}$ ~ -20-60 nm).

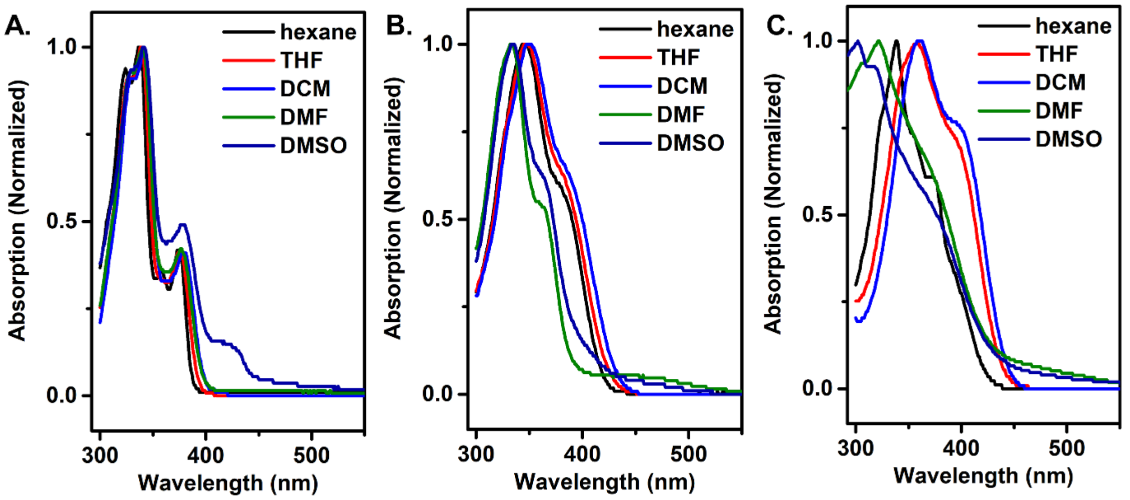

Figure 3.21 Optical absorption spectra of **D(C$_7$CO)-BTBT** (A), **C$_7$CO-BTBT-CC(CN)$_2$C$_7$** (B), and **D(C$_7$CC(CN)$_2$)-BTBT** (C) in hexane, tetrahydrofuran (THF), dichloromethane (DCM), N,N'-dimethylformamide (DMF), and dimethyl sulfoxide (DMSO).

The absorption maximum for **D(C$_7$CC(CN)$_2$)-BTBT** in DMSO is very similar to those of non-functionalized BTBT compounds [42,61]. This unexpected hypsochromic shift in highly polar medium seem to originate from reduced π-delocalization on the molecular backbone, most likely through intramolecular BTBT-dicyanovinylene rotations. In contrast, coplanar dicarbonyl compound **D(C$_7$CO)-BTBT** did not exhibit any spectral shift upon going to highly polar medium; instead, n-π* transition becomes apparent at ~ 424 nm. A similar n-π* transition was also observed for **C$_7$CO-BTBT-C(CCN$_2$)C$_7$** in DMF at ~ 460 nm. When going from solution to solid-state, although unsymmetrical **C$_7$CO-BTBT-C(CCN$_2$)C$_7$** shows a slightly broadened spectrum with a small bathochromic shift ($\Delta\lambda_{onset}$ ~ 10 nm), **D(C$_7$CO)-BTBT** and **D(C$_7$CC(CN)$_2$)-BTBT** exhibit obvious J-aggregate like spectral changes with large bathochromic shifts ($\Delta\lambda_{max}$ ~ 60-70 nm/$\Delta\lambda_{onset}$ ~ 20-45 nm). This indicates significantly enhanced intermolecular interactions (*cohesive energetics*) in the solid-state of these two molecules as compared to **C_7CO-BTBT-C(CCN_2)C_7**, which is consistent with the measured melting temperatures (*vide supra*).

Considering that alkyl substituted non-functionalized **C_8-BTBT** shows only an oxidation peak at 1.35 V (*vs.* Ag/AgCl) (Figure 3.22-inset), the electron withdrawing carbonyl and dicyanovinylene functionalizations at BTBT's 2,7-positions clearly increase π-electron deficiency and enable reduction process. The unsymmetrically functionalized **D(C_7CC(CN)$_2$)-BTBT** shows two consecutive reductions at -0.95 V/-1.12 V, and each reduction alone follows the electrochemical behavior of carbonyl- and dicyanovinylene-functionalized BTBT π-units. The LUMO energy levels of the current molecules are estimated to be −3.51 eV, -3.45 eV, and −3.30 eV, respectively, which are in the range of those (-2.9 eV – -4.3 eV) previously reported for *n*-channel organic semiconductors [194,195]. These LUMOs are greatly stabilized (ΔE_{LUMO} = -1.2 eV–1.4 eV) with respect to that of **C_8-BTBT** (E_{LUMO} = -2.10 eV) pointing out strong negative resonance (-*R*)/inductive(-*I*) effects of the carbonyl/dicyanovinylene units at 2,7-positions. Also, highly delocalized LUMOs calculated over the entire molecular π-backbones could be advantageous for electron transport. As compared with our recently developed **D(Ph_FCO)-BTBT** having pentafluorophenyl units, the slightly higher (~0.13 eV) LUMO estimated for **D(C_7CO)-BTBT** is ascribed to the electron-donating ability of the heptyl chains. Interestingly, the LUMO level was found to increase upon carbonyl-to-dicyanovinylene conversions in the order of **D(C_7CO)-BTBT → C_7CO-BTBT-C(CCN_2)C_7 → D(C_7CC(CN)$_2$)-BTBT**. Considering that dicyanovinylene has a much stronger electron withdrawing ability typically leading to LUMO stabilization of ~0.5-1.0 eV with respect to its carbonyl-functionalized counterpart [102,176,204], this rather surprising frontier molecular orbital energy trend implies deteriorated π-conjugation between dicyanovinylene and BTBT units in solution. The solid-state molecular structure of **D(C_7CC(CN)$_2$)-BTBT** confirms the formation of large intramolecular twists upon dicyanovinylene functionalization ($\theta_{dihedral}$ = 47.55° for BTBT/C=C(CN)$_2$), which is very likely to increase in solution going beyond the limiting dihedral angle (>> 40°) to support efficient intramolecular π-overlap [208,211].

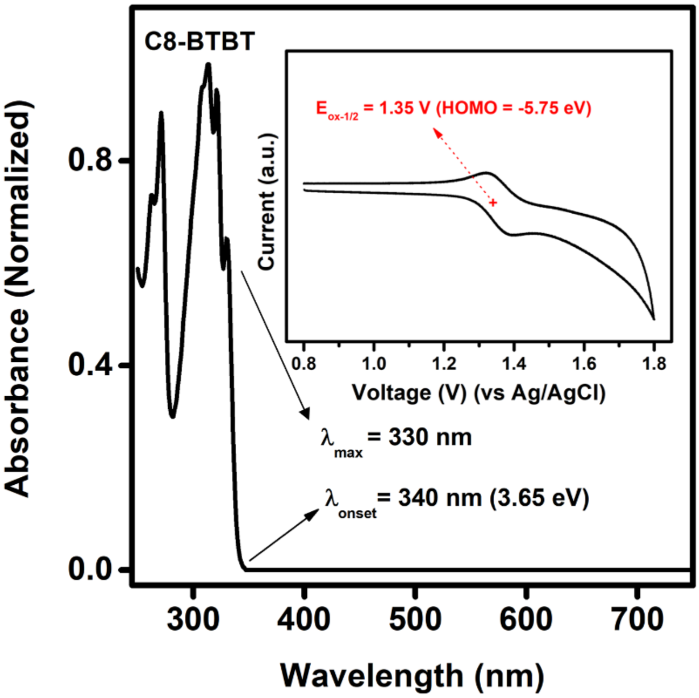

Figure 3.22 Optical absorption spectrum and cyclic voltammogram (0.1 M $Bu_4N^+PF_6^-$, scan rate = 50 mV/s) of **C_8-BTBT** in dichloromethane solutions.

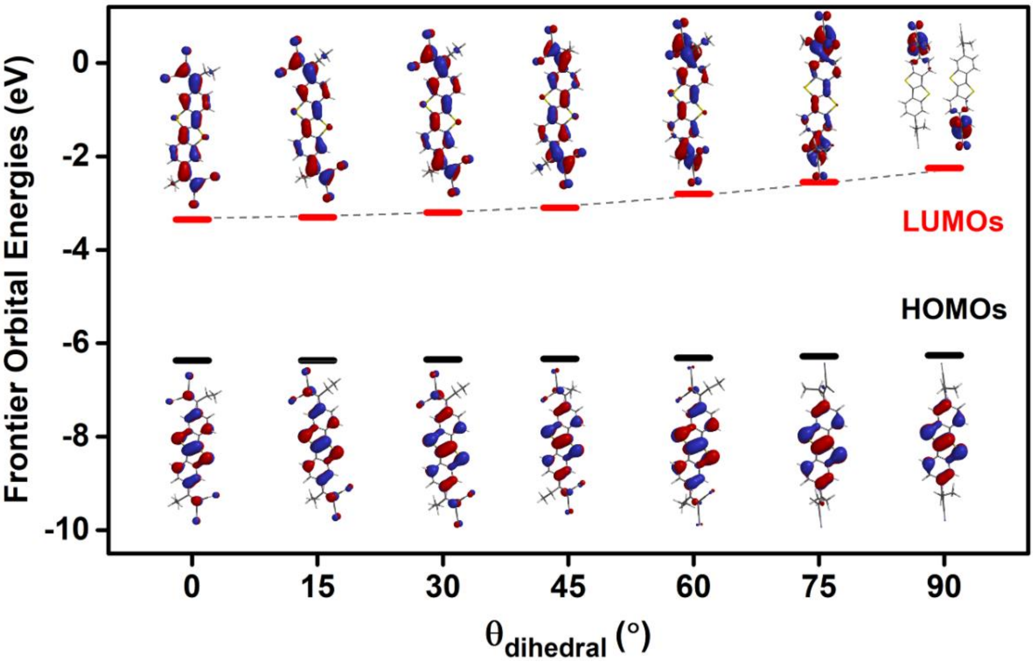

Figure 3.23 Theoretical (DFT/B3LYP/6-31G**) frontier orbital energies along with topographical representations for conformations of **$D(C_7CC(CN)_2)$-BTBT** with varied dihedral angles ($\theta_{dihedral}$) between the BTBT π-system and dicyanovinylene units.

The theoretical calculations on **D(C_7CC(CN)$_2$)-BTBT** conformations with varied dihedral angles (Figure 3.23) indeed show that the degree of LUMO destabilization becomes much faster at higher dihedral angles of > 45° (ΔE_{LUMO} ~ 0.85 eV for $\theta_{dihedral}$ = 45° → 90° *vs.* ΔE_{LUMO} ~ 0.3 eV for $\theta_{dihedral}$ = 0° → 45°), and the corresponding wave functions eventually get localized on the dicyanovinylenes.

The steady-state fluorescence and time-resolved photoluminescence decays (λ_{exc} = 375 nm and 200 ps pulse width) of **D(C_7CO)-BTBT** and **D(C_7CC(CN)$_2$)-BTBT** were studied in order to better understand the optoelectronic effects of in-plane carbonyls *vs.* twisted dicyanovinylenes. As shown in Figure 3.24A, for the same concentrations (1.0×10^{-5} M) in dichloromethane, **D(C_7CC(CN)$_2$)-BTBT** showed a much weaker fluorescence peak with decreased (10×) quantum yield (Φ_{PL} = 0.1 → 0.01) and increased Stokes shift ($\Delta\lambda_{Stokes\ shift}$ ~ 60 nm) in comparison to **D(C_7CO)-BTBT**. Similarly, time-resolved photoluminescence decay measurements indicated a faster decay profile for **D(C_7CC(CN)$_2$)-BTBT** with the lifetime of 0.19 ns (τ_1 = 0.40 ns for **D(C_7CO)-BTBT**). Therefore, it is apparent that highly twisted dicyanovinylene units adjacent to the BTBT π-system induce significant non-radiative relaxations of the excited state (*fluorescence quenching*) in solution as compared to in-plane carbonyls. To better understand the origin of the non-radiative decay, PL properties for **D(C_7CC(CN)$_2$)-BTBT** were measured in a solvent system with similar polarities but different viscosities (i.e., methanol (0.54 cP) and ethylene glycol (16.1 cP)) [212]. As shown in Figure 3.24B, the photoluminescence intensity was found to be enhanced (~4×) and the corresponding PL decay profile became slower (τ_1 = 0.17 ns → 0.39 ns) in the higher viscosity medium, which implies that BTBT/dicyanovinylene rotations are more constrained in the higher viscosity medium to partially deactivate non-radiative decay [213]. Similarly, going into solid-state, the PL quantum yield of **D(C_7CC(CN)$_2$)-BTBT** was found to dramatically increase (Φ_{PL} = 0.01 → 0.11). Based on these results and considering that solvent polarity-dependent PL (Figure 3.25) does not reveal a charge-transfer excited state formation, it is clear that highly twisted dicyanovinylenes in **D(C_7CC(CN)$_2$)-BTBT** activates non-radiative decay channels in solution through intramolecular rotations (*free-rotor effect*). Similar free-rotor effects have been observed in previously reported aryl-dicyanovinylene molecules [214,215].

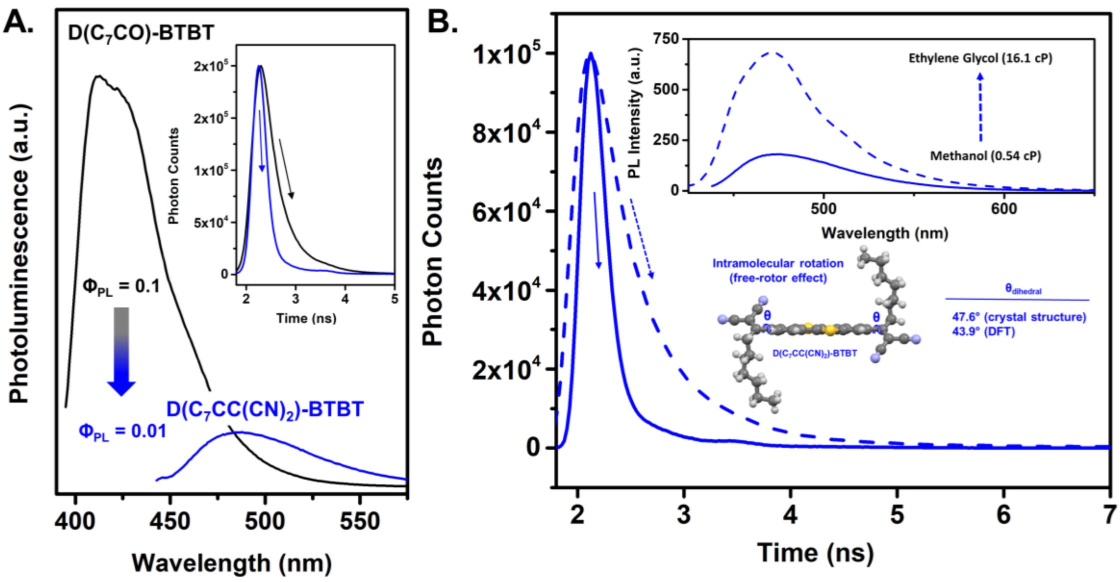

Figure 3.24 A. Photoluminescence spectra of **D(C$_7$CO)-BTBT** (λ_{exc} = 385 nm) and **D(C$_7$CC(CN)$_2$)-BTBT** (λ_{exc} = 405 nm) in dichloromethane (1.0×10^{-5} M). The inset shows the transient photoluminescence decay profiles (λ_{exc} = 375 nm and 200 ps pulse width) measured at 410 nm and 483 nm for **D(C$_7$CO)-BTBT** and **D(C$_7$CC(CN)$_2$)-BTBT**, respectively, in dichloromethane (10^{-5} M) under nitrogen atmosphere. B. The transient photoluminescence decay profiles measured at 483 nm for **D(C$_7$CC(CN)$_2$)-BTBT** (λ_{exc} = 375 nm and 200 ps pulse width) in methanol (solid) and ethylene glycol (dashed) solutions (10^{-5} M) under nitrogen atmosphere. Inset shows the solvent viscosity-dependent (methanol (0.54 cP) and ethylene glycol (16.1 cP)) photoluminescence spectra for **D(C$_7$CC(CN)$_2$)-BTBT**

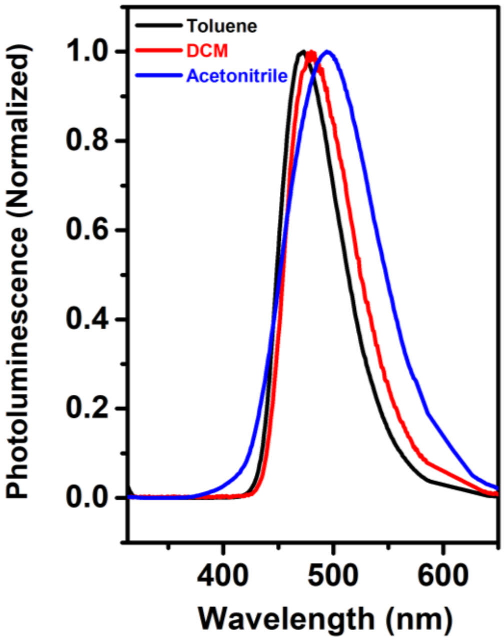

Figure 3.25 The solvent polarity-dependent (toluene (f (ε,n) = 0.014) → dichloromethane (f (ε,n) = 0.217) → acetonitrile (f (ε,n) = 0.305)) photoluminescence spectra of **D(C$_7$CC(CN)$_2$)-BTBT** (λ_{exc} = 405 nm) in solution (1.0×10^{-5} M).

BTBT-dicyanovinylene compounds, especially when combined with their optoelectronic and semiconducting properties, could constitute a novel rotor family for various molecular sensing applications. Here, it's noteworthy that high frequency vibrations (*loose-bolt effect*) could also be somewhat contributing to the observed non-radiative decay in the dicyanovinylene units [216].

3.3.4 Thin-Film Microstructure/Morphology and Field-Effect Transistor Characterization

The charge transport characteristics of **D(C_7CO)-BTBT** and **D(C_7CC(CN)$_2$)-BTBT** were studied in top-contact/bottom-gate (TC/BG) OFETs by thermally evaporating semiconductor thin films (30 nm) onto temperature controlled (25 and 70 °C) n^{++}-Si/SiO_2(200 nm)/HMDS substrates. Source and drain electrodes (Au (50 nm) for *p*-channel and LiF (1nm)/Au (50 nm) for *n*-channel) were defined via thermal evaporation. Prior to the charge-transport measurements, the morphology and microstructure of the BTBT thin films were studied by atomic force microscopy (AFM) and grazing-incidence X-ray diffraction (GIXD). As shown in Figures 3.26A and 3.26B, the thin film surface morphologies of both molecules show well-interconnected crystalline domains, and clear transitions from relatively small (~150-200 nm) granular shaped grains to micron-sized (~0.6-2.0 μm) 2D plate-like grains of terraced islands along the substrate plane were observed upon increasing the deposition temperature. The out-of-plane θ–2θ GIXD analysis shows the major diffraction peaks at $2\theta = 5.80°/8.68°$ for **D(C_7CO)-BTBT** and at $2\theta = 5.21°$ for **D(C_7CC(CN)$_2$)-BTBT** (Figure 3.26C), which correlates perfectly with the single-crystal lattice planes of (400)/(600) and (100), respectively, based on the corresponding powder pattern simulations (Figure 3.27). Using the single crystal structural data, the Bravais-Friedel-Donnay-Harker (BFDH) theoretical crystal morphologies were predicted for both semiconductors, which confirm the growth of 2D plate-like crystalline domains on the substrate plane and along the (400)/(600) (for **D(C_7CO)-BTBT**) and (100) (for **D(C_7CC(CN)$_2$)-BTBT**) lattice planes (Figure 3.26D). This indicates a great agreement between single-crystal structures and thin film microstructures/morphologies, and it suggests that the in-plane packing motifs of the observed 2D plate-like crystalline grains in thin film phase have herringbone-like intermolecular interactions similar to the corresponding single-crystal structures. Interestingly, **D(C_7CO)-BTBT** thin film deposited at room temperature shows a clear high-angle diffraction peak at 2θ = 23.09° that corresponds to (020) lattice planes formed with entirely face-on oriented molecules (Figure 3.28). This facile control between face-on and edge-on orientations with deposition temperature is a unique feature to study charge transport in various optoelectronic devices. The face-on molecular arrangement could be quite useful for the fabrication of functional semiconductor layers in which vertical charge transport is required along with low LUMO and wide optical band gap (e.g., passivation layer on metal oxide thin-film electronics, photodiodes, and organic photovoltaics) [107,217–222].

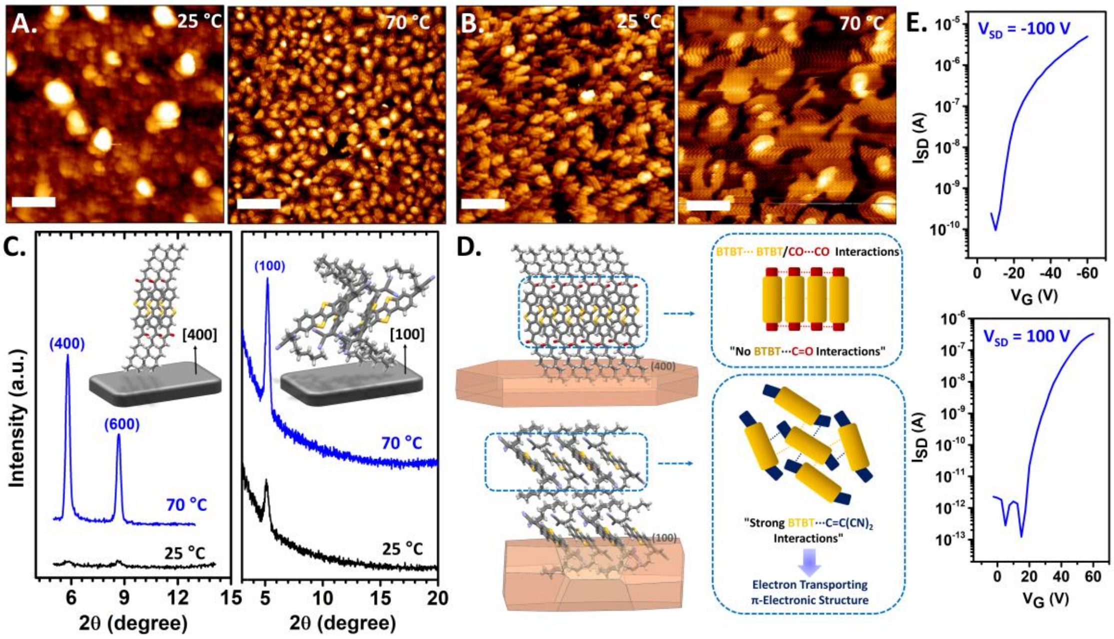

Figure 3.26 Tapping mode atomic force microscopy (AFM) topographic images and grazing incidence X-ray diffraction (GIXRD) scans for **D(C_7CO)-BTBT** (A and C-left) and **D(C_7CC(CN)$_2$)-BTBT** (B and C-right) thin films deposited on n^{++}-Si/SiO$_2$(200 nm)/HMDS at 25 °C and 70 °C, and the molecular arrangements in the out-of-plane directions. The scale bar denotes 1 μm. D. The Bravais-Friedel-Donnay-Harker (BFDH) theoretical crystal morphologies, the views of the packing arrangements in the 2D plate-like crystalline grains, and the corresponding lattice planes. E. Transfer (V_{SD} = -100 V for **D(C_7CO)-BTBT** and V_{SD} = 100 V for **D(C_7CC(CN)$_2$)-BTBT**) characteristics for the n^{++}-Si/SiO$_2$(200 nm)/HMDS/**D(C_7CO)-BTBT**(30 nm)/Au(50 nm) (top) and n^{++}-Si/SiO$_2$(200 nm)/HMDS/**D(C_7CC(CN)$_2$)-BTBT**(30 nm)/LiF(1 nm)/Au(50 nm) (bottom) OFET devices.

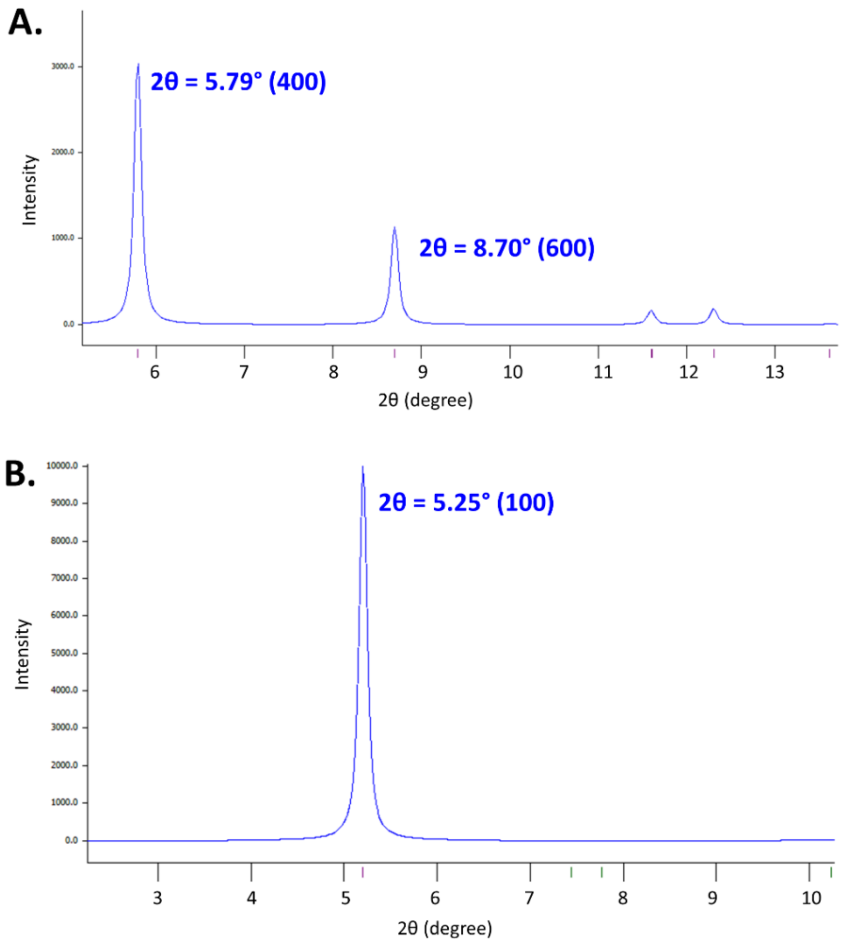

Figure 3.27 Simulated XRD powder patterns based on the single-crystal structures for **D(C$_7$CO)-BTBT** (A) and **D(C$_7$CC(CN)$_2$)-BTBT** (B) indicating the selected matching diffraction peaks and lattice planes at 2θ = 5.79(400)/8.70˚(600) and at 2θ = 5.25˚(100), respectively.

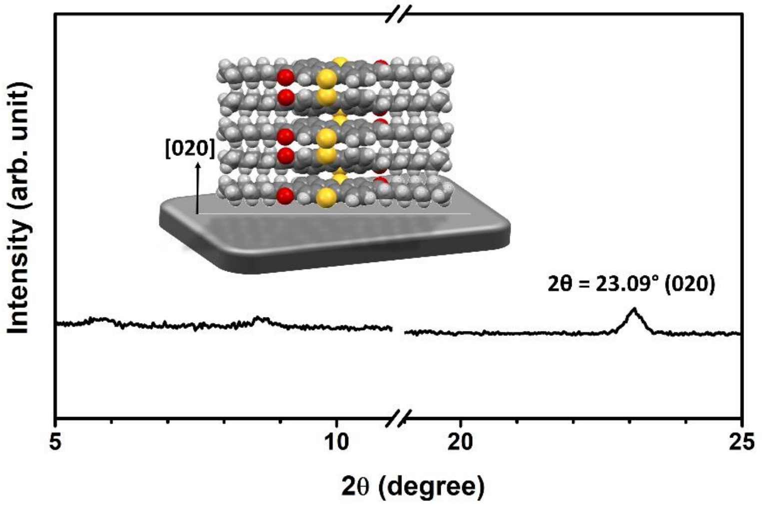

Figure 3.28 Grazing incidence X-ray diffraction (GIXD) of **D(C$_7$CO)-BTBT** (30 nm) thin film deposited on n^{++}-Si/SiO$_2$(200 nm)/HMDS substrate at a deposition temperature of 25 °C and the corresponding (020) lattice plane/molecular arrangement.

The electrical characteristics of the OFETs were measured under both positive and negative gate biases to reveal the majority charge carriers and semiconducting performances. Here, we note that we were not able to measure the charge transport characteristics of these molecules from their spin-coated/drop-casted thin films due to undesirable film formation. As shown in Figure 3.26E, **D(C_7CO)-BTBT** and **D(C_7CC(CN)$_2$)-BTBT** exhibit *p*-type and *n*-type semiconducting behaviors with appreciable hole and electron mobilities of 0.03 $cm^2/V\cdot s$ ($I_{on}/I_{off} = 10^4$-10^5 and V_{th} = -10 V) and 0.004 $cm^2/V\cdot s$ ($I_{on}/I_{off} = 10^6$-10^7 and V_{th} = +27 V), respectively. Following our initial report on high electron mobility **D(Ph_FCO)-BTBT**, **D(C_7CC(CN)$_2$)-BTBT** now becomes a novel and rare *n*-type DAcTT semiconductor, which contributes to the development of electron transporting DAcTT library by not only adding new functionalities (i.e., introducing solubility and using new π-extended functional groups) but also elucidating “structure-molecular properties-semiconductivity” relationships. In this new family of functionalized low LUMO BTBTs, from a molecular design perspective, the observed trends in the majority charge carriers (*p*-type for **D(C_7CO)-BTBT** *vs.* *n*-type for **D(C_7CC(CN)$_2$)-BTBT/D(Ph_FCO)-BTBT**) could not be explained simply by frontier molecular orbital energies/topographies as typically approached in the field of organic optoelectronics [174,223,224]. The anomalies are, (i) for the carbonyl-functionalized BTBTs, although they share the common coplanar “CO-BTBT-CO” π-backbone leading to similar LUMO energies (~ -3.5 eV)/topographies (delocalized on the CO-BTBT-CO π-system), **D(C_7CO)-BTBT** behaves as *p*-type while **D(Ph_FCO)-BTBT** is an *n*-type semiconductor, (ii) for the alkyl substituted BTBTs, despite its lower LUMO energy (E_{LUMO} = -3.51 eV), **D(C_7CO)-BTBT** behaves as *p*-type while **D(C_7CC(CN)$_2$)-BTBT** is an *n*-type semiconductor, and (iii) considering that substituents are not part of the LUMOs in functionalized low-LUMO BTBTs, how do they contribute to the observed majority charge carrier inversion? These findings strongly suggest that low LUMO energies and π-delocalized LUMO topographies should be evaluated in combination with additional structural/optoelectronic parameters. Our detailed analysis has indeed revealed that the observed semiconducting behaviors reflect an interplay of two additional factors, (i) functional group contribution in the π-electronic structure along the charge transport direction and (ii) relative intramolecular reorganization energies for hole- *vs.* electron transport. Firstly, although all three BTBT semiconductors exhibit herringbone-like packing along the charge transport direction, a subtle packing difference, which is not obvious at first glance, is identified in the formation of π-electronic structures between *n*- and *p*-type semiconductors. In the herringbone motifs of *n*-type **D(C_7CC(CN)$_2$)-BTBT** and **D(Ph$_F$CO)-BTBT**, electron deficient carbonyl/dicyanovinylene functional groups continuously interact with the BTBT π-sytem (BTBT···carbonyl ~ 3.5 Å/BTBT···dicyanovinylene ~ 3.5-3.8 Å) in a three dimensional alternating fashion to form a π-electronic structure that is favorable for electron transport (Figure 3.26D-bottom). However, in *p*-type **D(C_7CO)-BTBT**, similar type of BTBT···carbonyl interactions was not present, and the BTBT π-units are found to interact only with themselves (Figure 3.26D-top), as in non-functionalized *p*-type thienoacenes, that enables a hole transporting π-electronic structure. Secondly, the relative intramolecular reorganization energies for hole *vs.* electron transport are found to be greatly affected with the substituents. As a key charge transport parameter, λ defines the intramolecular structural reorganization needed to accommodate a certain charge carrier type, and a smaller λ_e is typically desired for efficient electron transport [225]. Herein, we compare *p*-type **D(C_7CO)-BTBT** with *n*-type **D(Ph$_F$CO)-BTBT** because these molecules have the common charge transporting CO-BTBT-CO π-segment with similar π-electron deficiency, and any difference in λ's should be the direct result of substituent modification (alkyl *vs.* pentafluorophenyl). While the reorganization energy associated with the electron transfer in *n*-type **D(Ph$_F$CO)-BTBT** is smaller than that with the hole transfer (λ_e = 317 meV < λ_h = 360 meV), λ_e is calculated to be much larger than λ_h (355 meV >> 252 meV) in *p*-type **D(C_7CO)-BTBT**. These results are in great agreement with the observed majority charge carrier types. The effect of substituents on λ's has been demonstrated for different π-systems in former theoretical and experimental studies [89,226,227]. On the other hand, the larger λ_e calculated for the new *n*-type **D(C_7CC(CN)$_2$)-BTBT** as compared to **D(Ph$_F$CO)-BTBT** (λ_e = 509 meV >> 317 meV) might reflect the enhanced dihedral angle of the dicyanovinylenes to partly explain the observed lower electron mobility [228]. In our OFET studies, semiconductor thin films with proper surface coverage could not be achieved with unsymmetrical **C_7CO-BTBT-C(CCN$_2$)C_7**, which is probably due to unfavorably weak cohesive forces present in the solid-state of this molecule as discussed earlier.

3.4 Conclusions

In summary, a series of systematically functionalized [1]benzothieno[3,2-b][1]benzothiophene (BTBT)-based small molecules, **D(C_7CO)-BTBT**, **C_7CO-BTBT-CC(CN)$_2$C$_7$**, and **D(C_7CC(CN)$_2$)-BTBT**, has been developed, which, when combined with our previously reported first *n*-type BTBT semiconductor **D(Ph$_F$CO)-BTBT**, gives the first molecular library of low LUMO DAcTTs. The molecules are designed in "S-F-BTBT-F-S (F/S: functional group/substituent)" molecular architecture, in which BTBT π-core is systematically functionalized with carbonyl and dicyanovinylene functional groups, and heptyl chains are used as substituents to enable solubility for convenient synthesis/purification. The structural, physicochemical, photophysical/electrochemical, and OFET charge transport characteristics have been studied in detail. The new molecules exhibit large optical band gaps (2.8-3.1 eV) and highly stabilized ($-\Delta E_{LUMO}$ = 1.2 eV-1.4 eV)/π-delocalized lowest unoccupied molecular orbitals (LUMOs) as compared to *p*-type DAcTTs. Symmetric functionalization was found to be important to enable strong intermolecular interactions in solid-state. Single-crystal structural/packing analysis have revealed that all symmetrically functionalized low LUMO BTBT molecules show alternately stacked layers of "F-BTBT-F" and "S" with strong herringbone-like interactions (2.8-3.6 Å distances) between π-cores. The carbonyl functional groups adopt coplanar conformations with the BTBT π-backbone; however, dicyanovinylenes are found to be twisted (47.5°). This conformational change at the molecular level is found to have unusual effects on π-electron deficiencies (high-field ^{1}H NMR peaks and shielding effects, $-\Delta\delta_{Ar\text{-}H}$ = 0.4-0.5 ppm), thermal properties (lowered melting point, $-\Delta T_{mp}$ = 55 °C), frontier molecular orbital energetics (increased LUMOs, ΔE_{LUMO} = 0.2 eV), photophysical properties (PL quenching and free-rotor effect), and π-electronic structures (3D electron transporting BTBT$\cdots$dicyanovinylene network and increased λ_e). Herein, dicyanovinylenes are demonstrated for the first time to yield electron transport in DAcTTs despite their twisted conformations. **D(C_7CC(CN)$_2$)-BTBT** becomes a rare example of *n*-type DAcTT with an appreciable μ_e of 0.004 cm^2/V·s (I_{on}/I_{off} = 10^6-10^7). Although low energy delocalized LUMO, mainly governed by functional groups, is clearly required for electron transport, our results suggest that substituents are the key substructures to control intermolecular interactions in the charge transporting direction and the relative electron *vs.* hole intramolecular reorganization energies. With the findings presented herein, we take the first step of establishing important and unique relationships between structure, various molecular properties, and semiconductivity in this new class of functionalized low LUMO BTBTs, and hope to stimulate further research on *n*-type DAcTTs in wide-ranging aspects of organic optoelectronics.

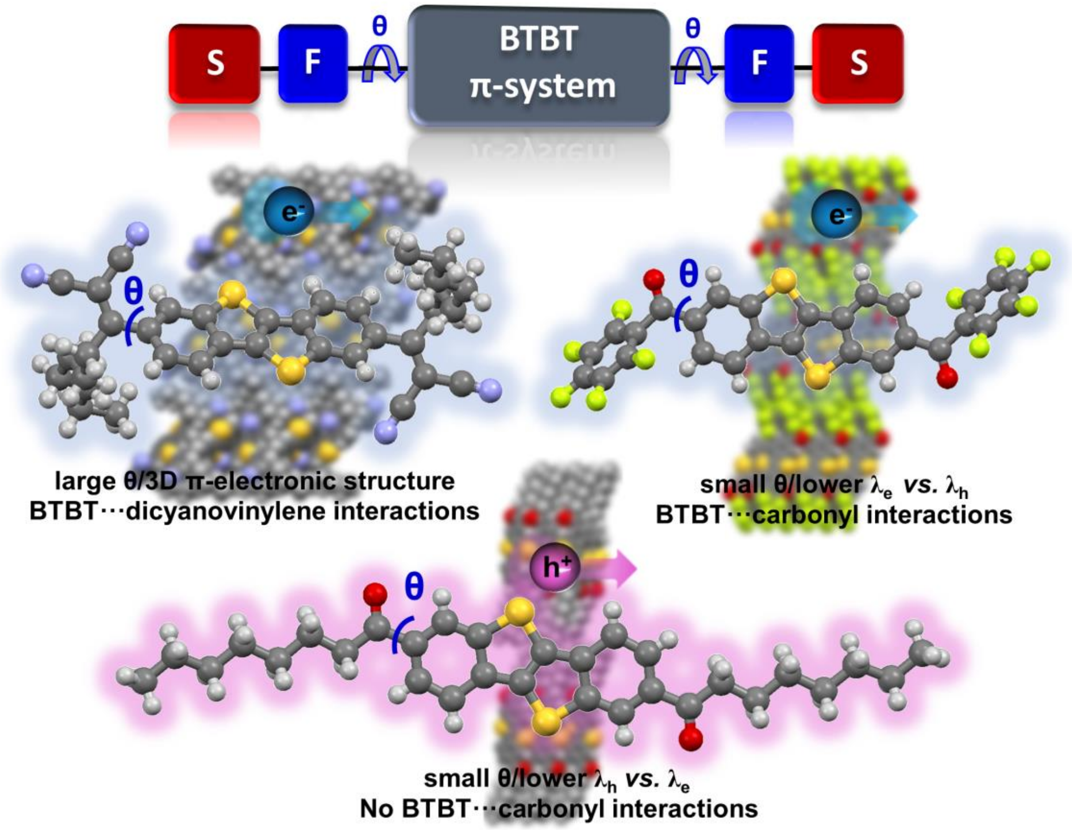

Figure 3.29 A unique molecular library of functionalized low LUMO BTBT semiconductors was developed and studied in detail to reveal key design principles for electron transport in DAcTTs.

Chapter 4

Conclusions and Future Prospects

4.1 Conclusions

The first example of a BTBT-based *n*-type molecular semiconductor, **D(Ph$_F$CO)-BTBT**, has been designed, synthesized and characterized. The new semiconductor was synthesized in a two-step transition metal-free process without using chromatographic purification. The significant lowering of the LUMO level for **D(Ph$_F$CO)-BTBT**, versus other BTBTs, is attributed to extended π-conjugation along the molecular backbone including the BTBT and *in-plane* carbonyl units, and, to a less extent, the inductive effect of the *out-of-plane* pentafluorophenyl groups. Polycrystalline **D(Ph$_F$CO)-BTBT** thin-films exhibit large grains (~2-5 μm sizes) with "layer-by-layer" packing motifs on the substrate surface forming an *in-plane* herringbone packing with short intermolecular distances (3.25-3.46 Å), which doubtless favors two-dimensional (2D) source-to-drain (S→D) charge transport. TC/BG-OFET devices comprising a thermally evaporated **D(Ph$_F$CO)-BTBT** film on the hydrophobic HMDS-treated SiO_2 substrate and LiF/Au contacts exhibit high electron mobilities of ~0.6 cm^2/Vs and I_{on}/I_{off}'s over 10^7. The observed high electron mobility for **D(Ph$_F$CO)-BTBT** undoubtedly reflects a combination of highly π-delocalized/energetically stabilized LUMO, large film grain sizes with high crystallinity, and excellent texture with preferential *edge-on* molecular orientation and *in-plane* herringbone packing facilitating strong intermolecular π-orbital overlaps, as supported by DFT computations.

In addition, a series of systematically functionalized [1]benzothieno[3,2-b][1]benzothiophene (BTBT)-based small molecules, **D(C$_7$CO)-BTBT**, **C$_7$CO-BTBT-CC(CN)$_2$C$_7$**, and **D(C$_7$CC(CN)$_2$)-BTBT**, has been developed, which, when combined with our previously reported first *n*-type BTBT semiconductor **D(Ph$_F$CO)-BTBT**, gives the first molecular library of low LUMO DAcTTs. The molecules are designed in "S-F-BTBT-F-S (F/S: functional group/substituent)" molecular architecture, in which BTBT π-core is systematically functionalized with carbonyl and dicyanovinylene functional groups, and heptyl chains are used as substituents to enable solubility for convenient synthesis/purification. The new molecules exhibit large optical band gaps (2.8-3.1 eV) and highly stabilized ($-\Delta E_{LUMO}$ = 1.2 eV-1.4 eV)/π-delocalized lowest unoccupied molecular orbitals (LUMOs) as compared to *p*-type DAcTTs. Symmetric functionalization was found to be important to enable strong intermolecular interactions in solid-state. Single-crystal structural/packing analysis have revealed that all symmetrically functionalized low LUMO BTBT molecules show alternately stacked layers of "F-BTBT-F" and "S" with strong herringbone-like interactions (2.8-3.6 Å distances) between π-cores. The carbonyl functional groups adopt coplanar conformations with the BTBT π-backbone; however, dicyanovinylenes are found to be twisted (47.5°). This conformational change at the molecular level is found to have unusual effects on π-electron deficiencies (high-field ^{1}H NMR peaks and shielding effects, $-\Delta\delta_{Ar\text{-}H}$ = 0.4-0.5 ppm), thermal properties (lowered melting point, $-\Delta T_{mp}$ = 55 °C), frontier molecular orbital energetics (increased LUMOs, ΔE_{LUMO} = 0.2 eV), photophysical properties (PL quenching and free-rotor effect), and π-electronic structures (3D electron transporting BTBT···dicyanovinylene network and increased λ_e). Herein, dicyanovinylenes are demonstrated for the first time to yield electron transport in DAcTTs despite their twisted conformations. **D(C$_7$CC(CN)$_2$)-BTBT** becomes a rare example of *n*-type DAcTT with an appreciable μ_e of 0.004 cm^2/V·s (I_{on}/I_{off} = 10^6-10^7). Although low energy delocalized LUMO, mainly governed by functional groups, is clearly required for electron transport, our results suggest that substituents are the key substructures to control intermolecular interactions in the charge transporting direction and the relative electron *vs.* hole intramolecular reorganization energies.

4.2 Societal Impact and Contribution to Global Sustainability

Since the 1950s scientific research and technological studies in micro- and opto-electronics fields have been leading progressed swiftly. Therefore, semiconductor based devices such as thin-film/field-effect transistors (FETs/TFTs), photovoltaics (PVs) and light emitting diodes (LEDs) have becomed a crucial part of our lives as functional components in many technology applications. Basic motivation of this field using carbon-based organic semiconductors instead of inorganic-based conventional semiconductors (i.e. Si, Ge and GaAs) to produce cost-effective, flexible (compatibility with plastic substrate) and light weight (opto) electronic devices. Organic semiconductors have a much richer synthesis chemistry than conventional elemental semiconductors and they do not require high cost micro-fabrication techniques. To this end, numerous π-conjugated small molecular/polymeric semiconductors have been developed up to now. Among them, [1]benzothieno[3,2-b][1]benzothiophene (BTBT)-π-framework, a member of DAcTT family, has stepped forward because of its superior structural properties including optical transparency (wide band gap <3.5 eV), air-stable hole transport ability (deeper HOMO energy level < 5.5 eV) and high charge carrier mobility (favorable solid state packing and intermolecular interactions). But, all BTBT derivatives developed until today was *p*-type semiconductors and realized with only di-(mono-) alkyl/aryl substitution. There was no information about low LUMO BTBT-based small molecular semiconductors in the literature. So, we designed, synthesized and characterized the first BTBT-based *n*-type molecular semiconductor, **D(Ph$_F$CO)-BTBT**. In addition, a series of systematically functionalized BTBT-based small molecules, **D(C$_7$CO)-BTBT**, **C$_7$CO-BTBT-CC(CN)$_2$C$_7$**, and **D(C$_7$CC(CN)$_2$)-BTBT** have been developed. When combined with **D(Ph$_F$CO)-BTBT**, all these semiconductors gives the first molecular library of low LUMO DAcTTs. More importantly, we developed a new molecular synthetic approach because these molecules have been realized with electron witdrawing groups rather than substitution.

This increased structural diversity of organic semiconductors in the field of optoelectronics and improved corresponding device performances is not only related with the above-mentioned device technologies, but also important for a wide range applications from biological sensor devices to spectroscopic applications.

4.3 Future Prospects

Our results demonstrate that *n*-type semiconductors based on BTBT cores are possible which, based on the very large intrinsic charge transport capabilities of BTBT (> 10 $cm^2/V{\cdot}s$) and its good optical transparency, may open new pathways to realize unconventional devices for next generation high performance organic (opto)electronics.

With the findings presented herein, we take the first step of establishing important and unique relationships between structure, various molecular properties, and semiconductivity in this new class of functionalized low LUMO BTBTs, and hope to stimulate further research on *n*-type DAcTTs in wide-ranging aspects of organic optoelectronics.

BIBLIOGRAPHY

[1] The Nobel Prize in Chemistry 2000, https://www.nobelprize.org/prizes/chemistry/2000/summary/ (18 Feb 2021)

[2] T. W. Kelley, P. F. Baude, C. Gerlach, D. E. Ender, D. Muyres, M. A. Haase, D. E. Vogel, S. D. Theiss, "Recent Progress in Organic Electronics: Materials, Devices, and Processes," Chemistry of Materials, 16, 4413–4422 (2004).

[3] H. Klauk, "*Organic Electronics*," Wiley (2006).

[4] A. Tsumura, H. Koezuka, T. Ando, "Macromolecular electronic device: Field-effect transistor with a polythiophene thin film," Applied Physics Letters, 49, 1210–1212 (1986).

[5] H. Klauk, "Organic thin-film transistors," Chemical Society Reviews, 39, 2643–2666 (2010).

[6] Y. Galagan, I. G. de Vries, A. P. Langen, R. Andriessen, W. J. H. Verhees, S. C. Veenstra, J. M. Kroon, "Technology development for roll-to-roll production of organic photovoltaics," Chemical Engineering and Processing: Process Intensification, 50, 454–461 (2011).

[7] R. Farchioni, G. Grosso, "*Organic Electronic Materials: Conjugated Polymers and Low Molecular Weight Organic Solids*," Springer (2001).

[8] L. S. Miller, J. B. Mullin, "*Electronic Materials: From Silicon to Organics*," Plenum Press (1991).

[9] H. S. Nalwa, "*Handbook of Organic Conductive Molecules and Polymers*," Wiley (1997).

[10] J. Cornil, S. Verlaak, N. Martinelli, A. Mityashin, Y. Olivier, T. Van Regemorter, G. D'Avino, L. Muccioli, C. Zannoni, F. Castet, D. Beljonne, P. Heremans, "Exploring the Energy Landscape of the Charge Transport Levels in Organic Semiconductors at the Molecular Scale," Accounts of Chemical Research, 46, 434–443 (2013).

[11] C. Wang, H. Dong, W. Hu, Y. Liu, D. Zhu, "Semiconducting π-conjugated systems in field-effect transistors: A material odyssey of organic electronics," Chemical Reviews, 112, 2208–2267 (2012).

[12] J. Rivnay, S. C. B. Mannsfeld, C. E. Miller, A. Salleo, M. F. Toney, "Quantitative Determination of Organic Semiconductor Microstructure from the Molecular to Device Scale," Chemical Reviews, 112, 5488–5519 (2012).

[13] T. M. Figueira-Duarte, K. Müllen, "Pyrene-Based Materials for Organic Electronics," Chemical Reviews, 111, 7260–7314 (2011).

[14] N. Karl,"Charge carrier transport in organic semiconductors," Synthetic Metals, 133–134, 649–657 (2003).

[15] H. Sirringhaus, "An equal-opportunity conductor," Nature Materials, 2, 641–642 (2003).

[16] G. Horowitz, "Organic Semiconductors for new electronic devices," Advanced Materials, 2, 287–292 (1990).

[17] S. Allard, M. Forster, B. Souharce, H. Thiem, U. Scherf, "Organic semiconductors for solution-processable field-effect transistors (OFETs)," Angewandte Chemie - International Edition, 47, 4070–4098 (2008).

[18] H. E. Katz, "Recent Advances in Semiconductor Performance and Printing Processes for Organic Transistor-Based Electronics," Chemistry of Materials, 16,

4748–4756 (2004).

[19] R. Hamilton, C. Bailey, W. Duffy, M. Heeney, M. Shkunov, D. Sparrowe, S. Tierney, I. McCulloch, R. J. Kline, D. M. DeLongchamp, M. Chabinyc, "The influence of molecular weight on the microstructure and thin film transistor characteristics of pBTTT polymers.," Proc. SPIE 6336, Organic Field-Effect Transistors V, 633611 (2006).

[20] R. J. Kline, M. D. McGehee, E. N. Kadnikova, J. Liu, J. M. J. J. Fréchet, M. F. Toney, "Dependence of Regioregular Poly(3-hexylthiophene) Film Morphology and Field-Effect Mobility on Molecular Weight," Macromolecules, 38, 3312–3319 (2005).

[21] R. Zhang, B. Li, M. C. Iovu, M. Jeffries-EL, G. Sauvé, J. Cooper, S. Jia, S. Tristram-Nagle, D. M. Smilgies, D. N. Lambeth, R. D. McCullough, T. Kowalewski, "Nanostructure Dependence of Field-Effect Mobility in Regioregular Poly(3-hexylthiophene) Thin Film Field Effect Transistors," Journal of the American Chemical Society, 128, 3480–3481 (2006).

[22] A. Zen, M. Saphiannikova, D. Neher, J. Grenzer, S. Grigorian, U. Pietsch, U. Asawapirom, S. Janietz, U. Scherf, I. Lieberwirth, G. Wegner, "Effect of Molecular Weight on the Structure and Crystallinity of Poly(3-hexylthiophene)," Macromolecules, 39, 2162–2171 (2006).

[23] J.-F. Chang, B. Sun, D. W. Breiby, M. M. Nielsen, T. I. Sölling, M. Giles, I. McCulloch, H. Sirringhaus, "Enhanced Mobility of Poly(3-hexylthiophene) Transistors by Spin-Coating from High-Boiling-Point Solvents," Chemistry of Materials, 16, 4772–4776 (2004).

[24] L. A. Majewski, J. W. Kingsley, C. Balocco, A. M. Song, "Influence of processing conditions on the stability of poly(3-hexylthiophene)-based field-effect transistors," Applied Physics Letters, 88, 222108 (2006).

[25] M. Surin, P. Leclère, R. Lazzaroni, J. D. Yuen, G. Wang, D. Moses, A. J. Heeger, S. Cho, K. Lee, "Relationship between the microscopic morphology and the charge transport properties in poly(3-hexylthiophene) field-effect transistors," Journal of Applied Physics, 100, 033712 (2006).

[26] H. Jia, S. Gowrisanker, G. K. Pant, R. M. Wallace, B. E. Gnade, "Effect of poly (3-hexylthiophene) film thickness on organic thin film transistor properties," Journal of Vacuum Science & Technology A: Vacuum, Surfaces, and Films, 24, 1228–1232 (2006).

[27] Y. D. Park, D. H. Kim, Y. Jang, J. H. Cho, M. Hwang, H. S. Lee, J. A. Lim, K. Cho, "Effect of side chain length on molecular ordering and field-effect mobility in poly(3-alkylthiophene) transistors," Organic Electronics, 7, 514–520 (2006).

[28] Z. Bao, Y. Feng, A. Dodabalapur, V. R. Raju, A. J. Lovinger, "High-Performance Plastic Transistors Fabricated by Printing Techniques," Chemistry of Materials, 9, 1299–1301 (1997).

[29] B. S. Ong, Y. Wu, P. Liu, S. Gardner, "High-Performance Semiconducting Polythiophenes for Organic Thin-Film Transistors," Journal of the American Chemical Society, 126, 3378–3379 (2004).

[30] M. L. Chabinyc, F. Endicott, B. D. Vogt, D. M. DeLongchamp, E. K. Lin, Y. Wu, P. Liu, B. S. Ong, "Effects of humidity on unencapsulated poly(thiophene) thin-film transistors," Applied Physics Letters, 88, 113514 (2006).

[31] M. Heeney, C. Bailey, K. Genevicius, M. Shkunov, D. Sparrowe, S. Tierney, I. McCulloch, "Stable Polythiophene Semiconductors Incorporating Thieno[2,3- b]thiophene," Journal of the American Chemical Society, 127, 1078–1079 (2005).

[32] L.-L. Chua, P. K. H. Ho, H. Sirringhaus, R. H. Friend, "Observation of Field-

Effect Transistor Behavior at Self-Organized Interfaces," Advanced Materials, 16, 1609–1615 (2004).

[33] H. Yan, M.-H. Yoon, A. Facchetti, T. J. Marks, "Organic field-effect transistors based on a crosslinkable polymer blend as the semiconducting layer," Applied Physics Letters, 87, 183501 (2005).

[34] K. Ogawa, J. A. Stafford, S. D. Rothstein, D. E. Tallman, S. C. Rasmussen, "Nitrogen-functionalized polythiophenes: Potential routes to new low band gap materials," Synthetic Metals, 152, 137–140 (2005).

[35] K. Ogawa, S. C. Rasmussen, "N-Functionalized Poly(dithieno[3,2- b :2‘,3‘- d]pyrrole)s: Highly Fluorescent Materials with Reduced Band Gaps," Macromolecules, 39, 1771–1778 (2006).

[36] J. Liu, R. Zhang, G. Sauvé, T. Kowalewski, R. D. McCullough, "Highly Disordered Polymer Field Effect Transistors: N -Alkyl Dithieno[3,2- b :2′,3′- d]pyrrole-Based Copolymers with Surprisingly High Charge Carrier Mobilities," Journal of the American Chemical Society, 130, 13167–13176 (2008).

[37] T. Yamamoto, H. Kokubo, M. Kobashi, Y. Sakai, "Alignment and Field-Effect Transistor Behavior of an Alternative π-Conjugated Copolymer of Thiophene and 4-Alkylthiazole," Chemistry of Materials, 16, 4616–4618 (2004).

[38] M. He, J. Li, M. L. Sorensen, F. Zhang, R. R. Hancock, H. H. Fong, V. A. Pozdin, D.-M. Smilgies, G. G. Malliaras, "Alkylsubstituted Thienothiophene Semiconducting Materials: Structure−Property Relationships," Journal of the American Chemical Society, 131, 11930–11938 (2009).

[39] M. He, J. Li, A. Tandia, M. Sorensen, F. Zhang, H. H. Fong, V. A. Pozdin, D.-M. Smilgies, G. G. Malliaras, "Importance of C 2 Symmetry for the Device Performance of a Newly Synthesized Family of Fused-Ring Thiophenes," Chemistry of Materials, 22, 2770–2779 (2010).

[40] J. Nakayama, T. Fujimori, "Preparation of a Series of Oligo[thiophene-2,5-diyl]vinylenes," Heterocycles, 32, 991 (1991).

[41] Y. Fu, H. Cheng, R. L. Elsenbaumer, "Electron-Rich Thienylene−Vinylene Low Bandgap Polymers," Chemistry of Materials, 9, 1720–1724 (1997).

[42] H. Ebata, T. Izawa, E. Miyazaki, K. Takimiya, M. Ikeda, H. Kuwabara, T. Yui, "Highly soluble [1]benzothieno[3,2-b]benzothiophene (BTBT) derivatives for high-performance, solution-processed organic field-effect transistors," Journal of the American Chemical Society, 129, 15732–15733 (2007).

[43] S. Shinamura, E. Miyazaki, K. Takimiya, "Synthesis, Properties, Crystal Structures, and Semiconductor Characteristics of Naphtho[1,2- b :5,6- b ′]dithiophene and -diselenophene Derivatives," The Journal of Organic Chemistry, 75, 1228–1234 (2010).

[44] I. Osaka, T. Abe, S. Shinamura, E. Miyazaki, K. Takimiya, "High-Mobility Semiconducting Naphthodithiophene Copolymers," Journal of the American Chemical Society, 132, 5000–5001 (2010).

[45] R. Stalder, J. Mei, J. R. Reynolds, "Isoindigo-Based Donor−Acceptor Conjugated Polymers," Macromolecules, 43, 8348–8352 (2010).

[46] Wang, E., Z. Ma, Z. Zhang, K. Vandewal, P. Henriksson, O. Inganäs, F. Zhang, M. R. Andersson. "An easily accessible isoindigo-based polymer for high-performance polymer solar cells," Journal of the American Chemical Society, 133, 14244–14247 (2011).

[47] L. Bürgi, M. Turbiez, R. Pfeiffer, F. Bienewald, H. J. Kirner, C. Winnewisser, "High-mobility ambipolar near-infrared light-emitting polymer field-effect transistors," Advanced Materials, 20, 2217–2224 (2008).

[48] Y. Li, P. Sonar, S. P. Singh, M. S. Soh, M. van Meurs, J. Tan, "Annealing-Free High-Mobility Diketopyrrolopyrrole−Quaterthiophene Copolymer for Solution-Processed Organic Thin Film Transistors," Journal of the American Chemical Society, 133, 2198–2204 (2011).

[49] X. Zhang, L. J. Richter, D. M. DeLongchamp, R. J. Kline, M. R. Hammond, I. McCulloch, M. Heeney, R. S. Ashraf, J. N. Smith, T. D. Anthopoulos, B. Schroeder, Y. H. Geerts, D. A. Fischer, M. F. Toney, "Molecular Packing of High-Mobility Diketo Pyrrolo-Pyrrole Polymer Semiconductors with Branched Alkyl Side Chains," Journal of the American Chemical Society, 133, 15073–15084 (2011).

[50] H. Bronstein, Z. Chen, R. S. Ashraf, W. Zhang, J. Du, J. R. Durrant, P. Shakya Tuladhar, K. Song, S. E. Watkins, Y. Geerts, M. M. Wienk, R. A. J. Janssen, T. Anthopoulos, H. Sirringhaus, M. Heeney, I. McCulloch, "Thieno[3,2- b]thiophene−Diketopyrrolopyrrole-Containing Polymers for High-Performance Organic Field-Effect Transistors and Organic Photovoltaic Devices," Journal of the American Chemical Society, 133, 3272–3275 (2011).

[51] J. Li, Y. Zhao, H. S. Tan, Y. Guo, C.-A. Di, G. Yu, Y. Liu, M. Lin, S. H. Lim, Y. Zhou, H. Su, B. S. Ong, "A stable solution-processed polymer semiconductor with record high-mobility for printed transistors," Scientific Reports, 2, 754 (2012).

[52] I. Kang, H.-J. Yun, D. S. Chung, S.-K. Kwon, Y.-H. Kim, "Record High Hole Mobility in Polymer Semiconductors via Side-Chain Engineering," Journal of the American Chemical Society, 135, 14896–14899 (2013).

[53] Y. Li, P. Sonar, L. Murphy, W. Hong, "High mobility diketopyrrolopyrrole (DPP)-based organic semiconductor materials for organic thin film transistors and photovoltaics," Energy & Environmental Science, 6, 1684 (2013).

[54] R. Hajlaoui, G. Horowitz, F. Garnier, A. Arce-Brouchet, L. Laigre, K. A. El, F. F. Demanze, F. F. Kouki, A. El Kassmi, F. F. Demanze, F. F. Kouki, "Improved field-effect mobility in short oligothiophenes: Quaterthiophene and quinquethiophene," Advanced Materials, 9, 389–391 (1997).

[55] A. Dodabalapur, L. Torsi, H. E. Katz, "Organic Transistors - 2-Dimensional Transport and Improved Electrical Characteristics," Science, 268, 270–271 (1995).

[56] R. Hajlaoui, D. Fichou, G. Horowitz, B. Nessakh, M. Constant, F. Garnier, "Organic transistors using α-octithiophene and α, ω-dihexyl-α-octithiophene: Influence of oligomer length versus molecular ordering on mobility," Advanced Materials, 9, 557–561 (1997).

[57] F. Garnier, G. Horowitz, D. Fichou, A. Yassar, "Molecular order in organic-based field-effect transistors," Synthetic Metals, 81, 163–171 (1996).

[58] P. Ostoja, P. Maccagnani, M. Gazzano, M. Cavallini, J. C. Kengne, R. Kshirsagar, F. Biscarini, M. Melucci, M. Zambianchi, G. Barbarella, "FET device performance, morphology and X-ray thin film structure of unsubstituted and modified quinquethiophenes," Synthetic Metals, 146, 243–250 (2004).

[59] M. E. Hajlaoui, F. Garnier, L. Hassine, F. Kouki, H. Bouchriha, "Growth conditions effects on morphology and transport properties of an oligothiophene semiconductor," Synthetic Metals, 129, 215–220 (2002).

[60] M. A. Loi, E. da Como, F. Dinelli, M. Murgia, R. Zamboni, F. Biscarini, M. Muccini, "Supramolecular organization in ultra-thin films of α-sexithiophene on silicon dioxide," Nature Materials, 4, 81–85 (2004).

[61] K. Takimiya, S. Shinamura, I. Osaka, E. Miyazaki, "Thienoacene-Based Organic

Semiconductors," Advanced Materials, 23, 4347–4370 (2011).
[62] H. Sirringhaus, R. H. Friend, C. Wang, J. Leuninger, K. Müllen, "Dibenzothienobisbenzothiophene-a novel fused-ring oligomer with high field-effect mobility," Journal of Materials Chemistry, 9, 2095–2101 (1999).
[63] J. G. Laquindanum, H. E. Katz, A. J. Lovinger, "Synthesis, Morphology, and Field-Effect Mobility of Anthradithiophenes," Journal of the American Chemical Society, 120, 664–672 (1998).
[64] M. M. Payne, S. R. Parkin, J. E. Anthony, C. C. Kuo, T. N. Jackson, "Organic field-effect transistors from solution-deposited functionalized acenes with mobilities as high as 1 cm2/Vs," Journal of the American Chemical Society, 127, 4986–4987 (2005).
[65] K. Takimiya, H. Ebata, K. Sakamoto, T. Izawa, T. Otsubo, Y. Kunugi, "2,7-Diphenyl[1]benzothieno[3,2-b]benzothiophene, a new organic semiconductor for air-stable organic field-effect transistors with mobilities up to 2.0 cm2 V-1 s-1," Journal of the American Chemical Society, 128, 12604–12605 (2006).
[66] T. Yamamoto, K. Takimiya, "Facile Synthesis of Highly π-Extended Heteroarenes, Dinaphtho[2,3- b :2‘,3‘- f]chalcogenopheno[3,2- b]chalcogenophenes, and Their Application to Field-Effect Transistors," Journal of the American Chemical Society, 129, 2224–2225 (2007).
[67] M. J. Kang, I. Doi, H. Mori, E. Miyazaki, K. Takimiya, M. Ikeda, H. Kuwabara, "Alkylated Dinaphtho[2,3-b:2′,3′-f]Thieno[3,2-b]Thiophenes (Cn-DNTTs): Organic Semiconductors for High-Performance Thin-Film Transistors," Advanced Materials, 23, 1222–1225 (2011).
[68] K. Niimi, S. Shinamura, I. Osaka, E. Miyazaki, K. Takimiya, "Dianthra[2,3-b :2′,3′- f]thieno[3,2- b]thiophene (DATT): Synthesis, Characterization, and FET Characteristics of New π-Extended Heteroarene with Eight Fused Aromatic Rings," Journal of the American Chemical Society, 133, 8732–8739 (2011).
[69] L. Chua, J. Zaumseil, J. Chang, E. C.-W. Ou, P. K.-H. Ho, H. Sirringhaus, R. H. Friend, "General observation of n-type field-effect behaviour in organic semiconductors.," Nature, 434, 194–199 (2005).
[70] A. Babel, S. A. Jenekhe, "High Electron Mobility in Ladder Polymer Field-Effect Transistors," Journal of the American Chemical Society, 125, 13656–13657 (2003).
[71] J. A. Letizia, M. R. Salata, C. M. Tribout, A. Facchetti, M. A. Ratner, T. J. Marks, "n-channel polymers by design: Optimizing the interplay of solubilizing substituents, crystal packing, and field-effect transistor characteristics in polymeric bithiophene-imide semiconductors," Journal of the American Chemical Society, 130, 9679–9694 (2008).
[72] X. Zhan, Z. Tan, B. Domercq, Z. An, X. Zhang, S. Barlow, Y. Li, D. Zhu, B. Kippelen, S. R. Marder, "A high-mobility electron-transport polymer with broad absorption and its use in field-effect transistors and all-polymer solar cells," Journal of the American Chemical Society, 129, 7246–7247 (2007).
[73] A. S. Lang, M.-A. Muth, C. D. Heinrich, M. Carassco-Orozco, M. Thelakkat, "Pendant perylene polymers with high electron mobility," Journal of Polymer Science Part B: Polymer Physics, 51, 1480–1486 (2013).
[74] Z. Chen, Y. Zheng, H. Yan, A. Facchetti, "Naphthalenedicarboximide- vs Perylenedicarboximide-Based Copolymers. Synthesis and Semiconducting Properties in Bottom-Gate N-Channel Organic Transistors," Journal of the American Chemical Society, 131, 8–9 (2009).
[75] Y.-J. Hwang, N. M. Murari, S. a. Jenekhe, "New n-type polymer semiconductors

based on naphthalene diimide and selenophene derivatives for organic field-effect transistors," Polymer Chemistry, 4, 3187 (2013).

[76] Y. Kim, J. Hong, J. H. Oh, C. Yang, "Naphthalene Diimide Incorporated Thiophene-Free Copolymers with Acene and Heteroacene Units: Comparison of Geometric Features and Electron-Donating Strength of Co-units," Chemistry of Materials, 25, 3251–3259 (2013).

[77] R. Kim, P. S. K. Amegadze, I. Kang, H.-J. Yun, Y.-Y. Noh, S.-K. Kwon, Y.-H. Kim, "High-Mobility Air-Stable Naphthalene Diimide-Based Copolymer Containing Extended π-Conjugation for n-Channel Organic Field Effect Transistors," Advanced Functional Materials, 23, 5719–5727 (2013).

[78] T. Lei, J.-H. Dou, X.-Y. Cao, J.-Y. Wang, J. Pei, "Electron-Deficient Poly(p -phenylene vinylene) Provides Electron Mobility over 1 cm 2 V –1 s –1 under Ambient Conditions," Journal of the American Chemical Society, 135, 12168–12171 (2013).

[79] H. Li, F. S. Kim, G. Ren, E. C. Hollenbeck, S. Subramaniyan, S. A. Jenekhe, "Tetraazabenzodifluoranthene Diimides: Building Blocks for Solution-Processable n-Type Organic Semiconductors," Angewandte Chemie International Edition, 52, 5513–5517 (2013).

[80] Y. Takeda, T. L. Andrew, J. M. Lobez, A. J. Mork, T. M. Swager, "An Air-Stable Low-Bandgap n-Type Organic Polymer Semiconductor Exhibiting Selective Solubility in Perfluorinated Solvents," Angewandte Chemie International Edition, 51, 9042–9046 (2012).

[81] C. Kanimozhi, N. Yaacobi-Gross, K. W. Chou, A. Amassian, T. D. Anthopoulos, S. Patil, "Diketopyrrolopyrrole-diketopyrrolopyrrole-based conjugated copolymer for high-mobility organic field-effect transistors," Journal of the American Chemical Society, 134, 16532–16535 (2012).

[82] G. Guillaud, M. Al Sadoun, M. Maitrot, J. Simon, M. Bouvet, "Field-effect transistors based on intrinsic molecular semiconductors," Chemical Physics Letters, 167, 503–506 (1990).

[83] Z. Bao, A. J. Lovinger, J. Brown, "New Air-Stable n -Channel Organic Thin Film Transistors," 7863, 207–208 (1998).

[84] M.-M. Ling, Z. Bao, P. Erk, "Air-stable n-channel copper hexachlorophthalocyanine for field-effect transistors," Applied Physics Letters, 89, 163516 (2006).

[85] H. Wang, F. Zhu, J. Yang, Y. Geng, D. Yan, "Weak Epitaxy Growth Affording High-Mobility Thin Films of Disk-Like Organic Semiconductors," Advanced Materials, 19, 2168–2171 (2007).

[86] A. Facchetti, M. Mushrush, M. H. Yoon, G. R. Hutchison, M. A. Ratner, T. J. Marks, "Building blocks for n-type molecular and polymeric electronics. Perfluoroalkyl- versus alkyl-functionalized oligothiophenes (nT; n = 2-6). Systematics of thin film microstructure, semiconductor performance, and modeling of majority charge injection in fie," Journal of the American Chemical Society, 126, 13859–13874 (2004).

[87] A. Facchetti, M. H. Yoon, C. L. Stern, G. R. Hutchison, M. A. Ratner, T. J. Marks, "Building blocks for N-type molecular and polymeric electronics. Perfluoroalkyl- versus alkyl-functionalized oligothiophenes (nTs; n = 2-6). Systematic synthesis, spectroscopy, electrochemistry, and solid-state organization," Journal of the American Chemical Society, 126, 13480–13501 (2004).

[88] A. Facchetti, Y. Deng, A. Wang, Y. Koide, H. Sirringhaus, T. J. Marks, R. H.

Friend, "Tuning the Semiconducting Properties of Transistors **," Angewandte Chemie International Edition, 39, 4547–4551 (2000).

[89] J. A. Letizia, A. Facchetti, C. L. Stern, M. A. Ratner, T. J. Marks, "High Electron Mobility in Solution-Cast and Vapor-Deposited Phenacyl−Quaterthiophene-Based Field-Effect Transistors: Toward N-Type Polythiophenes," Journal of the American Chemical Society, 127, 13476–13477 (2005).

[90] T. M. Pappenfus, R. J. Chesterfield, C. D. Frisbie, K. R. Mann, J. Casado, J. D. Raff, L. L. Miller, "A π-Stacking Terthiophene-Based Quinodimethane Is an n-Channel Conductor in a Thin Film Transistor," Journal of the American Chemical Society, 124, 4184–4185 (2002).

[91] J. Kastner, J. Paloheimo, H. Kuzmany, "Fullerene Field-Effect Transistors," Springer (1993).

[92] R. C. Haddon, A. S. Perel, R. C. Morris, T. T. M. Palstra, A. F. Hebard, R. M. Fleming, "C 60 thin film transistors," Applied Physics Letters, 67, 121–123 (1995).

[93] R. C. Haddon, "C 70 Thin Film Transistors," Journal of the American Chemical Society, 118, 3041–3042 (1996).

[94] K. Itaka, M. Yamashiro, J. Yamaguchi, M. Haemori, S. Yaginuma, Y. Matsumoto, M. Kondo, H. Koinuma, "High-Mobility C60 Field-Effect Transistors Fabricated on Molecular- Wetting Controlled Substrates," Advanced Materials, 18, 1713–1716 (2006).

[95] T. D. Anthopoulos, B. Singh, N. Marjanovic, N. S. Sariciftci, A. Montaigne Ramil, H. Sitter, M. Cölle, D. M. de Leeuw, "High performance n-channel organic field-effect transistors and ring oscillators based on C60 fullerene films," Applied Physics Letters, 89, 213504 (2006).

[96] M. Chikamatsu, S. Nagamatsu, Y. Yoshida, K. Saito, K. Yase, K. Kikuchi, "Solution-processed n-type organic thin-film transistors with high field-effect mobility," Applied Physics Letters, 87, 203504 (2005).

[97] P. H. Wöbkenberg, D. D. C. Bradley, D. Kronholm, J. C. Hummelen, D. M. de Leeuw, M. Cölle, T. D. Anthopoulos, "High mobility n-channel organic field-effect transistors based on soluble C60 and C70 fullerene derivatives," Synthetic Metals, 158, 468–472 (2008).

[98] Y. Qiao, Y. Guo, C. Yu, F. Zhang, W. Xu, Y. Liu, D. Zhu, "Diketopyrrolopyrrole-Containing Quinoidal Small Molecules for High-Performance, Air-Stable, and Solution-Processable n-Channel Organic Field-Effect Transistors," Journal of the American Chemical Society, 134, 4084–4087 (2012).

[99] X. Gao, C. Di, Y. Hu, X. Yang, H. Fan, F. Zhang, Y. Liu, H. Li, D. Zhu, "Core-Expanded Naphthalene Diimides Fused with 2-(1,3-Dithiol-2-Ylidene)Malonitrile Groups for High-Performance, Ambient-Stable, Solution-Processed n-Channel Organic Thin Film Transistors," Journal of the American Chemical Society, 132, 3697–3699 (2010).

[100] F. Zhang, Y. Hu, T. Schuettfort, C. Di, X. Gao, C. R. McNeill, L. Thomsen, S. C. B. Mannsfeld, W. Yuan, H. Sirringhaus, D. Zhu, "Critical Role of Alkyl Chain Branching of Organic Semiconductors in Enabling Solution-Processed N-Channel Organic Thin-Film Transistors with Mobility of up to 3.50 cm 2 V–1 s–1," Journal of the American Chemical Society, 135, 2338–2349 (2013).

[101] J. Mei, Y. Diao, A. L. Appleton, L. Fang, Z. Bao, "Integrated materials design of organic semiconductors for field-effect transistors," Journal of the American Chemical Society, 135, 6724–6746 (2013).

[102] R. Ozdemir, D. Choi, M. Ozdemir, G. Kwon, H. Kim, U. Sen, C. Kim, H. Usta, "Ultralow bandgap molecular semiconductors for ambient-stable and solution-processable ambipolar organic field-effect transistors and inverters," Journal of Materials Chemistry C, 5, 2368–2379 (2017).

[103] M. Yilmaz, M. Ozdemir, H. Erdogan, U. Tamer, U. Sen, A. Facchetti, H. Usta, G. Demirel, "Micro-/Nanostructured Highly Crystalline Organic Semiconductor Films for Surface-Enhanced Raman Spectroscopy Applications," Advanced Functional Materials, 25, 5669–5676 (2015).

[104] E. K. Burnett, J. Ly, M. R. Niazi, L. Zhang, S. R. McCuskey, A. Amassian, D. Smilgies, S. C. B. Mannsfeld, A. L. Briseno, "Bistetracene Thin Film Polymorphic Control to Unravel the Effect of Molecular Packing on Charge Transport," Advanced Materials Interfaces, 5, 1701607 (2018).

[105] G. Demirel, H. Usta, M. Yilmaz, M. Celik, H. A. Alidagi, F. Buyukserin, "Surface-enhanced Raman spectroscopy (SERS): an adventure from plasmonic metals to organic semiconductors as SERS platforms," Journal of Materials Chemistry C, 6, 5314–5335 (2018).

[106] V. Figa, C. Chiappara, F. Ferrante, M. P. Casaletto, F. Principato, S. Cataldo, Z. Chen, H. Usta, A. Facchetti, B. Pignataro, "Symmetric naphthalenediimidequaterthiophenes for electropolymerized electrochromic thin films," Journal of Materials Chemistry C, 3, 5985–5994 (2015).

[107] M. G. Kim, M. G. Kanatzidis, A. Facchetti, T. J. Marks, "Low-temperature fabrication of high-performance metal oxide thin-film electronics via combustion processing," Nature Materials, 10, 382–388 (2011).

[108] L. Zhang, N. S. Colella, B. P. Cherniawski, S. C. B. Mannsfeld, A. L. Briseno, "Oligothiophene Semiconductors: Synthesis, Characterization, and Applications for Organic Devices," ACS Applied Materials & Interfaces, 6, 5327–5343 (2014).

[109] Y. Liu, L. Zhang, H. Lee, H.-W. Wang, A. Santala, F. Liu, Y. Diao, A. L. Briseno, T. P. Russell, "NDI-Based Small Molecule as Promising Nonfullerene Acceptor for Solution-Processed Organic Photovoltaics," Advanced Energy Materials, 5, 1500195 (2015).

[110] J. O. Kim, S. Y. Kwon, Y. Kim, H. B. Choi, J. C. Yang, J. Oh, H. S. Lee, J. Y. Sim, S. Ryu, S. Park, "Highly Ordered 3D Microstructure-Based Electronic Skin Capable of Differentiating Pressure, Temperature, and Proximity," ACS Applied Materials and Interfaces, 11, 1503–1511 (2019).

[111] M. Ozdemir, D. Choi, G. Kwon, Y. Zorlu, H. Kim, M.-G. Kim, S. Seo, U. Sen, M. Citir, C. Kim, H. Usta, "Design, synthesis, and characterization of α,ω-disubstituted indeno[1,2-b]fluorene-6,12-dione-thiophene molecular semiconductors. Enhancement of ambipolar charge transport through synthetic tailoring of alkyl substituents," RSC Advances, 6, 212–226 (2016).

[112] S. Y. Son, G. Lee, S. Kim, W. Park, S. A. Park, Y. Noh, T. Park, "Control of Crystallite Orientation in Diketopyrrolopyrrole-Based Semiconducting Polymers via Tuning of Intermolecular Interactions," ACS Applied Materials & Interfaces, 11, 10751–10757 (2019).

[113] B. Nketia-yawson, A. Jung, H. D. Nguyen, K. Lee, B. Kim, Y. Noh, "Difluorobenzothiadiazole and Selenophene-Based Conjugated Polymer Demonstrating an Effective Hole Mobility Exceeding 5 cm2 V–1 s–1 with Solid-State Electrolyte Dielectric," ACS Applied Materials & Interfaces, 10, 32492–32500 (2018).

[114] J. O. Kim, J. C. Lee, M. J. Kim, H. Noh, H. I. Yeom, J. B. Ko, T. H. Lee, S. H.

Ko Park, D. P. Kim, S. Park, "Inorganic Polymer Micropillar-Based Solution Shearing of Large-Area Organic Semiconductor Thin Films with Pillar-Size-Dependent Crystal Size," Advanced Materials, 30, 1–7 (2018).

[115] S. Shi, H. Wang, M. A. Uddin, K. Yang, M. Su, L. Bianchi, P. Chen, X. Cheng, H. Guo, S. Zhang, H. Y. Woo, X. Guo, "Head-to-Head Linked Dialkylbifuran-Based Polymer Semiconductors for High-Performance Organic Thin-Film Transistors with Tunable Charge Carrier Polarity," Chemistry of Materials, 31, 1808–1817 (2019).

[116] Y. Shi, H. Guo, M. Qin, Y. Wang, J. Zhao, H. Sun, H. Wang, Y. Wang, X. Zhou, A. Facchetti, X. Lu, M. Zhou, X. Guo, "Imide-Functionalized Thiazole-Based Polymer Semiconductors: Synthesis, Structure-Property Correlations, Charge Carrier Polarity, and Thin-Film Transistor Performance," Chemistry of Materials, 30, 7988–8001 (2018).

[117] G. Horowitz, D. Fichou, X. Peng, F. Garnier, "Thin-film transistors based on alpha-conjugated oligomers," Synthetic Metals, 41, 1127–1130 (1991).

[118] J. E. Anthony, "Functionalized acenes and heteroacenes for organic electronics," Chemical Reviews, 106, 5028–5048 (2006).

[119] A. Facchetti, "Semiconductors for organic transistors," Materials Today, 10, 28–37 (2007).

[120] A. Wesley Horton, "The mechanism of the reactions of hydrocarbons with sulfur," Journal of Organic Chemistry, 14, 761–770 (1949).

[121] P. Kaszynski, D. A. Dougherty, "Synthesis and Properties of Diethyl 5,10-Dihetera-5,10-dihydroindeno[2,1-a]indene-2,7-dicarboxylates," Journal of Organic Chemistry, 58, 5209–5220 (1993).

[122] B. Košata, V. Kozmik, J. Svoboda, V. Novotná, P. Vaněk, M. Glogarová, "Novel liquid crystals based on [1]benzothieno[3,2-b][1]benzothiophene," Liquid Crystals, 30, 603–610 (2003).

[123] M.-C. Um, J. Kwak, J.-P. Hong, J. Kang, D. Y. Yoon, S. H. Lee, C. Lee, J.-I. Hong, "High-performance organic semiconductors for thin-film transistors based on 2,7-divinyl[1]benzothieno[3,2-b]benzothiophene," Journal of Materials Chemistry, 18, 4698–4703 (2008).

[124] A. Y. Amin, A. Khassanov, K. Reuter, T. Meyer-Friedrichsen, M. Halik, "Low-voltage organic field effect transistors with a 2-tridecyl[1] benzothieno[3,2-b][1]benzothiophene semiconductor layer," Journal of the American Chemical Society, 134, 16548–16550 (2012).

[125] H. Iino, T. Usui, J.-I. Hanna, "Liquid crystals for organic thin-film transistors," Nature Communications, 6, 6828 (2015).

[126] G. Schweicher, V. Lemaur, C. Niebel, C. Ruzié, Y. Diao, O. Goto, W. Y. Lee, Y. Kim, J. B. Arlin, J. Karpinska, A. R. Kennedy, S. R. Parkin, Y. Olivier, S. C. B. Mannsfeld, J. Cornil, Y. H. Geerts, Z. Bao, "Bulky end-capped [1]Benzothieno[3,2-b]benzothiophenes: Reaching high-mobility organic semiconductors by fine tuning of the crystalline solid-state Order," Advanced Materials, 27, 3066–3072 (2015).

[127] Y. He, M. Sezen, D. Zhang, A. Li, L. Yan, H. Yu, C. He, O. Goto, Y.-L. Loo, H. Meng, "High Performance OTFTs Fabricated Using a Calamitic Liquid Crystalline Material of 2-(4-Dodecyl phenyl)[1]benzothieno[3,2- b][1]benzothiophene," Advanced Electronic Materials, 2, 1600179 (2016).

[128] K. He, W. Li, H. Tian, J. Zhang, D. Yan, Y. Geng, F. Wang, "Asymmetric Conjugated Molecules Based on [1]Benzothieno[3,2- b][1]benzothiophene for High-Mobility Organic Thin-Film Transistors: Influence of Alkyl Chain Length,"

ACS Applied Materials & Interfaces, 9, 35427–35436 (2017).

[129] M. R. Reddy, H. Kim, C. Kim, S. Seo, "2-Thiopene[1]benzothieno[3,2- b]benzothiophene derivatives as solution-processable organic semiconductors for organic thin-film transistors," Synthetic Metals, 235, 153–159 (2018).

[130] Y. He, W. Xu, I. Murtaza, D. Zhang, C. He, Y. Zhu, H. Meng, "Molecular phase engineering of organic semiconductors based on a [1]benzothieno[3,2-b][1]benzothiophene core," RSC Advances, 6, 95149–95155 (2016).

[131] Y. Yuan, G. Giri, A. L. Ayzner, A. P. Zoombelt, S. C. B. Mannsfeld, J. Chen, D. Nordlund, M. F. Toney, J. Huang, Z. Bao, "Ultra-high mobility transparent organic thin film transistors grown by an off-centre spin-coating method.," Nature communications, 5, 3005 (2014).

[132] H. Minemawari, T. Yamada, H. Matsui, J. Y. Tsutsumi, S. Haas, R. Chiba, R. Kumai, T. Hasegawa, "Inkjet printing of single-crystal films," Nature, 475, 364–367 (2011).

[133] T. Mori, T. Nishimura, T. Yamamoto, I. Doi, E. Miyazaki, I. Osaka, K. Takimiya, "Consecutive Thiophene-Annulation Approach to π-Extended Thienoacene-Based Organic Semiconductors with [1]Benzothieno[3,2- b][1]benzothiophene (BTBT) Substructure," Journal of the American Chemical Society, 135, 13900–13913 (2013).

[134] K. Takimiya, T. Yamamoto, H. Ebata, T. Izawa, "Design strategy for air-stable organic semiconductors applicable to high-performance field-effect transistors," Science and Technology of Advanced Materials, 8, 273–276 (2007).

[135] A. Facchetti, J. Letizia, M. H. Yoon, M. Mushrush, H. E. Katz, T. J. Marks, "Synthesis and characterization of diperfluorooctyl-substituted phenylene-thiophene oligomers as n-type semiconductors. Molecular structure-film microstructure-mobility relationships, organic field-effect transistors, and transistor nonvolatile memory elem," Chemistry of Materials, 16, 4715–4727 (2004).

[136] J. Tsutsumi, S. Matsuoka, S. Inoue, H. Minemawari, T. Yamada, T. Hasegawa, "N-type field-effect transistors based on layered crystalline donor-acceptor semiconductors with dialkylated benzothienobenzothiophenes as electron donors," Journal of Materials Chemistry C, 3, 1976–1981 (2015).

[137] M. L. Tang, Z. Bao, "Halogenated materials as organic semiconductors," Chemistry of Materials, 23, 446–455 (2011).

[138] M. J. Frisch, G. W. Trucks, H. B. Schlegel, G. E. Scuseria, M., H. A. Robb, J. R. Cheeseman, G. Scalmani, V. Barone, B. Mennucci, G. A. Petersson, J. L. Nakatsuji, M. Caricato, X. Li, H. P. Hratchian, A. F. Izmaylov, J. Bloino, G. Zheng, T. Sonnenberg, M. Hada, M. Ehara, K. Toyota, R. Fukuda, J. Hasegawa, M. Ishida, F. Nakajima, Y. Honda, O. Kitao, H. Nakai, T. Vreven, J. A. Montgomery, Jr., J. E. Peralta, R. Ogliaro, M. Bearpark, J. J. Heyd, E. Brothers, K. N. Kudin, V. N. Staroverov, J. Kobayashi, J. Normand, K. Raghavachari, A. Rendell, J. C. Burant, S. S. Iyengar, C. Tomasi, M. Cossi, N. Rega, J. M. Millam, M. Klene, J. E. Knox, J. B. Cross, V. Bakken, C. Adamo, J. Jaramillo, R. Gomperts, R. E. Stratmann, O. Yazyev, A. J. Austin, R. Cammi, P. Pomelli, J. W. Ochterski, R. L. Martin, K. Morokuma, V. G. Zakrzewski, G. A. Voth, J. V. Salvador, J. J. Dannenberg, S. Dapprich, A. D. Daniels, Ö. Farkas, J. B. Foresman, and D. J. F. Ortiz, J. Cioslowski, D. J. Fox, "Gaussian 09, Revision C.01," Gaussian, Inc., Wallingford CT (2010).

[139] J.-L. Brédas, D. Beljonne, V. Coropceanu, J. Cornil, "Charge-Transfer and Energy-Transfer Processes in π-Conjugated Oligomers and Polymers: A

Molecular Picture," Chemical Reviews, 104, 4971–5004 (2004).

[140] E. F. Valeev, V. Coropceanu, D. A. da Silva Filho, S. Salman, J.-L. Brédas, "Effect of Electronic Polarization on Charge-Transport Parameters in Molecular Organic Semiconductors," Journal of the American Chemical Society, 128, 9882–9886 (2006).

[141] A. D. Becke, "Density-functional thermochemistry. III. The role of exact exchange," The Journal of Chemical Physics, 98, 5648–5652 (1993).

[142] C. Lee, W. Yang, R. G. Parr, "Development of the Colle-Salvetti correlation-energy formula into a functional of the electron density," Physical Review B, 37, 785–789 (1988).

[143] J. P. Perdew, J. A. Chevary, S. H. Vosko, A. J. Koblar, M. R. Pederson, D. J. Singh, C. Fiolhais, "Atoms, molecules, solids and surfaces: Applications of the GGA for exchange correlation," Physical Review B, 46, 6671–6687 (1992).

[144] J. P. Perdew, J. A. Chevary, S. H. Vosko, K. A. Jackson, M. R. Pederson, D. J. Singh, C. Fiolhais, "Erratum: Atoms, molecules, solids, and surfaces: Applications of the generalized gradient approximation for exchange and correlation," Physical Review B, 48, 4978 (1993).

[145] W. J. Hehre, K. Ditchfield, J. A. Pople, "Self-consistent molecular orbital methods. XII. Further extensions of gaussian-type basis sets for use in molecular orbital studies of organic molecules," The Journal of Chemical Physics, 56, 2257–2261 (1972).

[146] M. M. Francl, W. J. Pietro, W. J. Hehre, J. S. Binkley, M. S. Gordon, D. J. DeFrees, J. A. Pople, "Self-consistent molecular orbital methods. XXIII. A polarization-type basis set for second-row elements," The Journal of Chemical Physics, 77, 3654–3665 (1982).

[147] G. Sini, J. S. Sears, J. L. Brédas, "Evaluating the performance of DFT functionals in assessing the interaction energy and ground-state charge transfer of donor/acceptor complexes: Tetrathiafulvalene-tetracyanoquinodimethane (TTF-TCNQ) as a model case," Journal of Chemical Theory and Computation, 7, 602–609 (2011).

[148] M.-C. Chen, Y.-J. Chiang, C. Kim, Y.-J. Guo, S.-Y. Chen, Y.-J. Liang, Y.-W. Huang, T.-S. Hu, G.-H. Lee, A. Facchetti, T. J. Marks, "One-pot [1+1+1] synthesis of dithieno[2,3-b:3′,2′-d]thiophene (DTT) and their functionalized derivatives for organic thin-film transistors," Chemical Communications, 1846–1848 (2009).

[149] A. Schwarzer, W. Seichter, E. Weber, H. Stoeckli-Evans, M. Losada, J. Hulliger, "Supramolecular control of fluorinated benzophenones in the crystalline state," CrystEngComm, 6, 567–572 (2004).

[150] M. H. Yoon, A. Facchetti, C. E. Stern, T. J. Marks, "Fluorocarbon-modified organic semiconductors: Molecular architecture, electronic, and crystal structure tuning of arene- versus fluoroarene-thiophene oligomer thin-film properties," Journal of the American Chemical Society, 128, 5792–5801 (2006).

[151] G. M. Sheldrick, "SHELXT - Integrated space-group and crystal-structure determination," Acta Crystallographica Section A: Foundations of Crystallography, 71, 3–8 (2015).

[152] G. M. Sheldrick, "Crystal structure refinement with SHELXL," Acta Crystallographica Section C Structural Chemistry, 71, 3–8 (2015).

[153] A. L. Spek, "Structure validation in chemical crystallography," Acta Crystallographica Section D: Biological Crystallography, 65, 148–155 (2009).

[154] C. F. Macrae, P. R. Edgington, P. McCabe, E. Pidcock, G. P. Shields, R. Taylor,

M. Towler, J. Van De Streek, "Mercury: Visualization and analysis of crystal structures," Journal of Applied Crystallography, 39, 453–457 (2006).

[155] H. Usta, A. Facchetti, "Organic Semiconductors for Transparent Electronics," in *Flexible Carbon-based Electronics* 13–50 (Wiley-VCH Verlag GmbH & Co. KGaA, 2018).

[156] R. Capelli, S. Toffanin, G. Generali, H. Usta, A. Facchetti, M. Muccini, "Organic light-emitting transistors with an efficiency that outperforms the equivalent light-emitting diodes.," Nature materials, 9, 496–503 (2010).

[157] H. E. Katz, J. Johnson, A. J. Lovinger, W. Li, "Naphthalenetetracarboxylic diimide-based n-channel transistor semiconductors: Structural variation and thiol-enhanced gold contacts," Journal of the American Chemical Society, 122, 7787–7792 (2000).

[158] B. A. Jones, A. Facchetti, M. R. Wasielewski, T. J. Marks, "Tuning Orbital Energetics in Arylene Diimide Semiconductors. Materials Design for Ambient Stability of n-Type Charge Transport," Journal of the American Chemical Society, 129, 15259–15278 (2007).

[159] I. Yagi, K. Tsukagoshi, Y. Aoyagi, "Modification of the electric conduction at the pentacene SiO2 interface by surface termination of SiO2," Applied Physics Letters, 86, 1–3 (2005).

[160] H. Yang, T. J. Shin, M. M. Ling, K. Cho, C. Y. Ryu, Z. Bao, "Conducting AFM and 2D GIXD studies on pentacene thin films," Journal of the American Chemical Society, 127, 11542–11543 (2005).

[161] C.-W. Chu, S.-H. Li, C.-W. Chen, V. Shrotriya, Y. Yang, "High-performance organic thin-film transistors with metal oxide/metal bilayer electrode," Applied Physics Letters, 87, 193508 (2005).

[162] Y. Zhou, C. Fuentes-Hernandez, J. Shim, J. Meyer, A. J. Giordano, H. Li, P. Winget, T. Papadopoulos, H. Cheun, J. Kim, M. Fenoll, A. Dindar, W. Haske, E. Najafabadi, T. M. Khan, H. Sojoudi, S. Barlow, S. Graham, J.-L. Bredas, S. R. Marder, A. Kahn, B. Kippelen, "A Universal Method to Produce Low-Work Function Electrodes for Organic Electronics," Science, 336, 327–332 (2012).

[163] C. Liu, Y. Xu, Y.-Y. Noh, "Contact engineering in organic field-effect transistors," Materials Today, 18, 79–96 (2015).

[164] Z. Sun, S. Shi, Q. Bao, X. Liu, M. Fahlman, "Role of Thick-Lithium Fluoride Layer in Energy Level Alignment at Organic/Metal Interface: Unifying Effect on High Metallic Work Functions," Advanced Materials Interfaces, 2, 1400527 (2015).

[165] H. Usta, A. Facchetti, T. J. Marks, "n -Channel Semiconductor Materials Design for Organic Complementary Circuits," Accounts of Chemical Research, 44, 501–510 (2011).

[166] Z. Yan, B. Sun, Y. Li, "Novel stable (3E,7E)-3,7-bis(2-oxoindolin-3-ylidene)benzo[1,2-b:4,5- b′]difuran-2,6(3H,7H)-dione based donor-acceptor polymer semiconductors for n-type organic thin film transistors," Chemical Communications, 49, 3790–3792 (2013).

[167] J. Huang, Z. Mao, Z. Chen, D. Gao, C. Wei, W. Zhang, G. Yu, "Diazaisoindigo-Based Polymers with High-Performance Charge-Transport Properties: From Computational Screening to Experimental Characterization," Chemistry of Materials, 28, 2209–2218 (2016).

[168] H. Usta, W. C. Sheets, M. Denti, G. Generali, R. Capelli, S. Lu, X. Yu, M. Muccini, A. Facchetti, "Perfluoroalkyl-functionalized thiazole-thiophene oligomers as N-channel semiconductors in organic field-effect and light-emitting

transistors," Chemistry of Materials, 26, 6542–6556 (2014).

[169] M. C. R. Delgado, E.-G. Kim, D. A. da S. Filho, J.-L. Bredas, "Tuning the Charge-Transport Parameters of Perylene Diimide Single Crystals via End and/or Core Functionalization: A Density Functional Theory Investigation," Journal of the American Chemical Society, 132, 3375–3387 (2010).

[170] G. Nan, Z. Li, "Crystal structure versus charge transport in organic single crystals of [1]benzothieno[3,2-b][1]benzothiophene derivatives from a multiscale theoretical study," Journal of Materials Chemistry C, 2, 1447–1456 (2014).

[171] W. Wu, Y. Liu, D. Zhu, "π-Conjugated molecules with fused rings for organic field-effect transistors: design, synthesis and applications," Chem. Soc. Rev., 39, 1489–1502 (2010).

[172] H. Huang, L. Yang, A. Facchetti, T. J. Marks, "Organic and Polymeric Semiconductors Enhanced by Noncovalent Conformational Locks," Chemical Reviews, 117, 10291–10318 (2017).

[173] A. Punzi, A. Operamolla, O. Hassan Omar, F. Brunetti, A. D. Scaccabarozzi, G. M. Farinola, N. Stingelin, "Designing Small Molecules as Ternary Energy-Cascade Additives for Polymer:Fullerene Solar Cell Blends," Chemistry of Materials, 30, 2213–2217 (2018).

[174] J. T. E. Quinn, J. Zhu, X. Li, J. Wang, Y. Li, "Recent progress in the development of n-type organic semiconductors for organic field effect transistors," Journal of Materials Chemistry C, 5, 8654–8681 (2017).

[175] B. Lim, H. Sun, J. Lee, Y.-Y. Noh, "High Performance Solution Processed Organic Field Effect Transistors with Novel Diketopyrrolopyrrole-Containing Small Molecules," Scientific Reports, 7, 164 (2017).

[176] R. Ozdemir, S. Park, İ. Deneme, Y. Park, Y. Zorlu, H. A. Alidagi, K. Harmandar, C. Kim, H. Usta, "Triisopropylsilylethynyl-substituted indenofluorenes: Carbonyl: versus dicyanovinylene functionalization in one-dimensional molecular crystals and solution-processed n-channel OFETs," Organic Chemistry Frontiers, 5, 2912–2924 (2018).

[177] D. Khim, K.-J. Baeg, J. Kim, M. Kang, S.-H. Lee, Z. Chen, A. Facchetti, D.-Y. Kim, Y.-Y. Noh, "High Performance and Stable N-Channel Organic Field-Effect Transistors by Patterned Solvent-Vapor Annealing," ACS Applied Materials & Interfaces, 5, 10745–10752 (2013).

[178] C. Ruiz, I. Arrechea-Marcos, A. Benito-Hernández, E. Gutierrez-Puebla, M. A. Monge, J. T. López Navarrete, M. C. Ruiz Delgado, R. P. Ortiz, B. Gómez-Lor, "Solution-processed N -trialkylated triindoles for organic field effect transistors," Journal of Materials Chemistry C, 6, 50–56 (2018).

[179] D. Zhao, J. Chen, B. Wang, G. Wang, Z. Chen, J. Yu, X. Guo, W. Huang, T. J. Marks, A. Facchetti, "Engineering Intrinsic Flexibility in Polycrystalline Molecular Semiconductor Films by Grain Boundary Plasticization," Journal of the American Chemical Society, 142, 5487–5492 (2020).

[180] M. Mushrush, A. Facchetti, M. Lefenfeld, H. E. Katz, T. J. Marks, "Easily Processable Phenylene−Thiophene-Based Organic Field-Effect Transistors and Solution-Fabricated Nonvolatile Transistor Memory Elements," Journal of the American Chemical Society, 125, 9414–9423 (2003).

[181] A. R. Murphy, J. M. J. Fréchet, "Organic semiconducting oligomers for use in thin film transistors," Chemical Reviews, 107, 1066–1096 (2007).

[182] Y.-Y. Noh, R. Azumi, M. Goto, B.-J. Jung, E. Lim, H.-K. Shim, Y. Yoshida, K. Yase, D.-Y. Kim, "Organic Field Effect Transistors Based on Biphenyl, Fluorene End-Capped Fused Bithiophene Oligomers," Chemistry of Materials, 17, 3861–

3870 (2005).

[183] Y. Liu, C. Di, C. Du, Y. Liu, K. Lu, W. Qiu, G. Yu, "Synthesis, Structures, and Properties of Fused Thiophenes for Organic Field-Effect Transistors," Chemistry - A European Journal, 16, 2231–2239 (2010).

[184] W. Jiang, Y. Li, Z. Wang, "Heteroarenes as high performance organic semiconductors," Chemical Society Reviews, 42, 6113–6127 (2013).

[185] X.-C. Li, H. Sirringhaus, F. Garnier, A. B. Holmes, S. C. Moratti, N. Feeder, W. Clegg, S. J. Teat, R. H. Friend, "A Highly π-Stacked Organic Semiconductor for Thin Film Transistors Based on Fused Thiophenes," Journal of the American Chemical Society, 120, 2206–2207 (1998).

[186] M. L. Tang, A. D. Reichardt, P. Wei, Z. Bao, "Correlating Carrier Type with Frontier Molecular Orbital Energy Levels in Organic Thin Film Transistors of Functionalized Acene Derivatives," Journal of the American Chemical Society, 131, 5264–5273 (2009).

[187] C. D. Sheraw, T. N. Jackson, D. L. Eaton, J. E. Anthony, "Functionalized pentacene active layer organic thin-film transistors," Advanced Materials, 15, 2009–2011 (2003).

[188] X. Zhan, A. Facchetti, S. Barlow, T. J. Marks, M. A. Ratner, M. R. Wasielewski, S. R. Marder, "Rylene and related diimides for organic electronics," Advanced Materials, 23, 268–284 (2011).

[189] T. Mori, T. Oyama, H. Komiyama, T. Yasuda, "Solution-grown unidirectionally oriented crystalline thin films of a U-shaped thienoacene-based semiconductor for high-performance organic field-effect transistors," Journal of Materials Chemistry C, 5, 5872–5876 (2017).

[190] J. Il Park, J. W. Chung, J. Y. Kim, J. Lee, J. Y. Jung, B. Koo, B. L. Lee, S. W. Lee, Y. W. Jin, S. Y. Lee, "Dibenzothiopheno[6,5-b:6′,5′-f]thieno[3,2-b]thiophene (DBTTT): High-Performance Small-Molecule Organic Semiconductor for Field-Effect Transistors," Journal of the American Chemical Society, 137, 12175–12178 (2015).

[191] K. He, S. Zhou, W. Li, H. Tian, Q. Tang, J. Zhang, D. Yan, Y. Geng, F. Wang, "Five-ring-fused asymmetric thienoacenes for high mobility organic thin-film transistors: the influence of the position of the S atom in the terminal thiophene ring," Journal of Materials Chemistry C, 7, 3656–3664 (2019).

[192] H. Usta, D. Kim, R. Ozdemir, Y. Zorlu, S. Kim, M. C. Ruiz Delgado, A. Harbuzaru, S. Kim, G. Demirel, J. Hong, Y.-G. Ha, K. Cho, A. Facchetti, M.-G. Kim, "High Electron Mobility in [1]Benzothieno[3,2- b][1]benzothiophene-Based Field-Effect Transistors: Toward n-Type BTBTs," Chemistry of Materials, 31, 5254–5263 (2019).

[193] A. Naibi Lakshminarayana, A. Ong, C. Chi, "Modification of acenes for n-channel OFET materials," Journal of Materials Chemistry C, 6, 3551–3563 (2018).

[194] C. R. Newman, C. D. Frisbie, D. A. da Silva Filho, J.-L. Brédas, P. C. Ewbank, K. R. Mann, "Introduction to Organic Thin Film Transistors and Design of n-Channel Organic Semiconductors," Chemistry of Materials, 16, 4436–4451 (2004).

[195] J. Dhar, U. Salzner, S. Patil, "Trends in molecular design strategies for ambient stable n-channel organic field effect transistors," Journal of Materials Chemistry C, 5, 7404–7430 (2017).

[196] C. Zhang, Y. Zang, F. Zhang, Y. Diao, C. R. McNeill, C. Di, X. Zhu, D. Zhu, "Pursuing High-Mobility n-Type Organic Semiconductors by Combination of

“Molecule-Framework” and “Side-Chain” Engineering," Advanced Materials, 28, 8456–8462 (2016).

[197] C.-Y. Yang, W.-L. Jin, J. Wang, Y.-F. Ding, S. Nong, K. Shi, Y. Lu, Y.-Z. Dai, F.-D. Zhuang, T. Lei, C.-A. Di, D. Zhu, J.-Y. Wang, J. Pei, "Enhancing the n-Type Conductivity and Thermoelectric Performance of Donor-Acceptor Copolymers through Donor Engineering," Advanced Materials, 30, 1802850 (2018).

[198] G. Wang, F. S. Melkonyan, A. Facchetti, T. J. Marks, "All-Polymer Solar Cells: Recent Progress, Challenges, and Prospects," Angewandte Chemie - International Edition, 58, 4129–4142 (2019).

[199] D. Yang, D. Ma, "Development of Organic Semiconductor Photodetectors: From Mechanism to Applications," Advanced Optical Materials, 7, 1800522 (2019).

[200] D. Ho, R. Ozdemir, H. Kim, T. Earmme, H. Usta, C. Kim, "BODIPY-Based Semiconducting Materials for Organic Bulk Heterojunction Photovoltaics and Thin-Film Transistors," ChemPlusChem, 84, 18–37 (2019).

[201] M. Grabolle, M. Spieles, V. Lesnyak, N. Gaponik, A. Eychmüller, U. Resch-Genger, "Determination of the fluorescence quantum yield of quantum dots: Suitable procedures and achievable uncertainties," Analytical Chemistry, 81, 6285–6294 (2009).

[202] Y. Altintas, M. Y. Talpur, M. Ünlü, E. Mutlugün, "Highly Efficient Cd-Free Alloyed Core/Shell Quantum Dots with Optimized Precursor Concentrations," Journal of Physical Chemistry C, 120, 7885–7892 (2016).

[203] E. Jacques, M. Romain, A. Yassin, S. Bebiche, M. Harnois, T. Mohammed-Brahim, J. Rault-Berthelot, C. Poriel, "An electron deficient dicyanovinylene-ladder-type pentaphenylene derivative for n-type organic field effect transistors," Journal of Materials Chemistry C, 2, 3292–3302 (2014).

[204] H. Usta, C. Risko, Z. Wang, H. Huang, M. K. Deliomeroglu, A. Zhukhovitskiy, A. Facchetti, T. J. Marks, "Design, Synthesis, and Characterization of Ladder-Type Molecules and Polymers. Air-Stable, Solution-Processable n -Channel and Ambipolar Semiconductors for Thin-Film Transistors via Experiment and Theory," Journal of the American Chemical Society, 131, 5586–5608 (2009).

[205] M. Romain, M. Chevrier, S. Bebiche, T. Mohammed-Brahim, J. Rault-Berthelot, E. Jacques, C. Poriel, "The structure–property relationship study of electron-deficient dihydroindeno[2,1-b]fluorene derivatives for n-type organic field effect transistors," Journal of Materials Chemistry C, 3, 5742–5753 (2015).

[206] S. Inoue, H. Minemawari, J. Tsutsumi, M. Chikamatsu, T. Yamada, S. Horiuchi, M. Tanaka, R. Kumai, M. Yoneya, T. Hasegawa, "Effects of Substituted Alkyl Chain Length on Solution-Processable Layered Organic Semiconductor Crystals," Chemistry of Materials, 27, 3809–3812 (2015).

[207] V. S. Vyas, R. Gutzler, J. Nuss, K. Kern, B. V. Lotsch., "Optical gap in herringbone and π-stacked crystals of [1]benzothieno[3,2-b]benzothiophene and its brominated derivative," CrystEngComm, 16, 7389–7392 (2014).

[208] J. L. Brédas, G. B. Street, B. Thémans, J. M. André, "Organic polymers based on aromatic rings (polyparaphenylene, polypyrrole, polythiophene): Evolution of the electronic properties as a function of the torsion angle between adjacent rings," The Journal of Chemical Physics, 83, 1323–1329 (1985).

[209] A. Bondi, "van der Waals Volumes and Radii," The Journal of Physical Chemistry, 68, 441–451 (1964).

[210] O. V. Dolomanov, L. J. Bourhis, R. J. Gildea, J. A. K. Howard, H. Puschmann, "OLEX2 : a complete structure solution, refinement and analysis program ,"

Journal of Applied Crystallography, 42, 339–341 (2009).

[211] R. D. McCullough, "The Chemistry of Conducting Polythiophenes," Advanced Materials, 10, 93–116 (1998).

[212] D. R. Lide, "*CRC Handbook of Chemistry and Physics*," CRC Press (2004).

[213] S. C. Lee, J. Heo, H. C. Woo, J. A. Lee, Y. H. Seo, C. L. Lee, S. Kim, O. P. Kwon, "Fluorescent Molecular Rotors for Viscosity Sensors," Chemistry - A European Journal, 24, 13706–13718 (2018).

[214] B. Chen, Y. Ding, X. Li, W. Zhu, J. P. Hill, K. Ariga, Y. Xie, "Steric hindrance-enforced distortion as a general strategy for the design of fluorescence ‘turn-on’ cyanide probes," Chemical Communications, 49, 10136–10138 (2013).

[215] J. Shao, S. Ji, X. Li, J. Zhao, F. Zhou, H. Guo, "Thiophene-inserted aryl-dicyanovinyl compounds: The second generation of fluorescent molecular rotors with significantly redshifted emission and large stokes shift," European Journal of Organic Chemistry, 6100–6109 (2011).

[216] X. Sun, T. D. James, E. V. Anslyn, "Arresting ‘loose Bolt’ Internal Conversion from -B(OH)2 Groups is the Mechanism for Emission Turn-On in ortho-Aminomethylphenylboronic Acid-Based Saccharide Sensors," Journal of the American Chemical Society, 140, 2348–2354 (2018).

[217] G. Kwon, K. Kim, B. D. Choi, J. Roh, C. Lee, Y.-Y. Noh, S. Seo, M.-G. Kim, C. Kim, "Multifunctional Organic-Semiconductor Interfacial Layers for Solution-Processed Oxide-Semiconductor Thin-Film Transistor," Advanced Materials, 29, 1607055 (2017).

[218] H. Lee, D. Lee, D. H. Sin, S. W. Kim, M. S. Jeong, K. Cho, "Effect of donor–acceptor molecular orientation on charge photogeneration in organic solar cells," NPG Asia Materials, 10, 469–481 (2018).

[219] J.-W. Lee, M. J. Sung, D. Kim, S. Lee, H. You, F. S. Kim, Y.-H. Kim, B. J. Kim, S.-K. Kwon, "Naphthalene Diimide-Based Terpolymers with Controlled Crystalline Properties for Producing High Electron Mobility and Optimal Blend Morphology in All-Polymer Solar Cells," Chemistry of Materials, 32, 2572–2582 (2020).

[220] Y. Li, M. Kim, Z. Wu, C. Lee, Y. W. Lee, J.-W. Lee, Y. J. Lee, E. Wang, B. J. Kim, H. Y. Woo, "Influence of backbone modification of difluoroquinoxaline-based copolymers on the interchain packing, blend morphology and photovoltaic properties of nonfullerene organic solar cells," Journal of Materials Chemistry C, 7, 1681–1689 (2019).

[221] K.-J. Baeg, M. Binda, D. Natali, M. Caironi, Y.-Y. Noh, "Organic Light Detectors: Photodiodes and Phototransistors," Advanced Materials, 25, 4267–4295 (2013).

[222] Y. Liu, J. Zhao, Z. Li, C. Mu, W. Ma, H. Hu, K. Jiang, H. Lin, H. Ade, H. Yan, "Aggregation and morphology control enables multiple cases of high-efficiency polymer solar cells," Nature Communications, 5, 5293 (2014).

[223] Y. Zhao, Y. Guo, Y. Liu, "25th Anniversary Article: Recent advances in n-type and ambipolar organic field-effect transistors," Advanced Materials, 25, 5372–5391 (2013).

[224] Y. Sui, Y. Deng, T. Du, Y. Shi, Y. Geng, "Design strategies of n-type conjugated polymers for organic thin-film transistors," Materials Chemistry Frontiers, 3, 1932–1951 (2019).

[225] J. Cornil, D. Beljonne, J.-P. Calbert, J.-L. Brédas, "Interchain Interactions in Organic π-Conjugated Materials: Impact on Electronic Structure, Optical Response, and Charge Transport," Advanced Materials, 13, 1053–1067 (2001).

[226] G. R. Hutchison, M. A. Ratner, T. J. Marks, "Hopping transport in conductive heterocyclic oligomers: Reorganization energies and substituent effects," Journal of the American Chemical Society, 127, 2339–2350 (2005).

[227] O. Kwon, V. Coropceanu, N. E. Gruhn, J. C. Durivage, J. G. Laquindanum, H. E. Katz, J. Cornil, J. L. Brédas, "Characterization of the molecular parameters determining charge transport in anthradithiophene," Journal of Chemical Physics, 120, 8186–8194 (2004).

[228] N. Metri, X. Sallenave, C. Plesse, L. Beouch, P.-H. Aubert, F. Goubard, C. Chevrot, G. Sini, "Processable Star-Shaped Molecules with Triphenylamine Core as Hole-Transporting Materials: Experimental and Theoretical Approach," The Journal of Physical Chemistry C, 116, 3765–3772 (2012).

CURRICULUM VITAE

2004 – 2008	B.Sc., Chemistry, Ankara University, Ankara, TURKEY
2014 – 2016	M.Sc., Advanced Materials and Nanotechnology, Abdullah Gül University, Kayseri, TURKEY
2017 – Present	Ph.D. Candidate, Materials Science and Mechanical Engineering, Abdullah Gül University, Kayseri, TURKEY

Selected Publications and Presentations

J1) R. Ozdemir, K. Ahn, İ. Deneme, Y. Zorlu, D. Kim, M.-G. Kim, H.Usta* ”Engineering Functionalized Low LUMO [1]Benzothieno[3,2-b][1]benzothiophenes (BTBTs): Unusual Molecular and Charge Transport Properties” *Journal of Materials Chemistry C*, 2020, 8, 15253-15267.

J2) H. Usta*, D. Alimli, **R. Ozdemir**, E. Tekin, F. Alkan, R. Kacar, A. G. Altas, S. Dabak, A. G. Gürek, E. Mutlugun, A. F. Yazici, A. Can "A Hybridized Local and Charge Transfer Excited State for Solution-Processed Non-doped Green Electroluminescence Based on Oligo(p-phenyleneethynylene)" *Journal of Materials Chemistry C*, 2020, 8, 8047-8060. (**Selected as the the Back Cover**)

J3) G. Demirel*, R. L. Gieseking, **R. Ozdemir**, S. Kahmann, M. A. Loi,* G. C. Schatz*, A. Facchetti*, H. Usta* "Molecular Engineering of Organic Semiconductors Enables Noble Metal-Comparable SERS Enhancement and Sensitivity" *Nature Communications*, 2019, 10, 5502.

J4) H. Usta*, D. Alımlı, **R. Ozdemir**, Y. Zorlu, S. Dabak, E. Tekin, A. Can "Solution-Processable Donor-Acceptor Oligophenyleneethynylene-based Small Molecule for Highly Efficient Deep-Blue Organic Light-Emitting Diodes" *ACS Applied Materials & Interfaces*, 2019, 11, 44474-44486. (**Selected as the Front Cover**)

J5) H. Usta*, D. Kim, **R. Ozdemir**, Y. Zorlu, S. Kim, M. C. R. Delgado, A. Harbuzaru, S. Kim, G. Demirel, J. Hong, Y. G. Ha, K. Cho, A. Facchetti*, M. G. Kim* “High Electron Mobility in [1]Benzothieno[3,2-b][1]benzothiophene-Based Field-Effect Transistors: Toward n-Type BTBTs” Chem. Mater, 2019, 31, 5254-5263. (**Selected as the Cover**)

J6) D. Ho, **R. Ozdemir,** H. Kim, T. Earmme, H. Usta*, C. Kim* "BODIPY-Based Semiconducting Materials for Organic Bulk Heterojunction Photovoltaics and Thin-Film Transistors" *ChemPlusChem,* 2019, 84, 18–37. (**Among the most downloaded articles in 2019, Readers' Choice Special Collection**)

J7) R. Ozdemir, S. Park, İ. Deneme, Y. Park, Y. Zorlu, H. A. Alidağı, K. Harmandar, C. Kim*, H. Usta* "Triisopropylsilylethynyl-Substituted Indenofluorenes: Carbonyl versus Dicyanovinylene Functionalization in One-Dimensional Molecular Crystals and Solution-Processed N-Channel OFETs" *Organic Chemistry Frontiers,* 2018, 5, 2912-2924. (**Selected as the Cover**)

C1) R. Ozdemir, D. Kim, A. Facchetti, M. G. Kim, H. Usta "First Electron Transporting [1]Benzothieno[3,2-b][1]benzothiophene (BTBT)-Based Molecular Semiconductor in TFTs" 15th International Conference on Organic Electronics (ICOE), June 2019, Hasselt, Belgium.

C2) R. Ozdemir, H. A. Alidagi, H. Usta "Dicyanovinylene Functionalized Air Stable N-type Organic Field Effect Transistors" 3rd International Conference on Material Science and Technology in Cappadocia (IMSTEC), September 2018, Nevşehir, Turkey.

C3) R. Ozdemir, H. Usta "Solution-Processable Ambipolar Small Molecular Semiconductor based Diethynylindeno[1,2-b]fluorene-6,12-dione" 3rd International Conference on Material Science and Technology in Cappadocia (IMSTEC), September 2018, Nevşehir, Turkey.